Research on Engineering Structures & Materials

P-ISSN: 2148-9807 E-ISSN: 2149-4088

Volume 7 Issue 3 September 2021

J R E S M

www.jresm.org

Research Group

The International Journal of **Research on Engineering Structures and Materials (RESM**) is a peer-reviewed open access journal (p-ISSN: 2148-9807; o-ISSN: 2149-4088) published by MIM Research Group. It is published in February, June, September, and December.

The main objective of RESM is to provide an International academic platform for researchers to share scientific results related to all aspects of mechanical, civil and material engineering areas.

RESM aims the publication of original research articles, reviews, short communications technical reports, and letters to the editor on the latest developments in the related fields.

All expenditures for the publication of the manuscripts are most kindly reimbursed by *MIM Research Group*. Thus, authors do not need to pay for publishing their studies in the journal.

The scope of the journal covers (but not limited to) behavior of structures, machines and mechanical systems, vibration, impact loadings and structural dynamics, mechanics of materials (elasticity, plasticity, fracture mechanics), material science (structure and properties of concrete, metals, ceramics, composites, plastics, wood, etc.,), nano-materials performances of new and existing buildings and other structural systems, design of buildings and other structural systems, seismic behavior of buildings and other structural systems, repair and strengthening of structural systems, case studies and failure of structural systems, safety and reliability in structural and material engineering, use of new and innovative materials and techniques in energy systems and mechanical aspects of biological systems (biomechanics and biomimetics).

The topics covered in JRESM include:

- Structural Engineering
- Mechanical Engineering
- Material Engineering
- Earthquake Engineering
- Nano-technology
- Energy Systems
- Biomechanics and Biomimetics

Abstracting and Indexing
Please visit http://www.jresm.org for more information.

Graphics and Design

Yunus Demirtaş ydemirtas@jresm.net

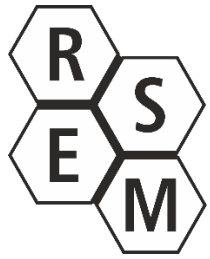

RESEARCH on ENGINEERING STRUCTURES & MATERIALS

Published by MIM Research Group

Advisory Board Members

Marijana Hadzima-Nyarko	University of Osijek	Croatia
Dulce Franco Henriques	Instituto Politécnico de Lisboa	Portugal
Manuel Horta	Universidade do Porto	Portugal
Ercan Isik	Bitlis Eren University	Turkey
Khairul Nizar Ismail	Universiti Malaysia Perlis	Malaysia
Sahar Ismail	Saint Joseph University of Beirut	Beirut
Berrin Ikizler	Ege University	Turkey
Atike İnce Yardımcı	Usak University	Turkey
Liyana Jamaludin	Universiti Malaysia Perlis	Malaysia
Saifulnizan Jamian	Universiti Tun Hussein Onn Malaysia	Malaysia
Md. Salim Kaiser	Bangladesh University of Engineering and Technology	Bangladesh
Sreevani Kannan	Chennai Institute of Technology	India
Gökhan Kaplan	Atatürk University	Turkey
Altug Karabey	Yuzuncu Yil University	Turkey
Abdulhalim Karasin	Dicle University	Turkey
Mehmet Kaya	Yozgat Bozok University	Turkey
Dogan Kaya	Cukurova University	Turkey
Deniz Kaya	Dokuz Eylul University	Turkey
Jibran Khaliq	Northumbria University	United Kingdom
Kadir Kılınç	Kırklareli University	Turkey
Sedat Kömürcü	Istanbul Technical University	Turkey
Salmabanu Luhar	Universiti Malaysia Perlis	Malaysia
Yelda Mert	Iskenderun Technical University	Turkey
Seyede Mahdieh Miralami	University of Rahman	Iran
Jinxu Mo	Yangtze University	China
Nebab Mokhtar	Hassiba Benbouali Universyt of Chlef	Algeria
Nahida Nazim Musayeva	Azerbaijan National Academy of Sciences	Azerbaijan

In This Issue

Research Article
331 **Atike Ince Yardimci, Ahmet Sabri Ogutlu, Deniz Ogutlu**
Oxidizer gases effects on the diameter-controlled synthesis of carbon nanotubes

Research Article
347 **Angelo Traina, Han J.G.E. Gardeniers, Burcu Gumuscu**
Self-powered microfluidic device for the colorimetric detection of lithium via sequential reagent mixing

Research Article
361 **Lütfiye Altay, Mehmet Sarikanat, Merve Sağlam, Tuğçe Uysalman, Yoldaş Seki**
The effect of various mineral fillers on thermal, mechanical, and rheological properties of polypropylene

Research Article
375 **P. N. Ojha, Brijesh Singh, Puneet Kaura, Abhishek Singh**
Lightweight geopolymer fly ash sand: an alternative to fine aggregate for concrete production

Research Article
393 **Hikmat Daou, Wassim Raphael**
A Bayesian regression framework for concrete creep prediction improvement: application to Eurocode 2 model

Research Article
413 **Ercan Işık, Ehsan Harirchian, Hüseyin Bilgin, Kirti Jadhav**
The effect of material strength and discontinuity in RC structures according to different site-specific design spectra

Research Article
431 **Ali Bozer**
Seismic performance of shallow depth tuned liquid damper

Research Article
445 **Yasin Onuralp Özkılıç**
Investigation of the effects of bolt diameter and end-plate thickness on the capacity and failure modes of end-plated beam-to-column connections

Technical Note

465 **Cameron R. Rusnak, Craig C. Menzemer**

Fatigue behavior of flush reinforced welded hand-holes in aluminum light poles

Research on Engineering Structures & Materials
MIM Reseach Group Publications
P-ISSN: 2148-9807
E-ISSN: 2149-4088
http://www.jresm.org

ABSTRACTING / INDEXING

The international journal of Research on Engineering Structures and Materials (RESM) is currently Absracted/Indexed by Asos Indeks, CiteFactor, Cosmos, CrossRef, Directory of Research Journal Indexing, Engineering Journals (ProQuest), EZB Electronic Journal Library, Global Impact Factor, Google Scholar, International Institute of Organized Research (I2OR), International Scientific Indexing (ISI), Materials Science & Engineering Database (ProQuest), Open Academic Journals Index, Publication Forum, Research BibleScientific Indexing Service, Root Indexing, Scopus, Ulakbim TR Index (Tubitak), Universal Impact Factor and under evaluation by many other respected indexes.

Check web site for current indexing info, www.jresm.org

Scopus®

DRJI

TÜBİTAK ULAKBİM

ProQuest

ASOS indeks

crossref

Google Scholar

Universal Impact Factor

Scientifically derived Journal Impact Factor

SIS Scientific Indexing Services

Journal Seeker Research Bible

CiteFactor Academic Scientific Journals

EZB Elektronische Zeitschriftenbibliothek

Open Academic Journals Index

GIF GLOBAL IMPACT FACTOR

ROOTINDEXING JOURNAL ABSTRACTING AND INDEXING SERVICE

Cosmos

Publication Forum

Research on Engineering Structures & Materials
journal homepage: http://jresm.org
Research Group

Research Article

Oxidizer gases effects on the diameter-controlled synthesis of carbon nanotubes

Atike Ince Yardimci[1,2,a,*], Ahmet Sabri Ogutlu[3,b], Deniz Ogutlu[4,c]

[1]*Department of Material Science and Engineering İzmir Institute of Technology, Urla, İzmir, Turkey*
[2]*Technology Transfer Office, Usak University, Usak, Turkey*
[3]*Department of Industrial Engineering Harran University, Haliliye, Şanlıurfa, Turkey*
[4]*Department of Physics İzmir Institute of Technology, Urla, İzmir, Turkey*

Article Info

Article history:
Received 19 Feb 2021
Revised 02 May 2021
Accepted 03 May 2021

Keywords:

Carbon nanotube;
Chemical Vapour;
Deposition;
Diameter Control;
Fe Catalyst

Abstract

In this study, the influence of the oxidizers on the synthesis of carbon nanotubes by C_2H_4 decomposition over Fe catalyst has been investigated. CO_2, O_2, and H_2O have been used as oxidizers, and to control catalyst particle formation and their sizes in the pretreatment stage. The same oxidizers have also been used in the growth stage to maintain the catalyst particle size, remove amorphous carbon formation to keep catalyst particle active. The results of scanning electron microscopy indicated that the average diameters of nanotubes decreased from 13.4±1.2 nm to 6.2±0.5 nm and extremely dense nanotubes were obtained when we added a small amount of CO_2. Adding O_2 extremely decreased the areal carbon nanotube density while widens the diameter distribution. H_2O addition resulted in larger average diameters and made the growth strongly pretreatment dependent. Within the parameters tried for catalyst pretreatment and CNT growth processes, CO_2 seemed the best choice for a weak oxidizing assistant. The strong dependency of the average diameter on pretreatment conditions indicated that pretreatment is a very important step in deciding the final diameters and their distribution.

1. Introduction

Carbon nanotubes (CNTs), due to their superior mechanical and physical properties [1], are undoubtedly one of the most promising nanomaterials for the growing number of applications in the nanotechnology era [2]. The distinctive characteristic properties of carbon nanotubes stem from the size of these materials and their atomic structure. Nanotubes can be either metals or semiconductors depending on their various helicity structure and diameters [3]. Also, the diameters of CNTs significantly affect their mechanical properties and thus influence their applications. Some of the applications to highly these growing areas include field emission device [4, 5], scanning probe [6-8], sensors [9, 10], high strength composite [11], and supercapacitors [12-14].

On the other hand, the growth process and controlling mechanisms of the CNTs are still not completely understood. Chemical Vapour Deposition (CVD) is the growth technique that allows control of the growth to a certain extent and it is scalable to industrial needs. All of the CVD techniques require catalyst nanoparticles for the growth of CNTs. The size of the catalyst particles which are usually chosen from transition metals plays an important role in determining the diameters of CNTs. These catalyst particles can be obtained using various techniques. Among these, the ones grown on a substrate [15] are crucially important since they will be building the bridge between microelectronics and nanotechnology. These very thin films (1-2 nm) will oxidize immediately once they are

*Corresponding author: tekin.3@osu.edu
[a] orcid.org/0000-0001-5482-4230; [b] orcid.org/0000-0003-1634-0600; [c] orcid.org/0000-0003-3135-6547
DOI: http://dx.doi.org/10.17515/resm2021.261na0219

exposed to air till CNT growth. Most assume that the effective CNT growth proceeds after metal oxide to metal reduction. It is also known that metal oxide does not coalesce completely without the reduction.

For the reduction, various oxidizers [16-18] besides hydrogen [19-21] have recently been used to adjust the reaction rate and etch away the amorphous carbon deposition during the CNT growth [22, 23]. The reduction pretreatment step and its duration are significant in defining CNT characteristics. If the pretreatment time was kept too long, the catalyst particles would have wider size distribution and larger sizes [24] due to the high temperatures needed for growth. It would lead to nanofiber formation having larger diameters and inferior characteristics compare to CNTs. All these indicators point that the reduction pretreatment and the growth start timing are the deciding factors in CNT formation. Based on this concept, there are significant efforts to optimize CNT growth conditions.

Recent efforts have focused on the oxidizers as the growth enhancers and optimization of forest growth related to CNT yields and heights in the presence of weak oxidizers [25]. Even though those are very important to improve for industrial applications, their diameters and keeping diameter distribution tightly narrow usually have not been paid enough attention. The diameter is the most important parameter in CNT production since it will be deciding the CNT characteristics [26]. For the diameter control, the thickness of the catalyst film is a good starting point however with the process parameters the diameter distribution can readily go off track.

Effective CNT growth was studied in different studies [27,28] and these studies indicated that the presence of CO_2 caused a domed CNT growth, and the height of CNT distributes was more uniformly and converted to radial block figure. CNT structures such as dishes were obtained by increasing line heights with the increased amount of CO_2. Different CNT morphologies occurred with the increase of CO_2 amount because of the change of CNT growth velocity and change of bonding force between CNT and support material. Futuba et al. studied H_2O vapor, acetone, ethanol, metilbenzoat, and CO_2 was used to improve CNT growth by etching amorphous carbon in catalysts particle poisoned. Their results indicated that from these enhancers H_2O provided the best CNT growth atmosphere among these gases and the highest CNTs were obtained with H_2O. Carpet height CNT arrays at some samples terminated after one minute. Li et all. indicated that the heights of CNT grown with the addition of air continuous to not decrease till 500 min. Average CNT diameters were 35 nm close areas of buffer layer and 100 nm up of buffer layer were obtained. These diameter values showed that the structure of CNTs was closer to fiber than a cylindrical structure [29]. CO_2 oxygenizes the amorphous carbon in CNT synthesis process, and hence the catalyst stays active longer time, and therefore length and yield of CNTs increase. Besides, CO_2 can be decomposed on the catalyst clusters surface and reacts with other molecules and radicals, resulting in intermediates that can be more effective for the CNT growth. However, in this present study, oxidizers were utilized to control catalyst size and hence CNT diameters. Besides, diameter distributions were 2-3 nm in terms of standard deviation. This value was similar to the diameters distribution of SWNT obtained in the literature [30].

This study aims to analyze and determine the role of oxidizer gases during both catalyst pretreatment and CNT growth processes. The effects of the ratios of oxidizer gases in pretreatment to those in growth, time of oxidizer gas introduction in pretreatment process, and CNT growth temperature on CNT morphologies. CO_2, O_2, and H_2O were used in small amounts as oxidizers. The main aim was to utilize oxidizers to control catalyst particle size during the reducing pretreatment process and the growth process at the same time

preventing amorphous carbon deposition over the outer walls of CNTs and catalyst particles.

All as-grown samples were characterized by scanning electron microscopy (SEM), CNT diameters were measured and diameters distributions were obtained. CNT diameters within very narrow ranges were controlled. The growth with CO_2 yielded samples with better characteristics. Lower CNT density was observed by using O_2 compared to the other oxidizers. Using oxidizers both in the pretreatment and in the growth, stages helped to keep wider metal catalyst sizes and hence CNT diameters in narrow ranges which lead to effective CNT growth.

2. Experimental Section

In this study, Fe thin films were utilized as the catalyst material for CNT growth. $Fe/Al_2O_3/SiO_2$ Commercially purchased Si substrates were utilized as a support layer and cleaned in methanol by rinsing for 15 min in an ultrasonic bath and then in ultra-pure water for 15 min. Cleaned silicon substrates were oxidized by a dry thermal oxidation system. 10-15 nm thick Al2O3 and then 1.0-1.5 nm thick Fe layers were deposited on SiO2 substrate by DC magnetron sputtering technique. In the sputtering process, base pressure was 1×10^{-6} Torr prior to catalyst film growth while film growth was carried out at a deposition rate of 0.1 Ao/s, 20 W, and a growth pressure of 0.5 mTorr.

The thermal chemical vapor deposition (CVD) method was used for the CNT growth process. In a typical experiment, 4x4 mm2 $Fe/Al_2O_3/SiO_2$ thin film samples were put into a quartz boat and placed in the middle of the quartz tube and the CVD furnace was heated to 760° C. Experiments were carried out at atmospheric pressure. C_2H_4 was utilized as a carbon source and Ar was used as the carrier gas to carry the oxide gases to the reaction chamber. At a growth temperature of 760° C, gas flows were then switched to C_2H_4, oxide gases (CO_2, O_2, H_2O), and H2 for the desired growth time. The total gas flow was kept at 250 sccm at growth. Different gas flow rates and pretreatment times for oxidizers were investigated. The flow rates of other gases were constant in all experiments and 150 sccm for Ar gas, 140 sccm for H_2 gas, and 180 sccm for C_2H_4 gases. After growth, C_2H_4, H_2O, and H2 flows were turned off and CNTs were kept to cool down to ambient temperature under Ar flow with a flow rate of 150 sccm.

In order to analyze the morphology of CNTs scanning electron microscopy (SEM) was utilized. The quality and type of CNTs were examined with Raman Spectroscopy with He-Ne laser with the excitation wavelength of 632.8 nm.

3. Results and Discussion

One of the primary objectives of this study was to examine various oxidizers effects in the catalyst pretreatment and CNT growth stages. It has been suggested that “weak” oxidizers play a sanitary role by etching away amorphous carbon accumulation over catalyst particles which poison them and, thus, extending their life so that they can remain active longer for CNT growth [31]. This way highly efficient growth could be achieved. To do this, we studied four different pretreatment times and various amounts of CO_2, O_2, H_2O. We continued to send the smaller amount of oxidizers during growth time. Consequently, we reached narrow diameter distributions in the presence of various oxidizers. Standard deviations and standard errors of the average CNT diameters were analyzed and standard deviations of all samples were obtained in the range of 1-2 nm. The standard error of the average CNT diameter was found moderately small.

3.1. The role of CO_2 for effective CNT growth

In this study, influences of CO_2 were analyzed on a variety of growth conditions to control CNT diameter at a constant CNT growth temperature. SEM images were utilized to analyze CNT diameter and more than 70 tubes diameter were counted for each sample.

3.1.1 Catalyst pretreatment time effect

The effect of CO_2 in the CNT growth using C_2H_4 as a carbon source was studied by changing both pretreatment time and CO_2 level using the $Fe/Al_2O_3/SiO_2$ thin film as catalyst material and a smaller amount of CO_2 proceeded to be sent during CNT growth. Four different pretreatment times were tested in this part of the study and these were 2, 5, 10, 15 minutes. Besides, CO_2 flow rates were sent into the CVD system during both catalyst pretreatment and CNT growth as 10:1, 10:2, 5:1, 5:2, 2:1, and 2:2 sccm, respectively. The effects of CO_2 under growth conditions were investigated by SEM images of CNTs. The catalyst particle sizes were increasing with increased pretreatment time at the ratios of 10:1 and 5:1 gas flow.

This growth carried possibly out converting elemental form after the reduction of metal-oxide to metal film with H_2 and CO_2 controlled the reduction velocity of the metal oxide film.

Catalyst immediately clustered with the effect of high temperature on the elemental metal form and especially the SiO_2 layer. Also, these clusterings were active on the surface and occurred larger nanoparticles the results of collisions with others during these motions. Large nanoparticle influence negatively CNT growth, they decreased the density of CNT at the unit area. Here are significant amounts of H_2 and CO_2. The results showed that ideal particle sizes were obtained by adjusting both pretreatment time and CO_2 level (Table 1).

Once we carefully examined that the samples of CNTs exposed to shorter pretreatment time have more uniformity, smaller average diameters, and more density of growth. This supported our events that longer pretreatment time caused more growth of catalyst particles. Once we looked from the sides and anglely (Fig. 1), we observed that 15 and 10 min. samples include much more space than samples of 5 and 2 min. This state could be explained by decreased density of CNTs by forming bigger particles of the catalyst particle. When we calculated diameter, CNT diameters change among 5nm-8nm at short pretreatment time.

The dependence of CNT diameters on pretreatment time was analyzed in detail and the results were given in Fig. 2. A high concentration of CO_2 (10 sccm) during the pretreatment process and short pretreatment time resulted in larger CNT diameters without depending on CO_2 amount during growth time. When pretreatment time was increased at high amounts of CO_2, diameters of the CNTs grown under 2 sccm CO_2 were directly decreased. However, at growth time, diameters of CNTs grown under 1 sccm CO_2 were increasing because in the presence of high CO_2, reduction of metal oxide to metal was not completely achieved, therefore large nanoparticle clustered and CNT diameter got larger. CNT diameter decreased with pretreatment time because samples were grown at high CO_2 during pretreatment time and 2 sccm CO_2 during growth prevented sufficient oxygen and smaller catalyst particle growth occurred.

The studies with low CO_2 during pretreatment time supported that 2 sccm CO_2 flow rate provided smaller diameters than 1 sccm CO_2 flows during growth time.

Table 1 Catalyst pretreatment and CNT growth parameters and average CNT diameters in the presence of CO_2/H_2 for both different pretreatment times and growth times (CNT Growth temperature: 740 °C).

Sample	Pretreatment time (min.)	CO_2(p)/CO_2(g) (sccm)	Ave. diameters (nm)
CNT1	15	10/1	12. 5
CNT2	10	10/1	10. 0
CNT3	5	10/1	9. 5
CNT4	2	10/1	8. 8
CNT5	15	10/2	6. 1
CNT6	10	10/2	6. 7
CNT7	5	10/2	6. 8
CNT8	2	10/2	11. 2
CNT9	15	5/1	9. 8
CNT10	10	5/1	9. 3
CNT11	5	5/1	8. 9
CNT12	2	5/1	6. 1
CNT13	15	5/2	5. 7
CNT14	10	5/2	6. 3
CNT15	5	5/2	7. 3
CNT16	2	5/2	7. 3

3.1.2 Temperature effect

The temperature effect in CO_2-assisted CVD was studied for four different pretreatment times at two different growth temperatures. CO_2 effects with a flow rate of 2 sccm at different growth temperatures were investigated. The results showed that average diameters were ranging between 15-29 nm at 740 °C and 5-8 nm at 760 °C (Table 2). High CNT growth temperature provided thinner nanotubes.

Carbon-oxygen reaction resulted in CO owing to catalyst particle metal oxide form [32]. If catalyst particle did not keep suitable pretreatment time and growth parameters, then catalyst surface is coated by amorphous carbon and CNT formation did not occur. The coming gas amount should be optimized and mixed with an appropriate amount of H_2.

It was expected that film coalesces by removing from the surface with the effect of temperature and hydrogen and catalyst nanoparticles properly spread the whole surface. Uniform and small particle size was necessary for efficient CNT growth.

The Fe particles were expected to diffuse uniformly on the whole surface and coalesce removing the surface with the effect of temperature and hydrogen. The temperature was more important in this situation. The coalescence was carried out after the metal oxide film

was converted to the metal film. During pretreatment, CO_2 provided controlled coalescences by controlling the speed of this translation. Also, CO_2 assisted to remove amorphous carbon that forms throughout CNT growth. Our results showed that particle size decreased with increasing temperature because more effectively reduced metal oxide form to metal form with increased temperature. At this state converter particle state from the film was easier.

By using H_2 and CO_2, smaller CNT diameters and more density CNTs were obtained at high temperatures when compared to 740 and 760 °C (Figure3). CNT growth temperatures of 740 and 760 °C displayed similar behavior depending on pretreatment time. Temperature is also a significant parameter to determine CNT diameters, as well as CO_2.

According to SEM analysis results (Fig. 4) CNT density on the surface was rare and diameters change between 15-20 nm at 740 °C. However, at 760 °C, growth on the surface enhanced and the average diameter of CNTs decreased to the range of 5-6 nm at 760 °C.

Fig. 5 showed the relationship between average CNT diameter and pretreatment time for the growths carried out at 740 and 760°C. The results indicated that firstly, CNT diameters were increasing with increasing pretreatment time and then slowly decreasing for pretreatment time of 10:1 sccm. Average diameters of both short pretreatment time and CO_2 level of 1 sccm were smallest. At large parts of 1 sccm oxidizer, this identified that catalyst nanoparticle clustering through high temperature could not prevent more large catalyst particles to occur.

3.1.3 Effect of discontinuous catalyst pretreatment

CO2 effect on CNT growth with thermal CVD has investigated the states that the pretreatment duration of CO_2 was shorter than H_2. CO_2 flow rates were 10:1, 10:2, 5:2, 5:1, 2:2 ve 2/1 sccm and pretreatment time for H2 was studied 15 and 10 min., pretreatment time for CO_2 was studied for 5 and 2 min. (Table 3). Diameters chanced between 5-8 nm. Shorter CO_2 pretreatment time according to H_2 caused by keeping a narrow range of the diameters (Figure 6).

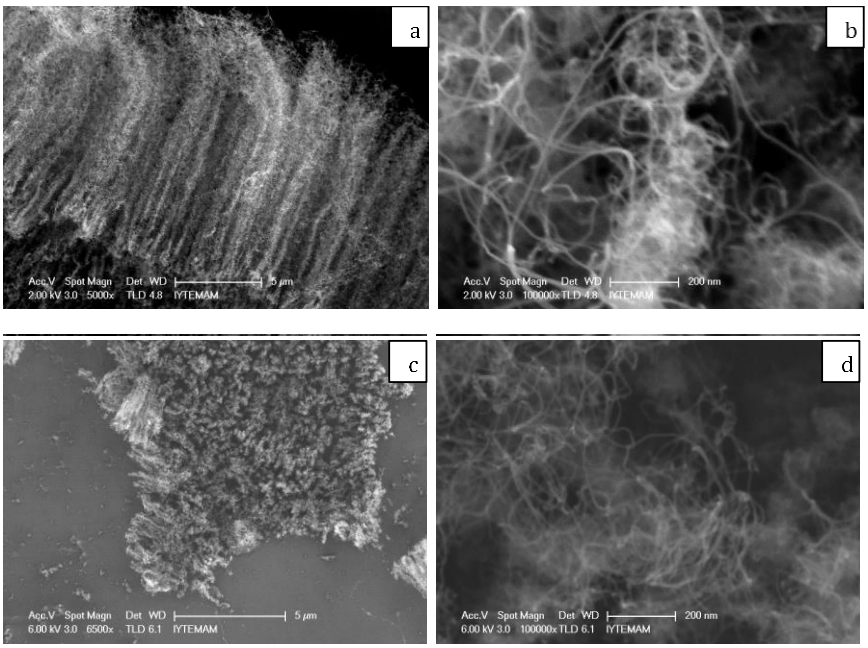

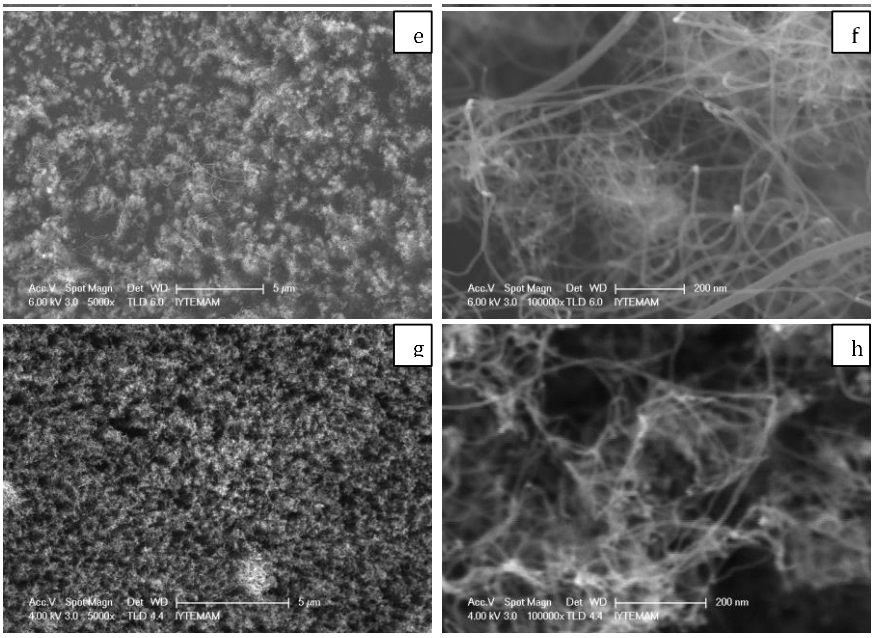

Fig. 1 SEM images of the nanotubes grown with CO2 as oxidizer at 740°C for different pretreatment times a), b) CNT1 15 min., c), d) CNT2 10 min., e), f) CNT3 5 min., g), h) CNT4 2min

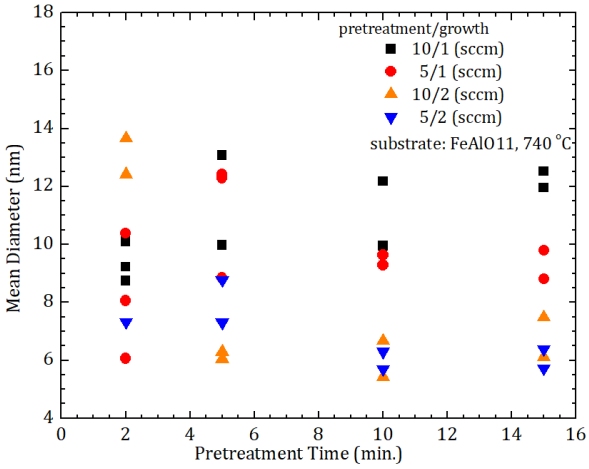

Fig. 2. Dependence of obtained average values of diameters on pretreatment time and CO_2 ratio

Table 1. Catalyst pretreatment and CNT growth parameters and average CNT diameters in the presence of CO_2/H_2 at different temperatures

Sample	Temperature (°C)	Pretreatment time (min.)	CO_2/H_2(sccm)	Ave. diameters(nm)
CNT17	740	15	2/140	20. 74
CNT18	740	10	2/140	18. 57
CNT19	740	5	2/140	17. 36
CNT20	740	2	2/140	21. 91
CNT21	760	15	2/140	6. 77
CNT22	760	10	2/140	5. 72
CNT23	760	5	2/140	5. 12
CNT24	760	2	2/140	6. 10

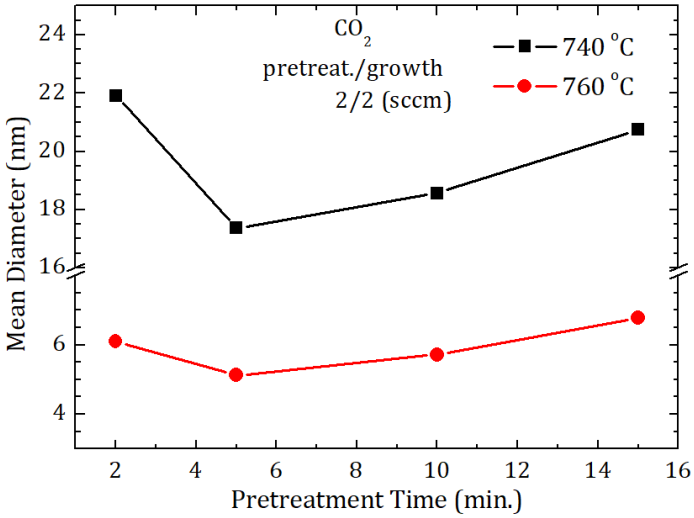

Fig. 3. Mean CNT diameters vs. catalyst pretreatment time for 740 and 760 °C, CO_2 flow rate: 2 sccm and 2 sccm during pretreatment and growth processes, respectively

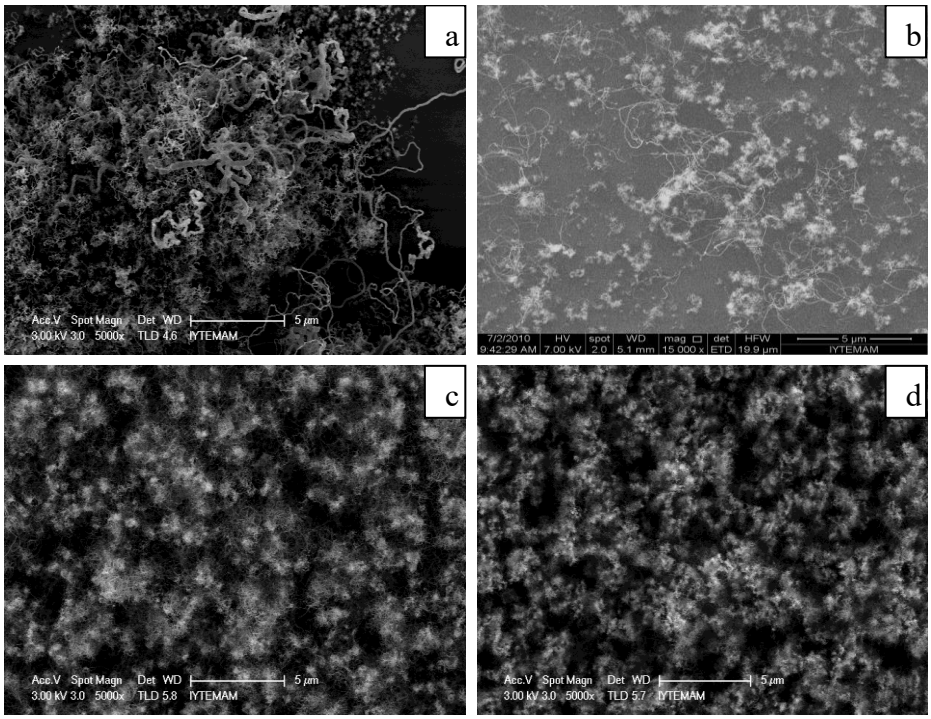

Fig. 4. SEM images of CNTs grown with CO_2, a) 740°C, CNT17, 15 min. b) 740°C, CNT18, 10 min. c) 760°C, CNT21, 15 min. d) 760°C, CNT23, 5 min

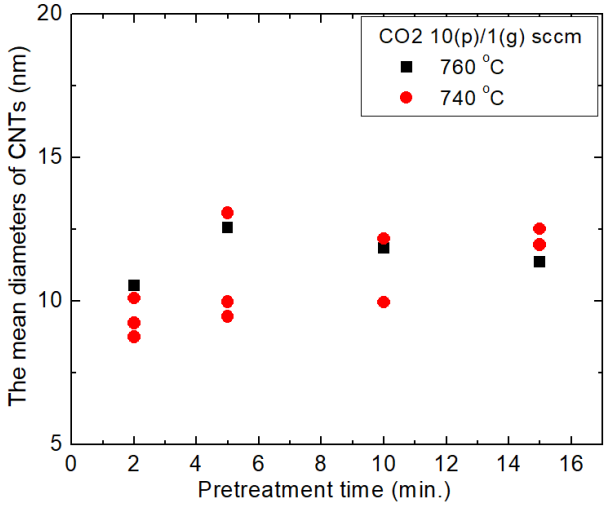

Fig. 5. Mean CNT diameter vs. catalyst pretreatment time, CO_2 flow rate: 10 sccm and 1 sccm during pretreatment and growth processes, respectively

Table 2. Catalyst pretreatment and CNT growth parameters and average CNT diameters in the presence of CO_2 +H_2 gases for different pretreatment time (CNT Growth temperature: 760 °C)

Sample	Pretreatment (min) H_2/CO_2	CO_2(p)/CO_2(g) (sccm)	Ave. diameters (nm)
CNT25	15/5	10/2	5. 96
CNT26	15/10	10/1	8. 07
CNT27	15/2	10/1	6. 60
CNT28	15/2	5/2	7. 02
CNT29	15/5	5/1	7. 50
CNT30	15/2	2/2	5. 45
CNT31	10/5	10/2	6. 82
CNT32	10/5	5/2	4. 69
CNT33	10/5	2/1	7. 29
CNT34	5/2	5/1	8. 90

3.2. The role of O_2 for effective CNT growth

The effect of O_2 for effective CNT growth with C_2H_4-CVD technique on the Fe/Al_2O_3/SiO_2 thin film was investigated for different pretreatment times and different O_2 flow rates. Examined pretreatment times were 15, 10, 5, 2 minutes. Studied O_2 flow rates during catalyst pretreatment and CNT growth were 5:1, 5:2, 2:2, 2:0.5, respectively. SEM images showed that Fe/Al_2O_3/SiO_2 thin film samples exposed to O_2 gas flow of 5:2, 5:1, 2:2, 2:0.5 sccm, resulted in larger CNT diameters while pretreatment time decreased. This growth carried out translating elemental form by removing the oxide via H_2 the catalyst being metal-oxide form. As a result, small CNT diameters ranging between 6-8 nm at the pretreatment time of 15 minutes were obtained in the presence of O_2. Average CNT diameters for pretreatment times of 10, 5, 2 min. were in the range of 9-14 nm (Table 4).

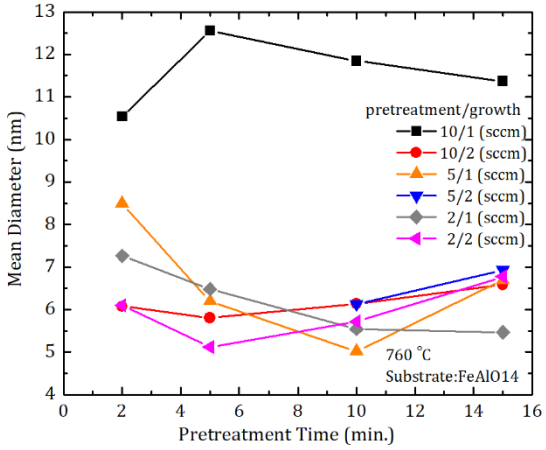

Fig. 6. Mean CNT diameter vs. catalyst pretreatment time for different pretreatment/growth CO_2 amount at growth temperature of 760 °C

Table 3. Catalyst pretreatment and CNT growth parameters in the presence of O_2 for different pretreatment times (P: 1 atm., T: 760 °C, Ar: 150 sccm H_2: 140 sccm).

Sample name	Pretreatment		CNT Growth		
	O_2 (sccm)	Time (min.)	C_2H_4 (sccm)	O_2 (sccm)	Time (min.)
CNT35	5	15	180	2	15
CNT36	5	10	180	2	15
CNT37	5	5	180	2	15
CNT38	5	2	180	2	15
CNT39	5	15	180	1	15
CNT40	5	10	180	1	15
CNT41	5	5	180	1	15
CNT42	5	2	180	1	15
CNT43	2	15	180	2	15
CNT44	2	10	180	2	15
CNT45	2	10	180	2	15
CNT46	2	15	180	0. 5	15
CNT47	2	5	180	0. 5	15
CNT48	0. 5	15	180	-	15
CNT49	-	15	180	-	15

3.3. The role of H_2O vapor for effective CNT growth

A small amount of H_2O vapor in the CNT growth process reduces amorphous carbon amounts and provided more effective production [32]. H_2O extends catalyst lifetime during pretreatment and therefore assisting efficient CNT growth.

In this part of the study, under the same parameters, the influences of H_2O vapor for effective CNT growth on the $Fe/Al_2O_3/SiO_2$ thin film were investigated. The effect of H_2O on CNT growth was examined. Pretreatment time was kept constant (15 min) and different H2O vapor levels were tested. To send H_2O vapor, a new apparatus was added to the system (Figure 7). A expressed a little amount of Ar of H_2O vapor was sent during pretreatment time. B expressed much more H_2O and Ar than A, namely B was more diluted than A. Studied H_2O vapour amounts were 50°C(A)/50°C(A), 50°C(A)/50°C(B), 50°C(B)/50°C(B), 50°C(B)/50°C(A), 60°C(A)/60°C(A), 60°C(A)/60°C(B), 60°C(B)/60°C(B), 60°C(B)/60°C(A), 70°C(A)/70°C(A), 70°C(A)/70°C(B), 70°C(B)/70°C(B), 70°C(B)/70°C(A). The results of the H2O vapor study indicated that the optimum level was 60°C(A)/60°C(A). Dense CNT growth and narrow average diameters were obtained as the samples grown with CO_2 (Table 5).

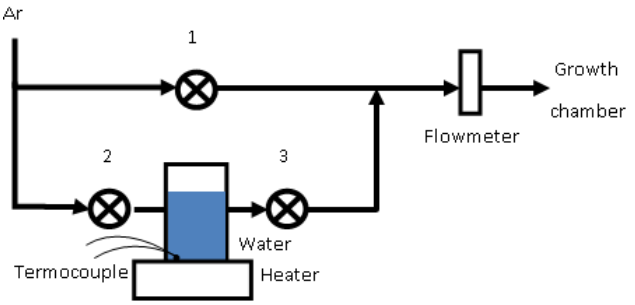

Fig. 7. The setup integrated to send H_2O vapour in the different amounts A: valve1 off, valve2 ve valve3 on, B: all valves on, C: valve1 on, valve2 ve valve3 off

Table 4. Catalyst pretreatment and CNT growth parameters and average CNT diameters in the presence of H_2O vapor (CNT growth temperature: 760 °C)

Sample Name	Pretreatment (min.)	H_2O(p)/ H_2O(g) (°C)	Ave. diameter (nm)
CNT50	15	60^0C(A)/60^0C(A)	7. 01
CNT51	15	60^0C(A)/60^0C(B)	7. 47
CNT52	15	60^0C(B)/60^0C(A)	8. 04
CNT53	15	60^0C(B)/60^0C(B)	6. 80
CNT54	15	50^0C(A)/50^0C(A)	7. 60
CNT55	15	50^0C(A)/50^0C(B)	9. 11

3.4. Raman Analysis of CNTs

Raman spectroscopy is an important characterization method to analyze the type and quality of the CNTs. In the Raman spectrum, the G-peak of the CNT sample is a characteristic feature of the graphitic layers placed at ~1580 cm^{-1}. The other characteristic CNT peak is D-peak, an indicative peak of graphitic structure defects such as amorphous carbon, soot and additional carbon structures placed at ~1335 cm^{-1}. The ratios of intensities of D/G peaks represent the quality of CNT samples. Representative Raman spectrum of a CNT sample grown under 760 °C growth temperature by utilizing CO^2 as an oxidizer with pretreatment/growth: 5/1(sccm) flow rates is given in Fig. 8. The high D peak intensity of this sample indicated defects presence in the obtained CNTs structures, I_D/I_G was calculated as 0.68 for this sample indicating a significant level of defective carbonous products. A third peak named the radial breathing mode (RBM) being very sensitive to the CNT diameter, giving information about CNT type and placed at between 100–300 cm^{-1}.

RBM peaks were not observed for the CNTs grown by utilizing CO_2 as an oxidizer and it means this sample includes multi walled CNTs. CNTs exhibit metallic or semiconducting characteristics depending on their chirality (how the graphitic sheets are rolled) [33] and the splitting of G band to G- and G+ bands (tangential modes) in Raman spectroscopy highly reveal semiconducting or metallic properties of CNTs [34]. As seen in Fig. 8, G-band did not split G- and G+ bands for the sample grown with CO_2 as oxidizer indicating the abundance of metallic multi walled CNTs.

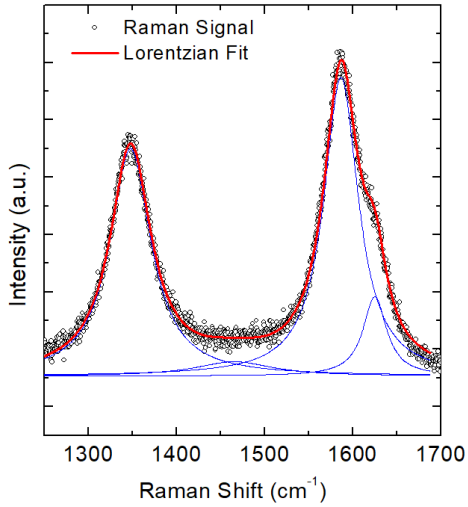

Fig. 8. Raman spectrum of CNT grown under 760 °C growth temperature by utilizing CO_2 as oxidizer with pretreatment/growth: 5/1(sccm) flow rates

4. Conclusions

In this study, the diameter-controlled synthesis of CNTs under different oxidizer gases was discussed. Systematic ways of obtaining controlled nanoparticles from catalyst film to grow the effective CNT were presented with oxidizer gases. Utilized oxidizer gases were CO_2, O_2, and H_2O vapor. Among these oxidizers, the best results were obtained by using CO_2 which provided dense CNT growth and narrow CNT diameter range.

Pretreatment time was another parameter affecting CNT quality and diameter. CNTs exposed to a shorter pretreatment time deposited uniformly and had smaller average diameters and showed more density of CNT. Longer pretreatment time caused bigger catalyst particles resulted with larger CNT diameter.

740 and 760 °C growth temperature of CNT was examined to determine the effect of temperature on CNT diameter and average diameters were significantly decreased for higher temperature.

Overall, obtained CNTs in this study were multi walled CNTs in the diameter range of 5-22 nm. By using oxidizers, a narrow range of metal catalyst sizes and thus narrow diameters of CNTs were maintained. Therefore, diameter-controlled effective production of CNTs was provided. The ability to control over diameters of CNTs makes easier to understand the fundamental properties of CNTs and develop new CNT applications.

Acknowledgments

This study was supported by The Scientific and Technological Research Council of Turkey (TUBITAK) with the project no. 109T534. We are very thankful to Yusuf Selamet for his support in all the studies mentioned in this work. Additionally, we thank İzmir Institute of Technology Material Research Center for SEM pictures.

References

[1] Endo M, Kim Y, Hayashi T, Muramatsu H, Terrones M, Saito R, Villalpando Paez F, Chou S, Dresselhaus M. Nanotube Coalescence Inducing Mode: A Novel Vibrational Mode in Carbon Systems. Small, 2006; 2:1031-1036. https://doi.org/10.1002/smll.200600087

[2] Avouris P. Carbon nanotube electronics and photonics. Physics Today, 2009; 62:34-40. https://doi.org/10.1063/1.3074261

[3] Odom T, Huang J, Kim P, Lieber C. Atomic structure and electronic properties of single-walled carbon nanotubes. Nature, 1998; 391:62-64. https://doi.org/10.1038/34145

[4] Yuan Z, Huang H, Dang H, Cao J, Hu B, Fan S. Field emission property of highly ordered monodispersed carbon nanotube arrays. Applied Physics Letters, 2001; 78: 3127. https://doi.org/10.1063/1.1372205

[5] Alvi M, Al-Ghamdi A, Husain M. Field emission studies of CNTs/ZnO nanostructured thin films for display devices. Physica B: Condensed Matter, 2017; 521:312-316. https://doi.org/10.1016/j.physb.2017.07.015

[6] Dai H, Hafner J, Rinzler A, Colbert D, Smalley R. Nanotubes as nanoprobes in scanning probe microscopy, 1996. https://doi.org/10.1038/384147a0

[7] Hafner J, Cheung C, Oosterkamp T, Lieber C. High-yield assembly of individual single-walled carbon nanotube tips for scanning probe microscopies. J. Phys. Chem. B, 2001; 105:743-746. https://doi.org/10.1021/jp003948o

[8] Tachizaki T, Nakata T, Zhang K, Yamakawa I, Taniguchi S.-i. Nanometer-precise optical length measurement using near-field scanning optical microscopy with sharpened single carbon nanotube probe. Ultramicroscopy, 2018; 186:18-22. https://doi.org/10.1016/j.ultramic.2017.12.006

[9] Kong J, Franklin N, Zhou C, Chapline M, Peng S, Cho K, Dai H. Nanotube molecular wires as chemical sensors. Science, 2000; 287: 622. https://doi.org/10.1126/science.287.5453.622

[10] Kauffman DR, Star A. Carbon nanotube gas and vapor sensors. Angewandte Chemie International Edition, 2008; 47:6550-6570. https://doi.org/10.1002/anie.200704488

[11] Chen L, Pang X, Yu Z. Study on polycarbonate/multi-walled carbon nanotubes composite produced by melt processing. Materials Science and Engineering: A, 2007; 457:287-291. https://doi.org/10.1016/j.msea.2007.01.107

[12] Dalton A, Collins S, Razal J, Munoz E, Ebron V, Kim B, Coleman J, Ferraris J, Baughman R. Continuous carbon nanotube composite fibers: properties, potential applications, and problems. Journal of Materials Chemistry, 2004; 14:1-3. https://doi.org/10.1039/b312092a

[13] Futaba D, Hata K, Yamada T, Hiraoka T, Hayamizu Y, Kakudate Y, Tanaike O, Hatori H, Yumura M, Iijima S. Shape-engineerable and highly densely packed single-walled carbon nanotubes and their application as super-capacitor electrodes. Nature Materials, 2006; 5:987-994. https://doi.org/10.1038/nmat1782

[14] Yang L, Zheng W, Zhang P, Chen J, Tian W, Zhang Y, Sun Z. MXene/CNTs films prepared by electrophoretic deposition for supercapacitor electrodes. Journal of Electroanalytical Chemistry, 2018; 830:1-6. https://doi.org/10.1016/j.jelechem.2018.10.024

[15] Jung, M, Yong Eun K, Lee J, Baik Y, Lee K, Wan Park J. Growth of carbon nanotubes by chemical vapor deposition. Diamond and Related Materials, 2001; 10:1235-1240. https://doi.org/10.1016/S0925-9635(00)00446-5

[16] Zhang G, Mann D, Zhang L, Javey A, Li Y, Yenilmez E, Wang Q, McVittie J, Nishi Y, Gibbons J. Ultra-high-yield growth of vertical single-walled carbon nanotubes: Hidden roles of hydrogen and oxygen. Proceedings of the National Academy of Sciences of the United States of America, 2005; 102:16141. https://doi.org/10.1073/pnas.0507064102

[17] Qu J, Zhao Z, Wang Z, Wang X, Qiu J. Carbon dioxide-assisted fabrication of self-organized tubular carbon micropatterns on silicon substrates. Carbon, 2010; 48:1465-1472. https://doi.org/10.1016/j.carbon.2009.12.041
[18] Amama P, Pint C, McJilton L, Kim S, Stach E, Murray P, Hauge R, Maruyama B. Role of water in super growth of single-walled carbon nanotube carpets. Nano letters, 2008; 9:44-49. https://doi.org/10.1021/nl801876h
[19] Rao F, Li T, Wang Y. Effect of hydrogen on the growth of single-walled carbon nanotubes by thermal chemical vapor deposition. Physica E: Low-dimensional Systems and Nanostructures, 2008; 40:779-784. https://doi.org/10.1016/j.physe.2007.09.185
[20] Kuo D, Su M. The effects of hydrogen and temperature on the growth and microstructure of carbon nanotubes obtained by the Fe (CO) 5 gas-phase-catalytic chemical vapor deposition. Surface and Coatings Technology, 2007; 201:9172-9178. https://doi.org/10.1016/j.surfcoat.2007.04.083
[21] Ince Yardimci A, Yılmaz S, Selamet Y. The effects of catalyst pretreatment, growth atmosphere and temperature on carbon nanotube synthesis using Co-Mo/MgO catalyst. Diamond and Related Materials, 2015; 60:81-86. https://doi.org/10.1016/j.diamond.2015.10.025
[22] Yamada T, Maigne A, Yudasaka M, Mizuno K, Futaba D, Yumura M, Iijima S, Hata K. Revealing the Secret of Water-Assisted Carbon Nanotube Synthesis by Microscopic Observation of the Interaction of Water on the Catalysts. Nano Letters, 2008; 8:4288-4292. https://doi.org/10.1021/nl801981m
[23] Zhu L, Xiu Y, Hess D, Wong C. Aligned carbon nanotube stacks by water-assisted selective etching. Nano Lett, 2005; 5:2641-2645. https://doi.org/10.1021/nl051906b
[24] Terrado E, Muñoz E, Maser W, Benito A, Martínez M. Important parameters for the catalytic nanoparticles formation towards the growth of carbon nanotube aligned arrays. Diamond and Related Materials, 2007; 16:1082-1086. https://doi.org/10.1016/j.diamond.2006.11.004
[25] Nessim G, Hart A, Kim J, Acquaviva D, Oh J, Morgan C, Seita M, Leib J, Thompson C. Tuning of vertically-aligned carbon nanotube diameter and areal density through catalyst pre-treatment. Nano letters, 2008; 8:3587-3593. https://doi.org/10.1021/nl801437c
[26] Nam TH, Goto K, Yamaguchi Y, Premalal E, Shimamura Y, Inoue Y, Naito K, Ogihara S. Effects of CNT diameter on mechanical properties of aligned CNT sheets and composites. Composites Part A: Applied Science and Manufacturing, 2015; 76:289-298. https://doi.org/10.1016/j.compositesa.2015.06.009
[27] Huang J, Zhang Q, Zhao M, Wei F. Process intensification by CO₂ for high quality carbon nanotube forest growth: Double-walled carbon nanotube convexity or single-walled carbon nanotube bowls? Nano Research, 2009; 2:872-881. https://doi.org/10.1007/s12274-009-9088-6
[28] Futaba D, Goto J, Yasuda S, Yamada T, Yumura M, Hata K. General Rules Governing the Highly Efficient Growth of Carbon Nanotubes. Advanced Materials, 2009; 21:4811-4815. https://doi.org/10.1002/adma.200901257
[29] Li X, Zhang X, Ci L, Shah R, Wolfe C, Kar S, Talapatra S, Ajayan P. Air-assisted growth of ultra-long carbon nanotube bundles. Nanotechnology, 2008; 19:455609. https://doi.org/10.1088/0957-4484/19/45/455609
[30] Hata K. Water-Assisted Highly Efficient Synthesis of Impurity-Free Single-Walled Carbon Nanotubes. Science, 2004; 306:1362-1364. https://doi.org/10.1126/science.1104962
[31] Hata K, Futaba D, Mizuno K, Namai T, Yumura M, Iijima S. Water-assisted highly efficient synthesis of impurity-free single-walled carbon nanotubes. Science, 2004; 3060:1362. https://doi.org/10.1126/science.1104962
[32] Nikolaev P, Bronikowski M, Bradley R, Rohmund F, Colbert D, Smith K, Smalley R. Gas-phase catalytic growth of single-walled carbon nanotubes from carbon monoxide.

Chemical Physics Letters, 1999; 313:91-97. https://doi.org/10.1016/S0009-2614(99)01029-5

[33] Talla J, Zhang D, Kandadai M, Avadhanula A, Curran S. A resonance Raman study of carboxyl induced defects in single-walled carbon nanotubes. Physica B: Condensed Matter, 2010; 405:4570-4573. https://doi.org/10.1016/j.physb.2010.08.041

[34] Dresselhaus MS, Dresselhaus G, Saito R, Jorio A. Raman spectroscopy of carbon nanotubes. Physics reports, 2005; 409:47-99. https://doi.org/10.1016/j.physrep.2004.10.006

Research on Engineering Structures & Materials
journal homepage: http://jresm.org
MIM Research Group

Research Article

Self-powered microfluidic device for the colorimetric detection of lithium via sequential reagent mixing

Angelo Traina[1,2,a], Han J.G.E. Gardeniers[1,b], Burcu Gumuscu[1,3,4,c]

[1]*Mesoscale Chemical Systems Group, University of Twente, Enschede, The Netherlands*
[2]*Department Information Engineering, Electronics and Telecommunications, Sapienza University of Rome, Rome, Italy*
[3]*BioInterface Science Group, Eindhoven University of Technology, Eindhoven, The Netherlands*
[4]*Biosensors and Devices Group, Eindhoven University of Technology, Eindhoven, The Netherlands*

Article Info

Article history:
Received 25 Jan 2021
Revised 19 Mar 2021
Accepted 31 Mar 2021

Keywords:

Lithium detection;
Colorimetric detection;
Microfluidic circuits;
Finger-driven pump

Abstract

Continuous monitoring of lithium concentration fluctuations in blood plasma is essential for patients with bipolar disorder and manic depression since lithium has a low therapeutic index. While blood plasma concentrations between 0.4 and 1.0 mmol/L are considered to be in the therapeutic zone, the concentrations exceeding 1.3 mmol/L are toxic to the patients. Most of the point-of-care devices for lithium monitoring have bulky peripherals and require extensive operator handling, yet simple-to-use devices are in demand for 2–5% of the worldwide population receiving lithium therapy. This paper aims to develop a self-contained microfluidic device to run colorimetric lithium assays without the need for dedicated personnel or equipment. In the developed microchip, the assay reagents are mixed in sequential order via custom-designed microfluidic capillary circuits with the aid of a finger pump. The operation of the finger pump was characterized mathematically and demonstrated experimentally. The finger-driven pump achieved 45.9 mm/s flow velocity when 8.3 µL liquid was placed in a 160 mm long channel with 200 µm height, as such rapid triggering was a requirement for the colorimetric lithium test. The final device is able to quantify the lithium concentrations between 0 and 2.0 mM using a smartphone camera. The detection limit of this microchip was calculated as 0.1 mM. This device presents a portable alternative to on-site quantitative detection techniques with bulky and expensive tools.

1. Introduction

Lithium is used as a mood stabilizer medication in clinics. Patients with bipolar disorders and recurrent depression often are prescribed lithium salts for treatment, although the administration of lithium bears its risks. While lithium levels below 0.1 mmol/L do not pose an effective treatment, levels above 1.3 mmol/L can lead to toxic effects on critical organs including the brain, liver, and kidneys. [1-3] Currently lithium monitoring in patients is predominantly based on laborious and time-consuming laboratory testing techniques. Therefore, the development of alternative measurement techniques that can be used in resource-limited settings would be of great benefit. The World Health Organization (WHO) requires that newly developed diagnostic measurement tools should be "assured"; in other words, they should be affordable, sensitive, specific, user-friendly, rapid and robust, equipment-free, and deliverable to end-users. [4] The availability of

*Corresponding author: b.gumuscu@tue.nl
[a]https:/orcid.org/0000-0001-5374-8360; [b]orcid.org/0000-0003-0581-2668;
[c]orcid.org/0000-0003-4843-4724
DOI: http://dx.doi.org/10.17515/resm2021.251ma0125

"assured" diagnostic tools is the key to future scalability in terms of the number of users that can be reached, thus facilitating a convenient therapy for the patients.

Blood testing has been the workhorse of lithium monitoring since alternative approaches, such as urine or saliva readings, do not give reliable results. [5] The standard laboratory tests to detect lithium from blood include colorimetry [6], photometry [7], and atomic absorption spectroscopy [8]. A more recent technique is called thermal ionization ion mobility spectrometry, which detected lithium from serum samples by following the steps of vaporization, ionization and separation while traveling in a weak electric field under atmospheric pressure. [9] All of these techniques require dedicated equipment and an operator with suitable expertise. The demand for more accessible and straightforward ways to monitor lithium levels in blood has motivated the development of microfluidic tools. For example, a rapid test was developed based on the photometric reading of a microcuvette, where the colorimetric reaction takes place upon the mixing of plasma-separated blood and a pre-loaded colorimetric reagent has been introduced. [10] Capillary electrophoresis-based measurements were also employed using whole blood in disposable chips, which perform conductivity measurements for lithium content determination. [11-14] Paper-based microfluidics platforms and lateral-flow devices. [15, 16] Recently, the group of Tokeshi introduced a paper-based device for lithium detection which is achieved by folding absorbent papers for different steps of the process, involving blood separation, and colorimetric detection. [17] Another paper-based platform was developed to run potentiometric measurements from serum using solid-state ion-selective electrodes for lithium. [18] For the sophisticated capillarity-driven networks, colorimetric [19] and electrochemical [20] detection of lithium were also demonstrated without the use of an external pump. In a recent work, a self-powered pump was demonstrated by the group of Basabe-Desmonts, who created large-area PDMS micropumps with microfluidic cartridges produced by multilayer lamination of grafted plastic substrates. [21] All these devices paved the way towards advanced lithium detection tests, although problems associated with affordability, user-friendliness, and robustness of the platforms still need to be tackled.

This work presents a self-contained microfluidic platform that exploits the capabilities of conventional microfluidic devices with capillary networks. The platform can handle the suction of a large volume of liquid with high flow rates to be used for point-of-care analysis, which can be performed by the non-experts (e.g. patients). This work involves the following: (1) the working mechanism of the sequential liquid delivery and finger pump operation were explained theoretically, (2) design and fabrication of the microfluidic device and the finger pump were demonstrated, (3) an on-chip colorimetric assay for lithium quantification was demonstrated as a proof-of-concept demonstration. The platform operates with small volumes of liquids and no external supporting equipment or power because liquid movement in the platform is controlled by a finger pump and capillarity. This work opens new avenues for the control of lithium administration of patients and the implementation of self-contained analytical platforms in resource-limited settings.

2. Theory

2.1. Operation of capillary circuits for sequential liquid delivery

To understand the behaviour and estimate the performance of the developed microfluidic system, a theoretical model based on an equivalent fluidic circuit concept was constructed and solved numerically. The model is based on the Navier-Stokes equation (1):

$$\rho(\vec{v}\cdot\nabla)\,\vec{v} = -\nabla\rho + \eta\nabla^2\vec{v} + F \quad (1)$$

where $\vec{v}$ is the velocity field [m s−1], which is a distribution of velocity in a given region, and is denoted by $\vec{v} = \vec{v}(\vec{r}, t)$, ρ is the fluid density [kg m^{-3}]; η is the dynamic viscosity [Pa s]; F represents any external forces present [N]. Analogous to electrical resistance, fluid resistance is defined as the ratio of pressure drop over flow rate in Equation (2):

$$R = \frac{\Delta p}{Q} \tag{2}$$

where Δp is the applied pressure difference [N m^{-2}], and Q is the volume flow rate [m^3 s^{-1}]. Under the hypothesis of a channel with a rectangular shape with width w; length L; height h; laminar flow; unidirectional motion; integrating Equation (1), Equation (3) is obtained:

$$Q \approx \frac{h^3 w \Delta p}{12\eta L}\left(1 - 0.630\frac{h}{w}\right) \tag{3}$$

$$R = \frac{12\eta L}{1 - 0.630\left(\frac{h}{w}\right)}\frac{1}{h^3 w} \tag{4}$$

Equation (4) leads to important observations: (i) the pressure drop through a channel is proportional to the volumetric flow rate and the hydraulic resistance, where the local pressure drop in the section considered determines the volumetric flow rate and not the overall pressure drop. (ii) The hydraulic resistance R remains constant for a specific fluid as long as the geometry of the channel is fixed, and under these assumptions, proportional to the channel length L. All these parameters are fundamental in the design of our microfluidic device, which requires accurate control in terms of volume, channel filling times and functionalization of the reaction chambers.

The theoretical principle behind the operation of the capillary stop valves has been described in detail by Zimmermann et al [22]. The stop valves halt the flow of liquid in microchannels without external intervention, but using a sharp change in channel width creates a pressure barrier. The pressure barrier (ΔP) for a two dimensional stop valve is given by Equation (5):

$$P = -\gamma\left(\frac{cos\theta_t + cos\theta_b}{h} + \frac{cos\theta_r + cos\theta_l}{w}\right) \tag{5}$$

where w, h are the width and height respectively of the microchannel leading into the stop valve, and γ is the surface tension of the liquid. θ_t, θ_b, θ_r, θ_l, are the top, bottom, right, left channel wall contact angles. A numerical analysis was performed assuming that the liquid (reagent solution) advancement is stopped by an abrupt change in channel profile, due to the presence of the stop valves. Under these conditions the pressure in each channel junction P_n will be equal to the pressure exerted by the finger pump P_{max}. The reason is that the pressure generated by the pump is larger than the capillary pressure of the sides branches (Fig.1a), the liquid will be delivered from each branch to the channel junction P_n. To achieve a correct emptying of the i_{th} reservoir without activating the $R_{BV_{i+1}}$, it is essential to respect the condition at all times as shown in Equation (6):

$$|P_n| < |P_{i+1}| \tag{6}$$

where P_{i+1} with $i = 1, 2, 3$ is the capillary pressure at $(i+1)_{th}$ branches, R_{BV} is the resistance of one side branch; and P_n can be calculated using Kirchhoff's law and Ohm's law yielding Equation (7):

$$P_n = \frac{P_i \cdot R_C + P_{FP}(R_{SV} + R_i)}{(R_C + R_{RV} + R_i)} \quad (7)$$

where R_i is the series resistance between the R_{BV} and the reservoir resistance of each branch; R_{SV} is the resistance of the stop valve; R_C is the flow resistance of the colorimetric chamber.

2.2. Finger pump working principle

Under the assumptions of negligible gas leakage during the push-and-release process and constant temperature, it is possible to apply the ideal gas law using the geometric characteristics of the pump, as shown in Equation (8).

$$P_{max} = \left(\frac{V_0}{V_{min}} - 1\right) P_0 \quad (8)$$

where P_{max} is the pressure increase when the pressure chamber is fully deformed [Pa]; P_0 is atmospheric pressure [Pa]; V_0 is the volume of the pressure chamber in its original shape [L]; V_{min} is the remaining volume of the pressure chamber when it is maximally deformed [L]. The volume of drawn fluid in the microchannel is closely related to the volumetric capacity of the finger pump. Thus, the movement of the liquids in the microchannels can be controlled by changing the volume of the finger pump or by modulating the applied force, without any external pressure units.

3. Materials and Methods

3.1. Materials

Poly(dimethylsiloxane) (PDMS) was purchased from Dow Silicones Deutschland GMBH (Theingaustr, DE), and SU8-50 negative photoresist was obtained from MicroChem, Corp. (Newton, MA). The colorimetric reaction designed for the quantification of lithium levels in biological fluids (ab235613 Lithium Assay Kit) was obtained from Abcam (Cambridge, GB).

3.2. Fabrication of the microfluidic device

The microfluidic network was developed to accommodate the pre-programmed delivery of multiple liquids sequentially for improved assay sensitivity and specificity in lithium sensing. The self-contained platform consists of two functional parts: a microfluidic network and a finger pump to trigger the mixing of colorimetric reaction solutions and blood plasma. Sequential liquid delivery was made possible by the stop valves that use an abrupt change in channel geometry and hydrophobic channel walls made of PDMS. The volume of microchannels scales with the solution volumes described in Abcam lithium test kit. Accordingly, 200 µm high microchannels with width and height 1000 µm x 26 000 µm, 1000 µm x 20 900 µm, 1000 µm x 200 µm and 800 µm x 1300 µm were designed, respectively. The width and height of the stop valves were 288 µm x 734 µm, respectively (Fig. 1a).

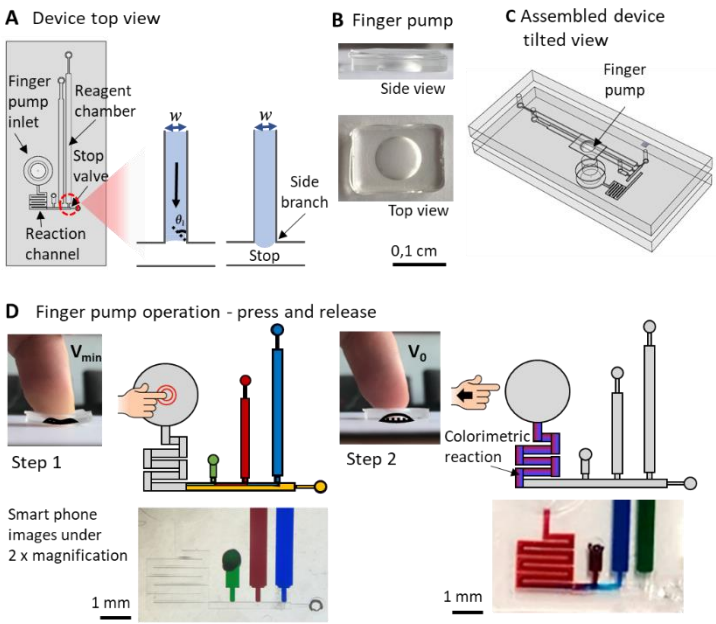

Fig. 1 (a) Device top view and its components. The stop valves are the T-junctions composed of two side branches. (b) Finger pump side and top views. (c) Assembled microchip with finger pump on top, finger pump, not to scale. (d) Finger pump operation is shown both in schematics and smartphone camera images.

The PDMS-based microfluidic device was fabricated using soft lithography. For the SU-8 mould preparation, a negative photoresist (MicroChem NANOTM SU-8 5) was spin-coated on a 4 inch silicon wafer, with a height of 200 µm, then baked on a hot plate at 95 °C. The baked photoresist was exposed to ultraviolet (UV) light with a dose of 12m W cm^{-2} for 5 sec. For the post-exposure baking, the wafer was baked at 50 °C for 1 min, 65 °C for 1 min and 80 °C for 2 min, respectively. The wafer was cooled down to room temperature with steps of 5 °C per 2 min. The baked photoresist was developed with RER600 solvent (PGMEA RER600, ARCH chemicals) for 3.5 min with a spray-gun. The slow cooling down steps helped to minimize the thermal stress on the photoresist, and reduced the possibility of crack formation based on material stress.

The microfluidic chips were fabricated using the SU-8 mould. A PDMS mixture (10 : 1 w/w ratio of the polymer base to the curing agent) was poured onto the SU-8 mould. The PDMS mixture was cured for 2 h at 65 °C and peeled off from the SU-8 mould after curing. Several inlet and outlet holes were punched using biopsy punches with 1 mm and 4 mm diameter. Finally, the PDMS layer was bonded with a clean glass slide using oxygen plasma treatment for 45 sec. The final chip was placed in an oven set at 65 °C for 1 h (Figure S1a).

3.3. Design and Fabrication of The Finger Pump

The finger-driven pump was designed to drive the liquids in the microfluidic device. The finger pump is a deformable pressure chamber that was made of PDMS (Fig. 1b,c). Before the operation, positive pressure was applied on the finger pump via a human finger to deform it downwards. After this step, the finger pump was placed on the outlet of the device. Upon releasing the finger, the PDMS chamber deformed upwards and created a negative pressure inside the microchannels to trigger the liquid flow. This operation is based on the energy stored in the form of elastic energy inside the finger pump, as

described in Equation 8. The liquid movement stops when the PDMS pump restores its original shape. The inner volume of the microchip was calculated to be approximately 16 μL and the finger pump had a total volume of 100 μL that can be provided with the necessary suction (Fig. 1d).

The finger pump was fabricated using a master mould made by drilling an aluminium plate at the technical workshop at the University of Twente. The PDMS mixture (10 : 1 w/w ratio of the polymer base to the curing agent) was poured into the mould and cured at 65 °C in an oven for 1 h. The cured PDMS was peeled off from the mould (Fig. S1b). The distance covered by the liquid in the microchannels was measured by processing the smartphone images using FiJi software.

3.4. Colorimetric Lithium assay

Lithium Assay Kit manufacturer's guidelines were followed to quantitatively detect the lithium levels in blood plasma. After preparing the standards and the samples, sodium masking solution, lithium assay buffer, probe solution were mixed in microfluidic sequentially. After incubation of the solutions for 5 min, the microchannels were imaged using a smartphone camera attached to a 2x magnification lens. For the magenta intensity measurements, FiJi software was used to extract magenta values from the smartphone images, where a blank measurement was done using an unfilled channel. The images were taken under uniform light, sourced by a white LED lamp attached to 2x magnification lens. For the absorbance measurements, the samples were measured at 540 nm and 630 nm separately, using a microplate reader (Thermo Fisher Scientific Multiskan Go, Netherlands). The ratio of the two absorbance measurements is used to accurately determine the lithium concentration in the sample or the standard. The colorimetric reaction relies on a lithium-selective bi-chromatic probe molecule which is subjected to change absorbance at two distinct wavelengths upon binding to lithium (λ_1 = 540 nm, λ_2 = 630 nm). The probe molecule is found in the probe solution. Sodium masking solution is used for eliminating the interference by supra-physiological levels of serum sodium. Other mono-, di-, and trivalent ions found in the blood plasma do not interfere with the assay. Finally, the magenta values were compared with absorbance values.

4. Results and Discussion

As the key advance, the presented device is self-contained and no longer requires external parts such as electrodes, power source, syringe pumps unlike the previously reported tools.

4.1. Design of the Microfluidic Platform, Flow Channels and Capillary Circuits

The microfluidic system was designed for the quantification of lithium levels via four parallel microfluidic channels connected via a vertical microchannel, where the colorimetric reaction took place. The parallel microfluidic channels were emptied in sequential order to ensure the mixing of reagents in a correct order to achieve the most reliable results. The microchip had five inlets; three of the inlets were used to introduce reaction reagents, one inlet to introduce the sample via an integrated filter paper, and one inlet to connect the system to a finger pump (Fig. 1c). We considered the total resistance of each branch forming the microfluidic network when designing such a network of microchannels, where sequential delivery of a different amount of liquids was performed. Fig. 2a demonstrates a circuit model of the microfluidic network, consisting of stop valves, flow resistor, inlets, and microfluidic pump. Despite the complexity of the model, the stop valve was the component that mainly influences the flow, playing a key role in the sequential delivery.

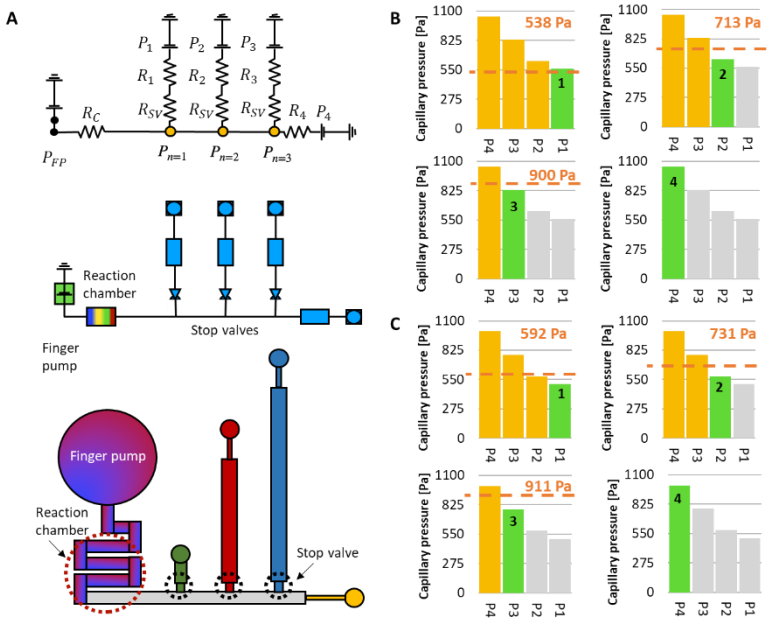

Fig. 2 (a) Symbolic and schematic representations and relative electric circuit analogue of microfluidic device propose. (b-c) Graphs show which reservoirs empty (in red) according to the sequential order for different surface contact angles θ = 89° in (b) and θ = 95° in (c). The numbers on green bars show the emptying order of the chambers shown in (a). Orange dashed lines show the pressure generated by the finger pump.

The microfluidic network was tested to understand how the geometry of stop valves influences their capacity of stopping the flow, and then sequentially releasing the liquid. Junker et al. [23] confirmed a success rate of 75% (n = 8) using a stop valve with w = 200 µm; h = 734 µm; and $\Delta h = 400\ \mu m$ (height difference between stop valves and release channel). Our design involved interconnected four reservoirs with 8.6, 7.3, 0.8, 0.3 µL, respectively. The height of the channels were kept the same due to fabrication limitations while the width and length of the channels were changed to obtain the desired volumes. This resulted in an increase in resistance in the reservoirs of each branch, making the fulfilment of the condition in Equation (6) more difficult.

Figure 2b and 2c show the results of the numeric analysis of hydrophobic ($\theta > 90^0$) and hydrophilic ($\theta < 90^0$) contact angles characteristic to PDMS and glass surfaces [24-26], where the orange dotted line represents the pressure value P_n according to Equation (7). In either case, it was possible to find a numeric solution for the model by changing the geometry parameters (w; L) of each reservoir. In this way, the sequential mixing of different reagents was obtained by fixing the channel height to 200 µm. In this way, liquid advancement was not observed while loading the long reagent microchannels. In some cases, the finger pump operation caused the emptying of the microchannels not in a sequential order. This was attributed to the high width-to-height ratio of the stop valves. Nevertheless, the experimental findings support the numerical analysis that was obtained by the sequential emptying of the microchannels according to the anticipated order, with a success rate of 70% (n = 15). These results are in accordance with the work by Olanrewaju et al. [27].

The pressure drop was calculated in the total system by linking each channel parallel to each other. The microchip was composed of several PDMS layers and the variations in layer thickness directly affected the success rate of the sequential mixing. Although the finger-driven pump had 6.25 times more capacity to withdraw the solutions in the microchannels, the poor alignment of layers occasionally resulted in narrower connection channels between the layers, resulting in higher resistance at the connection locations.

4.2. Finger Pump

The finger pump was designed to accommodate fluid flow in microchannels and the dimensions were selected accordingly. To quantify the relationship between the size of the finger pump and the total microchannel volume, PDMS pressure chamber units were tested using two microchannels with different dimensions (w_1 = 300 µm, w_2 = 600 µm, L = 160 mm, h = 200 µm) that are compatible with the final inner volume of the actual microchip design for colorimetric lithium monitoring. Figure 3a shows the microchips and the attached finger pump unit.

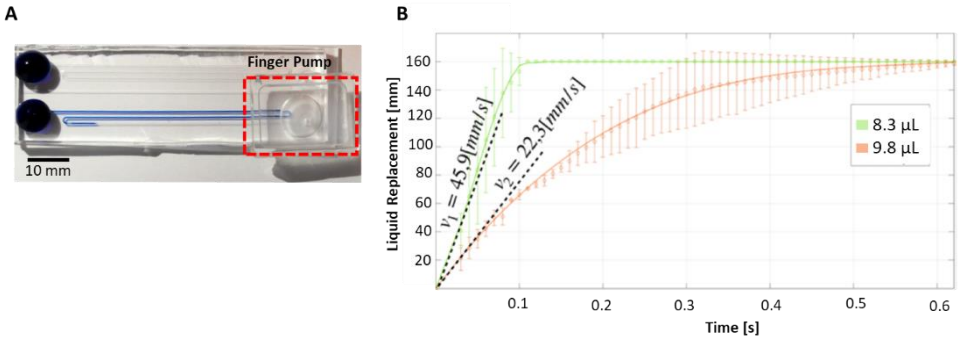

Fig. 3 The finger-driven pump induces fluid flow rate that is dependent on liquid volume in the microfluidic channels. (a) The finger-driven pumping system used for the characterization of the fabricated finger-driven pump with a diameter of 10 mm. (b) Liquid replacement by the micropump as a function of the time. Green and orange lines present the instant speed of the liquid in microchannels. The error bars in the graph show three separate measurements performed for this operation, n = 3.

For each width three emptying tests were ran using the finger pump. The selected diameter of the finger pump unit was sufficient to trigger the fluid flow in microchannels when fully deformed downwards. This finding matches the predicted behaviour described in Equation 8.

When microchannels were loaded with a larger volume of liquid ($V_1 = 9.8\ \mu L$), the liquid reached the outlet in $\Delta t_1 = 0.64\ s$, without breaking up of the liquid slug in the microfluidic channels. As shown in Figure 3b, the acceleration of the liquid follows the second law of dynamics as shown in Equation (9):

$$a = \frac{dv}{dt} = \frac{F_{tot}}{m} \tag{9}$$

where m is the mass of liquid; a the acceleration applies to liquid.

When a fixed force, such as suction, is applied, a liquid mass in a microchannel gains speeds inversely proportional to its mass. Accordingly, the movement of the liquid mass was

calculated for $0 < t < 0.03$ s, by assuming that the mass m constantly accelerates, as shown in Equation (10).

$$\begin{cases} a = a_0 \approx \dfrac{\Delta v}{\Delta t} = \dfrac{v_{fin} - v_{start}}{t_{fin} - t_{start}} \rightarrow \dfrac{v_{0.03}}{t_{0.03}} \\ v_{fin} = v_{start} + at \rightarrow v_{0.03} = 0 + a_0 t_{0.03} \\ x_{fin} = x_{start} + v_{start} t + \dfrac{1}{2} a t^2 \rightarrow x_{0.03} = 0 + 0 \cdot t_{0.03} + \dfrac{1}{2} a_0 t_{0.03}^2 \end{cases} \quad (10)$$

The variations of acceleration are based on the variations in the mass of the liquid moved in the microchannel, so the liquid with a lower mass will have a higher speed in this range. Analogously, a smaller volume of liquid $V_2 = 8.3\ \mu L$ was expected to accelerate slower than the larger volume $V_1 = 9.8\ \mu L$ in the time frame $0 < t < 0.03\ s$. Our observations in Figure 3b support this argument. The average velocity was calculated in each case as $v_1 = 2.3\ mm/s$ and $v_2 = 45.9\ mm/s$. We attribute the 2-fold velocity increase for 1.5 µL volume difference between the liquid masses to the possibility of unequal applied forces at each push and release cycle. These findings are in agreement with the findings of Xiang et al [25], as the finger pump successfully triggered fluid flow in microchannels with 160 mm length in 0.6 s.

The presented finger pump can trigger the fluid flow in a non-linear manner for shorter durations of time when compared to other self-powered microfluidic pumps in the literature. [26] Some of these pumps appear in the form of long and shallow microfluidic channels connected to a main channel, where the liquid suction takes place when the microchip is placed in a degassing chamber. In-parallel microchannels achieved a maximum suction velocity of 0.9 mm/s for when 1 mm to 3 mm diameter trenches were used. [21,28] The finger pump presented in this study is capable of triggering 20 to 40 times greater flow velocities for significantly longer microchannels. Another type of suction mechanism is based on paper-based microfluidics, where an absorbent fibrous paper is attached to the end of the microchannels. The liquid suction takes place due to capillary suction towards the absorbent material. In this manner, sequential mixing was made possible. The typical flow rates generated in such studies vary between 0.2 mm/s [29], and 0.2 to 0.1 µL/s [27]. The flow rates generated by the finger pump were 80 times greater than these values, although the paper-driven pumps can function for longer time spans (tens of minutes) when compared to under 5 min operation of the finger driven pump presented in this work. Either way could be of preference as a requirement of different applications.

4.3. Colorimetric lithium assay

The main aim of this research was to develop a low-cost point-of-care device that allows for colorimetric detection of lithium using a smartphone camera in a rapidly and cost-effectively. Before the analysis of the specimens with unknown concentrations, the performance of the device for colour sensitivity was evaluated by standard specimens. The results of the colorimetric assay were captured for different lithium concentrations ranging between 0 and 2 mM using a smartphone camera (iPhone X, 12 MP camera). The concentration of lithium was correlated with the colour intensity in the white-balanced images. As described in the manufacturer's datasheet, the associated change in colour from orange to red indicated the quantity of lithium inside the sample. Such a strategy was also previously followed by Tokeshi's group. [17] To analyse how the variation in the concentration of lithium is connected to the absorbance value, the magenta values of the smartphone camera images and absorbance readouts were compared. Figure 4a demonstrates that the absorbance value, magenta value and lithium concentration have a linear relationship between 0 and 2 mM with a limit of detection of 0.1 mM (n = 5,

R^2 = 0.99). This test is capable of detecting various concentrations of lithium quantitatively, and the detection range covers the typical maximum and minimum concentrations of lithium in blood serum [30-35]. Figures 4b and 4c show the colour change in the reaction channel where the magenta values were extracted using MATLAB and Fiji software. The obtained results were found to be in correlation although the images obtained from the microchip were more faint compared to the ones in the off-chip measurement.

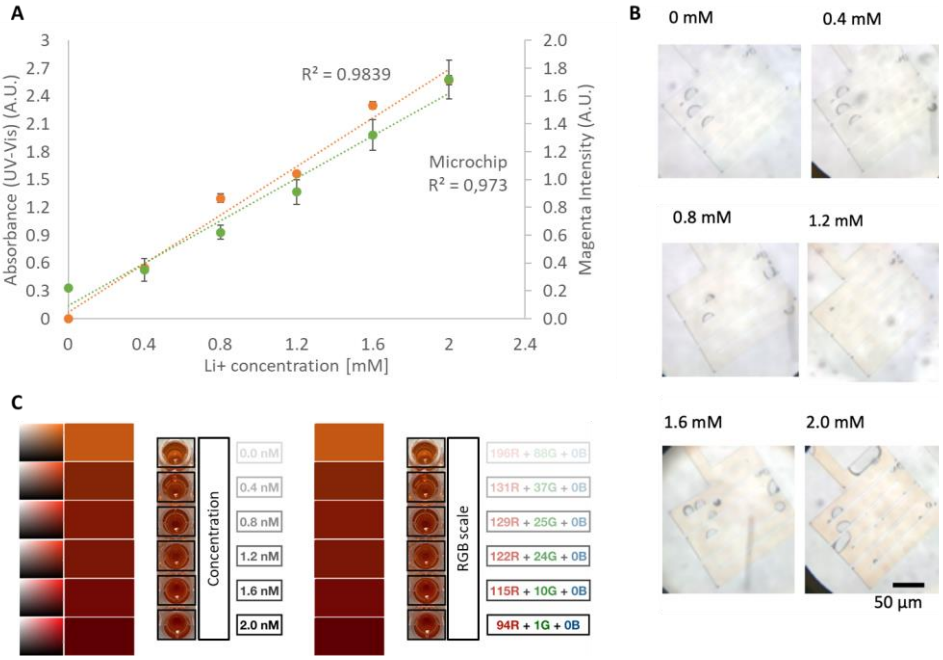

Fig. 4 (a) The quantitative calibration curve of different lithium concentrations for smartphone camera images (magenta only) and absorbance results. (b) On-chip assessment of the colorimetric reaction. Smartphone images of colorimetric detection of lithium in microchannels. (c) Off-chip correlation of the colorimetric reaction with RGB scale. The same methodology was followed to convert the detected colours on-chip.

5. Conclusions

We report here for the first time on the design, fabrication, and application of a self-standing device consisting of capillary microfluidic circuits for sequential mixing of reagents and a finger-driven pump for facilitating the fluid flow. As a proof-of-colorimetric lithium assay was performed in the device. The finger pump generated 20 to 40 times high flow rates when compared to the self-standing pumps reported in recent publications, while the pump operation time could be maintained in the range of minutes instead of hours as demonstrated in the previous studies. Nevertheless, the application selected for this work requires rapid mixing of reagents within minutes to start the colorimetric reaction. Therefore, the platform serves well to the aim of this work. The presented device meets the Affordability, Sensitivity, Specificity, User-friendliness, and Robustness (ASSURed) criteria requested by the World Health Organization (WHO). In this work, the request of the WHO was addressed by the two-pronged design of the self-powered microfluidic platform: First, in contrast to widely-used conductivity measurements, the platform requires no external electronic apparatus to run the lithium test. Second, the

proposed platform enables the mixing of reagents in a sequential order thanks to the finger-driven pump.

The finger pump assisted microfluidic system was designed and fabricated by using soft lithography. As a proof-of-concept study, a commercially available lithium kit was utilized to run the colorimetric lithium detection. The colorimetric reaction in the device occurred within 5 min after installing the reagents. A smartphone camera facilitated the image acquisition where colorimetric reaction detection was performed. The performance of the pump and liquid movement in microfluidic channels were characterized, and sequential emptying of the injected solutions. The detection limit of lithium concentration was measured to be 0.1 mmol/L. Our merging of rapid colorimetric lithium monitoring test with a stand-alone microfluidic device surmounts measurement challenges where (1) the measurement requires conductivity measurements, (2) there is the trade-off between the requirement of sequential mixing of reagents and assay sensitivity. The future work involves the implementation of a smartphone application, using the smartphone as a capture device and colour detector from a picture of the microfluidic device; and running the tests in spiked blood serum samples.

Acknowledgments

We thank all the Mesoscale Chemical Systems Lab members at the University of Twente for helpful discussions and suggestions throughout the study. We thank Stefan Schlautmann for helping with the production of the SU-8 moulds.

Annotations

$\vec{v}$	the velocity field
ρ	the fluid density
η	the dynamic viscosity
F	external forces
Δp	the applied pressure difference
Q	the volume flow rate
ΔP	the pressure barrier
R	the hydraulic resistance
L	the channel length
w	the width of the microchannel
h	the height of the microchannel
γ	the surface tension of the liquid
$\theta_t, \theta_b, \theta_r, \theta_l$	the top, bottom, right, left channel wall contact angles, respectively
P_n	the channel junction
P_{max}	the maximum pressure exerted by the finger pump

i_{th}	the number of the reservoirs
P_{i+1}	the capillary pressure at $(i+1)_{th}$ branches
R_{BV}	the resistance of one side branch;
R_i	the series resistance between the R_{BV} and the reservoir resistance of each branch
R_{SV}	the resistance of the stop valve
R_C	the flow resistance of the colorimetric chamber
P_0	the atmospheric pressure
V_0	the volume of the pressure chamber in its original shape
V_{min}	the remaining volume of the pressure chamber when it is maximally deformed
m	the mass of liquid
a	the acceleration that applies to liquid

References

[1] Hopkins S, Gelenberg J. Serum lithium levels and the outcome of maintenance therapy of bipolar disorder. Bipolar Disorder, 2000; 2: 174-179. https://doi.org/10.1034/j.1399-5618.2000.020304.x

[2] Christian GD, Reagents for lithium electrodes and sensors for blood serum analysis. Sensors, 2002; 2: 432-435. https://doi.org/10.3390/s21000432

[3] Reddy DS, Reddy MS. Serum lithium levels: Ideal time for sample collection! Are we doing it right?. Indian Journal of Psychological Medicine., 2014; 36: 346-7. https://doi.org/10.4103/0253-7176.135399

[4] Kosack CS, Page AL, Klatser PR. A guide to aid the selection of diagnostic tests. Bulletin of the World Health Organization, 2017; 95: 639. https://doi.org/10.2471/BLT.16.187468

[5] Shetty SJ, Desai PB, Patil NM, Nayak RB. Relationship between serum lithium, salivary lithium, and urinary lithium in patients on lithium therapy. Biological Trace Element Research., 2012; 147: 59-62. https://doi.org/10.1007/s12011-011-9295-3

[6] Gruson D, Lallali A, Furlan V, Taburet AM, Legrand A, Conti M. Evaluation of a new lithium colorimetric assay performed on the Dade Behring Dimension® X-pand™ system. Clinical Chemistry and Laboratory Medicine, 2004; 42: 1066-1068. https://doi.org/10.1515/CCLM.2004.214

[7] Christenson RH, Mandichak JJ, Duh SH, Augustyn JM, Thompson JC. Clinical performance characteristics of a new photometric lithium assay: a multicenter study. Clinica Chimica Acta, 2003; 327: 157-164. https://doi.org/10.1016/S0009-8981(02)00367-4

[8] Rumbelow B, Peake M, Performance of a novel spectrophotometric lithium assay on a routine biochemistry analyser. Annals of Clinical Biochemistry, 2001; 38: 684-686. https://doi.org/10.1258/0004563011900894

[9] Parchami R, Tabrizchi M, Shahraki H, Moaddeli A. Rapid analysis of lithium in serum samples by thermal ionization ion mobility spectrometry. International Journal for Ion Mobility Spectrometry, 2020; 23:117-25. https://doi.org/10.1007/s12127-020-00264-1
[10] Glazer WM, Sonnenberg JG, Reinstein MJ, Akers RF. A novel, point-of-care test for lithium levels: description and reliability. Journal of Clinical Psychiatry, 2004; 65: 652-655. https://doi.org/10.4088/JCP.v65n0508
[11] Vrouwe EX, Luttge R, Vermes I, Van Den Berg A. Microchip capillary electrophoresis for point-of-care analysis of lithium. Clinical Chemistry, 2007; 53: 117-123. https://doi.org/10.1373/clinchem.2007.073726
[12] Floris A, Staal S, Lenk S, Staijen E, Kohlheyer D, Eijkel J, van den Berg, A. A prefilled, ready-to-use electrophoresis based lab-on-a-chip device for monitoring lithium in blood. Lab on a Chip, 2010; 10: 1799-1806. https://doi.org/10.1039/c003899g
[13] Bidulock AC, Dubský P, van den Berg A, Eijkel J. Integrated internal standards: A sample prep-free method for better precision in microchip CE. Electrophoresis, 2019; 40: 756-765. https://doi.org/10.1002/elps.201800393
[14] Sewart R, Gärtner C, Klemm R, Schattschneider S, Becker H. Microfluidic device for fast on-site biomedical diagnostic on the example of lithium analysis in blood. Biomedical Engineering/Biomedizinische Technik, 2012; 57(SI-1 Track-L): 729-732. https://doi.org/10.1515/bmt-2012-4212
[15] Comer JP. Semiquantitative specific test paper for glucose in urine. Analytical Chemistry, 1956; 28: 1748-1750. https://doi.org/10.1021/ac60119a030
[16] Gaikwad PS, Banerjee R. Advances in point-of-care diagnostic devices in cancers. Analyst, 2018; 143:1326-48. https://doi.org/10.1039/C7AN01771E
[17] Komatsu T, Maeki M, Ishida A, Tani H, Tokeshi M. Based Device for the Facile Colorimetric Determination of Lithium Ions in Human Whole Blood. ACS Sensors. 2020; 5:1287-94. https://doi.org/10.1021/acssensors.9b02218
[18] Novell M, Guinovart T, Blondeau P, Rius FX, Andrade FJ. A paper-based potentiometric cell for decentralized monitoring of Li levels in whole blood. Lab on a Chip, 2014; 14: 1308-1314. https://doi.org/10.1039/c3lc51098k
[19] Martinez AW, Phillips ST, Carrilho E, Thomas SW, Sindi H, Whitesides GM. Simple telemedicine for developing regions: camera phones and paper-based microfluidic devices for real-time, off-site diagnosis. Analytical Chemistry, 2008; 80: 3699-707. https://doi.org/10.1021/ac800112r
[20] Nie Z, Deiss, F, Liu X, Akbulut O, Whitesides GM. Integration of paper-based microfluidic devices with commercial electrochemical readers. Lab on a Chip, 2010; 10: 3163-3169. https://doi.org/10.1039/c0lc00237b
[21] Etxebarria-Elezgarai J, Alvarez-Braña Y, Garoz-Sanchez R, Benito-Lopez F, Basabe-Desmonts L. Large-Volume Self-Powered Disposable Microfluidics by the Integration of Modular Polymer Micropumps with Plastic Microfluidic Cartridges. Industrial & Engineering Chemistry Research, 2020; 59: 22485–22491. https://doi.org/10.1021/acs.iecr.0c03398
[22] Zimmermann M, Hunziker P, Delamarche E. Valves for autonomous capillary systems. Microfluidics and Nanofluidics, 2008; 5: 395-402. https://doi.org/10.1007/s10404-007-0256-2
[23] Juncker D, Schmid H, Drechsler U, Wolf H, Wolf M, Michel B, de Rooij N, Delamarche E. Autonomous microfluidic capillary system, Analytical Chemistry, 2002; 74: 6139 - 6144. https://doi.org/10.1021/ac0261449
[24] Bhattacharya S, Datta A, Berg JM, Gangopadhyay S. Studies on surface wettability of poly(dimethyl) siloxane (PDMS) and glass under oxygen-plasma treatment and correlation with bond strength. Journal of Microelectromechanical Systems, 2005; 14: 590-597. https://doi.org/10.1109/JMEMS.2005.844746

[25] Xiang Z, Wang H, Pastorin G, Lee C. development of a flexible and disposable microneedle-fluidic-system with finger-driven drug loading and delivery functions for inflammation treatment. Journal of Microelectromechanics, 2015; 24: 565-574. https://doi.org/10.1109/JMEMS.2015.2429675
[26] Narayanamurthy V, Jeroish ZE, Bhuvaneshwari KS, Bayat P, Premkumar R, Samsuri F, Yusoff MM. Advances in passively driven microfluidics and lab-on-chip devices: a comprehensive literature review and patent analysis. RSC Advances, 2020; 10:11652-80. https://doi.org/10.1039/D0RA00263A
[27] Olanrewaju AO, Robillard A, Dagher M, Juncker D. Autonomous microfluidic capillaric circuits replicated from 3D-printed molds. Lab on a Chip, 2016; 16:3804-14. https://doi.org/10.1039/C6LC00764C
[28] Dimov IK, Basabe-Desmonts L, Garcia-Cordero JL, Ross BM, Ricco AJ, Lee LP. Stand-alone self-powered integrated microfluidic blood analysis system (SIMBAS). Lab on a Chip, 2011; 11:845-50. https://doi.org/10.1039/C0LC00403K
[29] Jang I, Carrão DB, Menger RF, Moraes de Oliveira AR, Henry CS. Pump-free microfluidic rapid mixer combined with a paper-based channel. ACS sensors, 2020; 5:2230-8. https://doi.org/10.1021/acssensors.0c00937
[30] Coskun AF, Wong J, Khodadadi D, Nagi R, Tey A, Ozcan A. A personalized food allergen testing platform on a cellphone. Lab on a Chip, 2013;13:636-40. https://doi.org/10.1039/C2LC41152K
[31] Shen L, Hagen JA, Papautsky I. Point-of-care colorimetric detection with a smartphone. Lab on a Chip, 2012;12:4240-3. https://doi.org/10.1039/c2lc40741h
[32] García A, Erenas MM, Marinetto ED, Abad CA, de Orbe-Paya I, Palma AJ, Capitán-Vallvey LF. Mobile phone platform as portable chemical analyzer. Sensors and Actuators B: Chemical. 2011;156:350-9. https://doi.org/10.1016/j.snb.2011.04.045
[33] Fang X, Chen H, Jiang X, Kong J. Microfluidic devices constructed by a marker pen on a silica gel plate for multiplex assays. Analytical Chemistry. 2011;83:3596-9. https://doi.org/10.1021/ac200024a
[34] Carrilho E, Phillips ST, Vella SJ, Martinez AW, Whitesides GM. Paper microzone plates. Analytical Chemistry. 2009;81:5990-8. https://doi.org/10.1021/ac900847g
[35] Teasdale PR, Hayward S, Davison W. In situ, high-resolution measurement of dissolved sulfide using diffusive gradients in thin films with computer-imaging densitometry. Analytical Chemistry. 1999;71:2186-91. https://doi.org/10.1021/ac981329u

Supplementary information

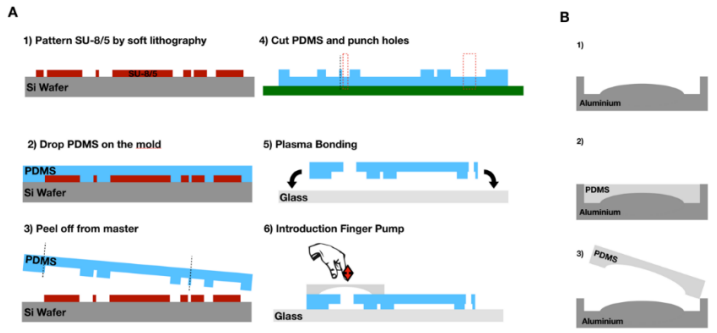

Supplementary image S1. Fabrication process of the PDMS finger-pump, and microfluidic platform by soft lithography. (a) Schematic diagram of all steps necessary for the realization of the device propose. (b) The PDMS mixture is poured in the 3D mould, cured, peeled off from the mould, then cut by a razor blade.

Research on Engineering Structures & Materials
journal homepage: http://jresm.org
Research Group

Research Article

The effect of various mineral fillers on thermal, mechanical, and rheological properties of polypropylene

Lütfiye Altay[1,a], Mehmet Sarikanat[*1,b], Merve Sağlam[2,c], Tuğçe Uysalman[2,d], Yoldaş Seki[3,e]

[1]*Ege University, Faculty of Engineering, 35100 İzmir, Turkey*
[2]*İzmir Eğitim Sağlık Sanayi Yatırım A.Ş., 45400, Manisa, Turkey*
[3]*Dokuz Eylul University, Faculty of Sciences, 35160, Isparta, Turkey*

Article Info

Article history:
Received 13 Feb 2021
Revised 10 May 2021
Accepted 21 May 2021

Keywords:

Composite materials;
Mechanical properties;
Thermal properties;
Rheological properties

Abstract

Polypropylene is one of the commodity thermoplastics that is widely used in many different applications such as automotive, building, electric-electronics, textile, and packaging industries due to its properties and favorable cost-benefit ratio. The incorporation of mineral fillers such as mica, talc, wollastonite, and calcium carbonate into thermoplastics is a common practice in the plastics industry in order to reduce the production costs of molded products and enhance processibility, mechanical, and thermal properties. Mineral filled polypropylene composites provides high mechanical stiffness, thermal stability, and good dimensional stability over a wide temperature range. The filler weight ratio, type, size, and dimension have significant effect on mechanical, thermal, physical, and rheological properties of composites. Four different mineral fillers (talc, mica, calcite, and feldspar) at weight fractions of 40% were compounded with polypropylene by using a twin-screw extruder. Test specimens were obtained by injection molding process. The effect of various filler types on rheological and mechanical properties of polypropylene was investigated in this study. It was found that talc and mica loadings at 40 wt. % into polypropylene increased the flexural strength of polypropylene. The rheological properties of samples were more affected by the talc than calcium carbonate.

1. Introduction

Polypropylene (PP) is one of the commodity thermoplastics that is used in various industrial applications including, but not limited to, automotive, electronics, construction, household appliances, films, fabrics, sheets, etc. Being lightest polymer with a very low density, polypropylene shows excellent mechanical properties and can be reprocessed several times without significant loss of its mechanical, physical and thermal properties[1-9]. Polypropylene based composite materials provide low-cost solutions to the needs of the many engineering problems. The biggest advantage of using PP as a matrix material is its compatibility with many fillers that will change its structure to have properties set for specific applications. That is to say, the incorporation of proper fillers into PP has been an accepted route to cost saving and enhancing material properties [1-3]. Among many filler types, metal powders, ceramics, carbons, and minerals have been investigated as promising fillers for thermoplastics-based composites. The studies about functional thermoplastics have shown that stiffness, durability, and dimensional stability could be improved by combination of these types of fillers [10].

[*]Corresponding author: sarikanat.mehmet@gmail.com
[a] orcid.org/0000-0003-4946-3615; [b] orcid.org/0000-0003-1094-2272; [c] orcid.org/0000-0002-7384-6459; [d] orcid.org/0000-0002-9845-4929; [e] orcid.org/0000-0003-1094-2272
DOI: http://dx.doi.org/10.17515/resm2021.258ma0213

Talc is one of the preferred mineral fillers, with platelet structure and low hardness, which improves processing properties and reduces costs [11]. Addition of talc in thermoplastics generally results in improvement in mechanical properties, but it decreases impact strength [5, 12]. Furthermore, talc, which reduces and homogenizes the molding shrinkage, also facilitates the shaping of polypropylene. The percentage of talc as a filler in thermoplastics is usually between 20 and 40 wt. % [13]. Mica also has a layered crystal structure, but the bonds between the layers are stronger than the talc. It is particularly used in large proportions in thermoplastic polymers to provide mechanical reinforcement along a plane with excellent electrical characteristics [14]. Calcium carbonate, referred as calcite, which can be produced from chalk, limestone and marble, is one of the most widely used mineral in the end-use industries (plastic, paper, adhesive, sealants, coatings, and paints etc.) as a filler. Calcite is preferred as a mineral filler in large number of thermoplastics due to its low cost, good stability, white color, easy processing and many other advantages [14]. Feldspars, forming about 51% of the rocks on Earth's crust, are the most abundant group of tectosilicate minerals. The use of feldspar in thermoplastics has attracted great attention because of its cost efficiency and abundance. Feldspars have a cubic shape, high energy adsorption capacity and are capable of exchanging ions on silicate layers with reactive groups on the surface. Also, due to their optical and thermal properties, feldspars are preferably used in light and thermal management applications[15].

The aim of this article is to investigate the effects of four different types of mineral fillers on the tensile, flexural, impact, thermal and rheological properties of PP based composites. For this reason, talc, calcite, mica and feldspar at 40 % weight fraction were used in polypropylene during compounding with a twin-screw extruder. Mineral filled polypropylene composites test specimens were obtained by injection molding of composite granules. The effects of the filler loading on the physical, mechanical, thermal and rheological properties of mineral filled polypropylene composites were investigated by several characterization methods.

2. Materials and Methods

2.1. Materials

Homo-polymer-grade polypropylene (PP) (IMS Polymers, Turkey) resin with melt flow index of 25 g/10 min used in this study. Four types of minerals that were incorporated into PP were talc, calcite, mica and feldspar. Talc and calcite with a density of 2.78 g/cm^3 and 2.71 g/cm^3, respectively were purchased from Omya Mining, Turkey. Mica and feldspar with a density of 2.81 g/cm^3 and 2.62 g/cm^3, were obtained from Mikron'S, Turkey and Şişecam, Turkey, respectively.

Bulk densities and chemical compositions of the fillers provided by the suppliers are given in Table 1. Talc is a natural fine powder with its 42% SiO2 and 29% MgO content. Feldspar is naturally occurring aluminum silicate as it is understood from its chemical composition. Calcium carbonate powder obtained from high purity white marble and its CaCO3 content is around 98.5%. Feldspar has mostly 70% SiO2, 18.5% Al2O3 and 10.5% Na2O content. Mica is produced from deposits with high quality SiO2 and Al2O3.

Table 1. Bulk density and chemical composition of the fillers.

Filler	Bulk Density (g/cm^3)	Chemical Composition (%)								
		SiO_2	MgO	CaO	$CaCO_3$	$MgCO_3$	Al_2O_3	Na_2O	Fe_2O_3	K_2O
Talc	0.55	42	29	9	-	-	-	-	-	-
Calcite	1.3	-	-	-	98.5	1.5	-	-	-	-
Feldspar	0.61	70	0.1	0.7	-	-	18.5	10.5	0.02	-
Mica	0.31	53.02	-	-	-	-	29.5	-	1.13	9.1

2.2. Manufacturing of Compound

PP and mineral fillers at 40 wt. % were compounded with twin screw extruder at different barrel temperatures (195-215 °C) and screw speeds (200-300 rpm). The amount of each mineral added to the extruder was controlled by the help of gravimetric feeders (Figure 1a). The extrusion run condition for the all the composite formulations were kept the same. Polymer strands with a diameter of 3 mm were obtained after mineral filled polymer melt passed through the extruder die. Then, following the water bath, composite granules were produced by pelletizer. The water bath used during compounding process was kept at 16 °C. Figure 1b shows a picture of the water bath and the pelletizer. In order to produce test specimens injection molding machine was used (Figure 1c). The injection molding conditions for each test sample were kept constant as long as the samples could be molded.

(a) (b) (c)

Fig. 1. a) twin screw extruder and b) water bath and pelletizer c) Injection molding

2.3. Characterization Methods

In this study, the effects of various minerals on density, tensile properties, flexural properties, impact properties, melt flow index, rheological properties, vicat softening temperature, melting and crystallization and decomposition temperatures, and thermal expansion coefficient of mineral filled PP composites were examined. Density measurement of the mineral filled PP composite specimens was done using Densimeter MD-200S by following the ISO1183 standard [16]. Hegewald & Peschke Inspect 20 tensile-compression testing machine was used to investigate the tensile and flexural properties. Tensile tests were done according to the ISO 527 standard with 50 mm/min and non-contact video extensometer [17]. Three-point bending tests were done with a 1 mm/min deformation rate according to the ISO 178 standard for flexural properties [18]. Izod notched and un-notched impact strengths of the samples were determined according to ISO 180 standard by using a pendulum-type tester [19]. Göttfert Melt indexer mi2.2 was used to measure melt flow index (MFI) of the samples. The used melt temperature and piston load were 230 °C and 2.16 kg, respectively during the MFI tests according to ASTM D-1238 standard [20]. Capillary rheometer (Göttferd, Rheograph 20) was used to determine the viscosity of PP and mineral filled polypropylene composites. The vicat softening temperature was measured according to the ISO 75-1 standard with an applied

load of 10 N in the testing apparatus [21]. Differential scanning calorimeter (DSC-Q20, TA Instruments, Inc.,) and TG Analyzer (TA Instruments, Inc., TGA-Q50) were used in order to investigate thermal properties of polypropylene and its composites. Both analyses were done under nitrogen environment with a heating rate of 10 ^{0}C/min. Thermo-mechanical analyzer (TA Instruments, Inc., TMA 400) was used to determine the thermal expansion coefficient of the samples.

3. Results and Discussion

3.1. Density

Density values of PP and mineral filled polypropylene composites are given in Figure 2. The density of the talc, calcium carbonate, mica and feldspar is relatively higher than that of PP (0.900 g/cm^3); thus, it can be said that the incorporation of minerals into PP increases the density of the neat PP. Since feldspar is found to be 6% lighter compared to talc, it shows promise to be used in various applications where being lightweight is significantly important.

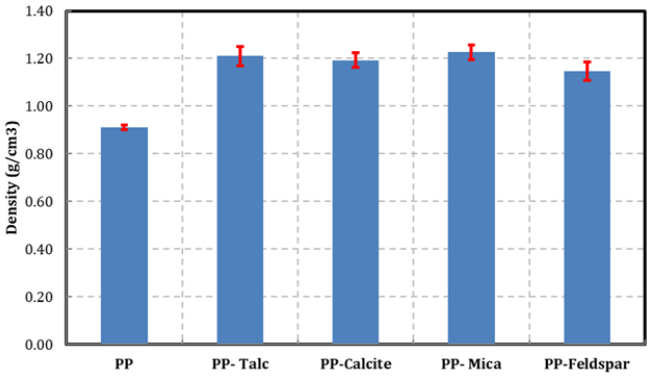

Fig. 2. The effects of mineral types on density of mineral filled PP composites

3.2. Mechanical Testing

Table 2 shows the effect of mineral types on mechanical properties of PP and mineral filled PP composites. The tensile and flexural strength of the PP were about 31 and 39 MPa, respectively. Tensile strength values of PP-Talc, PP-Calcite, PP-Mica and PP-Feldspar were obtained to be 30, 21, 29, and 21 MPa, respectively. It can be seen from Table 2 that talc and mica filled PP composites have not led to considerable variation in tensile strength value of PP. While talc and mica loadings into PP increased the flexural strength of PP, calcium carbonate and feldspar loadings decreased the flexural strength of PP. One can say that the polymer matrix could wet the fillers in a better way since talc and mica have a high aspect ratio and layered silicate structures[22]. This has been stated before that this phenomenon creates fewer micro-voids between the fillers and matrix [23, 24] resulting enhanced wettability. Calcium carbonate and feldspar loading into PP decreased the tensile and flexural strengths of PP remarkably due to relatively low aspect ratio of calcium carbonate and feldspar compared to talc and mica. PP-Talc and PP-Mica composites showed increased tensile strength values as compared to PP-Calcite and PP-Feldspar composites. This improvement shows better surface interactions between filler and matrix, which results in better stress transfer from matrix to the filler under high loadings.

As shown in Table 2, flexural and tensile moduli of PP increased with mineral filler loadings. The increase in tensile and flexural properties could be because of the reduced mobility and limited deformability of the matrix as a result of filler incorporation[22]. The limitation on the mobility of polymer chains decreases the stress transfer from the whole composite which in turn causes increase in rigidity and stiffness. An increase in flexural and tensile moduli by a maximum of about 257% and 268 %, respectively, was observed in PP-Mica composites. Also, larger mica particles with rigid molecular structure compared to smaller talc, calcium carbonate and feldspar particles could have resulted in worse stress transfer in mica filled PP based composites.

As can be observed from Table 2, impact strength values decreased when mineral fillers were used in PP composites. The un-notched and notched Izod impact strength of the PP was 54.16 and 5.79 kJ/m^2, respectively. Un-notched Izod impact strength for the PP-Talc, PP-Calcite, PP-Mica and PP-Feldspar composites decreased by 71, 61, 69, and 13% compared to the PP, respectively. When compared to PP without any mineral fillings, 40, 36, 32, and 10%, decreases in notched Izod impact strength values were obtained for PP-Talc, PP-Calcite, PP-Mica and PP-Feldspar, respectively. It can be noted that a considerable decrease in impact strength values were obtained. The less decrease in impact strength was obtained by loading feldspar rather than other fillers. In other words, feldspar is better than talc, calcium carbonate and mica in absorbing the impact energy [25].

Table 2. The effects of mineral types on mechanical properties of mineral filled PP composites

	Tensile Properties		Flexural Properties		Izod Impact Properties	
	Tensile Strength (MPa)	Tensile Modulus (MPa)	Flexural Strength (MPa)	Flexural Modulus (MPa)	Un-notched Impact Strength (kJ/m^2)	Notched Impact Strength (kJ/m^2)
PP	31.1±2.1	1200±65	39.1±2.3	1167±57	54.2±2.7	5.8±0.4
PP- Talc	30.3±1.7	2673±72	54.3±3.2	3540±62	15.7±2.0	3.5±0.3
PP-Calcite	20.9±1.5	2879±78	38.4±2.1	3806±69	21.0±1.8	3.7±0.4
PP- Mica	29.4±1.5	4417±102	48.2±2.8	4168±75	17.0±1.1	3.9±0.4
PP-Feldspar	21.2±1.4	2768±85	40.1±1.6	3782±82	47.3±2.5	5.2±0.4

3.3. Rheological Analysis

The rheological behavior of PP is highly affected by mineral fillers. It is expected that incorporation of minerals creates higher viscosity of PP melts compared to the pure PP matrix. The melt flow index (MFI) of mineral filled PP based composites are shown in Figure 3. As shown from Figure 2, lower MFI values in mineral filled composites were obtained compared to that of neat PP. This is because of the fact that when minerals are added to the polymer, viscosity of the polymer matrix increases which restricts polymer flow and decreases the value of MFI [23]. Among all the minerals that were used in this study, calcium carbonate and feldspar filled PP composites demonstrated higher MFI values than that of the other composites. One can say that, calcium carbonate and feldspar have the ability to increase the processability of the polymer. As can be seen, mica gave a slightly lower MFI than calcium carbonate and feldspar and lowest MFI was obtained when talc was the filler in PP composites.

The literature shows that due to their platelet/lamellar structure, talc and mica particles at lower weight fractions could slide against each other during the application of shear forces which increases flowability in the composites. Nevertheless, MFI values of talc or

mica filled PP composites were obtained to be low when minerals are used at 40 wt.% in the (Figure 3). It can be contributed to that, this ability depends on the location of the filler particles in the die which has significant effect on resulting MFI of the composites [23].

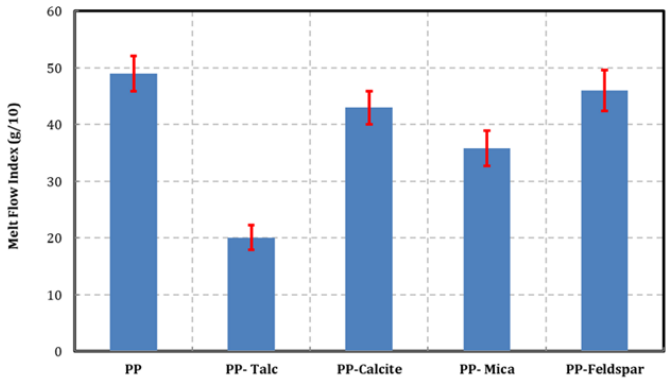

Fig. 3 MFI values of mineral filled PP composites

Change in viscosity values of PP and mineral filled PP composites as a function of shear rate is given in Figure 4. From Figure 4, decreasing trend on viscosity of the composites was seen with increasing shear rate. Especially at high shear rates, the lowest viscosity value was obtained in feldspar filled PP composites, which explains the highest MFI value in PP-Feldspar sample. It is known that at high shear rates due to broken structure of the composite, hydrodynamic interactions have a significant effect on the viscosity instead of filler particles[26].

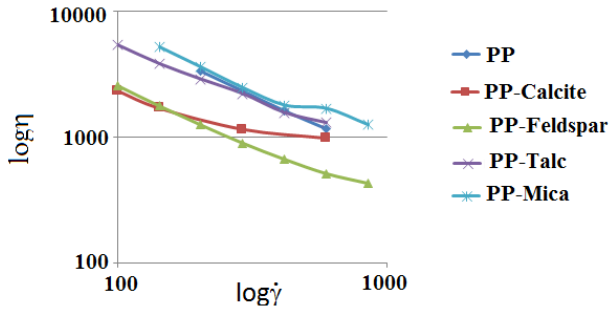

Fig. 4 log η vs. log $\dot{\gamma}$ plots of PP and mineral filled composites

The Power Law model is used to describe the rheological behavior of the apparent viscosity decreasing as the shear rate increases (shear thinning)[27]. The Power Law model is defined by

$$\eta = k\dot{\gamma}^{(n-1)} \tag{1}$$

where k is the consistency index and n is the power-law index. When n< 1 the fluid is called pseudoplastic and when n > 1, it is called dilatant [28].

The Power Law Index (n) was derived from the slope of the graphs for the logarithmic viscosity and the logarithmic shear rate [29]. Consistency index and power law index values of samples are given in Table 3. It is seen that calcite, feldspar, talc and mica filled PP composites exhibited more temperature sensitive than PP. Due to low power law index values, melt viscosity of PP-Feldspar, PP-Talc, and PP-mica changes more with increasing or decreasing shear rate than by changing the melt temperature.

Table 3. Power Law Index (n) values for PP and its composites

Sample	k-Consistency index	n-power law index
PP	6.70E+05	0.01
PP- Calcite	1.80E+04	0.52
PP-Feldspar	1.19E+05	0.15
PP-Talc	2.10E+05	0.20
PP-Mica	2.40E+05	0.21

3.4. Vicat Softening Temperature Tests

Vicat softening temperature is the point of softening when material is used at elevated temperatures. This temperature could be used to determine the potential of the material to be used as a useful product for practical applications [30]. Figure 5 shows the characteristics of vicat softening temperature with mineral types in the mineral filled PP composites. As shown in Figure 5, vicat softening temperature increased with mineral loading. It can be said that improved heat softening characteristics could be achieved in the case of mineral filled polypropylene composites. The low thermal conductivity of mineral fillers may be the reason for the increase in the vicat softening temperature of mineral filled polypropylene composites[30].

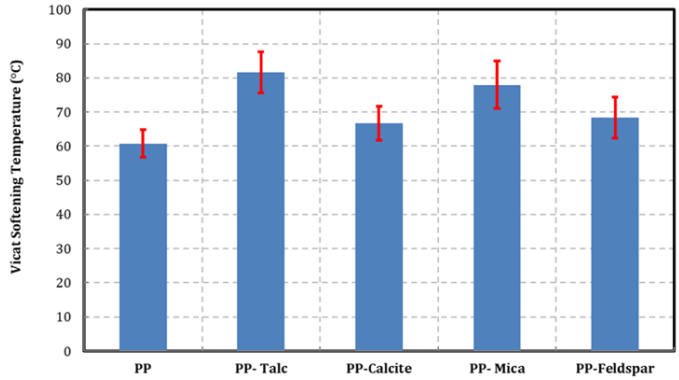

Fig. 5. Vicat softening temperature of PP and mineral filled composites

3.5. DSC Analysis

DSC analysis was performed to determine the melting and the crystallization behaviors of PP and mineral filled PP composites. With the DSC analysis, a graph of the heat flow for each sample is drawn depending on the temperature and is given in Figure 6. The melting and crystallization temperatures, the melting and crystallization enthalpies and degree of crystallinity obtained from the graph are given in Table 4. Degree of crystallinization (X_c) was calculated from Equation given below

$$X_c(\%) = \frac{\Delta H_m}{(1-w)\Delta H_{0m}} x100 \quad (2)$$

where w is the weight fraction of mineral fillers and ΔH_{0m} is the melting enthalpy value of 100% crystalline form of PP (209 J/g) [31]

It could be seen from Table 4 that the melting temperatures (T_m) decreased, and the crystallization temperatures (T_c) increased together with the addition of mineral fillers to PP composites. However, this increase and decrease were not very pronounced with mica, calcite and feldspar fillers, although the melting temperature remained constant with the addition of talc, there was an increase of 9 °C in the crystallization temperature. So it could be said that talc acts as a nucleating agent in PP composites thus the crystallization temperature of talc filled PP composites increased [32]. When melting and crystallization enthalpies were examined, it could be seen that there was a decrease in energies in both cases compared to that of polypropylene. The reason for the decrease in melting enthalpy could be the mineral fillers absorb more heat energy during the melting of composites so the melting enthalpy than the neat PP [33]. The biggest difference was seen with the addition of 40 wt. % by weight of mica. When it was focused on the degree of crystallization (X_c) of neat PP and its composites it was observed that the X_c value of the PP is 29.57 %. The crystallinity of polypropylene changed irregularly with the addition of mineral filler. Mica and feldspar decreased the X_c while calcite and talc increased. This situation can indicate that X_c is generally affected by dispersion, loading level or surface chemistry of fillers. This was consistent with the studies in literature [32, 34, 35].

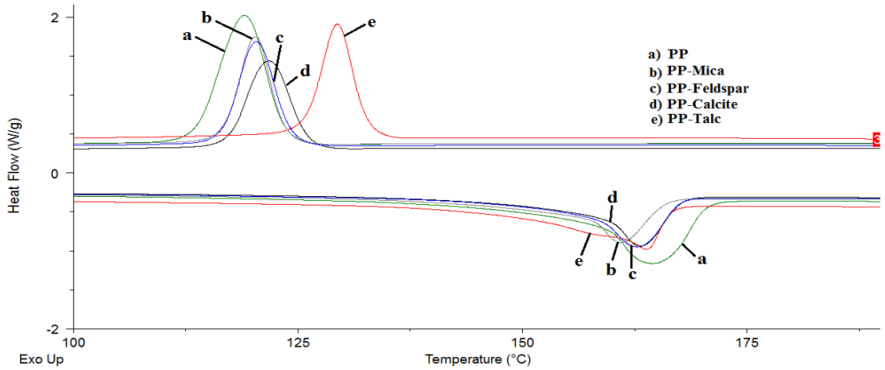

Fig. 6. DSC curves of PP and mineral filled PP composites

Table 4. DSC results for PP and mineral filled PP composites.

Sample	T_m (^0C)	T_c(^0C)	ΔH_m(J/g)	ΔH_c(J/g)	X_c (%)
PP	164	119	61.2	64.3	29.57
PP-Mica	161	120	34.3	38.3	27.62
PP-Calcite	163	122	37.8	40.1	30.43
PP-Feldspar	163	120	35.9	40.7	28.90
PP-Talc	164	129	40.0	42.9	32.21

3.6. TG Analysis

TG analysis was performed on the samples to determine the maximum degradation temperature, temperature of 5% of mass loss and the weight loss due to temperature change in PP and its composites. TG and DTG curves of the samples are given in Figure 7.

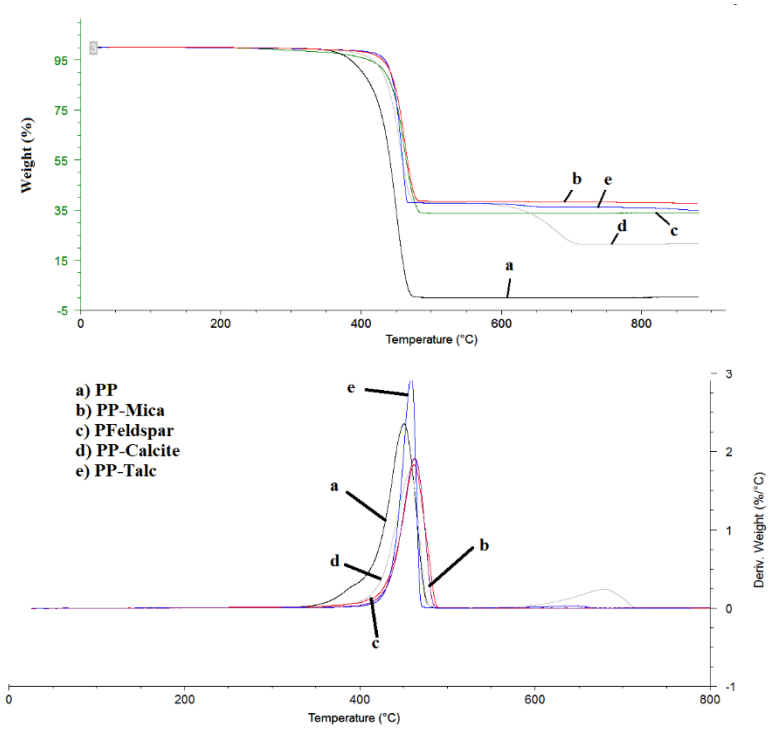

Fig. 7. TG/DTG curves for PP and its composites

Table 5 shows the maximum decomposition temperature obtained with the help of graph and the remaining weight without degradation after the temperature of 800 °C. From Table 5, it was seen that the decomposition temperature of PP increased when mineral fillers were used in PP composites. The largest increase was 22 °C with the addition of mica as a filler to PP, while the least increase was with the addition of calcite. It could be said that the mineral fillers can be improved the thermal stability of PP composites. The increased thermal stability can be attributed to the impeded diffusion of volatile degradation products in composites. Qin et al. have similar studies in the literature [36]. According to these results it was seen that most stable composite was mica-filled PP, while the least stable was calcite-filled PP. On the other hand, while PP lost 5% of its mass at 384 °C, this

temperature increased with the addition of minerals. Although the highest decomposition temperature was obtained with the addition of mica, the temperature at which talc-filled PP composites lose 5% by mass was higher. Looking at the percentage mass that remains un-degraded at the end of 800 °C, it was seen that the most temperature resistant composite was PP with mica filling.

Table 5. TGA results for PP and mineral filled PP composites

Sample	T_{max}(^{0}C)	Temperature of 5% mass loss (^{0}C)	Residual weight at 800 ^{0}C, %
PP	451	384	-
PP-Mica	463	431	38
PP-Calcite	457	416	22
PP-Feldspar	462	411	34
PP-Talc	459	433	36

T_{max}: maximum degradation temperature

3.7. TM Analysis

In order to determine the coefficient of thermal expansion (CTE) values thermomechanical analysis was done to the samples of PP and its composites. Table 6 and Figure 8 gives CTE values and TMA curves of PP and its composites, respectively.

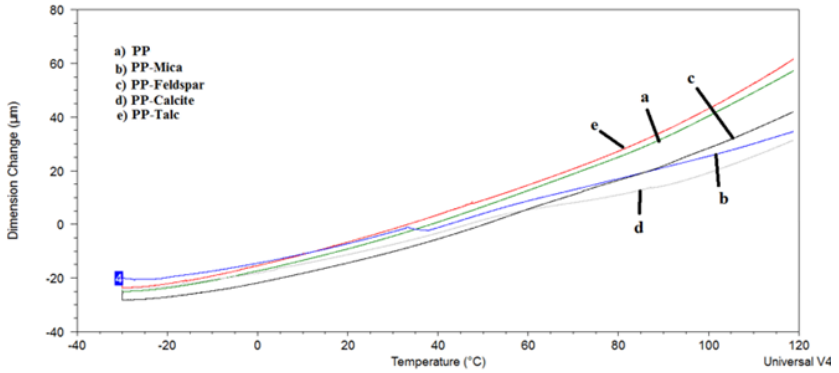

Fig. 8. Dimension change versus temperature curves for PP and mineral filled PP composites

The thermal expansion coefficient is one of the most important physical properties used to describe the changes in the size of materials with temperature. The thermal expansion coefficient is of great importance in determining the processing and application conditions of polymeric composites[37]. When compared to neat PP, it could be said that all mineral loadings, except talc, reduce the coefficient of thermal expansion. This may be because mineral fillers reduce the thermal expansion as a result of their interaction with the polymeric matrix and consequently the movement of the polymer chains is restricted [38] While the largest decrease was in mica loading, the least decrease was in feldspar filled PP composites.

Table 6. CTE values of PP and mineral filled PP composites

Sample	CTE(-10 to 50 °C) (μm/m)°C
PP	118
PP-Mica	87
PP-Calcite	92
PP-Feldspar	103
PP-Talc	120

4. Conclusion

In this study the effect of mineral types on the physical, mechanical, thermal and rheological properties of mineral filled polypropylene composites were investigated. According to this research; the higher density values were obtained with mineral filler loading. The lowest density of 1.15 g/cm^3 was obtained when feldspar was used as a filler. 40 wt. % mineral loading into PP decreased the tensile strength of PP. Tensile strength values of 31.1, 30.3, 20.9, 29.4 and 21.2 MPa was obtained for PP, PP- Talc, PP- Calcite, PP-Mica, and PP-Feldspar, respectively. It was demonstrated that the decrease in tensile strength in PP-Talc and PP-Mica composites were lower compared to the other mineral fillers. Mineral loadings into PP by 40 wt. % increased the tensile and flexural moduli of PP. Decrease in impact strength of PP was observed with the addition of minerals. The less decrease in impact strength was obtained by loading feldspar rather than talc, calcium carbonate and mica. MFI of PP decreased with addition of all minerals. Mineral addition increased the vicat softening temperature of PP. Vicat softening temperatures of PP, PP-Talc, PP-Calcite, PP-Mica, and PP-Feldspar were obtained to be 61, 82, 67, 78 and 68 °C, respectively. Lower viscosity rates were observed in the composites of PP-Calcite and PP-Feldspar. 40 wt. % mineral filled PP composites have higher degradation temperature than PP. Coefficient of thermal expansion decreased with all mineral loadings except talc in PP composites. Calcite, mica or feldspar loaded PP composites could be an alternative for use in automotive industry compared to the talc loaded PP composites due to their better impact properties.

Conflicts of Interest

No conflict of interest was declared by the authors.

References

[1] Chung TC, Rhubright D. Synthesis of functionalized polypropylene. Macromolecules, 1991, 24(4):970-972. https://doi.org/10.1021/ma00004a026

[2] Tjong SC, Xu S-A, Li RK-Y, Mai Y-W. Mechanical behavior and fracture toughness evaluation of maleic anhydride compatibilized short glass fiber/SEBS/polypropylene hybrid composites. Composites Science and Technology, 2002, 62(6):831-840. https://doi.org/10.1016/S0266-3538(02)00037-4

[3] D'Orazio L, Mancarella C, Martuscelli E, Sticotti G, Massari P. Melt rheology, phase structure and impact properties of injection-moulded samples of isotactic polypropylene/ethylene-propylene copolymer (iPP/EPR) blends: influence of molecular structure of EPR copolymers. Polymer, 1993, 34(17):3671-3681. https://doi.org/10.1016/0032-3861(93)90052-C

[4] Chan C-M, Wu J, Li J-X, Cheung Y-K. Polypropylene/calcium carbonate nanocomposites. Polymer, 2002, 43(10):2981-2992. https://doi.org/10.1016/S0032-3861(02)00120-9

[5] Lapcik Jr L, Jindrova P, Lapcikova B, Tamblyn R, Greenwood R, Rowson N. Effect of the talc filler content on the mechanical properties of polypropylene composites. Journal

of Applied Polymer Science, 2008, 110(5):2742-2747. https://doi.org/10.1002/app.28797
[6] Ray SS, Okamoto M. Polymer/layered silicate nanocomposites: a review from preparation to processing. Progress in polymer science, 2003, 28(11):1539-1641. https://doi.org/10.1016/j.progpolymsci.2003.08.002
[7] Fu SY, Lauke B, Mäder E, Yue CY, Hu X. Tensile properties of short-glass-fiber- and short-carbon-fiber-reinforced polypropylene composites. Composites Part A: Applied Science and Manufacturing, 2000, 31(10):1117-1125. https://doi.org/10.1016/S1359-835X(00)00068-3
[8] Xavier S, Sharma Y. Structure-property relations in polypropylene mica composites. Polymer Composites, 1986, 7(1):42-49. https://doi.org/10.1002/pc.750070109
[9] Mina MF, Seema S, Matin R, Rahaman MJ, Sarker RB, Gafur MA, et al. Improved performance of isotactic polypropylene/titanium dioxide composites: effect of processing conditions and filler content. Polymer Degradation and Stability, 2009, 94(2):183-188. https://doi.org/10.1016/j.polymdegradstab.2008.11.006
[10] Premalal HGB, Ismail H, Baharin A. Comparison of the mechanical properties of rice husk powder filled polypropylene composites with talc filled polypropylene composites. Polymer Testing, 2002, 21(7):833-839. https://doi.org/10.1016/S0142-9418(02)00018-1
[11] Kellar JJ. Functional fillers and nanoscale minerals: new markets/new horizons. SME, 2006.
[12] Leong Y, Ishak ZM, Ariffin A. Mechanical and thermal properties of talc and calcium carbonate filled polypropylene hybrid composites. Journal of Applied Polymer Science, 2004, 91(5):3327-3336. https://doi.org/10.1002/app.13543
[13] Ferrage E, Martin F, Boudet A, Petit S, Fourty G, Jouffret F, et al. Talc as nucleating agent of polypropylene: morphology induced by lamellar particles addition and interface mineral-matrix modelization. Journal of Materials Science, 2002, 37(8):1561-1573. https://doi.org/10.1023/A:101492912136 7
[14] Rothon R. Particulate-filled polymer composites. iSmithers Rapra Publishing, 2003.
[15] Zilles JU. Feldspar and Syenites. In: Palsule S, editor. Polymers and Polymeric Composites: A Reference Series. Springer Berlin Heidelberg, Berlin, Heidelberg, 2016. https://doi.org/10.1007/978-3-642-37179-0_5-6
[16] Standard I, ISO B. ISO 1183-1:2019(en) Plastics - Methods for determining the density of non-cellular plastics - Part 1: Immersion method, liquid pycnometer method and titration method. 2019.
[17] Standard I, ISO B. ISO 527-1:2019(en) Plastics - Determination of tensile properties - Part 1: General principles. 2019.
[18] Standard I, ISO B. Plastics-Determination of flexural properties. ISO Geneva, Switzerland:; 2019.
[19] ISO I. 180-Plastics-Determination of Izod Impact Strength. International Organization of Standards: Geneva, Switzerland, 2019.
[20] ASTM D. Standard Test Method for Melt Flow Rates of Thermoplastics by Extrusion Plastometer. 2004.
[21] ISO 75-1:2020 Plastics-Determination of temperature of deflection under load-Part 1: General test method, 2001.
[22] Mittal P, Naresh S, Luthra P, Singh A, Dhaliwal JS, Kapur GS. Polypropylene composites reinforced with hybrid inorganic fillers: Morphological, mechanical, and rheological properties. Journal of Thermoplastic Composite Materials, 2018: 848-864. https://doi.org/10.1177/0892705718785674
[23] Leong Y, Abu Bakar M, Ishak ZM, Ariffin A, Pukanszky B. Comparison of the mechanical properties and interfacial interactions between talc, kaolin, and calcium carbonate filled polypropylene composites. Journal of Applied Polymer Science, 2004, 91(5):3315-3326. https://doi.org/10.1002/app.13542

[24] Wake W. Fillers for Plastics; by the Plastics Institute. London; 1971.
[25] Liang J, Li R. Mechanical properties and morphology of glass bead-filled polypropylene composites. Polymer Composites, 1998, 19(6):698-703. https://doi.org/10.1002/pc.10142
[26] Samsudin M, Ishak ZM, Jikan S, Ariff Z, Ariffin A. Effect of filler treatments on rheological behavior of calcium carbonate and talc-filled polypropylene hybrid composites. Journal of Applied Polymer Science, 2006, 102(6):5421-5426. https://doi.org/10.1002/app.25054
[27] Green DW, Willhite GP. Enhanced oil recovery. Henry L. Doherty Memorial Fund of AIME, Society of Petroleum Engineers, Richardson, TX, 1998.
[28] Berker A. Rheology for adhesion science and technology. Adhesion Science and Engineering. Elsevier Science B.V., Amsterdam, 2002, 443-498. https://doi.org/10.1016/B978-0-444-51140-9.50039-1
[29] Güldaş A, Güllü A, Çankaya A. Determination of the Rheological Properties of Polypropylene Filled with Colemanite. Polymers for Advanced Technologies, 2017, 28(9):1179-1184. https://doi.org/10.1002/pat.4011
[30] Zheng Y, Shen Z, Cai C, Ma S, Xing Y. The reuse of nonmetals recycled from waste printed circuit boards as reinforcing fillers in the polypropylene composites. Journal of Hazardous Materials, 2009, 163(2-3):600-606. https://doi.org/10.1016/j.jhazmat.2008.07.008
[31] Altay L, Atagur M, Akyuz O, Seki Y, Sen I, Sarikanat M, et al. Manufacturing of recycled carbon fiber reinforced polypropylene composites by high speed thermo-kinetic mixing for lightweight applications. Polymer Composites, 2018, 39(10):3656-3665. https://doi.org/10.1002/pc.24394
[32] Yao Z, Chen T, Li H, Xia M, Ye Y, Zheng H. Mechanical and thermal properties of polypropylene (PP) composites filled with modified shell waste. Journal of hazardous materials, 2013, 262:212-217. https://doi.org/10.1016/j.jhazmat.2013.08.062
[33] Lee S, Kang I, Doh G, Kim W, Kim J, Yoon HG, et al. Thermal, mechanical and morphological properties of polypropylene/clay/wood flour nanocomposites. Express Polymer Letters, 2008, 2(2):78-87. https://doi.org/10.3144/expresspolymlett.2008.11
[34] Guo T, Wang L, Zhang A, Cai T. Effects of nano calcium carbonate modified by a lanthanum compound on the properties of polypropylene. Journal of Applied Polymer Science, 2005, 97(3):1154-1160. https://doi.org/10.1002/app.21804
[35] Zebarjad SM, Sajjadi SA, Tahani M. Modification of fracture toughness of isotactic polypropylene with a combination of EPR and $CaCO_3$ particles. Journal of Materials Processing Technology, 2006, 175(1-3):446-451. https://doi.org/10.1016/j.jmatprotec.2005.04.043
[36] Qin H, Zhang S, Zhao C, Feng M, Yang M, Shu Z, et al. Thermal stability and flammability of polypropylene/montmorillonite composites. Polymer Degradation and Stability, 2004, 85(2):807-813. https://doi.org/10.1016/j.polymdegradstab.2004.03.014
[37] Saba N, Jawaid M. A review on thermomechanical properties of polymers and fibers reinforced polymer composites. Journal of Industrial and Engineering Chemistry, 2018, 67:1-11. https://doi.org/10.1016/j.jiec.2018.06.018
[38] Kodal M, Karakaya N, Wis AA, Ozkoc G. Thermal properties (DSC, TMA, TGA, DTA) of rubber nanocomposites containing carbon nanofillers. Carbon-Based Nanofillers and Their Rubber Nanocomposites-Fundamentals and Applications. 2019,325-366. https://doi.org/10.1016/B978-0-12-817342-8.00011-1

Research on Engineering Structures & Materials
journal homepage: http://jresm.org
Research Group

Research Article

Lightweight geopolymer fly ash sand: an alternative to fine aggregate for concrete production

P. N. Ojha [a], Brijesh Singh*[b], Puneet Kaura [c], Abhishek Singh [d]

National Council for Cement and Building Materials, India

Article Info

Article history:
Received 05 Feb 2021
Revised 15 May 2021
Accepted 20 May 2021

Keywords:

Light Weight Geopolymer Fly Ash Sand;
Water Absorption;
Specific Gravity;
Compressive Strength;
Durability Studies

Abstract

The current study is aimed to evaluate and critically analyze the properties of Light Weight Geopolymer Fly Ash Sand (LWGFAS). LWGFAS has been prepared by geopolymerisation of the fly ash. Liquid solution of 4M NaOH, and Na2SiO3/NaOH=2 was used as an activator and post set heat treatment of 1 hour at 100 °C was applied for preparation of LWGFAS. The LWGFAS sample was analyzed for different physical and chemical parameters along with studies on mineralogy and alkali silica reactivity. The molar concentration of activator solution and duration of post set heat treatment plays vital role on the physical and mechanical properties (particularly specific gravity, bulk density and water absorption) of the Geopolymer fly ash sand. The specific gravity and water absorption of LWGFAS were 1.57 and 17.85% respectively. Experimental concrete mixes made with LWGFAS as a replacement of natural sand were evaluated for compressive strength and different durability properties of concrete. The study indicates that LWGFAS can be suitable for a wide range of applications in making concrete ranging from light weight in nature to normal weight concrete based on the physical and chemical characteristics of Geopolymer Fly Ash Sand.

1. Introduction

Depletion of the natural minerals and the over usage of the natural sources are consequences of the usage of the M-sand (Manufactured sand) and the natural sand respectively which in turn adversely affect the environmental balance that makes a call to identify the ideal replacement material for fine aggregate in the concrete preparation [1]. Worldwide consumption of concrete is estimated to be about 11.5 billion tons per year and by year 2050 it is expected to reach to 18 billion tons of concrete per year [2]. However, as per the Cement Sustainability Initiative (CSI) report-2009 by World Business Council for Sustainable Development, the annual consumption of concrete worldwide has gone upto 25 billion tons of concrete per year-by-year 2009 [3]. In order to achieve sustainability in construction industry, the use of alternate materials should be focused with comprehensive approach. Fine aggregate is an essential material in the concrete production. From many decades, river sand is used as fine aggregate but dredging of sand from river beds is adversely affecting environment across the world. Donza et al. [4] reported an increase in compressive strength of concrete mix by 10–15%, when crushed stone sand was used as a 100% replacement of natural sand. Such results led to increase in use of quarry dust as fine aggregate in concrete. However, particulate matter emitted from crushing units during mining and crushing of the stones for crushed sand causes air pollution and usage of heavy machinery during this process leads to noise, thereby causing

*Corresponding author: brijeshsehwagiitr96@gmail.com
[a] orcid.org/0000-0003-1754-4488; [b] orcid.org/0000-0002-6512-1968; [c] orcid.org/0000-0001-7237-8043; [d] orcid.org/0000-0002-2343-5934
DOI: http://dx.doi.org/10.17515/resm2021.257ma0205

negative impact on the environment. The fly ash generation in India through thermal power plants in 2014-15 was about 185 million tons and utilization was 55.69% [5, 6].

Research has been carried out for the use of waste material like bottom ash, construction and demolition waste, copper slag, iron and steel slag as a fine aggregate [7, 8, 9, 10]. Another alternative could be use of sintered fly ash lightweight aggregate which is now commercially available for use in structural concrete with an upper ceiling on grade of concrete in Indian specification IS 9142 Part 2 [11]. Along with the problem on the scarcity of natural river sand and finding its alternatives, growth of the construction and infrastructure industry throughout the globe is demanding the need to examine the feasibility of using other alternatives such as fly ash–geopolymerization reactions to produce fine aggregates as an alternative to natural sand. The geopolymerisation of the fly ash is the process wherein the fly ash is mixed with alkaline activator solution consisting of the hydroxides and the silicates which dissolves and transforms the vitreous phase present in the fly ash in to a three dimensional structure, leading to the solidification of the material [12- 15]. Due to their lower calcium content, they are more resistant to acid attack than Portland cement-based materials [16]. Limited number of studies related to manufacture and the use of the fly ash based geopolymer sand for construction purpose have been conducted by the researchers till date. Rao et al. [17] performed studies on characterization of geopolymer sand which was prepared on laboratory scale using fly ash. Similar study was also carried out by Agrawal et al. [18], where geopolymer sand was prepared on commercial scale and was characterized for its different parameters such as water absorption, specific gravity, soundness, particle size distribution etc. In both of these studies, preparation of fly ash based geopolymer sand was done using 10 M NaOH solution. On comparison of physical characteristics of river sand with geopolymer fly ash sand, it was observed that both fine aggregates had similar grain size distribution and specific gravity values.

The molar concentration of activator solution plays a very vital role on the mechanical properties of the product obtained from geopolymerisation. Higher concentration of activator leads to Geopolymeric products of higher strength, density (specific gravity) and lower water absorption [19]. Apart from molar concentration, heat treatment after initial mixing and granulation plays a vital role on the physical and mechanical properties of the final product. Rao et al. [17] heated cohesive mass (slurry formed from mixing fly ash with activator solution dried for 4 hours) obtained through 4 mm mesh at 100 oC for 7 days in a temperature-controlled oven to complete geopolymerisation reaction. Physical properties (specific gravity and bulk density) of geopolymer fly ash sand obtained from usage of high molar concentration and extended post-set heat treatment were comparable to conventional natural sand. However, preparation of geopolymer fly ash sand with activator solutions of very high molar concentrations and applying post set heat treatment for extended duration may not be the cost-effective approach while developing geopolymer fly ash sand as an alternative to the river sand.

2. Research Significance

Based on the literature studied, it was observed that only limited studies has been done on Geopolymer Fly ash sand. Research work to lower the molar concentrations and duration of post set heat treatment applied to Geopolymeric product while production of geopolymer fly ash sand shall be done in order to lower the production cost, without compromising the quality of the final product. Hence, in this study geopolymer fly ash sand was prepared with lower concentration of activator solution and significantly lower duration of post set heat treatment. In the current study, Light Weight Geopolymer Fly Ash Sand (LWGFAS) was evaluated as a potential alternative to natural fine aggregate. In the present investigation, characterization of LWGFAS was done for assessing its suitability to

be used in concrete and mortar. Further, concrete mixes containing geopolymer fly ash sand as replacement of natural sand were prepared and evaluated for different hardened and durability parameters and their performance was compared with control concrete mix made with 100% natural sand. Studies were also carried out on different grades of mortar prepared with LWGFAS and their subsequent comparison with mortar prepared with natural sand.

3. Preparation of Light Weight Geopolymer Fly Ash Sand (LWGFAS)

The geopolymerisation process depends on the reactivity and concentration of alkaline activator. The alkali-enrichment in lightweight geopolymer fly ash sand increases pore structure development of the concrete system, which considerably affects the sample with less water to binder ratio. Furthermore, the increase in alkalinity results in the degradation of mechanical strength. Therefore, the quantity of alkaline activators needs to be considered wisely while designing the light weight geopolymer fly ash concrete mix. In current study, Lightweight Geopolymer fly ash sand (LWGFAS) was prepared by using class F fly ash and alkaline activator solution. The fly ash used in the study was from NTPC Sipat, India. The specific gravity and Blaine's fineness of fly ash was 2.12 & 382 m^2/kg respectively. On the basis of SiO_2 (52.32%), Al_2O_3 (26.29%), and CaO (5.83%) contents, fly ash is categorized as Class F. The alkaline solution was prepared by mixing sodium hydroxide pellets (purity 90%) to water (4 M), and then adding sodium silicate (Na_2SiO_3) solution to it with SiO_2:Na_2O = 2 (SiO_2 = 29.8%, Na_2O = 14.98%). The ratio of sodium silicate solution to sodium hydroxide solution was 2 by weight [20]. Lightweight Geopolymer fly ash sand (LWGFAS) was prepared by mixing the fly ash in the alkaline solution (NaOH + Na_2SiO_3). The molarity of NaOH and ratio of Na2SiO3: NaOH was kept constant to 4 M and 2:1 respectively to make GFS cost effective. The alkaline activator solution was prepared and stored for 24 h prior to mixing it with the fly ash. Fly ash was heated up to a temperature of 60° C and mixed with the alkaline activator solution the ratio of 3:1 respectively. Elevating the curing temperature to 60^0C increases the extent and rate of reaction, through an increase in mesopore volume, surface area and an accelerated setting time. The kinetics appears to be temperature-controlled only before the material is hardened. The mixing was done in a centrifugal mixer machine wherein the fly ash was mixed with the alkaline solution for 10 minutes to produce a dry mix having workability of 24–30 s as per Vee-Bee Consistometer test. After the mixing, the dry mix was transferred to a vibro-sifter wherein the mix was vibrated and passed through 4.75 mm and 2.36 mm IS sieve to yield particles of varying size similar to the shape and size of the river sand. These particles were then heated to a temperature of about 100 ^{0}C for about one hour to harden the granules which are termed as LWGFAS as shown in Figure 1.

Fig. 1 Different Sizes of Light Weight Geopolymer Fly ash Sand (LWGFAS)

4. Experimental Work

The characterization of Light Weight Geopolymer Fly Ash Sand was performed. The LWGFAS was evaluated for various chemical and physical parameters as per IS 383: 2016 given in Table 1 & 2. The study also includes petrographic and mineralogical analysis of LWGFAS as per IS 2386 part VIII [21] and accelerated mortar bar test as per ASTM C1260 [22] to evaluate the expansion due to alkali-aggregate reactivity of LWGFAS. Other materials like cement sample, coarse aggregates, fine aggregates, chemical admixture were also tested for various physical and chemical parameters and were found conforming to their respective Indian and ASTM standards. The study also investigates the performance of concrete and mortar samples prepared with LWGFAS as fine aggregate. It has been compared with similar concrete and mortar samples prepared using river sand as fine aggregate. The durability studies on hardened concrete also evaluates the long term comparative behaviour of concrete made with LWGFAS with similar samples made with river sand.

5. Test Results and Discussion

5.1. Characterization of Light Weight Geopolymer Fly Ash Sand

The light weight geopolymer fly ash sand is evaluated for various chemical and physical parameters as per IS 383[23]. The results of physical and chemical analysis along with sieve analysis for LWGFAS are given in table 1 and 2 respectively.

Table 1. Physical and Chemical Test Results of Light Weight Geopolymer Fly Ash Sand

Sl. No.	Test Carried out	Result Obtained	Permissible Limits as Per IS: 383-2016
1	Specific gravity	1.57	2.1-3.2
2	Water absorption, %	17.85	5
3	Material finer than 75-micron, %	2.4	10.0
4	Soundness, Na2SO4 %	5.07	10
5	Organic impurities	Nil	--
6	Clay Lumps, %	Nil	1
7	Total deleterious material, % (except coal & lignite)	2.4	2
8	Silt by CPWD %	0.9	
9	Loss of Ignition (LOI)	3.12	--
10	Silica (SiO_2)	58.52	--
11	Iron oxide (Fe_2O_3)	3.55	--
12	Aluminium oxide (Al_2O_3)	22.94	--
13	Calcium oxide (CaO)	5.24	--
14	Magnesium oxide (MgO)	0.99	6.0 (Max)
15	Sulphate (SO_3)	0.30	0.5 (Max)
16	Total Alkalis as Na_2O eq.	3.37	0.3 (Max)
17	Chloride	0.030	0.040 (Max)

Table 2. Sieve Analysis Results of Light Weight Geopolymer Fly Ash Sand

	Percentage Passing	Percentage Passing for grading zone II as per IS 383-2016
10 mm	100	100
4.75 mm	100	90-100
2.36 mm	97	75-100
1.18 mm	79	55-90
600 µ	48	35-59
300 µ	20	8-30
150 µ	6	0-20
Zone	Zone II	

The specific gravity of LWGFAS is 1.57 and a loose bulk density of 780 kg/m3 which suggests that it is a light weight aggregate [24]. The specific gravity of geopolymer fly ash sand reported in literature [18] are higher than the geopolymer fly ash sand in this study.

It was observed that the specific gravity of the LWGFAS was observed as 1.57 which was comparatively less as compared to the river sand. The study conducted by Agrawal et al. [18] produced geopolymer fly ash sand with specific gravity as 2.46. The reduction in the specific gravity may be accounted due to the decrease in the molarity of the NaOH. The molarity of the NaOH is directly proportional to the strength of the geopolymer concrete, the geopolymer sand preparation was carried out using 10 M of NaOH solution, which may not be the cost effective alternative to the river sand. Along with higher concentration (10 M) of activator solutions, extended duration of post set heat treatment was applied to prepare the geopolymer fly ash sand in studies conducted by Agrawal et al [18]. However, in this study 4M NaOH solution and only 1 hour of post set heat treatment at 100oC was used for preparation of LWGFAS leading to lower specific gravity and higher water absorption. Due to lower specific gravity and high water absorption, use of LWGFAS may be restricted to concrete strength upto 35 MPa.

The values of water absorption (17.85%) and total deleterious materials (2.4%) are observed to be quite higher than the permissible limits of 5% and 2% respectively for manufactured aggregate as per IS:383-2016. The high value of water observation indicates the presence of voids in its molecular structure. It supports the light weight nature of the geopolymer fly ash sand sample. The chemical analysis of geopolymer fly ash sand indicates its high alkali content, 3.37% as total Na2O equivalent, quite evident from its alkaline process of manufacturing. As per results of sieve analysis, LWGFAS falls in grading zone II.

5.1.1. Petrographic and Mineralogical Analysis

Petrographic and mineralogical analysis of LWGFAS was carried out using Optical microscope as per IS 2386 part VIII. It was observed that the LWGFAS is a fine grained textured and the minerals present in order of their abundance are opaque minerals, calcite, quartz, plagioclase-feldspar, orthoclase-feldspar and iron oxide. Subhedral to anhedral opaque minerals with corroded margins were uniformly distributed in the sample. Majority of opaque minerals were in the size range of 150µm to 250 µm. Micro globular calcite grains with rounded margins were present as clusters in the sample. These clusters were brittle and fragile in nature and uniformly distributed in the sample. Subhedral to anhedral quartz grains with sharp angular margins were well graded and inhomogeneously distributed. Majority of quartz grains were in the size range of 100µm to 200 µm. Prismatic plagioclase and subhedral orthoclase grains were fresh in nature. Anhedral to subhedral iron oxide grains with rounded grain margins were randomly distributed. Mica Content (% by weight) was found to be nil. Modal composition has been

tabulated in Table 3 below. The microphotographs are given in figure 2 and 3. The strained quartz percentage is about 11% and their Undulatory Extinction Angle (UEA) varies from 120 to 140, which indicates that aggregates are non-reactive and not prone to expansion due to alkali aggregate reaction. The mineralogical composition, strained quartz percentage and UEA are similar to natural sand when compared with limits given IS 383: 2016.

Table 3. Modal Composition of LWGFAS (Results in %)

SI. No.	Sample No.	Type	MINERALS					
			Quartz	Plagioclase Feldspar	Opaque minerals	Orthoclase Feldspar	calcite	Iron Oxide
1.	FA/605	Fine Aggregate	8	5	67	4	13	3

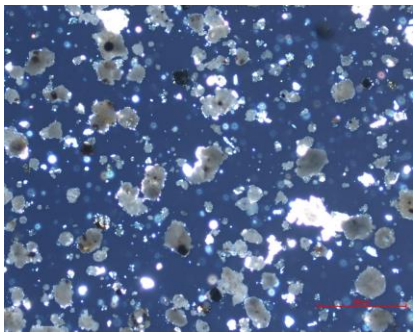

Fig. 2 FA (Plate-1): Distribution of Mineral Grains in LWGFAS. (5x, x-Nicols)

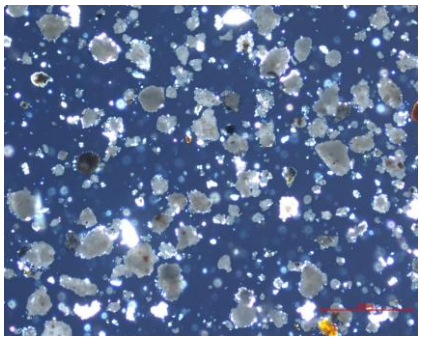

Fig. 3 FA (Plate-2): Distribution of Mineral Grains in LWGFAS. (5x, x-Nicols)

5.1.2 Accelerated Mortar Bar Test

Accelerated mortar bar test was performed as per ASTM C1260 to evaluate the expansion due to alkali-aggregate reactivity of LWGFAS. The results of accelerated mortar bar test, given in table 4 shows an expansion of 0.02% at 16 days after casting, lower than the permissible limit of 0.1% thus indicating innocuous nature of LWGFAS. However, high alkali content as observed in chemical analysis may aggravate alkali-silica expansion in concrete with doubtful or reactive coarse aggregate. The suspected behavior can be analyzed under long term testing using prism bar test as per ASTM C1293 [25].

Table 4. Accelerated Mortar Bar Test (as per ASTM C1260)

S. No.	Sample Type	1N NaOH 800C 14 Day Expansion %	Remarks
1	Light Weight Geo polymer fly ash sand	0.02	Innocuous

5.1.3 Long Term Prism Bar Test

The prism bar test was conducted using the standard mix prescribed in ASTM C 1293. The standard mix has a cement content of 420 kg/m3 with an alkali content of 0.9 ± 0.1 percent and a water/cement ratio in the range of 0.42 to 0.45 by mass. A sufficient amount of sodium hydroxide is added to the water used for the concrete mix to increase the cement alkali content to 1.25 percent. The reading was taken for one year. An average expansion is calculated from measurements on three replicate specimens. If the average expansion of the three concrete bars is equal to or greater than 0.04 percent at an age of one year, then the aggregate is considered to be potentially reactive. The results of prism bar test are given in figure 4. On perusal of expansion results, it was seen that expansion results of the fine aggregate samples, natural sand and LWGFAS (with innocuous coarse aggregates and doubtful coarse aggregates) are comparable at all ages and below the permissible limit of 00.04% at one year.

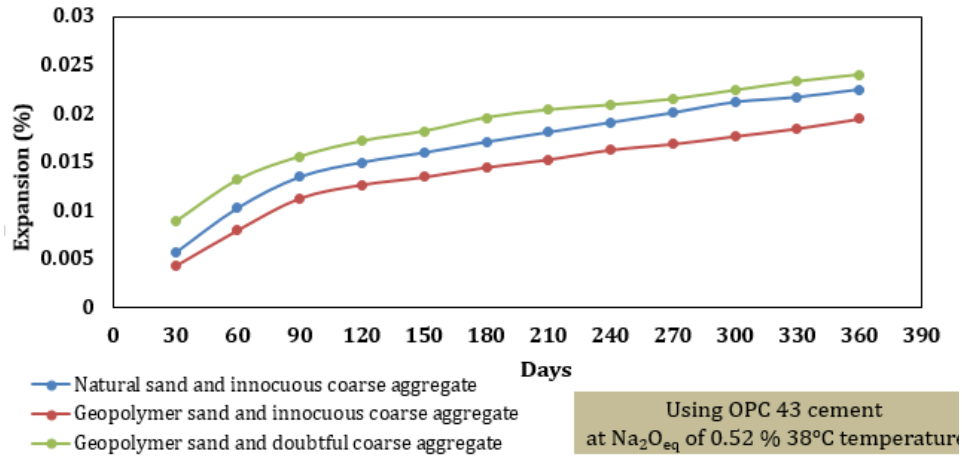

Fig. 4 Prism bar test (as per ASTM C 1293)

5.2 Hardened Concrete Properties

In this investigation two mixes of M25 grade were prepared, i.e. control mix with river sand as fine aggregate and experimental mix with LWGFAS as fine aggregate. Locally available cement sample (OPC-43 Grade without any performance improver, conforming to IS 269 [26]), coarse aggregates and a naphthalene based chemical admixture was used for preparation of both the mixes. All the component materials conform to their respective. The mix proportioning was done keeping the absolute volume constant to study the effect of LWGFAS and river sand on concrete properties. The mix proportion used is given in Table 5.

Table 5. Mix Proportion Used for Casting of Mixes

Mix Constituents (kg/one cubic meter)	M25 with natural fine aggregate (Control Mix)	M25 with 100% replacement of natural fine aggregate with LWGFAS (Experimental Mix)
Cement (OPC-43 grade)	320	320
Water	160	160
Fine Aggregate (Natural Sand/Geopolymer Fly ash Sand)	833 (Abs. vol. 0.3157 m^3)	499 (Abs. vol. 0.3166 m^3)
Coarse Aggregate		
Fraction –I) 20mm (60%)	632	631
Fraction –II) 10mm (40%)	517	516
Chemical Admixture @ by wt. of cementitious	2.56 (dosage at rate of 0.8% by weight of cementitious)	5.12(dosage at rate of 1.6 % by weight of cementitious)
Water – Cementitious Ratio	0.50	0.50
Workability obtained in terms of slump (after 90 mins of retention period)	80-90 mm	90-100 mm
Average fresh density (kg/m^3)	2485	2245

The two mixes, i.e. control and experimental mix were evaluated for following tests to study the performance of LWGFAS with respect to river sand as fine aggregate in concrete. The workability of the experimental mix and control mix was varying from 90-100 mm and 80-90 mm respectively. In case of experimental mix higher dosage of chemical admixture was required to achieve the same workability. It may be attributed to the irregular shape and rough texture of geopolymer fly ash sand [27].

5.2.1 Compressive Strength

The test was conducted on concrete cubes (of size 150 mm X 150 mm X 150 mm) as per IS: 516. Three concrete cubes were tested at 3, 7, 28, 56 & 90 days. The test results are given in Table 6. The compressive strength at 3 days in experimental mix is 51.68 % of that of control sample while the compressive strength at 28 days in experimental mix is 74.90 % of that of control sample. The observed gain from 7 to 28 days' strength may be attributed to the unreacted fly ash particles present in the sand which may have reacted with the cement hydration product such as lime and may have contributed to the later strength. The maximum pozzolanic activation activities of the fly ash occur between 56 to 90 days. Therefore, the continuous increase in concrete made with LWGFAS upto 90 days may be due to the late gain of strength by the fly ash present in the system [27, 28]. As discussed earlier, in this study NaOH solution of lower concentration and only 1 hour of post set heat treatment at 100°C was used for preparation of LWGFAS leading to lower specific gravity and higher water absorption, which might be the reason for lower compressive strength of experimental mixes containing LWGFAS in comparison to control concrete mixes containing natural sand.

Table 6. Compressive Strength Results

Sl. No.	Age of testing	M25 with natural fine aggregate (Control Mix) Average Value	Standard deviation M25 with natural fine aggregate	M25 with 100% replacement of natural fine aggregate with LWGFAS (Experimental Mix) Average Value	Standard Deviation M25 with 100% replacement of natural fine aggregate with LWGFAS	Percentage Compressive Strength (Experimental Mix/Control Mix)*100 Average Value
1.	3 days	19.87 MPa	1.05	10.27 MPa	0.85	51.68
2.	7 days	24.23 MPa	1.25	13.49 MPa	1.15	55.67
3.	28 days	36.06 MPa	1.41	27.01 MPa	1.75	74.90
4.	56 days	40.51 MPa	1.85	38.98 MPa	1.99	95.54
5.	90 days	44.14 MPa	1.95	42.96 MPa	2.06	97.32

5.2.2 Rapid Chloride Permeability Test (RCPT)

This test is used to evaluate the performance of concrete against the chloride ion penetration. RCPT test (as shown in figure 5(a) and 5(b)) was conducted as per ASTM C1202 [29] on concrete disc specimens of size 100 mm diameter and 50 mm thickness. Three concrete specimens were tested at 28, 56 & 90 days. The test setup consisted of two compartments or cells (cathode and anode) with a central hole of diameter 100 mm and the cylindrical disc specimen was placed firmly in between the two cells with the help of rubber washer. The cathode compartment was filled with 3% NaCl solution and anode compartment was filled with 0.3 M NaOH solution. Electrode dipped in NaCl was connected to negative terminal of the power supply and that of NaOH to the positive terminal. A potential difference of 60V DC was maintained across the ends of the specimen using a DC power source between the anode and cathode. The current was monitored up to 6 hours at an interval of 30 minutes. The current was measured and recorded using a data logger and the total charge passed through the specimen was computed by integrating the current and time. The total charge passing through the specimen gives a measure of resistance of the specimen to chloride ion penetration. The categorization of sample on the basis of charge passed is given in Table 7. Test results are tabulated in Table 8.

(a) (b)

Fig. 5. (a) Vacuum box, (b) DC voltage system for RCPT tests

The obtained value of charge passed in case of control mix lies in the range of 1,000-2000 coulombs corresponding to low permeability class as per ASTM C1202. However, the value is nearer to the lower limit of that class while in case of experimental mix the observed value lies in the range of 100-1000 coulombs corresponding to very low permeability class as per ASTM C1202. However, the value is nearer to the higher limit of that class. Thus, concrete made with LWGFAS has slightly improved performance in RCPT test compared to concrete made with natural sand.

Table 7. Chloride Ion Penetrability Based on Charge Passed

Sl. No.	Charge Passed (Coulombs)	Permeability Class as per ASTM C1202
1	>4,000	High
2	2,000-4,000	Moderate
3	1,000-2,000	Low
4	100-1000	Very Low
5	<100	Negligible

Table 8. RCPT Test Results

Sr. No	Age of testing	M25 with natural fine aggregate (Control Mix)	M25 with 100% replacement of natural fine aggregate with LWGFAS (Experimental Mix)
1.	28 days	1217 coulomb	904 coulomb
2.	56 days	1198 coulomb	895 coulomb
3.	90 days	1170 coulomb	882 coulomb

The obtained value of charge passed in case of control mix lies in the range of 1,000-2000 coulombs corresponding to low permeability class as per ASTM C1202. However, the value is nearer to the lower limit of that class. The obtained value of charge passed in case of experimental mix lies in the range of 100-1000 coulombs corresponding to very low permeability class as per ASTM C1202. However, the value is nearer to the higher limit of that class. The pozzolanic behaviour of unreacted supplementary materials such as fly ash led to improvement in the pore chemistry of the concrete. However, since RCPT provides exaggerated results in case of pozzolanic materials, Rapid Chloride Migration Test was also conducted. The reduction in chloride penetration in the concrete made with LWGFAS sand is directly proportional to the concentration of NaOH. In the experiment, geopolymer fly ash sand was manufactured by using 4 M NaOH while river sand did not have NaOH. Thus due to presence of NaOH, durability of the concrete improved.

5.2.3 Chloride Migration Test After 28 Days as per NT Build 492

In order to check the resistance of concrete against the chloride migration, NT Build 492 [30] test was conducted which is a non- steady state migration test. Three concrete specimens were tested at each age i.e. 28, 56 & 90 days from each concrete mix. The specimens were subjected to a voltage of 30 V initially, which was adjusted according to the current measured initially, which could vary between 10 and 60 V. The temperatures of the anodic solution were also measured at the beginning and at the end of the procedure. In the first stage of the test, the concretes are exposed to chlorides. After being subjected to ionic migration, the samples were diametrically broken and 0.1 M AgNO3 solution was sprayed on them to check the chloride penetration depth. Thereafter, the D_{nssm} was calculated using:

$$D_{nssm=} \frac{0.0239\,(273+T)L}{(U-2t)}\left(x_D - 0.0238\sqrt{\frac{(273+T)Lx_D}{U-2}}\right) \quad (1)$$

where D_{nssm} = non-steady state diffusion coefficient (× 10-12 m^2/s); T = average value of the initial and final temperatures in the anolyte solution (°C); L = thickness of the specimen (mm); U = absolute value of the applied voltage (V); x_D = average value of the penetration depths (mm); and t = test duration (h)

The test results are given in Table 9. The values obtained in case of control mix at 28, 56 & 90 days are greater than the values obtained in case of the experimental mix containing LWGFAS sand. This can be attributed to improvement in the pore chemistry of the concrete due to the pozzolanic behaviour of unreacted supplementary materials such as fly ash in LWGFAS. This reflects improved behaviour of concrete against the chloride diffusion, made with 100% replacement of natural aggregate with LWGFAS.

Table 9. Chloride Migration Results

Age of testing	M25 with natural fine aggregate (Control Mix)	M25 with 100% replacement of natural fine aggregate with LWGFAS (Experimental Mix)
28 days	6.62×10^{-12} m^2/s	4.65×10^{-12} m^2/s
56 days	6.45×10^{-12} m^2/s	4.23×10^{-12} m^2/s
90 days	6.43×10^{-12} m^2/s	4.16×10^{-12} m^2/s

5.2.4 Bulk Conductivity as per ASTM C 1760

This test method is used to determinate the bulk electrical conductivity of saturated specimens of hardened concrete to provide a rapid indication of the concrete's resistance to the penetration of chloride ions by diffusion [31]. This test method measures the electrical current through a saturated concrete specimen with a potential difference of 60 V dc maintained across the ends of the specimen (100 mm diameter and 200 mm height cylinders) at an age of 28 days. The current is measured 1 min after the voltage is first applied. The measured current, the applied voltage, and the specimen dimensions are used to calculate the bulk electrical conductivity of the concrete. Test results are given in Table 10. The difference between the bulk conductivity values of control mix and experimental mix is quite less. It suggests that the concrete prepared with LWGFAS is performing similar to concrete prepared with river sand against the passage of electric current through them. This indicates that the long term durability performance of LWGFAS will be similar to conventional aggregate.

Table 10. Results of Test of Bulk Conductivity as per ASTM C 1760

Age of testing	M25 with natural fine aggregate (Control Mix)	M25 with 100% replacement of natural fine aggregate with LWGFAS (Experimental Mix)
28 days	4.42	4.655

5.2.5 Volume of Air Permeable Voids

The test is conducted on 50mm thick concrete disc (diameter 100 mm) at an age of 28 days. As per ASTM C 642 [32], the Standard Test Method for Density, Absorption, and Voids in Hardened Concrete, estimates the volume of permeable pore space in a hardened concrete specimen by determining the hardened concrete's density in different states (oven dry, saturated, saturated-boiled). Test results are given in table 11. A significantly higher value of volume of air permeable voids has been observed in the case of experimental mix. The observed behaviour may be caused due to high water absorbing nature of geopolymer fly

ash sand. Thus, this is not a good parameter to compare the behaviour of concrete prepared with LWGFAS with concrete prepared with river sand.

Table 11. Results of Volume of Air Permeable Voids as per ASTM C 642

Age of testing	M25 with natural fine aggregate (Control Mix) Conductive	M25 with 100% replacement of natural fine aggregate with LWGFAS (Experimental Mix)
28 days	7.66	16.06

The results of volume of permeable voids are affected by a number of factors including compaction, curing, air entrainment, absorption and physical nature of the aggregate used. In Volume of Air Permeable Voids test, the observed value is higher which may be attributed to high water absorption of light weight geopolymer fly ash sand.

5.2.6 Accelerated Carbonation Test

Accelerated Carbonation test (ACT) was conducted on concrete beam specimen with dimension 100 ×100×500 mm as per ISO 1920 Part 12 [33]. After 28 days of water curing, the concrete specimens were shifted to laboratory environment (temperature = 27 ± 2 ^{o}C and relative humidity = 65 ± 5 %) for 14 days. After 42 days of laboratory conditioning, top and bottom longitudinal faces and two end faces of the beam were sealed using paraffin wax and carbonation was allowed on two cast longitudinal faces, in order to prevent multi-directional carbonation. After the sealing, the concrete beam specimens were shifted to the carbonation chamber (as shown in figure 6) having 4 ± 0.5 % concentration of carbon dioxide, temperature = 27 + 2 ^{o}C and relative humidity of 65±5%. The carbonation depth was measured after 70 days of exposure, by approximately cutting a slice of 50 mm thick from the concrete beam specimen and exposing the cut surface to 1% phenolphthalein solution. Test results have been tabulated in table 12.

Fig. 6. Carbonation Chamber for Accelerated Carbonation Test

Table 12. Results of Accelerated Carbonation Test (ACT)

Age of testing	M25 with natural fine aggregate (Control mix)	M25 with 100% replacement of natural fine aggregate with light weight geopolymer fly ash sand.
70 Days	8.2 mm	2.1 mm

The obtained value of carbonation depth of mix containing LWGFAS is lower than the carbonation depth obtained in control mix, which reflects improved behaviour of experimental concrete mix against carbonation. In case of GFS concrete, carbonation might have produced sodium carbonate products [34], and these sodium carbonate may have reduced the pH of the concrete by maximum 11, while, in case of river sand, the carbonation might have produced calcium carbonate, and these calcium carbonate may have reduced the pH of the concrete by less than 9 causes formation of $CaCO_3$ [35]. The GFS sand has high pH value as compared to the river sand concrete. The increased pH and the formation of the sodium carbonates may have protected the concrete from carbonation, hence improving the durability of the concrete and hence improving the service life of the concrete.

5.2.7 Drying Shrinkage

This test was conducted on concrete beam (length 300 mm & cross section 75 x 75 mm), water cured for 28 days as per IS 1199 [36, 37]. Test results for drying shrinkage at 28 days have been tabulated in table 13. The obtained value of drying shrinkage in case of mix containing LWGFAS is similar and comparable to the drying shrinkage obtained in control mix containing 100% natural aggregates, which shows that there is no negative impact of use of geopolymer as fine aggregate in concrete in terms of drying shrinkage.

Table 13. Results of Drying Shrinkage

Age of testing	M25 with natural fine aggregate (Control mix)	M25 with 100% replacement of natural fine aggregate with LWGFAS.
28 Days	0.0162%	0.0163%

Since the LWGFAS concrete had higher water absorption as compared to the river sand it necessitated to analyze the drying shrinkage of the concrete. The reason for the comparable drying shrinkage though the large water absorption may be due to the 'block polymerization' concept as in case of geopolymer concrete. The Silica and Alumina in the fly ash polymerizes with the liquid solution thus forming "blocks" containing geopolymer binders causing increase in the aggregate content of the concrete. This may also be the case with concrete made with LWGFAS sand. The alkaline liquid and the fly ash may have reacted and formed blocks which helped in filling the porosity of the concrete thus improving the durability properties of the concrete made with LWGFAS as replacement of natural sand.

5.3. Mortar Properties

This test was conducted on mortar cubes (of size 50mm × 50mm × 50mm) as per IS: 2250-1981 [38] in the ratio 1:3, 1:4 and 1:6 and tested for compressive strength at 7 and 28 days. The test results are given below in table 14. All the samples of mortar made with 100% replacement of natural fine aggregate with Light Weight Geopolymer Fly Ash Sand conform to the strength requirements as per IS 2250:1981. In case of mortar (ratio 1:3) made with 100% replacement of natural fine aggregate with LWGFAS, the strength at 7 days and 28 days is 38.11% and 38.70% respectively to that of control sample. In case of mortar (ratio 1:4) made with 100% replacement of natural fine aggregate with Light Weight Geopolymer Fly Ash Sand, the strength at 7 days and 28 days is 54.53 % and 59.77% respectively to

that of control sample. In case of mortar (ratio 1:6) made with 100% replacement of natural fine aggregate with LWGFAS, the strength at 7 days is 63.17 % to that of control sample. However, at 28 the strength at 7 days is 63.17 % to that of control sample. Use of NaOH solution of lower concentration and only 1 hour of post set heat treatment at 100°C for preparation of LWGFAS in this study led to lower specific gravity and higher water absorption, which might be the reason for lower compressive strength of experimental mixes containing LWGFAS in comparison to control mortar mixes containing natural sand.

Table 14. Test Results of Studies Conducted on Mortar

Sr. No.	Mortar Mix	Age of testing	Mortar with natural fine aggregate (Control Mix)	Mortar with 100% replacement of natural fine aggregate with Light Weight Geopolymer Fly Ash Sand (Experimental Mix)	Percentage Compressive Strength (Experimental Mix/Control Mix)*100
1.	M1 (1 : 3)	7 days	19.18	7.31	38.11
		28 days	27.83	10.77	38.69
2.	M2 (1 : 4)	7 days	12.36	6.74	54.53
		28 days	17.85	10.67	59.77
3.	M3 (1 : 6)	7 days	7.74	4.89	63.17
		28 days	14.68	8.45	57.56

6. Conclusions

Based on literature studied and experimental investigation done in the paper, following conclusions can be drawn:

- The light weight geopolymer fly ash sand was characterized and was used as a replacement of natural fine aggregate for preparation of concrete and mortar mixes and their performance was evaluated for various hardened and durability properties of concrete and mortar. The results have been compared with similar sample prepared with river sand.
- The LWGFAS was manufactured by preparing alkaline activator solution using 4 M NaOH solution and Na_2SiO_3: NaOH ratio as 2:1 and mixing this with fly ash.
- The LWGFAS showed similar properties as that of river sand except it had less specific gravity and high water absorption. The higher value of water absorption indicates presence of voids in its structure.
- The compressive strength of concrete mixes prepared with light weight geopolymer fly ash sand was observed to improve with age. At 28 days LWGFAS concrete attained 74.90 % strength as that of river sand concrete whereas at 90 days 97.32% strength was achieved indicating a continuous gain of strength in the GFS concrete.
- In terms of different durability related parameters such as RCPT, chloride migration test, bulk conductivity, accelerated carbonation test and drying shrinkage, experimental mixes containing light weight geopolymer fly ash sand as a replacement of natural aggregates showed comparable or better performance in comparison to their corresponding control concrete mixes containing 100 % natural aggregates. Significant reduction in chloride permeability was observed

in case of GFS concrete as compared to the river sand concrete. The chloride migration test also portrayed the similar result as that of rapid chloride penetration test. The accelerated carbonation test displayed a 4 times reduction in carbonation with the use of LWGFAS concrete. The higher water absorption though did not influenced the drying shrinkage of the concrete thus making GFS suitable as an alternative to river sand.

- In case of mortar samples, the experimental mix containing light weight geopolymer fly ash sand conform to their respective strength requirements of mortar but are lower in comparison to control mix containing natural fine aggregates. Current and past studies indicate that compressive strength of concrete and mortar mixes containing light weight geopolymer fly ash sand can be improved if activator solution of slightly higher concentration and increased post set heat treatment duration is used for preparation of light weight geopolymer fly ash sand. For normal grade concrete (in the range of M20 to M30), geopolymer fly ash sand can be a viable and sustainable solution.
- The study indicates that Geopolymer fly ash sand can be suitable for a wide range of applications in making concrete ranging from light weight in nature to normal weight concrete based on the physical and chemical characteristics of Geopolymer fly ash sand.

7. Acknowledgement

The authors would like to acknowledge Visvesvaraya National Institute of Technology (VNIT Nagpur) for providing light weight geopolymer fly ash sand for the above study.

References

[1] Wang R, Yu N, Li Y. Methods for improving the microstructure of recycled concrete aggregate: A review, Construction and Building Materials, Volume 242, May 2020 https://doi.org/10.1016/j.conbuildmat.2020.118164

[2] Palomo, Grutzeck MW, Blanco MT. Alkali-activated Fly Ashes A cement for the future, Journal of Cement and Concrete Research, 1999, Vol. 29, pp. 1323-1329. https://doi.org/10.1016/S0008-8846(98)00243-9

[3] World Business Council for Sustainable Development, Recycling Concrete-The Cement Sustainability Initiative Report, 2009.

[4] Donza H, Cabrera O, Irassar EF. High-strength concrete with different fine aggregate, Cement and Concrete Research, 2002; 32: 1755-1761. https://doi.org/10.1016/S0008-8846(02)00860-8

[5] Hardjito D, Wallah SE, Sumajouw DMJ, Rangan BV. Fly Ash-Based Geopolymer Concrete Australian Journal of Structural Engineering, January 2005; 6:1, 1-10. https://doi.org/10.1080/13287982.2005.11464946

[6] Report on Fly Ash Generation at Coal/ Lignite Based Power station and its Utilization in the Country for the Year 2014-15, Centre Electricity Authority, New Delhi, October 2015.

[7] Dasha MK, Patro SK, Ratha AK. Sustainable use of industrial-waste as partial replacement of fine aggregate for preparation of concrete - A review, International Journal of Sustainable Built Environment, 2016; 5:2, 484 - 516. https://doi.org/10.1016/j.ijsbe.2016.04.006

[8] James MN, Choi W, Abu-Lebdeh T. Use of Recycled Aggregate and Fly Ash in Concrete Pavement, Am. J. Engg. & Applied Science, 2011; 4: 201 – 208 https://doi.org/10.3844/ajeassp.2011.201.208

[9] Toshiki A, Osamu K, Kenji S. Concrete with copper slag fine aggregate, J. Soc. Mater. Sci. 2000; 49; 1097 - 1102. https://doi.org/10.2472/jsms.49.1097

[10] Nisnevich M, Sirotin G, Dvoskin L, Fishel J. Using High-Volume Fly Ash in Lightweight Concrete with Bottom Ash as Aggregate, Proceeding of the Seventh CANMET/ACI International Conference on Fly Ash, Silica Fume, Slag and Natural Pozzolans in Concrete, 2001, Madras, India, 99 - 114.
[11] IS 9142 Part 2:2018, Artificial lightweight aggregate for concrete - Sintered fly ash coarse aggregate.
[12] Palomo A, Macias A, Blanco MT, Puertas F. Physical, Chemical and Mechanical Characterization of Geopolymer, Proceedings of the 9th International Congress on the Chemistry of Cement, New Delhi, India, 23-28 November 1992.
[13] Duxson P, Lukey GC, Deventer V. Physical evolution of Na-geopolymer derived from metakaolin up to 1000°, Journal of Material Science. 2007; 42: 3044 - 3054. https://doi.org/10.1007/s10853-006-0535-4
[14] Davidovits J. Geopolymer, Chemistry and Applications, 3rd ed.; Institute Geopolymer: Saint-Quentin, France, 10 - 11, 2011.
[15] Ferone C, Colangelo F, Cioffi R, Montagnaro F, Santoro L. Mechanical performances of weathered coal fly ash based geopolymer bricks, Procedia Eng. 2011; 21: 745 - 752. https://doi.org/10.1016/j.proeng.2011.11.2073
[16] Hardjito D, Wallah SE, Sumajouw DMJ, Rangan BV. Fly Ash-Based Geopolymer Concrete, Australian Journal of Structural Engineering, January 2005; 6:1, 1 - 10. https://doi.org/10.1080/13287982.2005.11464946
[17] Rao SM, Acharya IP. Synthesis and characterization of fly ash geopolymer sand, Journal of Materials in Civil Engineering, 2014; 26:2, 186 - 190. https://doi.org/10.1061/(ASCE)MT.1943-5533.0000880
[18] Agrawal US, Wanjari SP, Naresh DN, Characteristic study of geopolymer fly ash sand as a replacement to natural river sand, Construction and Building Materials, 2017; 150: 681 - 688. https://doi.org/10.1016/j.conbuildmat.2017.06.029
[19] Agrawal US, Wanjari SP, Naresh DN. Impact of replacement of natural river sand with geopolymer fly ash sand on hardened properties of concrete, Construction and Building Materials 2019; 209: 499 – 507. https://doi.org/10.1016/j.conbuildmat.2019.03.134
[20] Wanjari SP, Agrawal US, Naresh DN. Geopolymer Sand as a replacement to Natural Sand in concrete, 14th International Conference on Concrete Engineering and Technology, IOP Conf. Series: Materials Science and Engineering 431, 2018. https://doi.org/10.1088/1757-899X/431/9/092011
[21] IS 2386 Part 8-1963, Methods of Test for Aggregates for Concrete - Part VIII: Petrographic Examination.
[22] ASTM C1260- 2014, Standard Test Method for Potential Alkali Reactivity of Aggregates (Mortar-Bar Method).
[23] IS 383-2016, Coarse and fine aggregate for concrete-specifications.
[24] ACI 213R-2014, Guide for Structural Lightweight-Aggregate Concrete.
[25] ASTM C1293:2020a, Standard Test Method for Determination of Length Change of Concrete Due to Alkali-Silica Reaction.
[26] IS 269-2015, Ordinary Portland Cement - Specification, Bureau of Indian Standards, New Delhi
[27] Agrawal US, Wanjari SP, Naresh DN, Characteristic study of geopolymer fly ash sand as a replacement to natural river sand, Construction and Building Materials, 2019; 150: 681 -688. https://doi.org/10.1016/j.conbuildmat.2017.06.029
[28] Rao SM, Acharya IP, Synthesis and characterization of fly ash geopolymer sand, Journal of Materials in Civil Engineering, 2014; 26:2, 186 - 190. https://doi.org/10.1061/(ASCE)MT.1943-5533.0000880
[29] ASTM C1202 - 2017a, Standard Test Method for Electrical Indication of Concrete's Ability to Resist Chloride Ion Penetration.
[30] NT BUILD 492, Chloride migration coefficient from non-steady-state migration experiments.

[31] ASTM C1760-2012, Standard Test Method for Bulk Electrical Conductivity of Hardened Concrete.
[32] ASTM C642-2013, Standard Test Method for Density, Absorption, and Voids in Hardened Concrete.
[33] ISO 1920 Part 12 (2015). Determination of Carbonation resistance of concrete.
[34] Palomo A, Gonza JA, Bastidas DM, Ferna A, A study on the passive state stability of steel embedded in activated fly ash mortars, Corr. Sci., 2008; 50: 1058 - 1065. https://doi.org/10.1016/j.corsci.2007.11.016
[35] Law DW, Arham A, Thomas A, Patnaikuni I, Wardhono A, Long term durability properties of class F fly ash geopolymer concrete, Mater. Struct. 2015; 721 - 731. https://doi.org/10.1617/s11527-014-0268-9
[36] 1S 1199-2004. Method of sampling and analysis of concrete.
[37] Ojha PN, Singh B, Singh A, Patel V, Arora VV, "Experimental study on creep and shrinkage behavior of high strength concrete for application in high rise buildings", Indian Concrete Journal, 2021; 95 (2), 30-42.
[38] IS 2250-1981, Code of practice for preparation and use of masonry mortars (First Revision).

Research on Engineering Structures & Materials
journal homepage: http://jresm.org
Research Group

Research Article

A Bayesian regression framework for concrete creep prediction improvement: application to Eurocode 2 model

Hikmat Daou*[a], Wassim Raphael[b]

Ecole Supérieure d'Ingénieurs de Beyrouth (ESIB), Saint-Joseph University, Lebanon

Article Info

Article history:
Received 03 Mar 2021
Revised 04 May 2021
Accepted 15 May 2021

Keywords:

Creep;
Concrete;
Eurocode 2;
Bayesian linear regression

Abstract

Concrete is the most widely used material in the construction industry due to its strength, workability and durability. But under a sustained load, concrete is prone to creep causing excessive long-term deflection of structural members, cracks in tensile members, redistribution of stresses over time in composite structures, and loss of prestressing force in prestressed concrete elements. Therefore, structural engineers must accurately predict the concrete creep over the long-term. The concrete creep coefficient is an important entry in many calculations and analyses of reinforced concrete structures. Currently, many models such as the Eurocode 2 model have predicted the concrete creep coefficient. Based on a large database for creep tests, this study aims to improve the prediction of the Eurocode 2 creep coefficient model at long-term by implementing correction coefficients into the model. Since Bayesian-type inferences are suitable tools for revising and updating design codes, the correction coefficients are calculated based on Bayesian linear regression. Statistical indicators demonstrate the accuracy and effectiveness of the proposed improvement and modification.

1. Introduction

Concrete is a composite material consisting of a mortar phase and aggregates and is known as a brittle material having low tensile strength and tensile strain capacity. For that, concrete is usually reinforced using different materials such as steel or fiber [1]. In literature, reinforced concrete structures are continually studied as being one of the world's most common building materials in the construction industry [2–4].

When concrete is subjected to long-term stresses, it is prone to creep. In other words, creep is the time-dependent movement or deformation of concrete. Indeed, creep can affect structural behavior by violating the service limit states, by losing the prestressing forces, or by redistributing the stress [5–9]. Therefore, creep is of great practical importance to structural engineers, and thus, it has been studied by many researchers [10–17]. Hence, designers must accurately predict creep strains using precise methods.

There are many sophisticated and practical models for predicting creep [18–22]. The Eurocode 2 model [19] is one of the most widely used models for predicting shrinkage and creep. Based on a large experimental database, the EC2 shrinkage model has been updated [23], and correction coefficients have also been proposed for the Eurocode 2 creep model [24] but the calculation of these correction coefficients are limited for a specific condition of initial time loading, relative humidity, or compressive strength. For that, it is necessary to improve the creep coefficient prediction by taking into consideration the different concrete mix compositions and the various environmental conditions.

*Corresponding author: hikmat.daou@net.usj.edu.lb
[a] orcid.org/0000-0003-3352-7135; [b] orcid.org/0000-0002-2960-8760
DOI: http://dx.doi.org/10.17515/resm2021.272ma0303

In order to optimize and improve a model, many optimization models have been developed in the literature [25–27]. Frequentist inference and Bayesian inference are two types of statistical inference. Frequentist ordinary least squares (OLS) regression models are perceived to handle large data sets and are easy to perform while Bayesian linear regression (BLR) models have been traditionally restricted to small sample sizes and have many things need to be specified such as prior distributions, initial values for numerical approximation, and the likelihood function. On the other hand, Bayesian inference allows informative priors where the prior knowledge or results of a previous model can be used to inform the current model and can avoid problems with model identification by manipulating prior distributions, especially in complex models. BLR model also delivers the answer to the right question in the sense that Bayesian inference provides answer to conditional on the observed data and not based on the distribution of estimators or test statistics over imaginary samples not observed [28]. Moreover, Bayesian inference has a decision theoretic foundation [29,30]. The purpose of most statistical inference is to facilitate decision-making, and the Bayesian decision is the optimal decision. Bayesian inference has been used in different civil engineering problems [31–34]. In addition, Bayesian inference is also an appropriate tool for revising and updating design codes; therefore, BLR is used in this study.

This study aims is to evaluate the long-term Eurocode 2 creep coefficient model and improve it by implementing correction coefficients to the model using Bayesian linear regression for different concrete mix compositions and under various environmental conditions.

2. Database and Methods

2.1. Northwestern University Database

During the period 2010-2013, a large database was assembled at Northwestern University (NU), mainly under the support of the U.S. Department of Transportation [24]. This NU database is based on information extracted from numerous reports, journal articles, and conference proceedings. The tests of this database are performed using different concrete mix compositions and under various environmental conditions such as aggregate-cement ratio (a/c), water-cement ratio (w/c), concrete compressive strength (f_{cm}), cement type, effective thickness (h_0), loading age (t_0), sustained stress over the compressive strength at loading age $\sigma/f_{cm(t0)}$, temperature (T), relative humidity (RH), etc.

2.2. Eurocode 2 creep predictions

The Eurocode 2 model (EC2) [15] predicts compliance according to Eq. (1). Compliance is defined as the total load-induced strain at age t per unit caused by a unit uniaxial sustained load applied since loading age t_0 [25].

$$J(t,t_0) = \frac{1}{E_{cmt0}} + \frac{\varphi_{28}(t,t_0)}{E_{cm28}} \quad (1)$$

where E_{cmt0} is the modulus of elasticity of concrete at the loading age t_0 (MPa), E_{cm28} is the mean modulus of elasticity at 28 days (MPa), and $\varphi_{28}(t,t_0)$ is the dimensionless 28-day creep coefficient.

The creep coefficient, $\varphi_{28}(t,t_0)$, gives the ratio of the creep strain since the start of age loading t_0 to the elastic strain due to constant stress applied at a concrete age of 28 days. Fig. 1 represents the plot of the natural logarithm of the EC2 creep coefficient ($\ln(\varphi_{EC2})$) versus the natural logarithm of the creep coefficient obtained from the NU database ($\ln(\varphi_{NU})$). In order to show the linearity between $\ln(\varphi_{EC2})$ and $\ln(\varphi_{NU})$, a quadratic term model has been proposed to fit the relation between these two variables. The polynomial

term for the second-order was not significant. Moreover, a comparison between the quadratic term model and the linear model was performed based on the Akaike information criterion (AIC) [35] and the results showed that the linear model is a good fit for the data. Therefore, the long-term creep coefficient is considered to be updated and calibrated based on the NU database by inserting correction coefficients, A and B, into the formula as shown in Eq. (2).

$$\varphi_{upd}(t,t_0) = A \times \varphi_{28}(t,t_0)^B \tag{2}$$

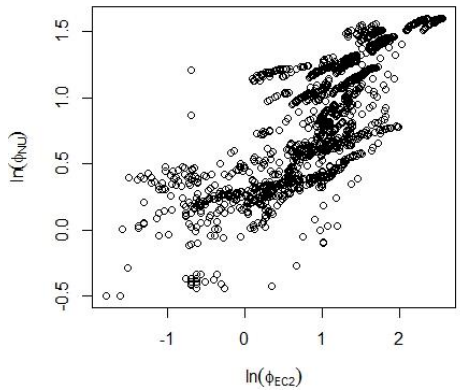

Fig. 1 Plot of the natural logarithm of the EC2 creep coefficient versus the natural logarithm of the actual creep coefficient

2.3 Bayesian Linear Regression

Bayesian statistics primarily involve conditional probability, which is the probability of an event X given event Y, and it can be calculated using Bayes' rule (Eq. (3)).

$$P(X|Y) = \frac{P(Y|X)\times P(X)}{P(Y)} \tag{3}$$

where X and Y are events, P(X) and P(Y) are the marginal probabilities of event X and event Y occurring respectively, P(X|Y) is the conditional probability that event X occurs given that event Y has already occurred, and P(Y|X) is the conditional probability that event Y occurs given that event X has already occurred.

Bayesian inference uses Bayes' theorem to deduce properties on a population or a probability distribution from data (Eq. (4)).

$$P(\Theta|data) = \frac{P(data|\Theta)xP(\Theta)}{P(data)} \tag{4}$$

where Θ = {μ, σ} represents the set of parameters of a Gaussian distribution where μ is the mean and σ is the standard deviation, P(Θ|data) is the posterior distribution, P(data|Θ) is the likelihood distribution, P(Θ) is the prior distribution.

Bayesian Linear Regression (BLR) is an approach to linear regression in which statistical analysis is undertaken within the context of Bayesian inference. Therefore, linear regression is formulated using probability distributions rather than point estimates. To apply the BLR model, and since linearization does not affect the results, the logarithm of

Eq. (2) is calculated, and the error ∈ is considered in the calculations as shown in the following equation:

$$ln\left(\varphi_{upd}(t,t_0)\right) = ln(A) + B \times ln\left(\varphi_{28}(t,t_0)\right) + \in \quad (5)$$

To calculate A and B, the updated creep coefficient is assumed to be the value obtained experimentally in the NU database.

Considering y = $\ln(\varphi_{upd}(t,t_0))$ and $x = \ln\left(\varphi_{28}(t,t_0)\right)$, Eq. (5) can be written as:

$$y = A + Bx + \epsilon \quad (6)$$

The equation of the i-th observation can be written as:

$$y_i = A + Bx_i + \epsilon_i \quad (7)$$

y is the response variable that corresponds to the i-th experimental value; x is the predictor variable that relates to the value predicted by the EC2 equation, A is the y-intercept parameter, B is the slope parameter, and ϵ_i is the i-th error.

2.3.1 Likelihood distribution $\mathcal{L}(A,B,\sigma^2)$

The error ϵ_i is assumed to be independent and identically distributed as normal random variables with zero mean and constant variance σ^2. Therefore, the random variable of each response y_i, conditioning on the observed data x_i and the parameters A, B and σ^2, is also normally distributed:

$$y_i\,|x_i, A, B, \sigma^2 \overset{iid}{\sim} Normal(A + Bx_i, \sigma^2), \qquad i = 1,..,n$$

Thus, the likelihood of each y_i given x_i, A, B, and σ^2 is given by:

$$p(y_i\,|x_i, A, B, \sigma^2) = \frac{1}{\sqrt{2\pi\sigma^2}}\, exp\left(-\frac{(y_i-(A+Bx_i))^2}{2\sigma^2}\right) \quad (8)$$

The likelihood of y1,..., yn, denoted as $\mathcal{L}(A,B,\sigma^2)$, is the product of each likelihood $P(y_i\,|x_i, A, B, \sigma^2)$ since each response yi is independent from each other.

$$p(y_1, \dots, y_n\,|x_i, A, B, \sigma^2) = \prod_{i=1}^{n} P(y_i\,|x_i, A, B, \sigma^2) \quad (9)$$

2.3.2 Prior distribution

Since no prior information is available, reference priors are used. The joint prior distribution of A, B under σ^2 is assumed to be a uniform prior, while the prior distribution of σ^2 proportional to the inverse of σ^2 [36]:

$$p(A,B|\,\sigma^2) \propto 1 \quad (10)$$

$$p(\sigma^2) \propto \frac{1}{\sigma^2} \quad (11)$$

By combining these two conditional probabilities, the joint prior distribution obtained is:

$$p(A,B,\sigma^2) \propto \frac{1}{\sigma^2} \quad (12)$$

2.3.3 Posterior distribution

According to Eq. (4), the joint posterior distribution of A, B, and σ^2 is proportional to the product of the likelihood and the joint prior distribution.

$$\begin{aligned} & p(A,B,\sigma^2|y_1,\dots,y_n) \propto \prod_{i=1}^{n} P(y_i\,|x_i,A,B,\sigma^2)\,p(A,B,\sigma^2) \\ & \propto \left[\left(\frac{1}{\sqrt{\sigma^2}}exp\left(-\frac{\left(y_1-(A+Bx_1)\right)^2}{2\sigma^2}\right)\right)\times\dots\times \right. \\ & \left.\left(\frac{1}{\sqrt{\sigma^2}}exp\left(-\frac{\left(y_n-(A+Bx_n)\right)^2}{2\sigma^2}\right)\right)\right]\times\left(\frac{1}{\sigma^2}\right) \\ & \propto \frac{1}{(\sigma^2)^{(n+2)/2}}exp\left(-\frac{\sum_{i=1}^{n}\left(y_i-(A+Bx_i)\right)^2}{2\sigma^2}\right) \end{aligned} \tag{13}$$

Considering $S_{xx}=\sum_{i=1}^{n}(x_i-\bar{x})^2$, $S_{yy}=\sum_{i=1}^{n}(y_i-\bar{y})^2$, $S_{xy}=\sum_{i=1}^{n}(x_i-\bar{x})(y_i-\bar{y})$, $SSE=\sum_{i=1}^{n}\hat{\epsilon}_i^{\,2}$, $\hat{B}=\frac{S_{xy}}{S_{xx}}$, $\hat{A}=\bar{y}-\frac{S_{xy}}{S_{xx}}\bar{x}$, and $\hat{\sigma}^2=\frac{SSE}{n-2}$ where $\bar{y}$ and $\bar{x}$ are the average of y and x, respectively, and n is the number of observations, and after making some calculations and simplifications, the posterior joint distribution of A, B, σ^2 can be simplified as:

$$\begin{aligned} & p(A,B,\sigma^2|y_1,\dots,y_n) \propto \\ & \frac{1}{(\sigma^2)^{\frac{n+2}{2}}}exp\left(-\frac{SSE+n[(A-\hat{A})+(B-\hat{B})\bar{x}]^2+(B-\hat{B})^2S_{xx}}{2\sigma^2}\right) \end{aligned} \tag{14}$$

2.3.4 Marginal Posterior Distribution of B

The marginal posterior distribution of B is obtained by integrating A and σ^2 out from the joint posterior distribution.

$$\begin{aligned} & p(B|y_1,\dots,y_n)=\int_0^{\infty}\left(\int_{-\infty}^{\infty}P(A,B,\sigma^2|y_1,\dots,y_n)\,dA\right)d\sigma^2 \\ & = \\ & \int_0^{\infty}\left(\int_{-\infty}^{\infty}\frac{1}{(\sigma^2)^{\frac{n+2}{2}}}exp\left(-\frac{SSE+n[(A-\hat{A})+(B-\hat{B})\bar{x}]^2+(B-\hat{B})^2S_{xx}}{2\sigma^2}\right)dA\right)d\sigma^2 \\ & = \int_0^{\infty}p(B,\sigma^2|y_1,\dots,y_n)d\sigma^2 \\ & p(B,\sigma^2|y_1,\dots,y_n)= \\ & \int_{-\infty}^{\infty}\frac{1}{(\sigma^2)^{\frac{n+2}{2}}}exp\left(-\frac{SSE+n[(A-\hat{A})+(B-\hat{B})\bar{x}]^2+(B-\hat{B})^2S_{xx}}{2\sigma^2}\right)dA \quad = \\ & \frac{1}{(\sigma^2)^{\frac{n+2}{2}}}exp\left(-\frac{SSE+(B-\hat{B})^2\sum_{i=1}^{n}(x_i-\bar{x})^2}{2\sigma^2}\right)\int_{-\infty}^{\infty}exp\left(-\frac{n[A-\hat{A}+(B-\hat{B})\bar{x}]^2}{2\sigma^2}\right)dA \end{aligned} \tag{15}$$

$$\propto \frac{1}{(\sigma^2)^{\frac{n+1}{2}}} exp\left(-\frac{SSE+(B-\hat{B})^2\sum_{i=1}^{n}(x_i-\bar{x})^2}{2\sigma^2}\right) \tag{16}$$

Considering $\emptyset = \frac{1}{\sigma^2}$,

$$\begin{aligned} p(B|y_1,\dots,y_n) &= \int_0^\infty \frac{1}{(\sigma^2)^{\frac{n+1}{2}}} exp\left(-\frac{SSE+(B-\hat{B})^2\sum_{i=1}^{n}(x_i-\bar{x})^2}{2\sigma^2}\right) d\sigma^2 \\ &= \int_0^\infty \emptyset^{\frac{n-3}{2}} exp\left(-\frac{SSE+(B-\hat{B})^2\sum_{i=1}^{n}(x_i-\bar{x})^2}{2\emptyset}\right) d\emptyset = \\ &\int_0^\infty p(B,\emptyset|y_1,\dots,y_n)d\emptyset \end{aligned} \tag{17}$$

After integrating Eq. (17), the following equation is obtained:

$$p(B|y_1,\dots,y_n) \propto \left(1+\frac{1}{n-2}\times\frac{(B-\hat{B})^2}{\hat{\sigma}^2/\sum_{i=1}^{n}(x_i-\bar{x})^2}\right)^{-\frac{(n-2)+1}{2}} \tag{18}$$

Finally, the marginal posterior distribution of B is the Student's t-distribution with degrees of freedom (n-2), center $\hat{B}$, and scale parameter $\frac{\hat{\sigma}^2}{\sum_{i=1}^{n}(x_i-\bar{x})^2}$.

$$B|y_1,\dots,y_n \sim t\left(n-2,\hat{B},\frac{\hat{\sigma}^2}{S_{xx}}\right) \tag{19}$$

2.3.5 Marginal Posterior Distribution of A

The marginal posterior distribution of A is obtained by integrating B and σ^2 out from the joint posterior distribution.

$$\begin{aligned} p(A|y_1,\dots,y_n) &= \int_0^\infty\left(\int_{-\infty}^\infty P(A,B,\sigma^2|y_1,\dots,y_n)\,dB\right)d\sigma^2 \\ &= \\ &\int_0^\infty\left(\int_{-\infty}^\infty \frac{1}{(\sigma^2)^{\frac{n+2}{2}}} exp\left(-\frac{SSE+n[(A-\hat{A})+(B-\hat{B})\bar{x}]^2+(B-\hat{B})^2S_{xx}}{2\sigma^2}\right)dB\right)d\sigma^2 \\ &= \int_0^\infty p(A,\sigma^2|y_1,\dots,y_n)d\sigma^2 \end{aligned} \tag{20}$$

$$\begin{aligned} &p(A,\sigma^2|y_1,\dots,y_n) = \\ &\int_{-\infty}^\infty \frac{1}{(\sigma^2)^{\frac{n+2}{2}}} exp\left(-\frac{SSE+n[(A-\hat{A})+(B-\hat{B})\bar{x}]^2+(B-\hat{B})^2S_{xx}}{2\sigma^2}\right)dB \\ &\propto \frac{1}{(\sigma^2)^{\frac{n+1}{2}}} exp\left(-\frac{SSE+\frac{(A-\bar{A})^2}{\frac{1}{n}+\frac{\bar{x}^2}{\sum_{i=1}^{n}(x_i-\bar{x})^2}}}{2\sigma^2}\right) \end{aligned} \tag{21}$$

Considering $\emptyset = \frac{1}{\sigma^2}$,

$$p(A|y_1,\dots,y_n) = \int_0^{\infty} p(A,\sigma^2|y_1,\dots,y_n)d\sigma^2$$

$$= \int_0^{\infty} \emptyset^{\frac{n-3}{2}} exp\left(-\frac{SSE+\frac{(A-\hat{A})^2}{\bar{x}^2}}{\frac{1}{n}+\frac{\bar{x}^2}{\sum_{i=1}^{n}(x_i-\bar{x})^2}}\emptyset\right)d\emptyset = \tag{22}$$

$$\int_0^{\infty} p(A,\emptyset|y_1,\dots,y_n)d\emptyset$$

After integrating Eq. (22), the following equation is obtained:

$$p(A|y_1,\dots,y_n) \propto \left(1+\frac{1}{n-2}\times\frac{(A-\hat{A})^2}{\hat{\sigma}^2\left(\frac{1}{n}+\frac{\bar{x}^2}{\sum_{i=1}^{n}(x_i-\bar{x})^2}\right)}\right)^{-\frac{(n-2)+1}{2}} \tag{23}$$

Finally, the marginal posterior distribution of A is the Student's t-distribution with degrees of freedom (n-2), center $\hat{A}$, and scale parameter $\hat{\sigma}^2\left(\frac{1}{n}+\frac{\bar{x}^2}{\sum_{i=1}^{n}(x_i-\bar{x})^2}\right)$.

$$A|y_1,\dots,y_n \sim t\left(n-2,\hat{A},\hat{\sigma}^2\left(\frac{1}{n}+\frac{\bar{x}^2}{\sum_{i=1}^{n}(x_i-\bar{x})^2}\right)\right) \tag{24}$$

2.3.6 Marginal Posterior Distribution of σ^2

If the prior distribution of σ^2,$p(\sigma^2)$, proportional to $\frac{1}{\sigma^2}$, then the prior distribution of the precision ϕ ($\emptyset=\frac{1}{\sigma^2}$), $p(\emptyset)$, is proportional to $\frac{1}{\emptyset}$ [36].

Therefore, the joint prior distribution is written as:

$$p(A,B,\emptyset) \propto \frac{1}{\emptyset} \tag{25}$$

As shown in Eq.(17), the joint distribution $p(B,\emptyset|y_1,\dots,y_n)$ is written as:

$$p(B,\emptyset|y_1,\dots,y_n)$$
$$\propto \emptyset^{\frac{n-3}{2}}\exp\left(-\frac{SSE+\left(B-\hat{B}\right)^2\sum_{i=1}^{n}(x_i-\bar{x})^2}{2}\emptyset\right) \tag{26}$$

By integrating $p(B,\emptyset|y_1,\dots,y_n)$ over B, the following equation is obtained:

$$p(\emptyset|y_1,\dots,y_n) \propto \emptyset^{\frac{n-2}{2}-1}\exp\left(-\frac{SSE}{2}\emptyset\right) \tag{27}$$

Finally, the marginal posterior distribution of $\emptyset$ is a Gamma distribution with a shape parameter $\frac{n-2}{2}$ and rate parameter $\frac{SSE}{2}$.

$$\emptyset|y_1,\dots,y_n \sim Gamma\left(\frac{n-2}{2},\frac{SSE}{2}\right) \tag{28}$$

Therefore, the updated σ^2 follows the inverse Gamma distribution.

2.3.7 Joint posterior distribution

Eq (26) can be reformulated as shown in Eq. (29).

$$\begin{aligned} &p(B,\emptyset|y_1,\dots,y_n) \\ &\propto \emptyset^{\frac{n-3}{2}}\exp\left(-\frac{SSE+\left(B-\hat{B}\right)^2\sum_{i=1}^{n}(x_i-\bar{x})^2}{2}\emptyset\right) \\ &\propto \left[\emptyset^{\frac{1}{2}}exp\left(-\frac{(B-\hat{B})^2\sum_{i=1}^{n}(x_i-\bar{x})^2}{2}\emptyset\right)\right]\left[\emptyset^{\frac{n-2}{2}-1}exp\left(-\frac{SSE}{2}\emptyset\right)\right] \end{aligned} \tag{29}$$

Therefore, the joint distribution $p(B,\emptyset|y_1,\dots,y_n)$ can be viewed as the product of the posterior distribution of B conditioning on ϕ and the posterior distribution of ϕ. The first term, $\emptyset^{\frac{1}{2}}\exp\left(-\frac{(B-\hat{B})^2\sum_{i=1}^{n}(x_i-\bar{x})^2}{2}\emptyset\right)$, is the Normal distribution with mean $\hat{B}$ and standard deviation $\frac{\sigma^2}{\sum_{i=1}^{n}(x_i-\bar{x})^2}=\frac{\sigma^2}{S_{xx}}$. The second term, $\emptyset^{\frac{n-2}{2}-1}\exp\left(-\frac{SSE}{2}\emptyset\right)$, is the Gamma distribution of the precision ϕ, or the inverse Gamma distribution of the variance σ^2.

$$B|\sigma^2,data \sim Normal\left(\hat{B},\frac{\sigma^2}{S_{xx}}\right) \tag{30}$$

$$1/\sigma^2|\,data \sim Gamma\left(\frac{n-2}{2},\frac{SEE}{2}\right) \tag{31}$$

Therefore, the joint distribution of B and σ^2, under the reference prior, is a Normal-Gamma distribution on σ^2.

As shown in Eq. (22), the joint distribution $p(A,\emptyset|y_1,\dots,y_n)$ is written as:

$$\begin{aligned} p(A,\emptyset|y_1,\dots,y_n) &\propto \emptyset^{\frac{n-3}{2}}exp\left(-\frac{SSE+\frac{\left(A-\hat{A}\right)^2}{\bar{x}^2}}{\frac{1}{n}+\frac{}{\sum_{i=1}^{n}(x_i-\bar{x})^2}}\emptyset\right) \\ &\propto \left[\emptyset^{\frac{1}{2}}exp\left(-\frac{\frac{\left(A-\hat{A}\right)^2}{\bar{x}^2}}{\frac{1}{n}+\frac{}{\sum_{i=1}^{n}(x_i-\bar{x})^2}}\emptyset\right)\right]\left[\emptyset^{\frac{n-2}{2}-1}exp\left(-\frac{SSE}{2}\emptyset\right)\right] \end{aligned} \tag{32}$$

As shown in Eq. (32), the joint distribution $p(A,\emptyset|y_1,\dots,y_n)$ can be viewed as the product of the posterior distribution of A conditioning on ϕ and the posterior distribution of ϕ. The first term, $\emptyset^{\frac{1}{2}}\exp\left(-\frac{\frac{\left(A-\hat{A}\right)^2}{\bar{x}^2}}{\frac{1}{n}+\frac{}{\sum_{i=1}^{n}(x_i-\bar{x})^2}}\emptyset\right)$, is the Normal distribution with mean $\hat{A}$ and standard

deviation $\sigma^2\left(\frac{1}{n}+\frac{\bar{x}^2}{\sum_{i=1}^{n}(x_i-\bar{x})^2}\right)=\sigma^2\left(\frac{1}{n}+\frac{\bar{x}^2}{S_{xx}}\right)$. The second term, $\emptyset^{\frac{n-2}{2}-1}\exp\left(-\frac{SSE}{2}\emptyset\right)$, is the Gamma distribution of the precision ϕ, or the inverse Gamma distribution of the variance σ^2.

$$A|\sigma^2, data \sim Normal\ (\hat{A}, \sigma^2\left(\frac{1}{n}+\frac{\bar{x}^2}{S_{xx}}\right)) \tag{33}$$

$$1/\sigma^2|\ data \sim Gamma(\frac{n-2}{2}, \frac{SEE}{2}) \tag{34}$$

Therefore, the joint distribution of A and σ^2, under the reference prior, is a Normal-Gamma distribution on σ^2.

2.4 Methods of evaluation

One of the problems with the comparison of creep data with a model's prediction is the increasing divergence and spread of data with time. Consequently, the divergence and spread are a measure of the limitation of the model's capabilities and variability in the experimental data The calculation of a coefficient of variation or standard error of regression normalized by the data centroid are from the methods commonly used for determining the deviation of a model from the data [18]. Several methods have been used for the evaluation of the accuracy of models to predict experimental data. In this study, Bazant and Panula (BP) coefficient of variation [37], Comité Européen du Béton (CEB) coefficient of variation [38] and Gardner coefficient of variation [39] are used.

2.4.1 BP coefficient of variation ($\bar{w}_{BP}$ %) method

A coefficient $\bar{w}_{BP}$ is determined for the data set [37]. Data points in each logarithmic decade, 0 to 9.9 days, 10 to 99.9 days, and so on, are considered as one group. Weight is assigned to each data point based on the decade in which it falls and the number of data points in that particular decade.

2.4.2 CEB coefficient of variation (V_{CEB})

The CEB statistical indicators were suggested by Muller and Hilsdorf [38]. The indicators are calculated in six-time ranges: 0 to 10 days, 11 to 100 days, 101 to 365 days, 366 to 730 days, 731 to 1095 days, and above 1095. The final V_{CEB} value is the root mean square (RMS) of the six interval values.

2.4.3 The Gardner coefficient of variation (ω_G)

The mean observed value and RMS of the difference between calculated and observed values are calculated in half-logarithmic time intervals: 3 to 9.9 days, 10 to 31.5 days, 31.6 to 99 days, 100 to 315 days, 316 to 999 days, 1000 to 3159, and above 3160 days. Then, the average values and RMSs are calculated without regard to the number of observations in each half-decade. Finally, the Gardner coefficient of variation, ω_G, is obtained by dividing the average RMS normalized by the average value [39].

3. Results and discussion

179 experiments performed under various conditions with 1488 readings having loading age equal or greater to 700 days ($t_0 \geq 700$ days) are chosen from the NU database for this study. The creep coefficient is calculated according to the EC2 model [19] for each observation. Finally, the linear regression presented in Eq. (7) is applied for these 1488 readings.

Fig. 2 shows the graph of the residuals obtained for the EC2 model plotted against the creep coefficient. Positive residuals mean that the model underestimates the creep coefficient while negative values indicate that the model overestimates the creep coefficient. An accurate creep coefficient prediction is illustrated by residuals close to zero. As shown in Fig. 2, the EC2 model may underestimate or overestimate the creep coefficient for a creep coefficient value less than 4; however, for higher values of the creep coefficient, the EC2 model underestimates the creep coefficient, and the residual magnitude is very high underlining the inadequacy of the EC2 in creep coefficient prediction.

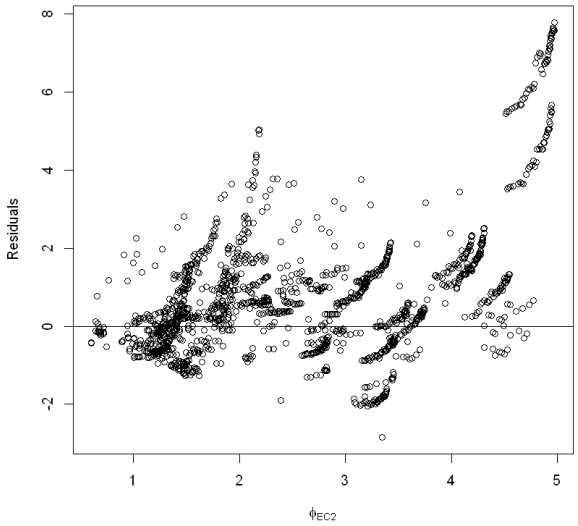

Fig. 2 Plot of creep coefficient residuals for the 1488 readings

As the EC2 model calculates the creep coefficient based on the value of the compressive strength (i.e. less or greater than 35 MPa), the data is first divided into two categories: group1 and group 2. Group 1 includes observations with compressive strength less or equal to 35 MPa. Group 2 is formed from observations having a compressive strength greater than 35 MPa. The goal is to find out in which combination of parameters the EC2 model underestimates or overestimates the creep coefficient. Further investigation and exploration of the data are made to obtain more precise results for the correction coefficients values and led to the division of the data into six groups (see Table 1) based on the underestimation and overestimation of the EC2 model.

Table 1. Properties of each group

Group a	$f_{cm} \leq 35$ MPa and $\frac{\sigma}{f_{cm(t_0)}} < 0.3$
Group b	$f_{cm} \leq 33$ MPa and $\frac{\sigma}{f_{cm(t_0)}} \geq 0.3$
Group c	33 MPa $< f_{cm} \leq 35$ MPa and $\frac{\sigma}{f_{cm(t_0)}} \geq 0.3$
Group d	35 MPa $< f_{cm} < 45$ MPa and RH $<$ 80%
Group e	$f_{cm} \geq 45$ MPa and RH $<$ 80%
Group f	$f_{cm} \geq 35$ MPa and RH $\geq$ 80%

Table 1 shows the properties of each of the six groups. Group 1 is mainly divided according to the value of the ratio of sustained load to compressive strength at loading age ($\frac{\sigma}{f_{cm(t_0)}}$). Group a includes the observations of group 1 with $\frac{\sigma}{f_{cm(t_0)}}$ less than 0.3. Observations where $\frac{\sigma}{f_{cm(t_0)}}$ equal to or greater than 0.3 are divided into group b and group c depending on the value of compressive strength (i.e. less or greater than 33 MPa). For group 2, observations are primarily divided according to the relative humidity (RH). For RH value less than 80%, the observations of group 2 with compressive strength less than 45 MPa and equal to or greater than 45 MPa are found in groups d and e, respectively. Group f includes observations from group 2 having relative humidity equal to or greater than 80%. The division is thus made according to the compressive strength (f_{cm}), ratio of sustained load to compressive strength at loading age ($\frac{\sigma}{f_{cm(t_0)}}$) and relative humidity (RH). The effect of loading age (t_0) is implicitly considered in the ratio of sustained load to compressive strength at loading age ($\frac{\sigma}{f_{cm(t_0)}}$) as the loading age greatly influences the compressive strength. Indeed, this division fits the results of studies found in the literature according to the most important factors affecting creep [12,40], where compressive strength, relative humidity, sustained load and loading age were the highest factors affecting creep.

Based on the data division shown in Table 1, Fig. 3 clearly shows that the EC2 model underestimates the creep coefficient in the case of groups b, d and e, while it overestimates the creep coefficient in the case of groups a and c.

In order to apply the BLR, the error ϵ_i should be normally distributed with zero mean and constant variance σ^2. Fig. 4 shows the histogram of the error ϵ_i, which is the difference between the observed value and the predicted value, for the six groups. The Shapiro-Wilk test is applied and the p-value for the six groups is greater than 0.05; thus, the normality of the error ϵ_i is verified and Bayesian linear regression can be applied. Therefore, the random variable of each response y_i, conditioning on the observed data x_i and the parameters A, B and σ^2, is also normally distributed.

By considering the likelihood distribution (see Eq. (9)) and the reference prior (see Eq. (12)), the marginal distributions of A, B and σ^2 are calculated as mentioned in section 2. The correction coefficients, A and B, and their 95% credible interval (CI) are calculated and listed in Table 2. For a 95% CI, the value of interest (i.e. A or B) lies with a 95% probability in the interval. For example, there is a 95% chance that the correction coefficient B will increase by 1.09% up to 1.26% for each additional increase in the EC2 creep coefficient in group a. In groups a and c where the EC2 model overestimates the creep coefficient (Fig. 3), the values of A are 0.67 and 0.58 for groups a and c, respectively, and the values of B are 1.18 and 1.02, respectively. The values of A and B in groups b, d and e are greater than one as the EC2 model underestimates the creep coefficient in these groups. The values of A and B in group f are 1.03 and 0.87, respectively. Fig. 5 shows the residuals plots of the six groups after the implementation of the correction coefficients into the EC2 creep model. Fig. 6 shows the x-y scatter plots of the six groups with the fitted line. The x-axis represents the natural logarithm of the EC2 creep coefficient and the y-axis represents the natural logarithm of the actual creep coefficient in the Northwestern University database.

Table 2. Values of the correction coefficients A and B and their 95% credible intervals

	Group a	Group b	Group c	Group d	Group e	*Group f*
A	0.67	1.43	0.58	1.13	1.20	1.03
95%CI of A	[0.63;0.72]	[1.34;1.55]	[0.50;0.68]	[1.01;1.28]	[1.06;1.36]	[0.87;1.22]
B	1.18	1.02	1.28	1.14	1.36	0.54
95%CI of B	[1.09;1.26]	[0.95;1.08]	[1.09;1.47]	[1.01;1.26]	[1.18;1.55]	[-0.09;1.16]

Table 3 shows the values of the statistical indicators before and after the implementation of the correction coefficient in the EC2 model (Eq. 2). These statistical indicators are calculated to verify the accuracy and effectiveness of the proposed improvement and modification of the EC2 model. As indicated in Table 3, the implementation of the correction coefficients, A and B, provides a significant improvement of the results where $\overline{w}_{BP}$, V_{CEB}, and ω_G decreased by 24%, 24%, and 26%, respectively; therefore, the updated model proves to be an effective solution to improve the prediction of creep coefficient.

Table 3. Statistical indicators of the EC2 model and the updated EC2 model

	$\overline{w}_{BP}$	V_{CEB}	ω_G
Target value	0	0	0
EC2 model	0.58	0.50	0.57
Updated EC2 model	0.44	0.38	0.42

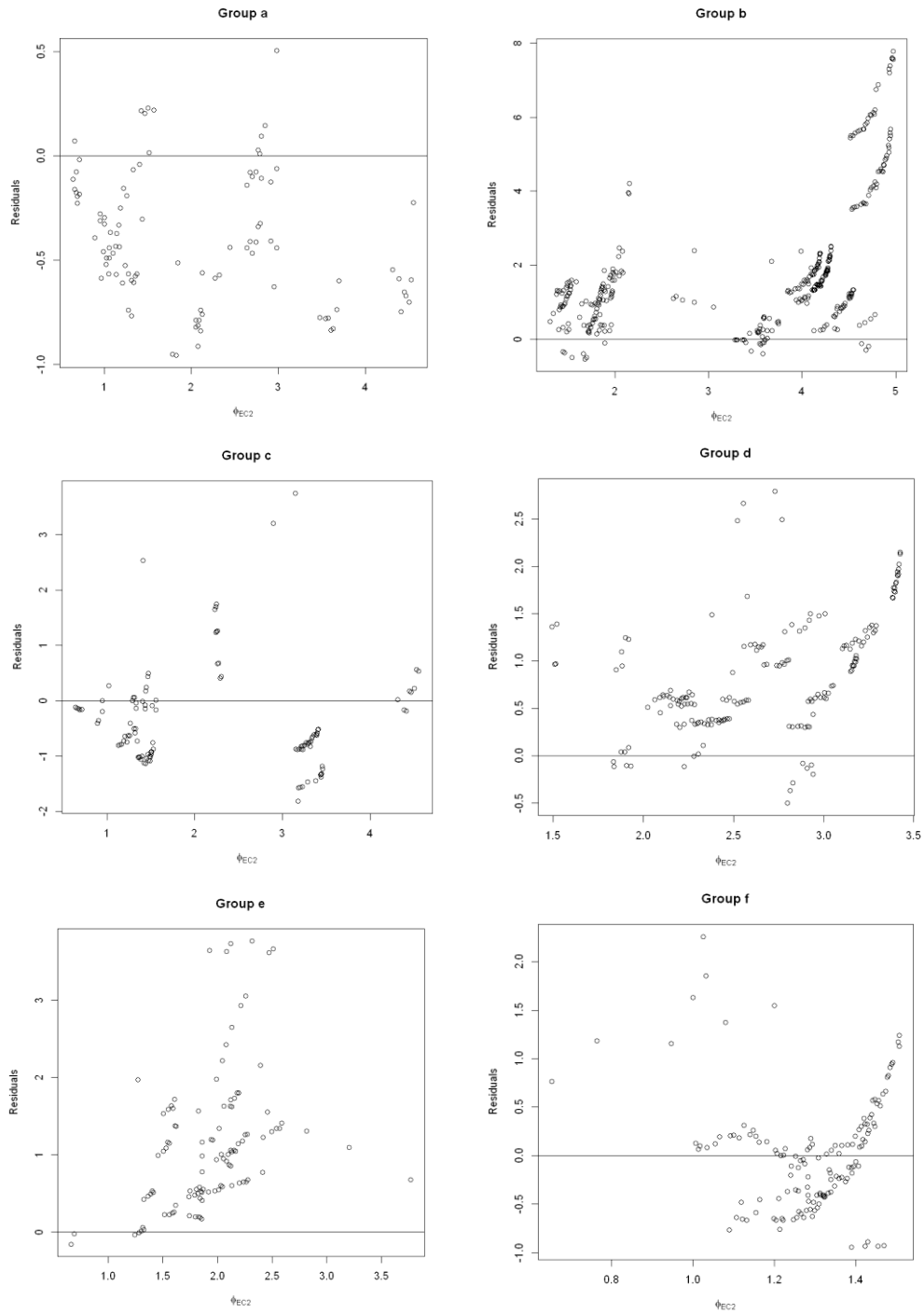

Fig. 3 Plot of creep coefficient residuals for the six groups (according to the EC2 model)

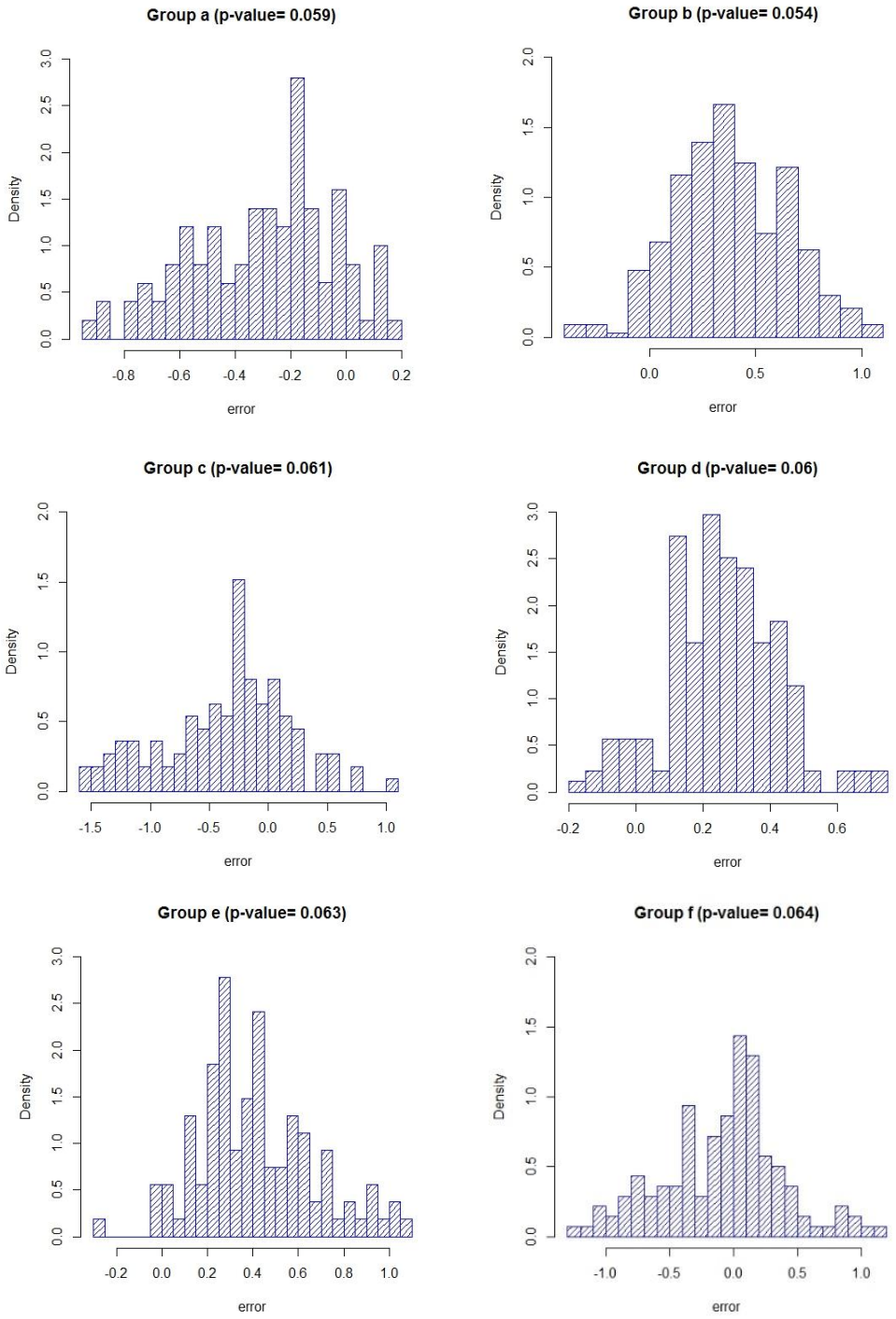

Fig. 4 Histogram of the error ϵ_i for the six groups with the p-value of the Shapiro-Wilk test

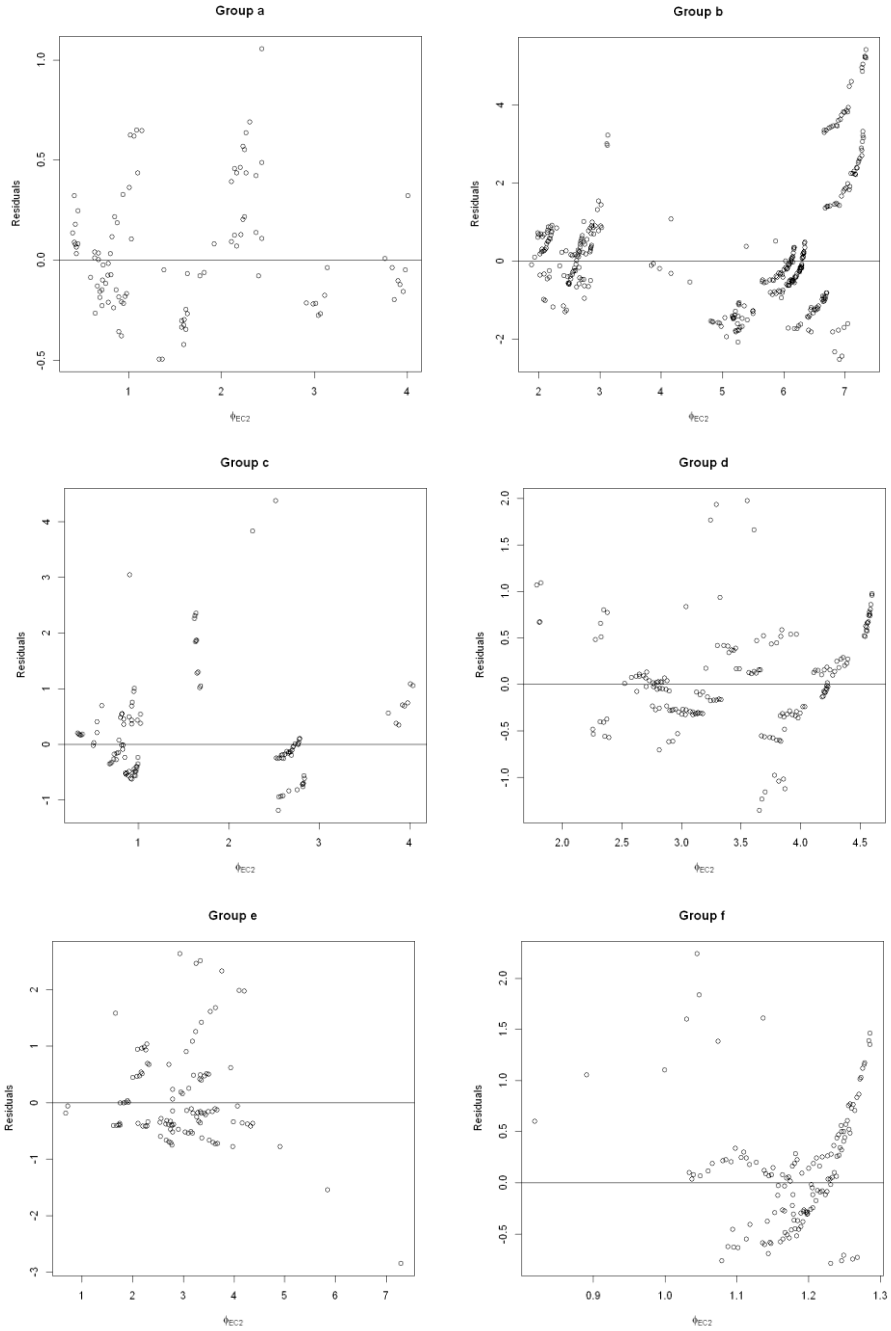

Fig. 5 Plot of creep coefficient residuals for the six groups (according to the updated EC2 creep model)

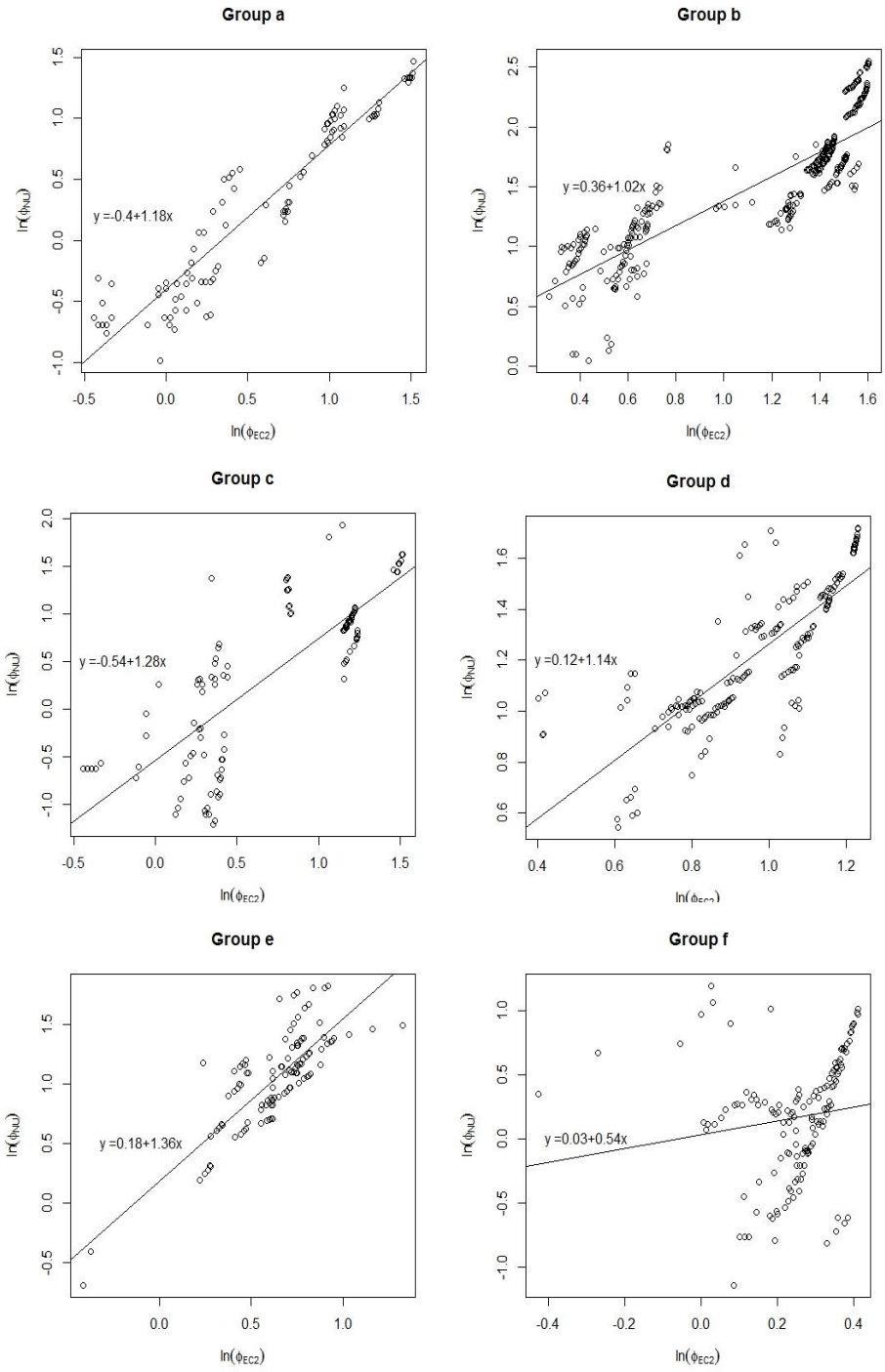

Fig. 6 Plots of the natural logarithm of the EC2 creep coefficient versus the natural logarithm of the actual creep coefficient for the six group

4. Conclusion

Creep can affect the structural behavior by violating the service limit states, losing the prestressing forces, or redistributing the stress in concrete members. For that, engineers should accurately predict creep. Therefore, this paper aims to update the EC2 creep coefficient prediction by implementing correction coefficients into the model. The Northwestern University dataset was used in this study, which contains a large number of creep tests that are performed using different concrete mix compositions and under various environmental conditions such as aggregate-cement ratio, water-cement ratio, concrete compressive strength, cement type, effective thickness, loading age, sustained stress over the compressive strength at loading age, temperature, and relative humidity.

Since Bayesian-type inferences are considered as suitable tools to revise and update design codes, the correction coefficients were calculated using Bayesian linear regression. An approach based on Bayesian linear regression was developed in this study to define a methodology for updating the EC2 model. This methodology allows determining the correction coefficients that must be introduced into the EC2 creep coefficient model.

A total of 1488 readings of creep coefficient, with loading age greater than 700 days, were extracted from the NU database. The data was then explored and divided into six groups according to the compressive strength, sustained stress over the compressive strength at loading age and relative humidity. Next, the normality of the data in the six groups was checked using the Shapiro-Wilk test. Finally, the correction coefficients were calculated for the different groups.

Statistical indicators (BP coefficient of variation, CEB coefficient of variation and Gardner coefficient of variation) have decreased by 24%, 24%, and 26%, respectively, after the implementation of the correction coefficients in the EC2 model. Therefore, the presented approach has proven to be an effective solution for improving the creep coefficient prediction. The adoption of the updated model would improve the long-term serviceability of structures subjected to time-dependent creep strains.

References

[1] Sankaya H, Susurluk G. Effect of polypropylene fiber addition on thermal and mechanical properties of concrete. Research on Engineering Structures & Materials, 2019;5(1):1-12. https://doi.org/10.17515/resm2018.72ma1109

[2] Palanci M. Yield response prediction of unsymmetrically reinforced concrete rectangular beams. Research on Engineering Structures & Materials, 2020;6(2):105-18. https://doi.org/10.17515/resm2019.141st0802

[3] Seranaj A, Elezi E, Seranaj A. Structural optimization of reinforced concrete spatial structures with different structural openings and forms. Research on Engineering Structures & Materials, 2018;4(2):79-89. https://doi.org/10.17515/resm2016.79st0726

[4] Yaghi K, Hammoud H. Strength evaluation of a fire damaged concrete slab : combined correlation approach. Research on Engineering Structures & Materials, 2018;4(4):231-40. https://doi.org/10.17515/resm2018.40me0127

[5] Raphael W, Zgheib E, Chateauneuf A. Experimental investigations and sensitivity analysis to explain the large creep of concrete deformations in the bridge of Cheviré. Case Studies in Construction Materials, 2018;9:e00176. https://doi.org/10.1016/j.cscm.2018.e00176

[6] Daou H, Abou Salha W, Raphael W, Chateauneuf A. Explanation of the collapse of Terminal 2E at Roissy-CDG Airport by nonlinear deterministic and reliability analyses.

Case Studies in Construction Materials, 2019;10. https://doi.org/10.1016/j.cscm.2019.e00222
[7] Raphael W, Faddoul R, Feghaly R, Chateauneuf A. Analysis of Roissy Airport Terminal 2E collapse using deterministic and reliability assessments. Engineering Failure Analysis, 2012;20:1-8. https://doi.org/10.1016/j.engfailanal.2011.10.001
[8] Daou H, Raphael W. Comparison between Various Creep Calculation Methods for the Time-dependent Analysis of Terminal 2E at Roissy. Jordanian Journal of Civil Engineering, 2021;15(1):64-76.
[9] Chateauneuf A, Raphael W, Rostand JB, Pitti M. Reliability of prestressed concrete structures considering creep models. Structure and Infrastructure Engineering: Maintenance, Management, Life-Cycle Design and Performance, 2014;10:12:1595-605. https://doi.org/10.1080/15732479.2013.835831
[10]Daou H, Raphael W, Chateauneuf A, Geara F. Probabilistic Assessment of Structural Safety of Complex Structures - Application to Terminal 2E at Roissy, CDG Airport. Procedia Structural Integrity, 2019;22:17-24. https://doi.org/10.1016/j.prostr.2020.01.003
[11] Daou H, Raphael W. Investigation of the Significance of Factors Affecting Long-Term Creep of Concrete using Screening Designs. IOP Conferences Series: Materials Science and Engineering, 2020;809. https://doi.org/10.1088/1757-899X/809/1/012016
[12] Daou H, Rapahel W. Identifying the Weight of Factors Affecting Creep of Concrete Using Factorial ANOVA. Key Engineering Materials, 2021;872:21-5. https://doi.org/10.4028/www.scientific.net/KEM.872.21
[13] Saad L, Chateauneuf A, Raphael W. Robust formulation for Reliability-based design optimization of structures. Structural and Multidisciplinary Optimization, 2018;57:2233-48. https://doi.org/10.1007/s00158-017-1853-7
[14] Gan Y, Romero Rodriguez C, Zhang H, Schlangen E, van Breugel K, Šavija B. Modeling of microstructural effects on the creep of hardened cement paste using an experimentally informed lattice model. Computer-Aided Civil and Infrastructure Engineering, 2021. https://doi.org/10.1111/mice.12659
[15] Zheng Z, Hu D, Liu P, Sha F, Liu L, Yu Z. Considering the effect of the randomness of concrete strength and relative humidity on concrete creep. Structural Concrete, 2020;1-15. https://doi.org/10.1002/suco.202000139
[16] Topçu İB, Uzunömeroğlu A. Experimental investigation of utilizing chemical additives and new generation corrosion inhibitors on reinforced concrete. Research on Engineering Structures & Materials, 2020. https://doi.org/10.17515/resm2020.214st0929
[17] Fares AM. The impact of RC shear wall openings at the lateral stiffness of the cantilever shear walls. Research on Engineering Structures & Materials, 2020. https://doi.org/10.17515/resm2020.208st0816
[18] ACI Committee 209. Guide for Modeling and Calculating Shrinkage and Creep in Concrete Structures. ACI 209.2R-08. American Concrete Institute Report 209.2R-08, Farmington Hills, 2008.
[19] CEN. EN 1992-1-1, Eurocode 2: Design of concrete structures - Part 1-1 : General rules and rules for buildings, 2004.
[20] Bažant ZP, Baweja S. Creep and shrinkage prediction model for analysis and design of concrete structures: Model B3, A. Al-Manaseer, editor. Adam Neville Symposium: Creep and Shrinkage Structural Design Effect, 2000.
[21] CEB. Structural Concrete-Textbook on Behaviour, Design and Performance. Updated Knowledge of the CEBI FIP Model Code 1990. fib Bull 2, 1999;2:37-52.
[22] Gardner NJ. Design provisions of shrinkage and creep of concrete. Al-Manaseer A, editor. Adam Neville Symposium: Creep and Shrinkage Structural Design Effect. 2000;101-4.

[23] Raphael W, Faddoul R, Geara F, Chateauneuf A. Improvements to the Eurocode 2 shrinkage model for concrete using a large experimental database. Structural Concrete, 2012;13(3):174-81. https://doi.org/10.1002/suco.201100029
[24] Raphael W, Faddoul R, Selouan DE-A, Chateauneuf A. Information-based formulation for Bayesian updating of the Eurocode 2 creep model. Structural Concrete, 2009;10(2):1-55. https://doi.org/10.1680/stco.2009.10.2.55
[25] Faddoul R, Soubra A, Raphael W, Chateauneuf A. Extension of dynamic programming models for management optimisation from single structure to multi-structures level. Structure and Infrastructure Engineering: Maintenance, Management, Life-Cycle Design and Performance, 2013;9:5:432-47. https://doi.org/10.1080/15732479.2011.557082
[26] Faddoul R, Raphael W, Chateauneuf A. Maintenance optimization of series systems subject to reliability constraints. Reliability Engineering and System Safety, 2018;180:179-88. https://doi.org/10.1016/j.ress.2018.07.016
[27] Faddoul R, Raphael W, Soubra A-H, Chateauneuf A. Incorporating Bayesian Networks in Markov Decision Processes. Journal of Infrastructure Systems, 2013;19(4):415-24. https://doi.org/10.1061/(ASCE)IS.1943-555X.0000134
[28] Rossi PE, Allenby GM, McCulloch R. Bayesian Statistics and Marketing. Bayesian Statistics and Marketing. West Sussex, England: John Wiley & Sons, 2005. https://doi.org/10.1002/0470863692
[29] Jose M. Bernardo, Adrian F. M. Smith. Bayesian Theory. West Sussex, England: John Wiley & Sons, 2000.
[30] Robert CP. The Bayesian Choice. New York, USA: Springer, 2007.
[31] Aladejare AE, Idris MA. Performance analysis of empirical models for predicting rock mass deformation modulus using regression and Bayesian methods. Journal of Rock Mechanics and Geotechnical Engineering, 2020;12:1263-71. https://doi.org/10.1016/j.jrmge.2020.03.007
[32] Ghosh S, Chakraborty S. Seismic fragility analysis of structures based on Bayesian linear regression demand models. Probabilistic Engineering Mechanics, 2020;61:103081. https://doi.org/10.1016/j.probengmech.2020.103081
[33] Cheng K, Lu Z. Adaptive Bayesian support vector regression model for structural reliability analysis. Reliability Engineering and System Safety, 2020;107286. https://doi.org/10.1016/j.ress.2020.107286
[34] Zhao H, Chen B, Li S, Li Z, Zhu C. Updating the models and uncertainty of mechanical parameters for rock tunnels using Bayesian inference. Geoscience Frontiers, 2021;12:101198. https://doi.org/10.1016/j.gsf.2021.101198
[35] Akaike H. A New Look at the Statistical Model Identification. IEEE Trans Automat Contr. 1974;19(6):716-23. https://doi.org/10.1109/TAC.1974.1100705
[36] Clyde M, Cetinkaya-Rundel M, Rundel C, Banks D, Chai C, Huang L. An Introduction to Bayesian Thinking A Companion to the Statistics with R Course, 2020.
[37] Bažant ZP, Panula L. Practical prediction of time-dependent deformations of concrete. Part II: Basic creep. Matériaux et Constructions, 1978;11:317-28. https://doi.org/10.1007/BF02473873
[38] Muller HS, Hilsdorf HK. Evaluation of the time-dependent behavior of concrete, summary report on the work of general task group 9. CEB Bull d'Information. 1990;199.
[39] Gardner NJ. Comparison of prediction provisions for drying shrinkage and creep of normal-strength concretes. Canadian Journal of Civil Engineering, 2004;31(5):767-75. https://doi.org/10.1139/l04-046
[40] Adam I, Taha MMR. Identifying the Significance of Factors Affecting Creep of Concrete: A Probabilistic Analysis of RILEM Database. International Journal of Concrete Structures and Materials, 2011;5(2):97-111. https://doi.org/10.4334/IJCSM.2011.5.2.97

Research on Engineering Structures & Materials
journal homepage: http://jresm.org
Research Group

Research Article

The effect of material strength and discontinuity in RC structures according to different site-specific design spectra

Ercan Işık[1,a], Ehsan Harirchian[2,b], Hüseyin Bilgin*[3,c], Kirti Jadhav [4,d]

[1]*Department of Civil Engineering, Bitlis Eren University, Bitlis, Turkey*
[2]*Institute of Structural Mechanics (ISM), Bauhaus-Universität Weimar, Weimar, Germany*
[3] *Department of Civil Engineering, Epoka University, Tirana, Albania*
[4] *Faculty of Civil Engineering , Bauhaus-Universität Weimar, Weimar, Germany*

Article Info

Article history:
Received 03 Mar 2021
Revised 02 Apr 2021
Accepted 04 May 2021

Keywords:

Structural analysis;
Design spectra;
Material strength;
Reinforced-concrete;

Abstract

Seismic-induced damages in reinforced-concrete (RC) buildings were primarily associated with materials' low strength and poor properties. This study aims to investigate the seismic response of RC structures according to the different material's strength and design spectra. Adaptive static pushover and eigenvalue analysis were performed for four different design spectra, five types of concrete, and two reinforcement grades. Four different design spectra were obtained by considering discrete geographical locations with different earthquake risks via the updated Turkish Earthquake Hazard Map 2018. Structural analysis was carried out for a sample RC building using these spectrum curves and material strengths. It has been observed that the structure becomes more rigid as the strength of concrete increases. This situation manifested itself with an increase in period values and a decrease in the stiffness values. Stiffness values of the building are independent of reinforcement. As the concrete strength decreases, the structure's seismic capacity decreases while the displacement's demand for predicted performance levels increases. Moreover, an increase in the tensile strength of reinforcements substantially increases the seismic capacity of the building. The study also determines that the site-specific design spectra obtained for different provinces are used in the analysis affects the demand displacements values considerably. The material differentiation between the stories in the building was also examined in this study. It can be a source in terms of how material discontinuity affects building performance.

1. Introduction

In recent years, destructive earthquakes have caused large-scale losses for lives and properties, bringing forward the importance of seismic studies, research, and scientific developments. Several parameters such as number of stories, soft/weak story, short column, irregularity in plan, local soil conditions and hill-slope effect will adversely affect the behaviour of structures following earthquake loads. These parameters were also investigated and considered for rapid evaluation of structures. Parameters that will decrease the structural resistance mechanism will increase the amount of damage that might occur [1,2]. Numerous methods are developed to evaluate the building's seismic safety and performance, such as rapid visual screening [3–8] and application of modern computational techniques including machine learning [9–11], but design spectra are one of the most essential parameters to be used in determining the seismic safety factor of buildings. Design spectra can be obtained by combining the local soil conditions and seismicity elements of that particular region. Local ground conditions significantly affect

*Corresponding author: hbilgin@epoka.edu.al
[a] orcid.org/0000-0001-8057-065X; [b] orcid.org/0000-0003-0113-2120; [c] orcid.org/0000-0002-5261-3939; [d] orcid.org/0000-0002-0048-3693
DOI: http://dx.doi.org/10.17515/resm2021.273st0303

the design spectra. Moreover, changes in spectra also affect the target displacements of structures [12–16]. Building design and evaluation become more meaningful by using site-specific earthquake spectra.

Reinforced-concrete (RC) structures are widely used in developed countries and have an important role in terms of seismic-induced damage [17-19]. In such structures, the structural elements are made by joining reinforcement and concrete. Earthquake resistance of such structures decreases due to weaknesses in resistance mechanisms. Their vulnerability increases even in low-intensity earthquakes, depending on the amount of these weaknesses. In RC structures, it is associated with low strength and weak properties of concrete as the first cause of damage. Also, it should not be overlooked that the reinforcement used is straight or ribbed.

Seismic zones were expressed in four different ways, according to the Turkish Seismic Design Code-2007 (TSDC-2007) [20]. These seismic zones were removed with the updated seismic design code in 2018 (TBEC-2018) [21]. Site-specific design spectra should be used for any geographic location. One of the aims of the study is to examine the effect of different design spectra. In terms of seismicity level, Bingöl is located on level 1, Ağrı on level 2, Artvin on level 3, and Konya level 4, respectively, which were selected as case studies. Site-specific design spectra were obtained for these settlements according to the updated Turkish Earthquake Hazard Map-2018. Eigenvalue and static adaptive pushover analyses were carried out separately for the five-story RC building using these design spectra. In addition, C8, C12, C16, C20 and C25 selections as a concrete class, S220, and S420 selections were made as to the reinforcement class. Concrete and reinforcement classes are taken into consideration as variables, and all other structural characteristics are kept constant. Interpretations were made by comparing all the obtained results.

This study aims to reveal how the material strengths predicted primarily affect building performance as a cause of damage, especially in RC structures after the earthquake. While acknowledging these differences, settlements with different seismicity risk were taken into consideration. The relationship between site-specific design spectra and material strengths has been tried to be revealed. Earthquake parameters were obtained for selected provinces by using updates earthquake hazard maps for Turkey. Short period mapping coefficient, spectral acceleration coefficient, maximum ground acceleration (PGA), maximum ground velocity (PGV), local ground effect coefficients, design spectral acceleration coefficients, and horizontal elastic spectrum curve were calculated individually here for selected provinces. The related information about earthquake damages due to concrete strength is also provided. Detailed information about obtaining design spectra for selected settlements is given. The RC building model used as an example is detailed. Information about the analysis used is presented.

Additionally, uncertainties in material strength are one of the essential factors to be taken into account. Concrete and reinforcement grades were selected when projecting RC buildings. In this case, it is impossible to attach the material grades selected at the project design stage on the building for various reasons. This means that the material strengths stipulated in the project cannot be achieved. Therefore, the calculations made during the projecting phase do not make any sense for the envisaged structure. This study also explains the failure of the stipulated material strengths at the project design stage. At the same time, the differentiation of material strength was also examined with the study. The discontinuities occur in material strength in RC structures due to different reasons for using different strength materials between stories.

2. Selection of Site-specific Earthquake Spectra

There are many useful structural analysis parameters under earthquake risk [22-27]. Seismicity elements are one of these parameters. These elements are briefly defined as local soil conditions, fault groups, and their characteristics, historical earthquakes, and necessary periods. These parameters vary based on different geographic locations. Within the study's scope, four various settlements with different seismic risks were selected as Bingöl, Ağrı, Artvin, and Konya. Changes in analysis with varying risks of earthquakes were tried to be revealed within the scope of the study. The seismic zone expressions are no longer used in the updated Turkish Earthquake Hazard Map [28]. The usage of site-specific design spectra has emerged as the most significant change in updated Turkish Building Earthquake Code -2018. The site-specific seismic hazard evaluation is the main advantage of the new seismic code. It is necessary to mention that the latest update yields more reasonable assessments in structural performance. The representation of the selected provinces on this map was shown in Figure 1.

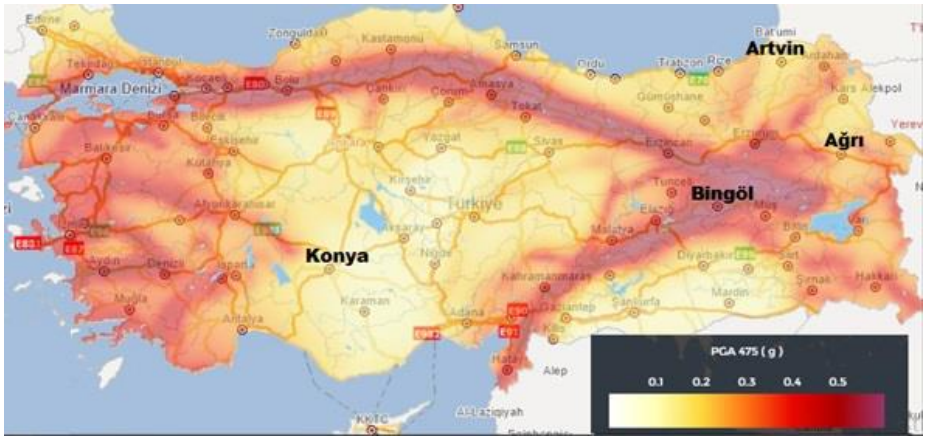

Fig. 1 Four different settlements that selected for this study

For all geographic locations, the standard design earthquake ground motion (DD-2) for an earthquake with a 10% annual probability of excess (recurrence period 475 years) and local soil conditions ZA class were selected for spectra curves and earthquake parameters. The properties of the ZA class were given in Table 1.

Table 1. Properties of ZA type according to TSDC-2018 [18]

Local Ground Type	Type of Ground	Average at the top 30 meters $(V_S)_{30}$ [m/s]
ZA	Strong, hard rocks	> 1500

In this study, the map spectral acceleration coefficient (SS), map spectral acceleration coefficient for the period of 1.0 second (S1), the most significant peak ground acceleration (PGA), the peak ground velocity (PGV), local ground impact coefficients (FS and F1), design spectral acceleration coefficients (short-period design spectral acceleration coefficient (SDS), and design spectral acceleration coefficient (SD1) for 1.0 second period) and horizontal elastic spectrum values were calculated separately via the Turkey Earthquake Hazard Maps Interactive Web Application [28]. SS for 0.2s and S1 spectral acceleration values in 1.0s are calculated directly from the application for a 5% damping ratio. Local

ground effect coefficient FS is derived from Table 2 in the short period zone and F1 was calculated according to Table 3 in the 1.0s period for local ground type ZA.

Table 2. Local soil effect coefficients (F_S) for ZA soil type according to TBEC-2018 [21]

Local Soil Type	Local ground effect coefficient F_S for the short period zone					
	$S_S \leq 0.25$	$S_S = 0.50$	$S_S = 0.75$	$S_S = 1.00$	$S_S = 1.25$	$S_S \geq 1.50$
ZA	0.8	0.8	0.8	0.8	0.8	0.8

Table 3. Local soil effect coefficients (F_1) for ZA soil type according to TBEC-2018 [21]

Local Soil Type	Local ground effect coefficient F_1 for 1.0 second period					
	$S_1 \leq 0.10$	$S_1 = 0.20$	$S_1 = 0.30$	$S_1 = 0.40$	$S_1 = 0.50$	$S_S \geq 0.60$
ZA	0.8	0.8	0.8	0.8	0.8	0.8

Referring to the Table 2 and Table 3, FS and F1 coefficients for ZA take a constant value of 0.8. This situation is also valid for ZB soil type and it differs for other soil types that given in TBEC-2018 (ZC, ZD; ZE). This is due to the fact that ZA and ZB soil types are solid ground. Short period design spectral acceleration coefficient (SDS) and design spectral acceleration coefficient (SD1) values for 1.0 seconds are calculated as follows;

$$S_{DS} = S_S . F_S \quad (1)$$

$$S_{D1} = S_1 . F_1 \quad (2)$$

The comparison of the earthquake parameters obtained for selected provinces in this study are presented in Table 4.

Table 4. Comparison of earthquake parameters for selected provinces

Parameter	Province			
	Bingöl	Ağrı	Artvin	Konya
S_S	1.596	0.547	0.425	0.307
S_1	0.419	0.152	0.116	0.073
PGA (g)	0.648	0.234	0.185	0.133
PGV(cm/s)	41.836	13.588	10.467	6.688
F_S	0.800	0.800	0.800	0.800
F_1	0.800	0.800	0.800	0.800
S_{DS}	1.277	0.438	0.341	0.246
S_{D1}	0.335	0.122	0.093	0.058

A comparison of horizontal elastic design spectra obtained for selected cities was shown in Figure 2. Here, the horizontal axis represents the period value (T), and the vertical axis represents the horizontal elastic design spectral acceleration (Sae).

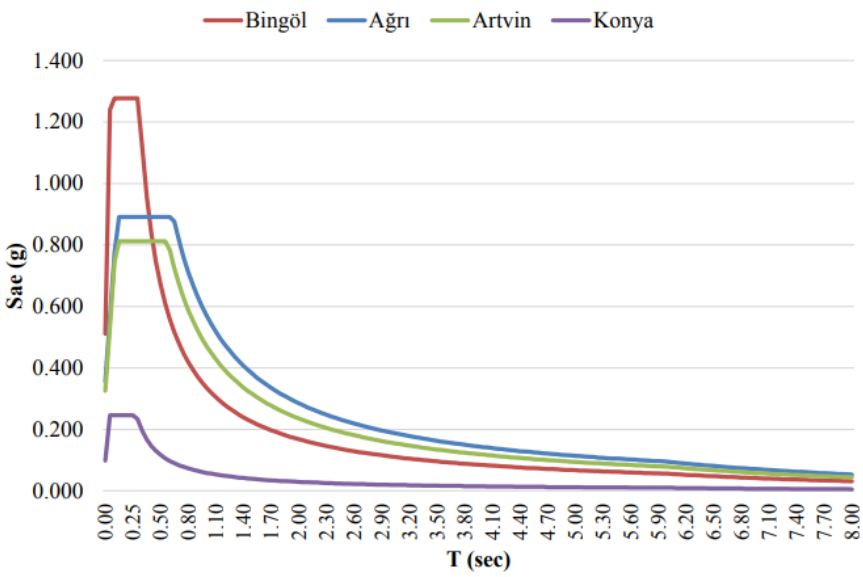

Fig. 2 Comparison of horizontal elastic design spectra

3. Failures According to Low Strength of RC

The strength of materials directly affects structures under various loads. Materials that are insufficient alone can become sufficient in terms of strength by combining additional materials. RC is a widely used composite building material that obtained by combining two different materials such as concrete and steel. The most important property expected from concrete is compressive strength and the tensile strength expected from steel. The classification of these two materials is made by considering these properties. Earthquake damages are primarily associated with concrete with poorer properties than these two materials in any RC structure. Therefore, the quality of these two materials largely determines the quality of any RC structural system. Concrete is a composite material, including various materials such as cement, aggregate, water and other additional materials. Furthermore, concrete production steps are very much, such as calculation of composition, transportation, concreting, compaction, and curing of concrete. The fact that it is obtained by combining many materials and the production stages are very different affects the concrete strength negatively. A concrete with low strength that seems sufficient under vertical loads cannot withstand horizontal loads during an earthquake. The concrete shows a more ductile behaviour as a result of the different reinforcements placed in the concrete in the RC structural system. However, if the compressive strength of concrete is low, it causes adherence between concrete and reinforcement to be sufficient even at low stresses. In this case, longitudinal reinforcements are easily stripped from the concrete, longitudinal reinforcements bonded with tight stirrups sprains. The materials contained in concrete, environmental conditions, application errors, bad workmanship, degree of compression, insufficient protection/maintenance and cement type generally cause low strength of concrete. However, inappropriate grain distribution and size in aggregate, direct use of aggregate obtained from rivers found in the region, and inadequate concrete compression processes led to concrete with a little resistance to segregation. The usage of smooth reinforcement in RC reduces the capacity in terms of both strength and adherence. This situation has been revealed again in the 2020 Sivrice (Elazığ) earthquake lastly in Turkey as presented in the Figure 3.

Fig. 3 Damages in RC according to poor/low strength after 2020 Sivrice earthquake

Due to the low concrete strength and the smooth reinforcement used, damage was observed in different earthquakes. Some of these damages were shown in Figure 4.

Fig. 4 Poor quality/ low strength material damages after different earthquakes [29–37]

4. Structural Analyses

Structural analysis for the provinces was performed using the Seismostruct software (Seismosoft, 2018). The static adaptive pushover analysis, which is applied in predicting the horizontal capacity of a structure, taking full account of the effect that the deformation of the latter and the frequency content of input motion have on its dynamic response characteristics, was used. Here, analyses were performed by considering the mode shapes and participation factors obtained from the eigenvalue analyses in each step during the adaptive pushover analysis. This method allows the use of site-specific spectra. Load control types used in this study are similar to conventional pushover analysis [38-46]. Material models have an essential place in structural analysis [47]. The nonlinear concrete model [48] and steel model [49] were used for concrete and steel material, respectively. The stress-strain relationship of the material models considered for these models is demonstrated in Figure 5. Here, the vertical axis represents stress and horizontal axis represents the strain under the stress.

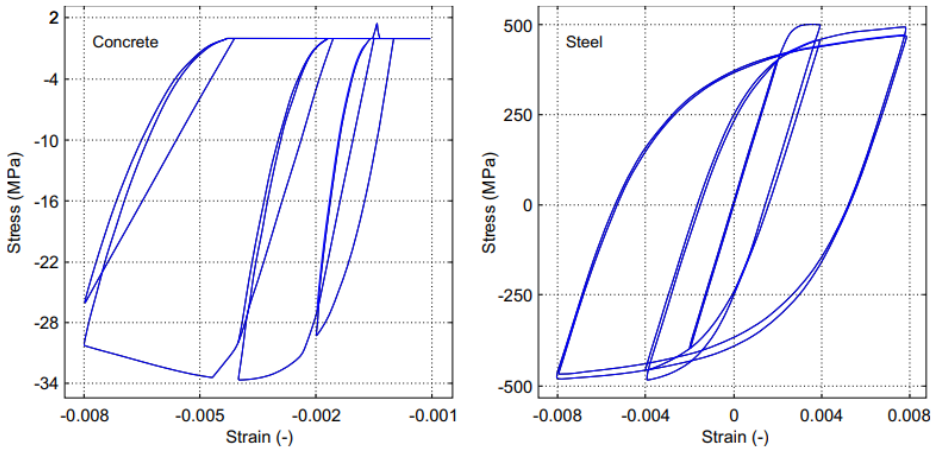

Fig. 5 Material models for concrete and steel considered in the study [50]

The characteristics of the five different concrete grades considered in this study are given in Table 5. The properties of the two different reinforcement grades considered in this study are given in Table 6.

Table 5. Properties of different concrete grades [51]

Parameter	C8	C12	C16	C20	C25
Mean compressive strength (kPa)	16000	20000	24000	28000	33000
Nominal value (kPa)	8000	12000	16000	20000	25000
Mean tensile strength (kPa)	1600	2000	2400	2800	3300
Modulus of elasticity (kPa)	1.88E+007	2.10E+007	2.30E+007	2.48E+007	2,69E+07
Strain at peak stress (m/m)	0.002	0.002	0.002	0.002	0.002
Specific weight (kN/m^3)	24.00	24.00	24.00	24.00	24.00

Table 6. Properties of different reinforcement grades [51]

Parameter	S220	S420
Mean compressive strength (kPa)	253000	483000
Modulus of elasticity (kPa)	2.00E+08	2.00E+08
Nominal value (kPa)	220000	420000
Yield strength (kPa)	253000	483000
Specific weight (kN/m3)	78	78
Strain hardening parameter (-)	0.005	0.005
Transition curve initial shape parameter	20	20
Transition curve shape calibrating coeff. A1 (-)	18.50	18.50
Transition curve shape calibrating coeff. A2 (-)	0.15	0.15
Isotropic hardening calibrating coeff. A3 (-)	0	0
Isotropic hardening calibrating coeff. A4 (-)	1.00	1.00
Fracture/buckling strain (-)	0.10	0.10

The blueprint of the selected RC structure is presented in Figure 6, and the 2D and 3D structural models and the applied loads are shown in Figure 7.

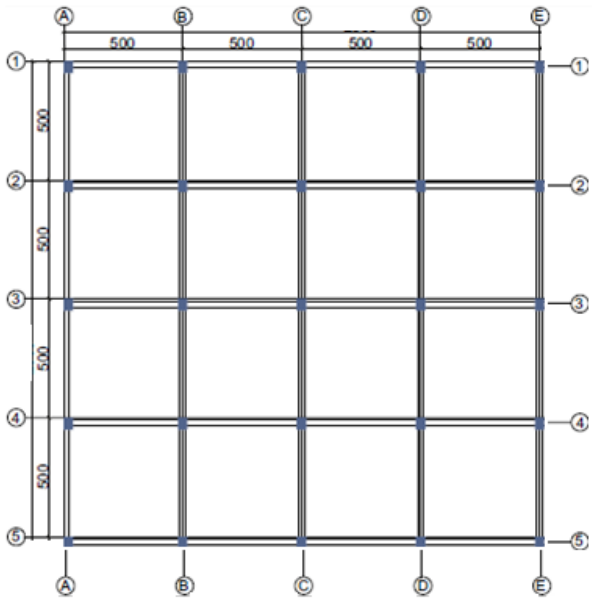

Fig. 6 The blueprint of sample model RC building

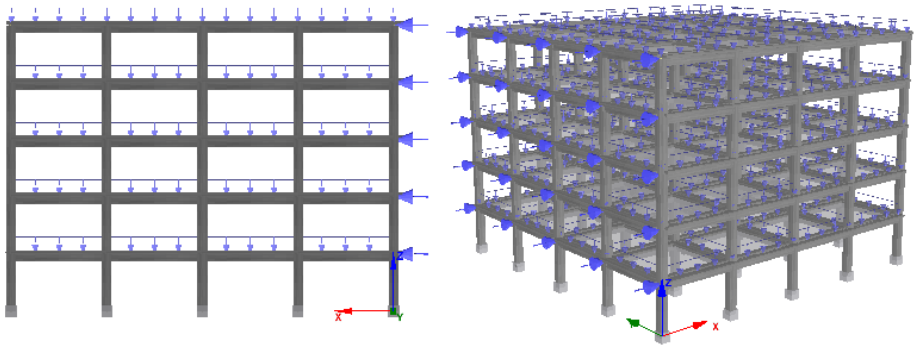

Fig. 7 2D and 3D models of the sample model RC building

Each story had an equal height and taken as 3 m. All columns were selected as 0.40 × 0.50m and beams were selected as 0.25×0.60m. The transverse reinforcements used in both elements were selected as ϕ10/10. The reinforcements used in the columns were selected as 4ϕ20 at corners and 4ϕ16 top bottom and left-right sides. The reinforcements used in the beams were selected as 4ϕ16 at lower side, 5ϕ14 upper side and 2ϕ12 at side. The columns and beams used in the structure are shown in Figure 8. The damping ratio was taken as % 5 in all structural models. The ZA soil type was chosen as the local soil condition. The importance of structure was taken into consideration as Class II. The slabs were selected as rigid diaphragms.

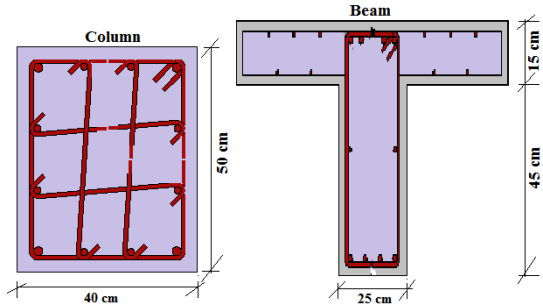

Fig. 8 Column and beam cross-sections

The dy value refers to displacement at the moment of yield and dint value refers to the intermediate displacement. Elastic stiffness (K_elas) and effective stiffness (K_eff) values were also calculated separately for selected provinces for different material strengths. Three different performance criteria were obtained for damage estimation. These are considered as near collapse (NC), significant damage (SD) and damage limitation (DL) according to Eurocode-8, (Part-3) [52].

5. The Interaction Between Material Strength and Site-Specific Spectra

The comparison of all values obtained in X direction for S220 and S420 has been presented in Tables 7 and 8, respectively. The comparison of the static pushover curves for S220 and S420 grades are presented in Figures 9.

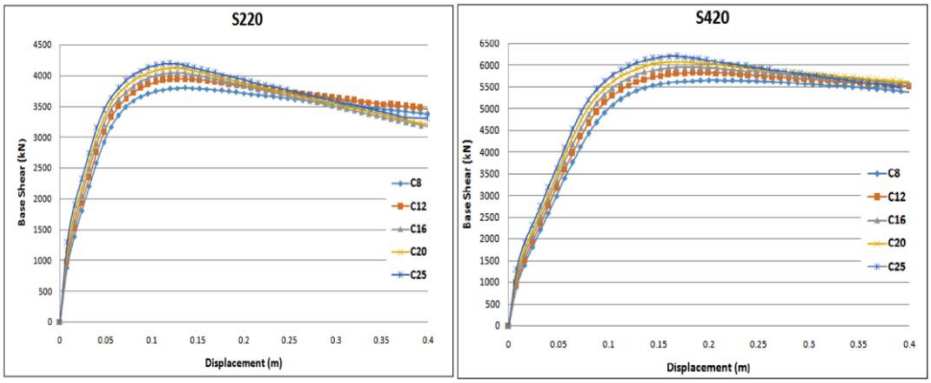

Fig. 9 Comparison of pushover curves for S220 and S420 for different concrete grades

Table 7. Comparison of values obtained in X direction for S220

Province	Concrete	Period	d_{int}	d_y	$K_{\_elas}$	$K_{\_eff}$	Base Shear	DL	SD	NC
Bingöl	C8	0.4429	0.061	0.136	109949.2	61788.6	3796.05	0.0948	0.1217	0.2109
	C12	0.4227	0.060	0.128	121202.8	65952.4	3943.33	0.0918	0.1178	0.2042
	C16	0.4066	0.058	0.128	132308.9	70333.2	4044.74	0.0889	0.1140	0.1977
	C20	0.3933	0.055	0.120	146060.4	74676.7	4118.61	0.0863	0.1107	0.1919
	C25	0.3795	0.052	0.120	160602.3	80067.8	4189.83	0.0833	0.1069	0.1853
Ağrı	C8	0.4429	0.061	0.136	109947.7	61783	3796.18	0.0342	0.0439	0.0762
	C12	0.4227	0.060	0.128	121201.6	65950.5	3943.51	0.0331	0.0425	0.0737
	C16	0.4066	0.058	0.128	132307.9	70332.8	4044.75	0.0321	0.0412	0.0714
	C20	0.3933	0.055	0.12	146059.6	74677.2	4118.51	0.0312	0.0400	0.0693
	C25	0.3795	0.052	0.12	160601.4	80069.6	4189.79	0.0301	0.0386	0.0669
Artvin	C8	0.4429	0.061	0.136	109948.2	61787.5	3796.04	0.0272	0.0349	0.0605
	C12	0.4227	0.060	0.128	121202	65954.2	3943.42	0.0263	0.0338	0.0586
	C16	0.4066	0.058	0.128	132308.1	70328.6	4044.85	0.0255	0.0327	0.0567
	C20	0.3933	0.055	0.12	146059.8	74677.5	4118.55	0.0248	0.0318	0.0551
	C25	0.3795	0.052	0.12	160601.6	80085.5	4190.07	0.0239	0.0307	0.0532
Konya	C8	0.4429	0.061	0.136	109951.8	61791.1	3796.04	0.0195	0.0250	0.0433
	C12	0.4227	0.060	0.128	121205.6	65959.6	3943.48	0.0188	0.0242	0.0419
	C16	0.4066	0.058	0.128	132312.0	70320.8	4045.17	0.0182	0.0234	0.0406
	C20	0.3933	0.055	0.12	146065.4	74677.3	4118.56	0.0177	0.0227	0.0394
	C25	0.3795	0.052	0.12	160608.4	80080.7	4189.87	0.0171	0.0219	0.0380

Table 8. Comparison of values obtained in X direction for S420

Province	Concrete	Period	d_{int}	d_y	K_{elas}	K_{eff}	Base Shear	DL	SD	NC
Bingöl	C8	0.4429	0.100	0.208	110005.30	56604.8	5651.61	0.099	0.127	0.220
	C12	0.4227	0.096	0.1917	121199.82	60691.12	5817.87	0.096	0.123	0.213
	C16	0.4066	0.092	0.1758	132293.06	64565.63	5950.22	0.093	0.119	0.206
	C20	0.3933	0.089	0.1681	146011.31	67995.43	6068.52	0.090	0.116	0.201
	C25	0.3795	0.087	0.1601	160527.06	71447.68	6201.31	0.088	0.113	0.196
Ağrı	C8	0.4429	0.100	0.2162	110003.83	56504.29	5656.65	0.036	0.046	0.080
	C12	0.4227	0.096	0.1917	121198.56	60685.68	5817.96	0.035	0.044	0.077
	C16	0.4066	0.092	0.1757	132292.02	64562.52	5950.07	0.034	0.043	0.043
	C20	0.3933	0.089	0.1681	146010.48	67994.95	6068.47	0.033	0.042	0.073
	C25	0.3795	0.087	0.1601	160526.14	71457.95	6201.32	0.032	0.041	0.071
Artvin	C8	0.4429	0.100	0.2157	110004.32	56587.24	5652.91	0.028	0.036	0.063
	C12	0.4227	0.096	0.1914	121198.95	60715.11	5817.7	0.027	0.035	0.061
	C16	0.4066	0.092	0.1758	132292.31	64563.81	5950.21	0.027	0.034	0.059
	C20	0.3933	0.089	0.1681	146010.69	67996.45	6068.59	0.026	0.033	0.058
	C25	0.3795	0.087	0.16	160526.38	71459.39	6201.24	0.025	0.032	0.056
Konya	C8	0.4429	0.100	0.2076	110007.89	56548.47	5653.91	0.020	0.026	0.045
	C12	0.4227	0.096	0.1916	121202.59	60688.62	5818.07	0.020	0.025	0.044
	C16	0.4066	0.092	0.1758	132296.18	64566.97	5950.38	0.019	0.024	0.042
	C20	0.3933	0.089	0.1681	146014.4	67997.1	6068.63	0.019	0.024	0.041
	C25	0.3795	0.087	0.1601	160530.61	71449.63	6201.2	0.018	0.023	0.040

The comparison of PGA and target displacements for damage estimation was given in Table 9.

Table 9. Comparisons of earthquake – structural parameters

Province	PGA	C25-S220			C25-S420		
Bingöl	0.648	0.0833	0.1069	0.1853	0.088	0.113	0.196
Ağrı	0.234	0.0301	0.0386	0.0669	0.032	0.041	0.071
Artvin	0.185	0.0239	0.0307	0.0532	0.025	0.032	0.056
Konya	0.133	0.0171	0.0219	0.038	0.018	0.023	0.040

6. The Effect of Material Discontinuity on Building Performance

The differentiation of material strengths in the building has also been taken into account within this study's scope. The construction of the stories can be built at different times due to various RC structures that have no engineering services. Since concrete casting is carried out at different times, discontinuities occur in material strength within the building. As a result, concrete and reinforcement are used in different qualities in the first built parts and later built parts. This situation increases the difference of material strength between stories, especially with the widespread of ready mixed concrete. The difference in material strengths within the building increases as the construction date of the first parts of the buildings gets older. These differences to reveal the name of the specified minimum concrete and reinforcement grade in Turkey in the last three regulations were taken into account. Analyses were carried out using the RC building example in the previous section and the design spectrum obtained for Bingöl province. The lowest concrete and reinforcement grades were considered, which were specified in the last three seismic design codes in Turkey. The building models selected in this context are given in Table 10.

Table 10. Models selected for material discontinuity

Model	Description
Model 1	C14 - S220 (In whole structure)
Model 2	C14 - S220 (only in 1st story)/ C20-S220 (All other stories)
Model 3	C14 - S220 (only in 1st story)/ C20-S420 (All other stories)
Model 4	C14 - S220 (only in 1st story)/ C25-S220 (All other stories)
Model 5	C14 - S220 (only in 1st story)/ C25-S420 (All other stories)
Model 6	C14-S220 (only in 1st and 2nd stories) C20-S220 (All other stories)
Model 7	C14-S220 (only in 1st and 2nd stories) C20-S420 (All other stories)
Model 8	C14-S220 (only in 1st and 2nd stories) C25-S220 (All other stories)
Model 9	C14-S220 (only in 1st and 2nd stories) C25-S420 (All other stories)
Model 10	C20-S220 (In whole structure)
Model 11	C25-S220 (In whole structure)

The analysis results obtained for the eleven different building models are shown in Table 11.

Table 11. Results obtained from the change of the material grade within the building

Model	Period	d_{int}	d_y	$K_{\_elas}$	$K_{\_eff}$	Base Shear	DL	SD	NC
Model 1	0.4142	0.0587	0.1280	126800.97	68139.18	4000.29	0.090	0.116	0.201
Model 2	0.4011	0.0531	0.1120	143574.93	75468.82	4011.05	0.086	0.111	0.192
Model 3	0.4011	0.5070	0.0880	143540.79	79580.68	4034.21	0.084	0.108	0.186
Model 4	0.3927	0.0496	0.1042	154168.61	80902.27	4015.26	0.083	0.107	0.186
Model 5	0.3927	0.0480	0.0880	154122.84	84990.65	4036.07	0.081	0.104	0.181
Model 6	0.4076	0.0551	0.1202	138776.00	72623.01	4003.96	0.088	0.112	0.195
Model 7	0.4076	0.0544	0.1200	138746.22	73661.28	4005.81	0.087	0.112	0.193
Model 8	0.4034	0.0529	0.1199	143621.45	75860.41	4005.73	0.086	0.110	0.191
Model 9	0.4034	0.0523	0.1120	143587.62	76593.32	4008.77	0.085	0.109	0.189
Model 10	0.3933	0.0890	0.1681	146011.31	67995.43	6068.52	0.090	0.116	0.201
Model 11	0.3795	0.087	0.1601	160527.06	71447.68	6201.31	0.088	0.113	0.196

Table 12 gives examples of the load factors obtained for equal displacements when structural building systems contain different material strengths. The concrete grade was selected as a variable by keeping the reinforcement grade constant while making these comparisons.

Table 12. Comparison of load factors for equal relative displacement

Model	Relative Displacement (m)					Load Factor
	N511	N411	N311	N211	N211	
Model 1						15.82
Model 10						17.71
Model 11						19.16
Model 2	0.016	0.015	0.012	0.008	0.0033	17.28
Model 4						18.31
Model 6						16.66
Model 8						17.16

The comparison of relative displacement values in building models under equal load factors were shown in Table 13. Two different load factor values have been taken into account as an example.

Table 13. Comparison of relative displacement under equal load factors

Model	Relative Displacement (m)									
	Load Factor = 25					Load Factor = 40				
	N511	N411	N311	N211	N111	N511	N411	N311	N211	N111
Model 1	0.034	0.031	0.0025	0.0167	0.071	0.127	0.121	0.109	0.088	0.046
Model 10	0.030	0.028	0.023	0.0153	0.064	0.089	0.084	0.074	0.055	0.026
Model 11	0.027	0.026	0.021	0.0141	0.059	0.079	0.075	0.065	0.048	0.023
Model 2	0.031	0.029	0.024	0.0163	0.069	0.104	0.098	0.089	0.070	0.039
Model 4	0.028	0.027	0.022	0.0154	0.068	0.096	0.091	0.082	0.065	0.037
Model 6	0.032	0.030	0.024	0.0166	0.070	0.120	0.115	0.101	0.081	0.043
Model 8	0.030	0.028	0.024	0.0166	0.070	0.111	0.106	0.097	0.079	0.041

7. Conclusions

Eigenvalue and static adaptive pushover analysis for sample RC buildings were made for three different variables. All three selected parameters directly affect the earthquake behaviour of the structures. The first variable is the site-specific design spectrum according to the updated Turkish Earthquake Building Code-2018, which is one of the most important changes in this code. An analysis was carried out for four different cities which each located on different seismicity levels. Five different concrete classes have been selected as another variable. Meanwhile, two different reinforcement grades were considered as the last variable. As concrete strength increases, the deformability of it decreases.

As the strength of the concrete increases, the building's period value decreases, and the elastic and effective stiffness values increase. These show that the structure will be more rigid with the rise of the strength of the concrete. The decrease in concrete strength reduces the seismic capacity of the building. With the reduction of concrete strength, the target displacement values foreseen for the performance criteria expected from the building have increased. These results on concrete strength have remained valid for both reinforcement classes. The period value of the buildings did not change according to the reinforcement class. Elastic and effective stiffness values, which are calculated over crack and cracked sections, also remained constant. The seismic capacity of the buildings was significantly increased due to increasing the reinforcement strength. With the increase of reinforcement strength, the target displacement values have increased. The highest risk values among the provinces considered were calculated for the Bingöl province. The site-specific design spectra did not change the period, elastic and effective stiffness, and seismic capacity values. However, the design spectra significantly altered the target displacement values for the performance criteria for damage estimation. The increase in PGA value also caused the target displacement to increase. The use of site-specific design spectra in the analysis and evaluation of structures allows a more realistic calculation of performance levels expected from the structure. It is clearly seen that a complete agreement was observed between the earthquake-structural analysis results by using the site-specific design spectra. The importance of material strength in RC structures with site-specific design spectra has been revealed once again in the light of the 2020 Sivrice earthquake. Since the seismicity elements of each geographic location are different, the results are expected to be varied. The construction of material strengths as projected in the project by obtaining engineering services will decrease the damage levels that may occur in the buildings to a lower level.

In columns and beams, both the normal and shear force capacities have increased with the increase in concrete strength. An effect of steel grade is not considered in seismic design code for limit values in normal force and shear force in columns and beams. The reinforcement ratios in the columns take constant values independently in the concrete and steel grade. However, this ratio of both concrete and reinforcement grade directly affects in the beams. As the concrete strength increased, the reinforcement ratios foreseen for the beams increased. As the reinforcement strength increased, the rate of reinforcement decreased. One of the most important causes of earthquake damages has revealed the effect of material strength on the building performance and limit conditions foreseen for forces with this study. In addition, analysis was carried out using the site-specific design spectra foreseen in the updated Turkish seismic design code. The final results obtained once again demonstrated the importance of obtaining site-specific design spectra.

The material strengths can vary between stories in RC structures that do not receive engineering services and whose stories are built at different times. This causes

discontinuity of the material in the building. In this context, analyses were performed by considering the minimum concrete grade, which was states in Turkey's last three seismic design codes. Low strength concrete is the leading cause of earthquake damage in RC structures in Turkey. In this respect, while the minimum concrete grade to be used in the 1975 code was C14, it was raised to C20 in 2007 and to C25 in the current 2018 regulation. The differentiation of the reinforcement grade within the structure affected the analysis results at minimal levels. With the increase in the number of low-strength concrete stories, the periods increased, and the structure's total rigidity decreased. The base shear forces obtained for building models with different strengths are very close to the whole structure's value for the lowest strength concrete in the structure. This situation has preserved its validity for the relative displacements. Equal displacements occurred at higher load factors with the increase in concrete strength in different building models. As the concrete strength increases, the structure behaves more rigid and makes fewer displacements. The change in concrete strength within the structure also negatively affected the relative displacement values. All the results obtained once again revealed that concrete strength directly affects the earthquake behaviour of structures.

References

[1] Yakut A. Preliminary seismic performance assessment procedure for existing RC buildings. Engineering Structures, 2004; 26:1447-1461. https://doi.org/10.1016/j.engstruct.2004.05.011

[2] Işık E, Isik M, Bülbül M. Web based evaluation of earthquake damages for reinforced concrete buildings. Earthquakes and Structures 2018; 13:423-432.

[3] Harirchian E, Lahmer T, Buddhiraju S, Mohammad K, Mosavi A. Earthquake safety assessment of buildings through rapid visual screening. Buildings, 2020;10:51. https://doi.org/10.3390/buildings10030051

[4] Harirchian E, Lahmer T, Earthquake hazard safety assessment of buildings via smartphone app: a comparative study. İOP Conference Series: Materials Science and Engineering, 2019;652:012069. https://doi.org/10.1088/1757-899X/652/1/012069

[5] FEMA P-154. Third Edition, Rapid visual screening of buildings for potential seismic hazards: A Handbook, Applied Technological Council (ATC) 2015.

[6] Vallejo CB, others. Rapid visual screening of buildings in the city of Manila, Philippines. 5th Civil Engineering Conference in the Asian Region and Australasian Structural Engineering Conference 2010, The. Engineers Australia, 2010.

[7] Tesfamariam S, Saatcioglu M. Seismic vulnerability assessment of reinforced concrete buildings using hierarchical fuzzy rule base modeling. Earthquake Spectra 2010;26: 235-256. https://doi.org/10.1193/1.3280115

[8] Harirchian E, Lahmer T. Improved rapid visual earthquake hazard safety evaluation of existing buildings using a type-2 fuzzy logic model. Applied Sciences,2020;10:2375. https://doi.org/10.3390/app10072375

[9] Harirchian E, Lahmer T, Kumari V, Jadhav K. Application of support vector machine modeling for the rapid seismic hazard safety evaluation of existing buildings. Energies 2020;13;3340. https://doi.org/10.3390/en13133340

[10] Harirchian E, Lahmer T, Rasulzade S. Earthquake hazard safety assessment of existing buildings using optimized multi-layer perceptron neural network. Energies 2020;13: 2060. https://doi.org/10.3390/en13082060

[11] Tesfamariam S, Liu Z. Earthquake induced damage classification for reinforced concrete buildings. Structural Safety 2010; 32:154-164. https://doi.org/10.1016/j.strusafe.2009.10.002

[12] Sextos A, De Risi R, Pagliaroli A, Foti S, Passeri F, Ausilio E, Cairo R, Capatti MC, Chiabrando F, Chiaradonna A, and others. Local site effects and incremental damage of

buildings during the 2016 Central Italy earthquake sequence. Earthquake Spectra 2018; 34:1639-1669. https://doi.org/10.1193/100317EQS194M
[13] Borcherdt RD. A theoretical model for site coefficients in building code provisions. Procs. 13thWorld Conference on Earthquake Engineering, 2004.
[14] Büyüksaraç A, Bektas Ö, Yılmaz H, Arısoy MÖ. Preliminary seismic microzonation of Sivas city (Turkey) using microtremor and refraction microtremor (ReMi) measurements. Journal of seismology, 2013;17:425-435. https://doi.org/10.1007/s10950-012-9328-1
[15] Iervolino I, Giorgio M, Cito P. Which earthquakes are expected to exceed the design spectra? Earthquake Spectra, 2019;35:1465-1483. https://doi.org/10.1193/032318EQS066O
[16] Kutanis M, Ulutas H, Işık E. PSHA of Van province for performance assessment using spectrally matched strong ground motion records. Journal of Earth System Science, 2018;127:99. https://doi.org/10.1007/s12040-018-1004-6
[17] Hadzima-Nyarko M, Nikić D, Pavić G. Seismic vulnerability assessment of reinforced concrete frame structure by finite element analysis. Acta Physica Polonica. A, 2019;135; 845-848. https://doi.org/10.12693/APhysPolA.135.845
[18] Hadzima-Nyarko M, Morić, D, Španić M. Spectral functions of RC frames using a new formula for Damage Index. Tehnički vjesnik, 2014;21:163-171.
[19] Işık MF, Işık E, Bülbül M.A. (2018). Application of iOS/Android based assessment and monitoring system for building inventory under seismic impact. 2018; 70:1043-1056. https://doi.org/10.14256/JCE.1522.2015
[20] TSDC (2007), Specification for Buildings to be Built in Seismic Zones (2007), Ministry of Public Works and Settlement, Ankara, 2007.
[21] TBEC (2018), Turkish Building Earthquake Code, Prime Ministry, Disaster and Emergency Management Presidency (AFAD), Ankara, 2018
[22] Avşar Ö, Yakut A, Caner A. Analytical fragility curves for ordinary highway bridges in Turkey. Earthquake Spectra. 2011; 27:971-996. https://doi.org/10.1193/1.3651349
[23] Bal IE, Bommer JJ, Stafford PJ, Crowley H, Pinho R. The influence of geographical resolution of urban exposure data in an earthquake loss model for Istanbul. Earthquake Spectra. 2010; 26:619-634. https://doi.org/10.1193/1.3459127
[24] Karaşin İB, Işık E, Demirci A, Aydın MC. The effect of site-specific design spectra for geographical location on reinforced-concrete structure performance. Dicle University journal of Engineering, 2020;13;1319-1330.
[25] Pavić G, Hadzima-Nyarko M, Bulajić B. A contribution to a uhs-based seismic risk assessment in Croatia-A case study for the city of Osijek. Sustainability, 2020;12:1796. https://doi.org/10.3390/su12051796
[26] Ademović N, Hadzima-Nyarko M, Zagora, N. Seismic vulnerability assessment of masonry buildings in Banja Luka and Sarajevo (Bosnia and Herzegovina) using the macroseismic model. Bulletin of Earthquake Engineering, 2020;18:3897-3933. https://doi.org/10.1007/s10518-020-00846-8
[27] Işık E, Büyüksaraç A, Ekinci YL, Aydın MC, Harirchian E. The effect of site-specific design spectrum on earthquake-building parameters: a case study from the Marmara Region (NW Turkey). Applied Sciences, 2020;10:7247. https://doi.org/10.3390/app10207247
[28] AFAD (2020), "Interactive earthquake map web page for the 10.01.2021 available at https://tdth.afad.gov.tr/ "
[29] Ates S, Kahya V, Yurdakul M, Adanur S. Damages on reinforced concrete buildings due to consecutive earthquakes in Van. Soil Dynamics and Earthquake Engineering. 2013;53. https://doi.org/10.1016/j.soildyn.2013.06.006
[30] Inel M, Senel S, Ün H. Experimental evaluation of concrete strength in existing buildings. Magazine of Concrete Research. 2008; 60:279-289. https://doi.org/10.1680/macr.2007.00091

[31] Binici H. March 12 and June 6, 2005 Bingol-Karliova earthquakes and the damages caused by the material quality and low workmanship in the recent earthquakes. Engineering Failure Analysis. 2007; 14:233 - 238. https://doi.org/10.1016/j.engfailanal.2005.10.020
[32] Su N. Structural evaluations of reinforced concrete buildings damaged by Chi-Chi Earthquake in Taiwan. 2001; 6:119-128. https://doi.org/10.1061/(ASCE)1084-0680(2001)6:3(119)
[33] Marshall J, Lang AF, Baldridge SM, Popp D. Recipe for disaster: construction methods, materials, and building performance in the January 2010 Haiti Earthquake. Earthquake Spectra.2011;27:323 - 343. https://doi.org/10.1193/1.3637031
[34] Alih SC, Vafaei M. Performance of reinforced concrete buildings and wooden structures during the 2015 Mw 6.0 Sabah earthquake in Malaysia. Engineering Failure Analysis, 2019;102:351-368 https://doi.org/10.1016/j.engfailanal.2019.04.056
[35] Yépez F, Yépez O. Role of construction materials in the collapse of R/C buildings after Mw 7.8 Pedernales - Ecuador earthquake, April 2016. Case Studies in Structural Engineering, 2017;7:24 - 31. https://doi.org/10.1016/j.csse.2016.12.001
[36] Varum H, Dumaru R, Furtado A, Barbosa A, Gautam D, Rodrigues H., Seismic performance of buildings in Nepal after the Gorkha Earthquake; In Impacts and insights of the Gorkha earthquake (pp. 47-63). Elsevier. https://doi.org/10.1016/B978-0-12-812808-4.00003-1
[37] Doğangün, A. Performance of reinforced concrete buildings during the May 1, 2003 Bingöl Earthquake in Turkey. Engineering Structures, 2004;26:841-856. https://doi.org/10.1016/j.engstruct.2004.02.005
[38] Antoniou A, Guney Y, Paudyal K. Determinants of corporate capital structure: evidence from European Countries. SSRN Electronic Journal 2002. https://doi.org/10.2139/ssrn.302833
[39] Antoniou S, Pinho R. Development and verification of a displacement-based adaptive pushover procedure. Journal of Earthquake Engineering, 2004;8:643-661. https://doi.org/10.1080/13632460409350504
[40] Ferracuti B, Pinho R, Savoia M, Francia R. Verification of displacement-based adaptive pushover through multi-ground motion incremental dynamic analyses. Engineering Structures, 2009;31:1789-1799. https://doi.org/10.1016/j.engstruct.2009.02.035
[41] Pinho R, Casarotti C, Antoniou S. A comparison of single-run pushover analysis techniques for seismic assessment of bridges. Earthquake Engineering Structural Dynamics, 2007;36:1347 - 1362. https://doi.org/10.1002/eqe.684
[42] Casarotti C, Pinho R. An adaptive capacity spectrum method for assessment of bridges subjected to earthquake action. Bulletin of Earthquake Engineering, 2007;5:377-390. https://doi.org/10.1007/s10518-007-9031-8
[43] Pinho R, Monteiro R, Casarotti C, Delgado R. Assessment of continuous span bridges through nonlinear static procedures. Earthquake Spectra, 2009;25:143-159. https://doi.org/10.1193/1.3050449
[44] Antoniou S, Pinho R. Advantages and limitations of adaptive and non-adaptive force-based pushover procedures. Journal of Earthquake Engineering, 2004;8; 497-522. https://doi.org/10.1080/13632460409350498
[45] Pinho R, Antoniou S. A displacement-based adaptive pushover algorithm for assessment of vertically irregular frames. Proceedings of the Fourth EuropeanWorkshop on the Seismic Behaviour of Irregular and Complex Structures, 2005.
[46]Aksoylu C, Arslan MH. Çerçeve türü betonarme binaların periyod hesaplarının farklı ampirik bağıntılara göre irdelenmesi. Bitlis Eren Üniversitesi Fen Bilimleri Dergisi, 2019;8:569-581. https://doi.org/10.17798/bitlisfen.476312

[47] Işık E, Özdemir M. Performance based assessment of steel frame structures by different material models. International Journal of Steel Structures, 2017;17: 1021-1031. https://doi.org/10.1007/s13296-017-9013-x
[48] Mander JB, Priestley MJ, Park R. Theoretical stress-strain model for confined concrete. Journal of Structural Engineering, 1988;114:1804-1826. https://doi.org/10.1061/(ASCE)0733-9445(1988)114:8(1804)
[49] Menegotto,M. Method of analysis for cyclically loaded RC plane frames including changes in geometry and non-elastic behavior of elements under combined normal force and bending. Proc. of IABSE symposium on resistance and ultimate deformability of structures acted on by well defined repeated loads, 1973.
[50] Antoniou, S.; Pinho, R. Seismostruct-Seismic Analysis program by Seismosoft. Technical manual and User manual 2003.
[51] Seismosoft [2014], "SeismoStruct v7.0 - A computer program for static and dynamic nonlinear analysis of framed structures," available from http://www.seismosoft.com .
[52] Pinto, P.E. The Eurocode 8-Part 3: the new European Code for the seismic assessment of existing structures, 2005.

Research on Engineering Structures & Materials
journal homepage: http://jresm.org
Research Group

Research Article

Seismic performance of shallow depth tuned liquid damper

Ali Bozer

Department of Civil Engineering, Nuh Naci Yazgan University, Kayseri, Turkey

Article Info

Article history:
Received 10 Dec 2020
Revised 28 Apr 2021
Accepted 20 May 2021

Keywords:

Tuned Liquid Damper;
Equivalent Mechanical Model;
Artificial Bee Colony;
Vibration Control;
Passive Control;
Energy Dissipation;
Earthquake Response

Abstract

Tuned Liquid Dampers (TLD) consist of a container that is generally partially filled with water. When the sloshing frequency of the water mass is tuned to the fundamental mode of the primary structure a significant amount of sloshing and wave breaking can be achieved which are the primary sources of energy dissipation. Although TLDs are easy to install, operate and maintain; it is generally challenging to model the nonlinear nature of sloshing water. Equivalent mechanical models provide a simplified solution in which sloshing liquid mass, liquid damping, and sloshing frequency are represented by an equivalent mass, damper, spring system. Equivalent mechanical model derivations are generally based on linear sloshing of water mass, which is possible when the water depth/tank length ratio is high and excitation amplitude is low. In this study, a well-known and widely accepted Housner equivalent mechanical model is used to model water sloshing. The water depth/tank length ratio is kept low to enhance the energy dissipation of TLD. The main objective of this study is to experimentally investigate the effectiveness of TLD and check the accuracy of Housner equivalent mechanical model under seismic excitations and low water depth/tank length ratio. Water depth is optimized by the Artificial Bee Colony algorithm which is a population-based optimization algorithm. Frequency sweep analysis and seismic excitations are employed to investigate TLD performance. It is shown that even TLD behavior is modeled by a simplified linear equivalent mechanical model, it is still effective in reducing structural response under large amplitude seismic excitations and low water level/tank length ratios. This is due to more energy dissipation with an increased amount of sloshing and wave breaking.

1. Introduction

Tuned-mass dampers (TMDs) are mass-spring systems where a moving auxiliary mass is attached to the primary structure. Auxiliary mass induces dynamic forces opposing the motion of the primary structure when the natural frequency of TMD is tuned to the fundamental mode of the primary structure. Tuned Mass Dampers are the origin of Tuned Liquid Dampers (TLDs) in which auxiliary mass is the sloshing of a liquid (usually water) mass contained either with a rectangular or circular tank. Lateral sloshing is the wave formation on the surface of a liquid when a tank partially filled with liquid oscillates. When a fluid container is subjected to horizontal accelerations, the free liquid surface moves up at one side of the container and moves down at the other forming a wave. Liquid sloshing frequency is a function of tank dimensions and liquid depth, thus it is easy to adjust the natural frequency of the TLD unit. By doing so any vibrational mode of the primary structure can be controlled, and possible variations in the dominant mode of the primary structure can easily be adapted.

Corresponding author: bozerali@gmail.com
orcid.org/0000-0002-3632-2605
DOI: http://dx.doi.org/10.17515/resm2020.235st1210

The idea of using TLD in civil engineering applications is first introduced by Bauer [1] and until that time the performance of TLD under seismic and wind excitations are investigated by many researchers [2-12].

Owing to their low maintenance requirement, cost-effectiveness, and ease of installation, TLDs attracted considerable attention in civil engineering applications. One important drawback on the other hand is the low inherent damping ratio of the sloshing liquid. The damping ratio of water is given as 0.5% in Eurocode 8 [14]. Özsarıyıldız and Bozer [15] utilized a differential evolution algorithm to obtain optimum parameters of TMD. Optimal damping ratios reported in their paper are far more than the natural damping ratio of linear sloshing water. Therefore lesser control performance is expected with TLD when compared to the TMD case.

When a TLD is subjected to motion with large amplitudes as expected in strong earthquake ground motions, wave breaking and shearing of the fluid is the primary form of mechanical damping, providing that the liquid level is low [4]. At this point, simple linear models can no longer describe the liquid behavior, and wave breaking changes the sloshing frequency of the liquid [8]. From a set of numerical simulations, Banerji et al. [9] showed that a low water depth/tank length ratio of 0.15 for a TLD, is more effective for large excitation amplitudes. Mars et al. [13] concluded that for shallow liquid levels traveling waves are generated whereas as the liquid level increases a transition to standing waves occurs. Energy dissipation in a sloshing liquid is mainly due to wave-to-wave and wave-to-wall interactions. Traveling waves can produce both interactions, whereas standing waves only produce wave-to-wall interactions.

The primary difficulties associated with the design of TLDs arise from the nonlinear nature of the sloshing fluid. Numerous fluid models have been proposed in the literature to describe sloshing, each of which is based upon simplifying assumptions that are valid for certain types of sloshing problems. The validity of many fluid models is dependent on the mean fluid depth to tank length ratio [16]. However complex nature of these models and necessary computational effort made these models impractical for TLD design. A simplified model was introduced by Housner [17] in which the sloshing liquid is represented by an equivalent mass, spring, and dashpot system. Whereas this equivalent model is derived for linear oscillations of liquid mass which is valid for small amplitude excitations and high (more than 0.20) liquid depth/tank length ratios.

In this study, a shallow depth TLD where water depth/tank length ratio kept below 0.15 is used to control seismic vibrations. Housner's [17] equivalent mechanical model is used to represent sloshing water in a rectangular tank. Housner's [17] equivalent model is valid for small liquid displacements where linear sloshing is expected. For shallow liquid levels and high amplitude excitations, on the other hand, nonlinear sloshing is likely to occur. However, the equivalent mechanical model is a simple tool and might be a good starting point for obtaining optimal TLD parameters. The main objective of this study is to experimentally investigate the effectiveness of TLD and check the accuracy of the Housner's [17] equivalent mechanical model when large amplitude vibrations and low water depth/tank length ratios present. The optimal water depth is obtained by Artificial Bee Colony (ABC) Algorithm [18] which is a population-based optimization algorithm. As to the best knowledge of authors, ABC Algorithm is first used in Finding Optimal Parameters of Tuned Liquid Dampers. The frequency-domain response is obtained by a frequency sweep analysis where large amplitude sinusoidal ground excitations are employed via a shaking table. The seismic performance of the tuned liquid damper is further investigated under seismic excitations.

2. Numerical Model

2.1. Equivalent Mechanical Model

The solution of the sloshing problem necessitates solving of some partial differential equations satisfying boundary conditions, however; Housner [17] presented an approximate method that avoids partial differential equations and presents solutions for several cases (rectangular tank, circular tank, elliptical tank) in simple closed form. Simplified formulas are given to estimate hydrodynamic pressures when a fluid container is subjected to horizontal accelerations. The essence of the method is the estimation of a simple type of flow that is similar to the actual fluid movement and this simple flow is used to determine the pressure. Basic assumptions for this method are a) fluid is incompressible b) fluid displacements are small c) fluid is constrained between rigid membranes and free to rotate.

If a tank with a free water surface is subjected to horizontal ground acceleration, a certain fraction of water is forced to participate in the back and forth motion of the tank which exerts an impulsive force on the tank. Impulsive force is equal to the inertia force of a rigidly attached mass M0 subjected to tank acceleration. Furthermore, the motion of the tank walls excites the water into oscillations which in turn exert an oscillating force on the tank. The oscillating force is equal to the oscillating mass M1 that is attached to a restraining spring. The mass M1 corresponds to the fundamental mode of oscillation of water.

For a rectangular container with a length L, fluid depth h and acceleration of the gravity g; stationary fluid mass M0, oscillating fluid mass M1 and natural sloshing frequency ω is given by the following equations:

$$\mathrm{M_0} = \mathrm{M}\frac{\tanh\left(\sqrt{3}\mathrm{L}/2\mathrm{h}\right)}{\sqrt{3}\mathrm{L}/2\mathrm{h}} \tag{1}$$

$$\mathrm{M_1} = \mathrm{M}\frac{1}{3}\sqrt{\frac{5}{2}}\frac{\mathrm{L}}{2\mathrm{h}}\tanh\left(\sqrt{\frac{5}{2}}\frac{2\mathrm{h}}{\mathrm{L}}\right) \tag{2}$$

$$\omega^2 = \frac{2\mathrm{g}}{\mathrm{L}}\sqrt{\frac{5}{2}}\tanh\left(\sqrt{\frac{5}{2}}\frac{2\mathrm{h}}{\mathrm{L}}\right) \tag{3}$$

Once the above equations are obtained, equivalent spring stiffness kd can be computed from:

$$k_d = \omega^2 M_1 \tag{4}$$

2.2. TLD-Structure Interaction Model

Considering an n-story MDOF linear building structure with a mass damper installed at the top floor, the equation of motion of the combined system subjected to ground acceleration can be written as:

$$\boldsymbol{M\ddot{X}}(t) + \boldsymbol{C\dot{X}}(t) + \boldsymbol{KX}(t) = -\boldsymbol{m}\ddot{x}_g(t) \tag{5}$$

where **X** is the (n+1)-dimensional response vector denoting the relative displacement with respect to the ground; $\ddot{x}_g$is the ground acceleration; **M**, **C**, and **K** are (n+1 x n+1)-dimensional positive-definite matrices corresponding to the mass, viscous damping, and the stiffness of the structure, respectively. More specifically they can be written as follows:

$$\boldsymbol{m} = [\mathrm{m}_1, \mathrm{m}_2, \ldots, \mathrm{m}_\mathrm{n}, \mathrm{m}_\mathrm{d}]^\mathrm{T} \tag{6}$$

$$\mathbf{X}(\mathrm{t}) = [\mathrm{x}_1, \mathrm{x}_2, \ldots, \mathrm{x}_\mathrm{N}, \mathrm{x}_\mathrm{d}]^\mathrm{T} \tag{7}$$

$$\mathbf{M} = \begin{bmatrix} \mathrm{m}_1 & & & & \\ & \mathrm{m}_2 & & 0 & \\ & & \cdot & & \\ & & & \cdot & \\ & 0 & & \mathrm{m}_\mathrm{n} & \\ & & & & \mathrm{m}_\mathrm{d} \end{bmatrix} \tag{8}$$

$$\boldsymbol{C} = \begin{bmatrix} (\mathrm{c}_1 + \mathrm{c}_2) & -\mathrm{c}_2 & & & \\ -\mathrm{c}_2 & (\mathrm{c}_2 + \mathrm{c}_3) & -\mathrm{c}_3 & 0 & \\ & -\mathrm{c}_3 & \cdot & \cdot & \\ & & \cdot & \cdot & -\mathrm{c}_\mathrm{n} \\ & 0 & & -\mathrm{c}_\mathrm{n} & (\mathrm{c}_\mathrm{n} + \mathrm{c}_\mathrm{d}) & -\mathrm{c}_\mathrm{d} \\ & & & & -\mathrm{c}_\mathrm{d} & \mathrm{c}_\mathrm{d} \end{bmatrix} \tag{9}$$

$$\boldsymbol{K} = \begin{bmatrix} (k_1 + k_2) & -k_2 & & & \\ -k_2 & (k_2 + k_3) & -k_3 & 0 & \\ & -k_3 & \cdot & \cdot & \\ & & \cdot & \cdot & -k_n \\ & 0 & & -k_n & (k_n + k_d) & -k_d \\ & & & & -k_d & k_d \end{bmatrix} \tag{10}$$

where, mi is the mass of i th floor; md is the mass of the damper; ci is the damping of the i th floor; cd is the damping of the damper; ki is the stiffness of i th floor; kd is the stiffness of the damper; xi is the displacement of i th floor relative to ground; xd is the displacement of the damper relative to ground. The equation of motion can then be converted to a state-space equation as:

$$\dot{\boldsymbol{Z}} = \boldsymbol{A}\boldsymbol{Z} + \boldsymbol{H}\ddot{x}_g(t) \tag{11}$$

Where

$$\boldsymbol{Z}(t) = \begin{bmatrix} \boldsymbol{X}(t) \\ \dot{\boldsymbol{X}}(t) \end{bmatrix}; \boldsymbol{A} = \begin{bmatrix} \boldsymbol{0} & \boldsymbol{I} \\ -\boldsymbol{M}^{-1}\boldsymbol{K} & -\boldsymbol{M}^{-1}\boldsymbol{C} \end{bmatrix}; \boldsymbol{H} = \begin{bmatrix} \boldsymbol{0} \\ \boldsymbol{M}^{-1}\boldsymbol{m} \end{bmatrix} \tag{12}$$

By transforming the equation of motion to the state space equation, the second-order differential equation is transformed to the first-order one. In this case, the transfer function is given by:

$$\boldsymbol{G}(i\omega) = \boldsymbol{C}_\boldsymbol{y}(i\omega\boldsymbol{I} - \boldsymbol{A})^{-1}\boldsymbol{H} \tag{13}$$

where $\mathbf{C}_\mathbf{y}$ is the 2x(n+1)-dimensional output matrix; $\mathbf{I}$ is the identity matrix and ω is the circular frequency argument.

2.3. ABC Optimization Algorithm

In this study, Artificial Bee Colony (ABC) optimization algorithm [18] is used to find optimal parameters of the TLD system. ABC algorithm is a swarm-based meta-heuristic optimization algorithm inspired by the intelligent foraging behavior of honey bees. ABC is

utilized in the optimization of Multiple Tuned Mass Dampers and proved to be powerful enough to handle a large number of design variables [19].

In ABC, a colony of artificial forager bees (agents) searches for rich artificial food sources (good solutions for a given problem). The colony contains three groups of bees: employed bees associated with specific food sources, onlooker bees watching the dance of employed bees within the hive to choose a food source, and scout bees searching for food sources randomly [20].

In the initial stage, scout bees discover all food source positions. Each food source xi,j is a solution vector to the optimization problem and the nectar amount of a food source corresponds to the quality (fitness) of the associated solution.

$$x_{i,j} = x_j^{min} + rand(0,1)(x_j^{max} - x_j^{min}) \tag{14}$$

where i = 1.SN, and j = 1..D. SN indicates the number of solutions and the number of parameters is presented as D.

In the employed bee stage, employed bees search for new food sources. They find a neighbor food source vi and then assess its fitness by the function given in Eq. 15.

$$v_{i,j} = x_{i,j} + \emptyset_{ij}\,(x_{j,j} - x_{k,j}) \tag{15}$$

where x_k is a randomly selected food source, j is a random index number within the limits of [1, D], $\emptyset_{i,j}$ is a uniformly distributed random number in the range [-1, 1]. The fitness value of the solution is calculated by:

$$fitness_i = f(x) = \{1 + abs(f_i), \qquad if\ x < 0\ 1\ /\ (1 - f_i), \qquad if\ x \geq 0 \tag{16}$$

where f_i is the cost function to a given the solution vi. Employed bees share their food source information with onlooker bees waiting in the hive and depending on this information, onlooker bees probabilistically choose their food sources based on the roulette wheel selection method. The probability value is calculated by:

$$p_i = fitness_i / \sum_{i=1}^{SN} fitness_i \tag{17}$$

Once the onlooker bees probabilistically chose a food source x_i, a neighboring food source v_i is determined and its fitness value is calculated. Employed bees whose solutions cannot be improved through a predetermined number of trials become scouts. The converted scouts start to search for new solutions, randomly.

In this study tank dimensions are kept fixed, thus water depth is the optimization parameter. For a possible water depth and fixed tank dimensions, a total water mass is obtained. Through Eqs. (1)-(4) stationary fluid mass M_0, oscillating fluid mass M_1, natural sloshing frequency ω, and equivalent spring stiffness k_d are calculated. Then mass, damping, and stiffness matrices are calculated by Eqs. (8)-(10). The state-space equation is then constructed by Eq. (12) and the transfer function is obtained by Eq. (13). The best possible solution is obtained by minimizing H2 norm of the transfer function. It is possible to adjust TLD mass/structure mass ratio by just varying tank width which does not affect sloshing frequency.

3. Experimental Setup

3.1. Shake Table

Servo motor driven small-scale shake table used in this study has a 50 kg work capacity and is capable of producing ±2g acceleration in one horizontal axis. The embedded PID controller makes it possible to simulate sinusoidal motions, real earthquake motions, and user-controlled movements (arbitrary waveforms). Roof displacements are measured via a laser displacement sensor.

3.2. Test Structure and System Matrices

The test structure is made of two steel plate walls connected with a steel plate deck on roof level (Fig. 1. a). Plate wall height is 140 cm, length is 35 cm, and thickness is 0.29 cm. Plate deck dimensions are 35 x 35 cm, and thickness is 1cm which provides the structure mass. According to free vibration analysis, the fundamental period of the structure is 0.82 sec (1.234 Hz) and the damping ratio calculated is 2% according to the logarithmic decrement method as described by Chopra [21].

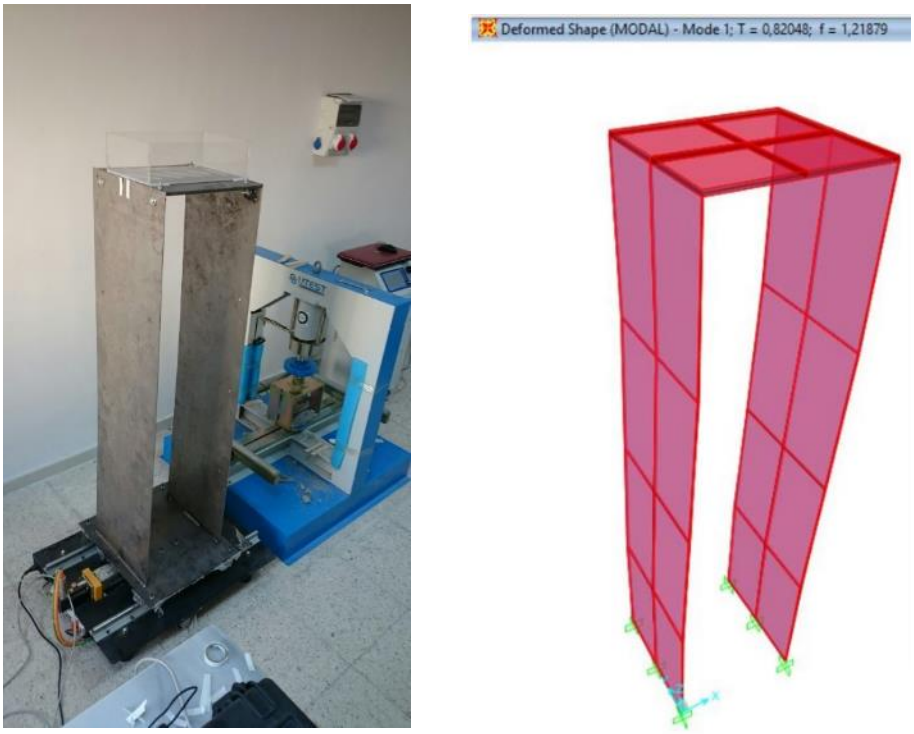

(a) (b)

Fig. 1 a) Test Structure b) 1. Modal Shape of Numerical Model

The numerical model of the test structure is constructed with SAP 2000 [22]. Plate walls and roof deck are modeled with shell elements. Rigid connection is assumed between plate walls and base plate, between plate walls and roof deck (Fig. 1 b). The estimated fundamental period is 0.72 sec in this case which indicates the rigid connection assumption is not truly valid. Thus Elasticity Modulus of steel is calibrated to match the fundamental periods of the numerical model and experimental findings. The mass, stiffness, and damping matrices of the calibrated model are given as:

$$\boldsymbol{M} = diag[5.5764,5.5764,5.5764,12.404] * 10^{-3}\text{ton} \quad (18)$$

$$\boldsymbol{K} = \begin{bmatrix} 105.59 & -67.87 & 29.10 & -7.27 \\ -67.87 & 84.84 & -67.77 & 25.35 \\ 29.10 & -67.77 & 106.03 & -60.08 \\ -7.27 & 25.35 & -60.08 & 40.17 \end{bmatrix} \text{kN / m} \quad (19)$$

$$\boldsymbol{C} = \alpha M + \beta K \quad (20)$$

α and β are Rayleigh coefficients and are calculated as α=0.2656 and β=6.94*10^{-4} for damping ratio %2 of first and second vibration periods of the structure.

3.3. Optimal TLD Parameters

A fiberglass tank with a length of 25 cm and a width of 20 cm is used as a TLD unit. The calculated optimal water depth is 3.1 cm which corresponds to the 0.12 water depth/tank length ratio. In this case, calculated stationary fluid mass, M_0 is 0.22 kg, oscillating fluid mass M_1 is 1.23 kg which corresponds to 4.1% of the total structural mass, and natural sloshing frequency ω is 0.92 Hz (1.087 sec).

4. Experimental Findings

4.1. Frequency Sweep Analysis

Frequency sweeps are conducted, in which the structure is excited at 17 discrete frequencies in the range of 0.8 to 1.2 times of fundamental structural frequency at a constant displacement amplitude. The system is excited for 10 cycles with an amplitude of 10 mm, and data is recorded until a steady-state condition is attained. A total of two frequency sweep tests are conducted which consider the structure with TLD (controlled) and without TLD (uncontrolled) settings.

Frequency response curves of both controlled and uncontrolled structures are constructed to show the roof displacement at each excitation frequency (Fig. 2). The roof displacement and excitation frequency are normalized by the maximum roof displacement and the fundamental natural frequency of the uncontrolled structure respectively.

Roof displacement time history plots are given in Figs. 3-5 for excitation frequencies of 0.8, 1, and 1.2 times the fundamental frequency of the uncontrolled structure respectively.

It should be noted from Fig. 2 that there is a slight shift (-2.5%) in the resonance frequency of the uncontrolled structure concerning the natural frequency identified from free vibration results. This is probably due to the loosening of connection bolts at 13% roof drift demands corresponding to the resonance frequency. It is observed that when a structure is equipped with TLD, additional water mass present in the water tank causes a further -5% frequency shift in the first mode frequency concerning uncontrolled structure.

When normalized roof displacements are considered, maximum efficiency is obtained when the structure is excited with a resonant frequency. In this case reduction in max roof displacement of the controlled structure is 55% with respect to uncontrolled structure. The primary means of energy dissipation seem to be strong wave breaking and wave-to-wall interactions. Displacement peaks take place at different frequencies for controlled and uncontrolled structures. Thus, when the entire frequency range is considered, the reduction in max roof displacement of the controlled structure is 37% with respect to uncontrolled structure.

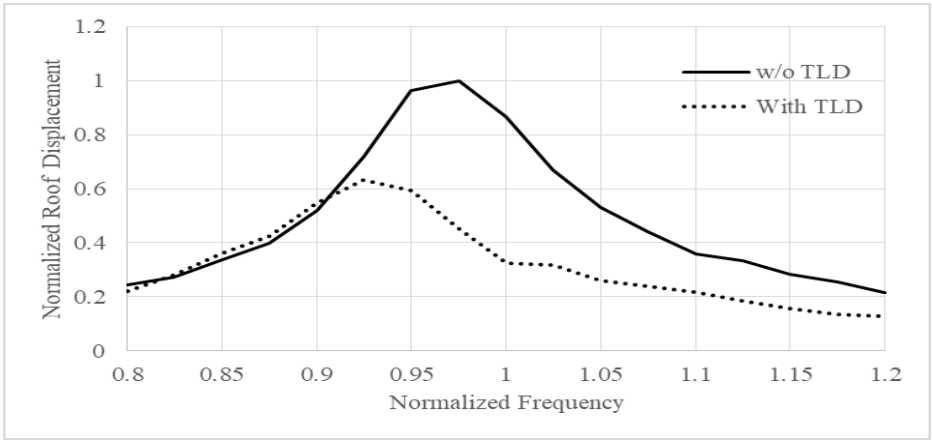

Fig. 2 Frequency Response Curves of Structure With and Without TLD Settings

At a normalized frequency range of 0.8 to 0.9, TLD is not effective in reducing roof displacement. At this low frequency (high period) range, due to low excitation acceleration almost linear single-mode wave formation and weak wave breaking is observed. At high frequency (short period) range, on the other hand, TLD is still effective probably due to high excitation acceleration. At a normalized frequency range of 1.1 to 1.2, multi-mode wave formation and strong wave breaking are observed.

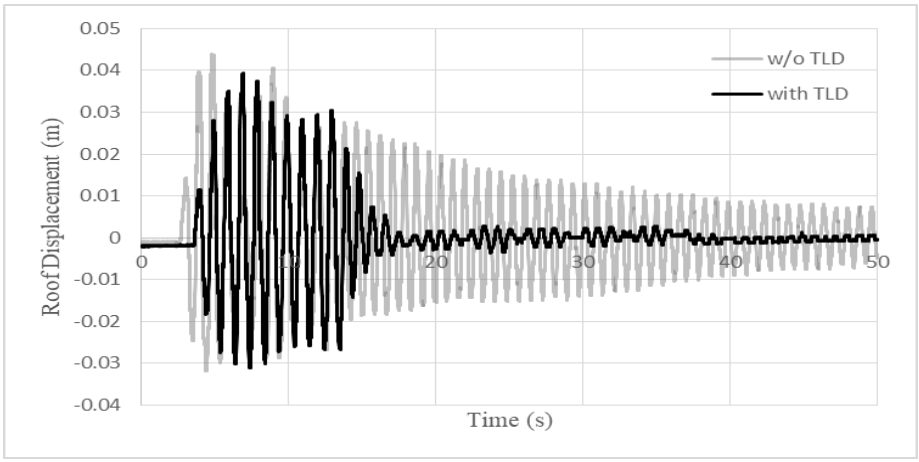

Fig. 3 Displacement Time History, Excitation Frequency is 0.8 Times Fundamental Natural Frequency

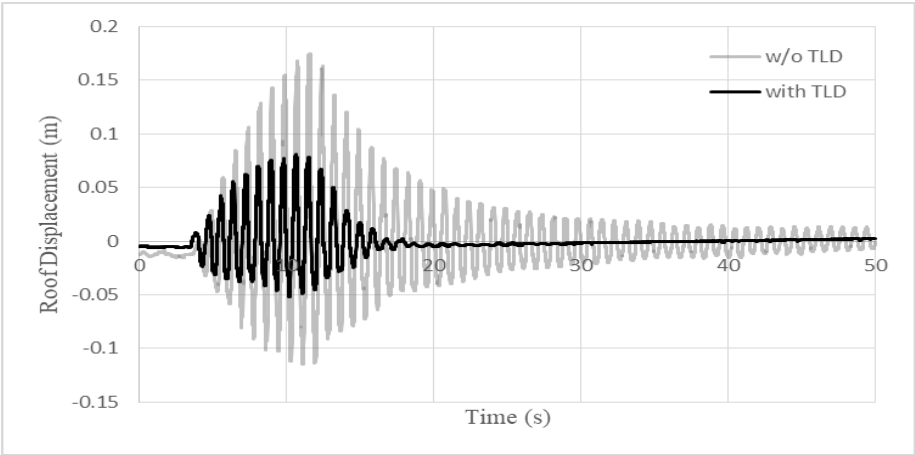

Fig. 4 Displacement Time History, Excitation Frequency is 1.0 Times Fundamental Natural Frequency

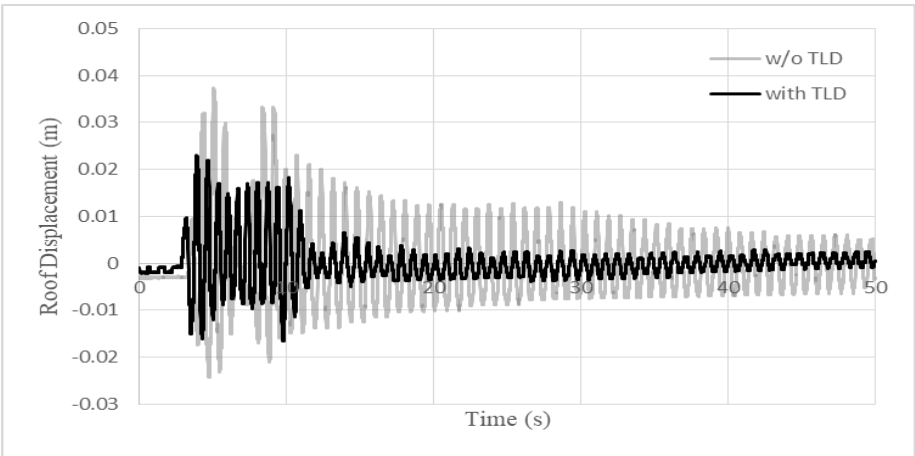

Fig. 5 Displacement Time History, Excitation Frequency is 1.2 Times Fundamental Natural Frequency

As can be seen from Figs. 3-5 the decay of motion of the controlled structure is fast at post excitation stage. The effective damping ratios are calculated to be 7.5%, 7.1%, and 11% corresponding to excitation frequencies of 0.8, 1, and 1.2 times the fundamental frequency of the uncontrolled structure respectively.

4.1. Response to Earthquake Ground Motions

Both controlled and uncontrolled structures are tested with different seismic records (Fig. 6) to better evaluate the performance of TLD under earthquake excitation. The seismic records are scaled in order not to exceed the stroke limit of the shake table. Scaling factors are 0.66, 1, 0.91, and 0.23 and Peak Ground Acceleration values are 0.218 g, 0.367 g, 0.315 g, and 0.144 g for El Centro, Loma Prieta, Kobe, and Sakarya records respectively.

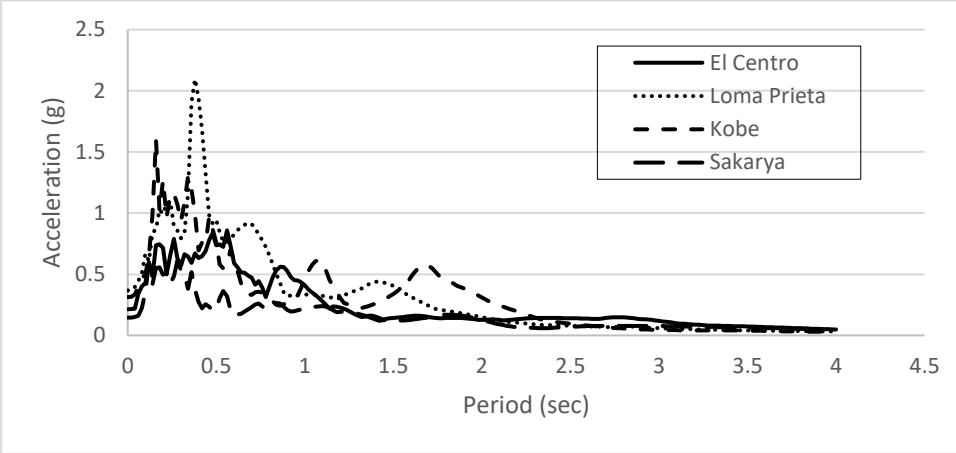

Fig. 6 %2 Damped Acceleration Response Spectra of Seismic Records

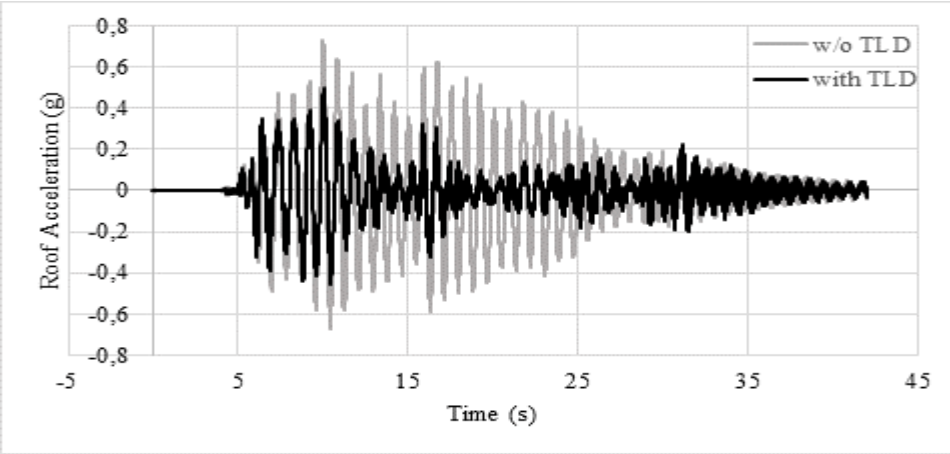

Fig. 7 Acceleration Time History, El Centro Earthquake

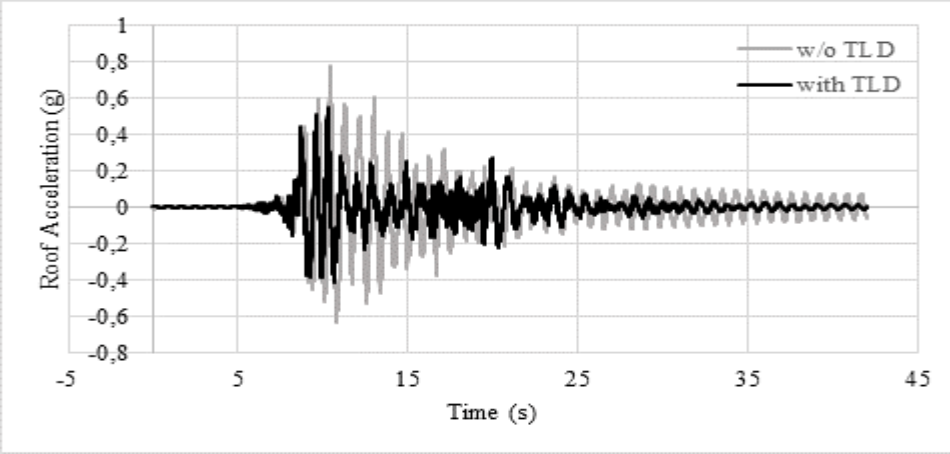

Fig. 8 Acceleration Time History, Kobe Earthquake

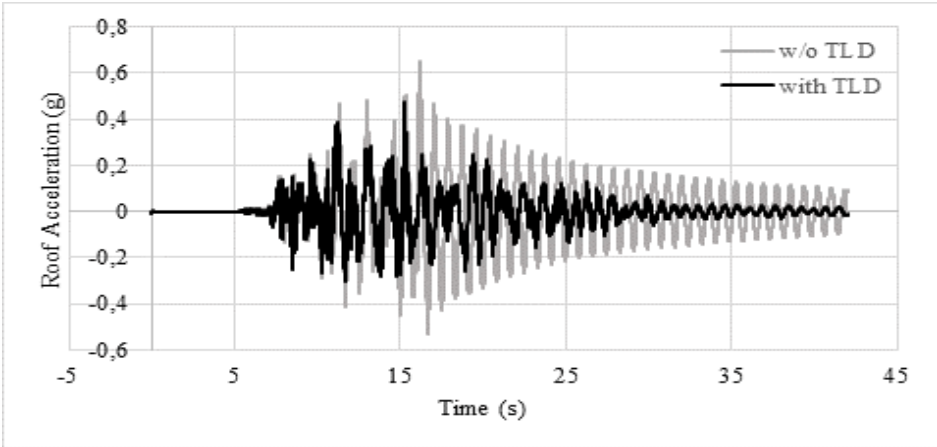

Fig. 9 Acceleration Time History, Loma Prieta Earthquake

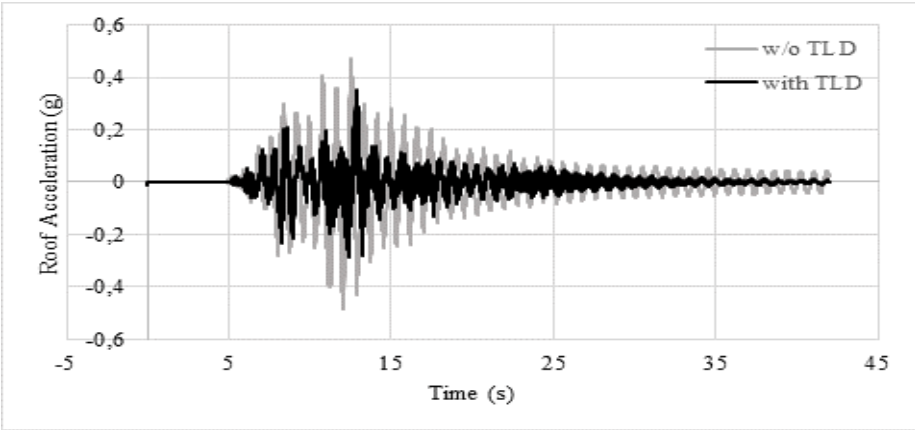

Fig. 10 Acceleration Time History, Sakarya Earthquake

Both controlled and uncontrolled structures are excited with El Centro, Loma Prieta, Kobe, and Sakarya earthquakes and roof accelerations are compared respectively in Figs. 7-10 and Table 1. RMS in Table 1 is the root mean square response of the system and can be interpreted as the energy of the response.

Table 1. Roof Acceleration and RMS comparison

Record	Roof Acceleration [g]		Change	RMS (g)		Change
	w/o TLD	with TLD	(%)	w/o TLD	with TLD	(%)
El Centro	0.73	0.49	32.01	0.218	0.107	50.92
Loma Prieta	0.77	0.55	28.57	0.145	0.081	44.14
Kobe	0.65	0.47	27.69	0.145	0.076	47.59
Sakarya	0.48	0.35	26.74	0.094	0.045	52.13

It can be seen from Fig. 2 that the natural frequency of the controlled structure is 0,925*1,234=1.14 Hz (T=0.88 sec). At that period, corresponding spectral accelerations are 0.56 g, 0,35 g , 0.26 g, and 0.23g (Fig. 6) for El Centro, Loma Prieta, Kobe, and Sakarya earthquakes respectively.

During the tests, it is observed that, when the dominant part of the El Centro and Loma Prieta earthquakes hits the structure, strong wave breaking and multi-mode wave formations occur which are the primary means of energy dissipation in the TLD unit. Although the equivalent mechanical model is not suitable for estimating the complex nature of nonlinear water sloshing, an excessive amount of wave-to-wall interactions seems to dissipate energy especially in the dominant part of ground motion. Thus the change in roof acceleration of the controlled structure with respect to uncontrolled one is relatively higher in these earthquake records. Spectral accelerations corresponding to the dominant vibration period of the controlled structure (Fig. 6) might also be evidence of this since the higher the spectral acceleration, the higher reduction in response is obtained (Table 1).

On the other hand, dissipated energy through the entire time range is best at the Sakarya earthquake which has the lowest spectral acceleration. Due to the low excitation amplitudes of Sakarya and Kobe earthquakes, it is observed weak wave breaking and almost linear sloshing behavior. Thus one possible explanation might be, TLD sloshing dynamics are well estimated by the equivalent mechanical model and optimal solution conditions are met.

5. Conclusions

Equivalent mechanical model derivations are based on linear sloshing of water mass, which is possible when the water depth/tank length ratio is high and excitation amplitude is low. On the other hand, when water depth/tank length is low, a larger volume of water sloshes without contributing significantly to the overall inertia of the system which enhances the TLD effectiveness greatly. However, at this point, the nonlinear nature of the sloshing fluid makes it challenging to construct a reliable model. In this study validity of the equivalent mechanical model is investigated when large amplitude vibrations and low water depth/tank length ratios present.

As a primary energy dissipation mechanism, strong wave breaking and wave-to-wall interactions occur at high structural displacements and accelerations. Thus TLD is more effective when the structure is excited with a resonant frequency. In this case reduction in max roof displacement of the controlled (with TLD) structure is 55% with respect to uncontrolled (without TLD) structure. When the entire frequency range is considered, however, the reduction in max roof displacement of the controlled structure is 37% with respect to uncontrolled structure. The effectiveness is reduced for low frequency and high-frequency excitations but still, TLD provides a high damping and fast decay of motion when compared to uncontrolled case.

When it comes to seismic excitations, strong vibrations (0.35 -0.55 g accelerations) reason to strong wave breaking and wave-to-wall interactions. Thus dissipated energy is higher leading to better control in max roof acceleration. On the other hand, medium vibrations (0.20 – 0.25 g accelerations) cause almost linear sloshing behavior so this optimal solution condition leads to better control in total energy of the response.

It can be concluded that a simplified mechanical model can be a good starting point in the optimization of shallow depth TLD. Even if sloshing is not linear thus estimated control parameters varied due to shifting of sloshing frequency, the dissipated energy through nonlinear behavior is satisfactory to enable a sound control.

It seems that inherent damping ratio of the water is underestimated in Eurocode 8 [14] when excitation amplitudes are high. This can be considered in future work.

Acknowledgement

The authors acknowledge that this study is supported by TUBITAK (Grant 2209-A 1919B011702712). The author would like to thank Mr. Halil Avcıoğlu for his technical assistance during shake table experiments.

References

[1] Bauer HF, Fluid Oscillations in The Containers of a Space Vehicle and Their Influence upon Stability, Report NASA TR R-187, 1964.
[2] Modi VJ, Welt F. Damping of wind induced oscillations through liquid sloshing, Journal of Wind Engineering and Industrial Aerodynamics, 1988; 30: 85-94. https://doi.org/10.1016/0167-6105(88)90074-8
[3] Fujii K, Tamura Y, Sato T, Wakahara T. Wind-induced vibration of tower and practical applications of Tuned Sloshing Damper, Journal of Wind Engineering and Industrial Aerodynamics, 1990; 33: 263-272. https://doi.org/10.1016/0167-6105(90)90042-B
[4] Kareem A. Reduction of Wind Induced Motion Utilizing a Tuned Sloshing Damper, Journal of Wind Engineering and Industrial Aerodynamics, 1990; 36: 725-737. https://doi.org/10.1016/0167-6105(90)90070-S
[5] Sun LM, Fujino Y, Pacheco BM, Chaiseri P. Modeling of Tuned Liquid Damper (TLD), Journal of Wind Engineering and Industrial Aerodynamics, 1992; 41: 1883-1894. https://doi.org/10.1016/0167-6105(92)90609-E
[6] Wakahara T, Ohyama T, Fujii K. Suppression of Wind-Induced Vibration of a Tall Building using Tuned Liquid Damper, Journal of Wind Engineering and Industrial Aerodynamics, 1992; 41: 1895-1906. https://doi.org/10.1016/0167-6105(92)90610-M
[7] Koh CG, Mahatma S, Wang CM. Theoretical and experimental studies on rectangular tuned liquid dampers under arbitrary excitations, Earthquake Engineering and Structural Dynamics, 1994; 23: 17-31. https://doi.org/10.1002/eqe.4290230103
[8] Reed DA, Yu J, Yeh H, Gardarsson S. Investigation of tuned liquid dampers under large amplitude excitation, Journal of Engineering Mechanics ASCE, 1998; 124(4): 405-413. https://doi.org/10.1061/(ASCE)0733-9399(1998)124:4(405)
[9] Banerji P, Murudi A, Shah AH, Poppelwell N. Tuned liquid dampers for controlling earthquake response of structures, Journal of Earthquake Engineering and Structural Dynamics, 2000; 29: 587-602. https://doi.org/10.1002/(SICI)1096-9845(200005)29:5<587::AID-EQE926>3.0.CO;2-I
[10] Tait MJ, Isyumov N, El Damatty AA. Effectiveness of a 2D TLD and its numerical modelling, Journal of Structural Engineering, 2007; 133(2): 251-263. https://doi.org/10.1061/(ASCE)0733-9445(2007)133:2(251)
[11] Malekghasemi H, Ashasi-Sorkhabi A, Ghaemmaghami A, Mercan O. Experimental and numerical investigations of the dynamic interaction of tuned liquid damper-structure systems, Journal of Vibration and Control, 2015; 21(14): 2707-2720. https://doi.org/10.1177/1077546313514759
[12] Pabarja A, Vafaei M, Alih SC, Yatim MY, Osman SA. Experimental study on the efficiency of tuned liquid dampers for vibration mitigation of a vertically irregular structure, Mechanical Systems and Signal Processing, 2019; 114: 84-105. https://doi.org/10.1016/j.ymssp.2018.05.008
[13] Marsh A, Prakash M, Semercigil E, Turan ÖF. A numerical investigation of energy dissipation with a shallow depth sloshing absorber, Applied Mathematical Modelling, 2010; 34: 2941-2957. https://doi.org/10.1016/j.apm.2010.01.004
[14] Eurocode 8, Part 4. Design of Structures for earthquake resistance, Silos, tanks and pipelines, EN 1998-4, 2006.

[15] Ozsariyildiz SS, Bozer A. Finding optimal parameters of tuned mass dampers, Structural Design of Tall and Special Buildings, 2015; 24(6): 461-475. https://doi.org/10.1002/tal.1174
[16] Love JS, Tait MJ. Parametric depth ratio study on tuned liquid dampers: Fluid modelling and experimental work, Computers and Fluids, 2013; 79: 13-26. https://doi.org/10.1016/j.compfluid.2013.03.004
[17] Housner GW. Dynamic pressure on accelerated containers, Bulletin of the Seismological Society of America, 1957; 47 (1): 15-35.
[18] Karaboga D. An Idea Based On Honey Bee Swarm for Numerical Optimization, Technical Report TR06, Erciyes University, 2015.
[19] Bozer A, Özsarıyıldız SS. Free parameter search of multiple tuned mass dampers by using artificial bee colony algorithm, Structural Control and Health Monitoring, 2018; 25, e2066. https://doi.org/10.1002/stc.2066
[20] Akay B, Karaboga D. A modified Artificial Bee Colony algorithm for real-parameter optimization. Information Sciences, 2012; 192: 120-142. https://doi.org/10.1016/j.ins.2010.07.015
[21] Chopra AK. Dynamics of Structures: Theory and Applications to Earthquake Engineering, 3rd edition Prentice Hall, New Jersey, USA, 2007.
[22] SAP 2000. Structural Software for Analysis and Design, Computers and Structures Inc., Berkeley, USA, 2016.

Research on Engineering Structures & Materials
journal homepage: http://jresm.org
Research Group

Research Article

Investigation of the effects of bolt diameter and end-plate thickness on the capacity and failure modes of end-plated beam-to-column connections

Yasin Onuralp Özkılıç

Department of Civil Engineering, Necmettin Erbakan University, Konya, Turkey.

Article Info

Article history:
Received 15 Mar 2021
Revised 17 Apr 2021
Accepted 16 May 2021

Keywords:
End-plate; Beam-to-column connections; Eurocode; Finite Element Method

Abstract

End-plated connections are frequently preferred in beam-to-column connections due to their advantages of high quality and fast assembly. The capacity of the end-plated connections depends on many parameters including the thickness of end-plate and bolt diameter. A comprehensive numerical parametric study was conducted in order to investigate the effects of these parameters on the capacity of the end-plated connections using the finite element tool, ABAQUS. The results of the numerical study were compared with the prediction of Eurocode provision in terms of the capacity and failure mode. The results showed that Eurocode accurately captures the failure modes and predicts the capacity of the connection except for thin plates with high accuracy. However, Eurocode provision significantly underestimated the capacity of the thin-plated extended end-plated connections.

1. Introduction

The provisions require that seismic resisting structures should provide sufficient ductility in order to prevent catastrophic failure [1-4]. Welded moment connections exhibited insufficient performance at the 1994 Northridge and 1995 Kobe earthquakes, which resulted in brittle failures. This leads to an increase in the demand for end-plated connections. Compared to welded moment connections, the end-plated connections provide prompt, high quality and economical construction. However, many variables including bolt diameter, thickness of end-plate, yield and ultimate strength of end-plate, bolt configuration, bolt grade, stiffening and the dimensions of beam and column affect the resistance of the end-plate connection. Therefore, more attention is required to calculate the capacity of the end-plated connections.

The end-plated connections can be categorized as flush end-plated connections and extended end-plated connections. The extended end-plated connections are utilized as moment connections and divided into two categories depending on the presence of stiffeners: unstiffened and stiffened extended end-plated connections. The unstiffened extended end-plated connection is shown in Fig. 1.

Corresponding author: yozkilic@erbakan.edu.tr
orcid.org/0000-0001-9354-4784
DOI: http://dx.doi.org/10.17515/resm2021.275st0315

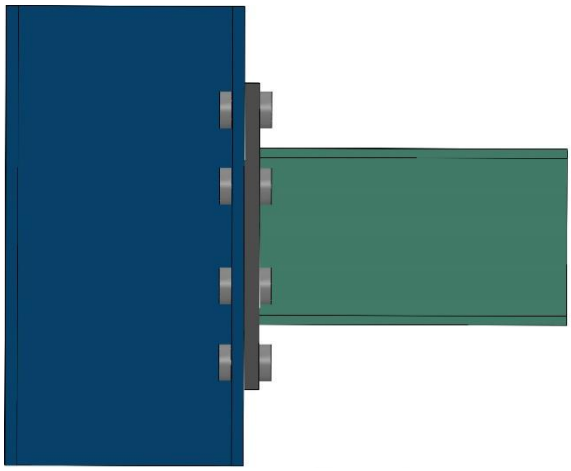

Fig. 1 Extended End-plated Connections

The tension zone of the extended end-plated connections can be idealized by equivalent T-stubs. The behavior of four bolted unstiffened connections can be examined with an unstiffened T-stub (Fig. 2). Eurocode (EC3) [5] utilizes equivalent T-stubs to compute the capacity of the end-plated connections (the details are provided in the following section).

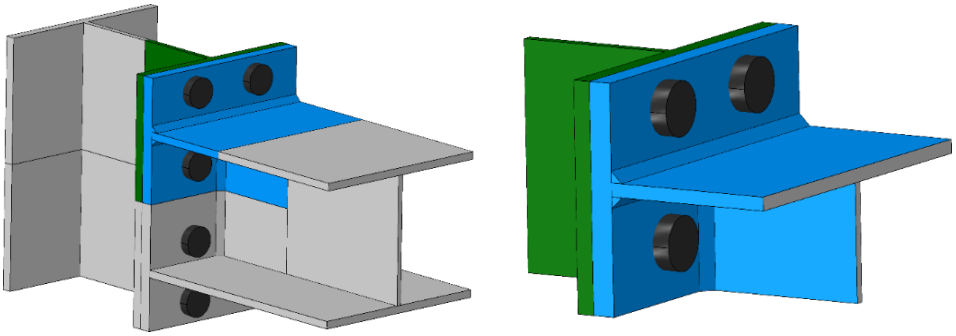

Fig. 2 The idealization of T-stubs

These connections are generally utilized in moment resisting frames as a beam-to-column connection. Moreover, the end-plated connections are also preferred in replaceable fuses in both moment resisting frames [6-9] and eccentrically braced frames [10-13]. The thickness of the end-plate plays a significant role in the weight of a member. Therefore, for replaceable fuses where light members are preferred, the thickness of the end-plate should be correctly designed in order to minimize the weight of the fuse member.

Ng et al. [14] tested six end-plated connections having different thickness of end-plates. The specimens were monotonically loaded up to failure. The results revealed that Eurocode 3 underestimates the ultimate moment capacity of the end-plated connections for all specimens. Yorgun [15] conducted an experimental study including three specimens under cyclic loading. It was indicated that Eurocode 3 showed conservative results compared to the experimental findings. Abidelah et al. [16] tested four extended end-plated connections under monotonic loading. The experimental findings demonstrated that Eurocode 3 gives safe proposals of the moment capacity of the extended end-plated connections. Coelho et al. [17] stated that the prediction of Eurocode 3 gives safe approaches based on the results of eight experimented specimens having extended end-

plated connections. Zue et al. [18] conducted an experimental program including 13 specimens having extended end-plate connections. It was emphasized that Eurocode 3 underestimated the ultimate capacity by 41-45%.

Özkılıç and Topkaya [19] collected the results of end-plated specimens from literature and compared with the prediction of Eurocode provision. It was reported that the difference between the experimental results and predicted value reached ratios of 1.73 and 3.0 for plastic and ultimate moment capacities, respectively. Apart from the studies of extended end-plated connections, the studies [20-25] conducted for T-stub joints revealed that the Eurocode also underestimates the resistance of T-stub joints.

In this study, the prediction of Eurocode 3 for unstiffened end-plated connections was evaluated using numerical analysis. A parametric study was conducted to further investigate the conservative prediction of Eurocode 3. Furthermore, failure modes obtained from numerical analysis are compared with the prediction of Eurocode 3.

2. The European Provisions

EN1998-1 [26] provides the design procedure of beam-to-column connections in moment resisting frames while EN1993-1-8 [5] provides the required calculations for designing joints. The component methods were adapted by Eurocode provisions to calculate the resistance of the bolted end-plated connections. In this method, the strengths of individual failure modes are computed.

Three different failure modes including complete flange yielding, flange yielding with bolt failure and bolt failure [27, 28] can develop on the T-stubs where the tension of the end-plated connection can be idealized. The first failure mode is a ductile behavior that resulted due to significantly large plastic deformation of the T-stub flange. This is achieved by forming plastic hinges in the flange of the T-stub. Unlike the first failure mode, limited ductility occurs in the third failure mode and is associated with failure of the bolts in tension. On the other hand, the second failure mode is combined both bolt failure and flange yielding. These failure modes are illustrated in Fig. 3. The resistance of the T-stub is taken as the weakest of these failure modes, which exhibits the lowest capacity.

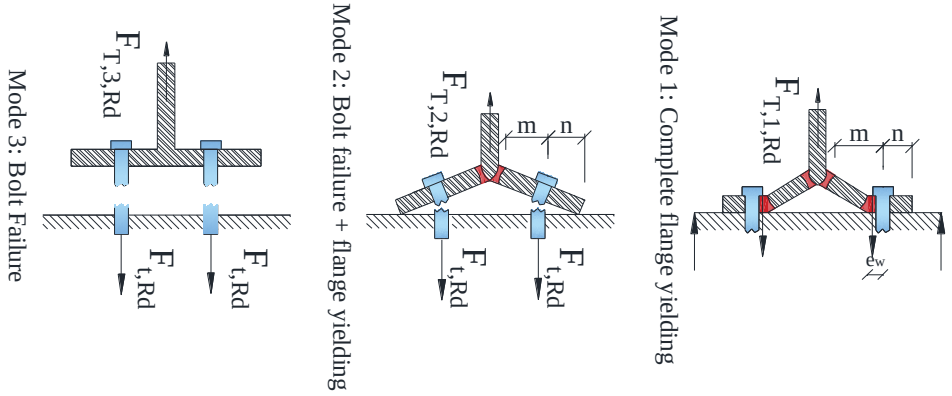

Fig. 3 Failure Modes of T-stub

The resistance of Failure Mode 1 can be computed by two different methods (Method 1 and Method 2). Method 1 assumes that the bolt forces concentrate on the centreline of the bolt. On the other hand, the effects of bolt/washer size are included in Method 2 which assumes that bolt forces are distributed under the washer/nut. In other words, Method 2 considers that the distance between two plastic hinges, which pass over the toe of the fillet

and next to the edges of the bolt row, are less than m. Therefore, it is expected that Method 2 results in a higher capacity than that of Method 1. These methods can be computed from the following equations [5].

Method 1:

$$F_{T,1Rd} = \frac{4M_{p,1Rd}}{m} \quad (1)$$

$$n = \min(e_x; 1.25m) \quad (2)$$

$$M_{p,1Rd} = 0.25 l_{eff,1} t_p^2 F_{yp} \quad (3)$$

Method 2:

$$F_{T,1Rd} = \frac{(32n - 2d_w)M_{p,1Rd}}{8mn - d_w(m+n)} \quad (4)$$

where d_w is diameter of washer, bolt head or nut, t_p is thickness of end-plate, e_x is the vertical edge distance for outside holes, m is the distance from the center of a bolt to fillet weld of flange. $l_{eff,1}$ is minimum of $l_{eff,cp}$ and $l_{eff,nc}$. $l_{eff,cp}$ is the length of the circular yield line pattern and $l_{eff,nc}$ is the length of the non-circular yield line pattern. Multiple yield line mechanisms depending on the geometry are available in P398 [29] . Individual or group yielding may occur relying on the gage distance (w). Fig. 4 illustrates the variables used in the calculation of end-plated connection capacity by Eurocode 3. Yield line mechanisms and their calculations for unstiffened end-plated connections are demonstrated in Figs. 5 and 6. Fig. 5(a) illustrates the defined parameters used in the calculations. Figs. 5(b-d) and Fig. 5(e-g) show circular and non-circular yield patterns for outer side of bolt (bolt row 1), respectively. On the other hand, Fig. 6 demonstrates the yield lines for inner bolt row (bolt row 2).

For Failure Mode 2:

$$F_{T,2Rd} = \frac{2M_{p,1Rd} + n2F_{T,Rd}}{(m+n)} \quad (5)$$

$$F_{T,Rd} = \frac{k_2 f_{ub} A_s}{\gamma_{M2}} \quad (6)$$

For Failure Mode 3:

$$F_{T,3Rd} = 2F_{t,Rd} \quad (7)$$

$$M_{p,2Rd} = 0.25 l_{eff,2} t_p^2 F_{yp} \quad (8)$$

where A_s is tensile stress are of a bolt, f_{ub} is the nominal ultimate strength of bolt, $l_{eff,2}$ is minimum of $l_{eff,nc}$. The minimum of these three failure modes is taken as the resistance of bolt row which should be calculated separately for each bolt row.

Resistance of bolt row 1 (bolt row above the top flange):

$$F_{t,1Rd} = \min(F_{T,R1d}; F_{T,R2d}; F_{T,R3d}) \quad (9)$$

Resistance of bolt row 2 (bolt row below the top flange):

$$F_{t,2Rd} = \min\left(F_{T,R1d}; F_{T,R2d}; F_{T,R3d}\right) \quad (10)$$

After calculating the design resistance of bolt rows, the design moment is calculated as follows:

$$M_{j,Rd} = h_1 F_{t,R1d} + h_2 F_{t,R2d} \quad (11)$$

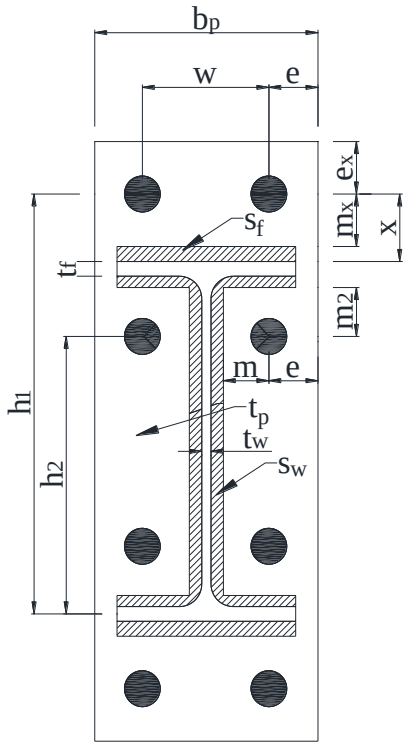

Fig. 4 Parameters used in Eurocode 3

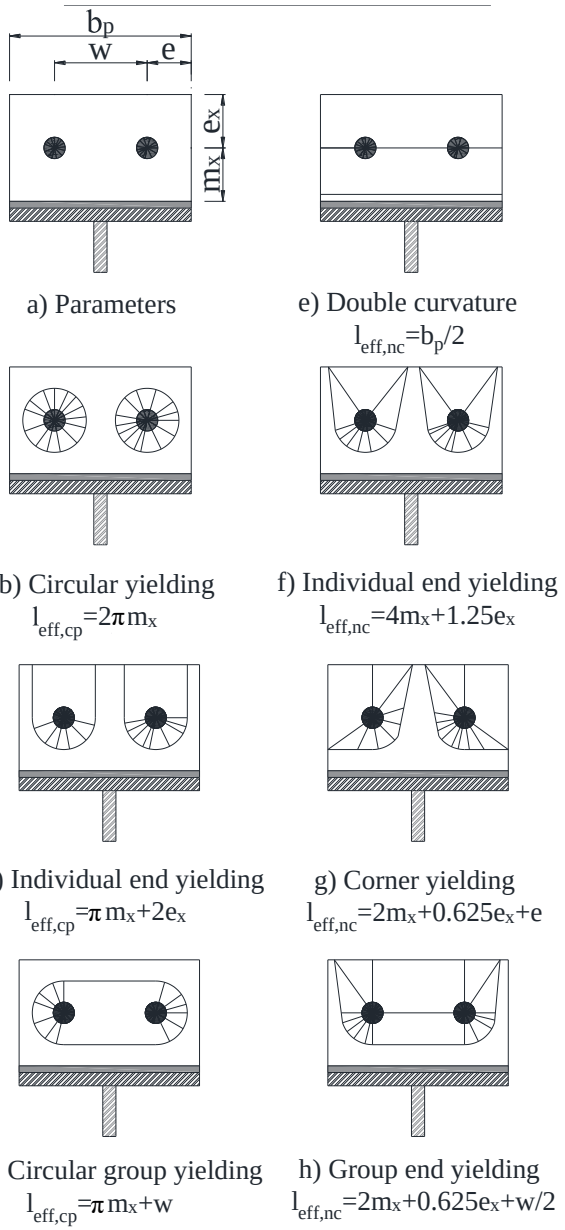

Fig. 5 Yield lines for outer bolt row

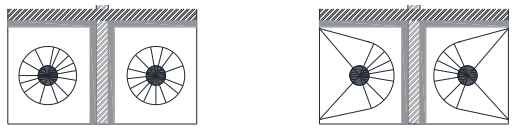

a) Circular yielding
$l_{eff,cp}=2\pi m$

b) Side yielding near beam or a stiffener
$l_{eff,nc}=\alpha m$

Fig. 6 Yield lines for inner bolt row

3. Numerical Study

A comprehensive numerical study was performed in order to investigate the effects of bolt diameter and end-plate thickness on the resistance and failure modes of extended end-plated connections. The numerical analyses were carried out using the finite element tool, ABAQUS. Three-dimensional elements were utilized to construct the models. The column was not modeled explicitly. Instead, a rigid flange was defined to simulate the connection between the column and beam.

Solid elements were utilized for all members. The element type of C3D8R was selected for all components. Fine mesh size was selected for the bolts, end-plate and welds whereas coarse mesh size was utilized for the beam. The selected mesh configuration is illustrated in Figure 7. In order to accurately simulate the bending behavior of the member, the thickness of members should be divided into at least four elements [6]. Therefore, 4 elements through the thickness of the end-plate and through the flanges and web of the beam were utilized.

Encastre boundary conditions were applied to the bottom of the rigid flange. The finite sliding surface to surface interaction was defined between end-plate and rigid flange, between bolts and rigid flange and between bolts and end-plate. The penalty method with a friction coefficient of 0.3 was applied for the tangential behavior. The bolts were pretensioned using Bolt-Load option. Both geometrical and material nonlinearities were implemented in the models. The loading was applied at the end of the beam. The beams were loaded up to 0.04 rad rotation since minumum rotation capacity of 0.035 rad rotation is required by Eurocode 8.

The welds were explicitly included in the models to simulate the behavior of the connection accurately. P398 [29] offers a simple solution for the thickness of the weld. 8 mm leg fillet welds for the entire web were utilized based on the recommendation of P398. On the other hand, the welds between the flange and end plate were designed as full strength. The strength of the weld was taken equal to the resistance of the tension flange. Based on the calculations, 10 mm leg fillet welds were utilized for both the tension and compression flanges.

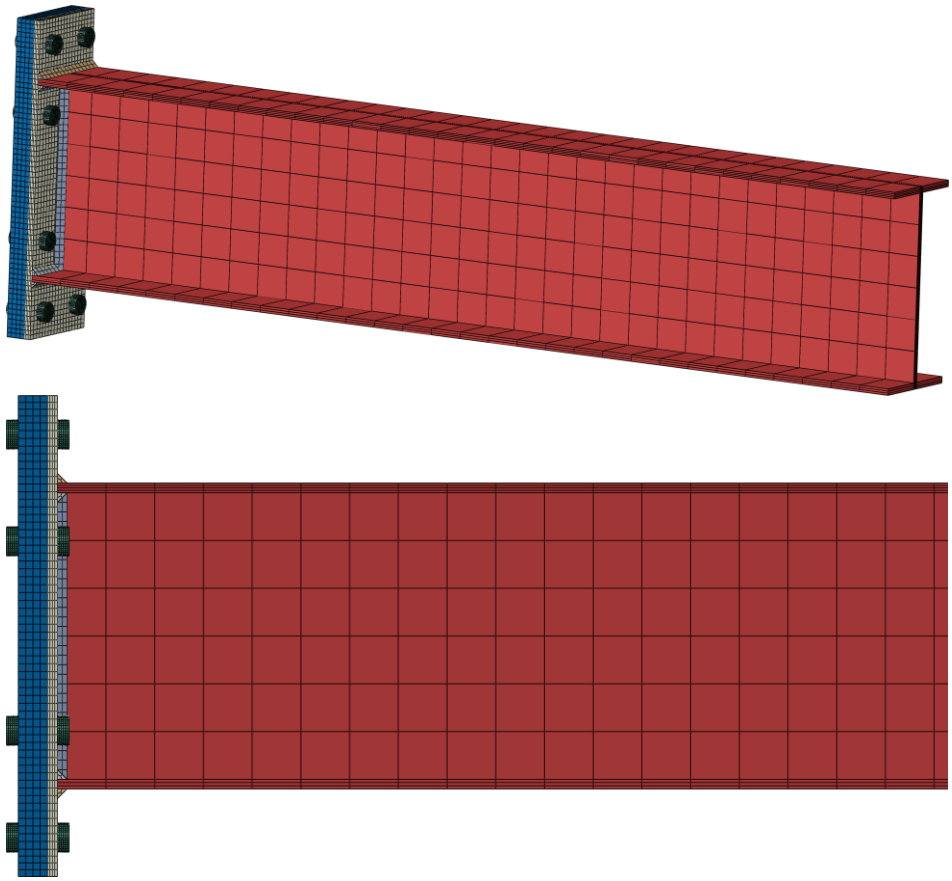

Fig. 7 Selected mesh configuration

The rigid flange was modeled as elastic. For material models of the end-plate and beam, the multilinear stress-strain curve developed by Yun and Gardner [30] was utilized. S275 and S420 were selected for material properties of the end-plate and beam, respectively. Young's modulus and Poisson's ratio were selected as 200 GPa and 0.3, respectively.

The assumptions utilized in the numerical study were verified using the study conducted by Qiang et al. [31]. Qiang et al. [31] monotonically tested specimens having extended end-plated connections. The beam utilized in the verification had the dimensions of 300, 180, 10 and 12 mm for depth, width, web thickness and flange thickness, respectively. A diameter of 27 mm and thickness of 12 mm was utilized for the bolts and end-plate. Fig. 8 compares the results of the numerical model and experimental findings. A difference of 5% was observed at the ultimate load. Moreover, the numerical model is slightly stiffer than the experimental results. This can be attributed to the rigid flange. It can be said that the numerical models are capable of predicting the behavior of the extended end-plate connections.

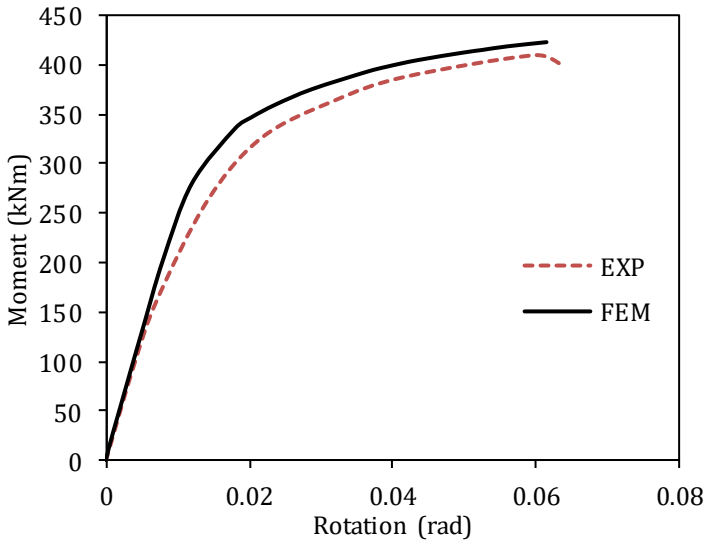

Fig. 8 The verification model

For the parametric study, the beam was selected for a typical beam section of European profiles which is approximately dimensions of IPE300 section since Eurocode provision is evaluated. The dimensions of the beam and end-plate are given in Table 1 and shown in Fig. 9. The selected parameters are shown in Table 2. Bolt diameters of 16 mm (M16), 20 mm (M20), 24 mm (M24), 27 mm (M27) and 30 mm (M30) and end-plate thickness (t_p) of 10 mm, 15 mm, 20 mm, 25 mm and 30 mm were selected as variables.

Table 1. The dimensions of the end-plate and beam

Variables	Value (mm)
b_f	150
b_p	150
w	90
m_2	40
m_x	40
e_x	40
s_w	8
t_w	8
s_f	10
t_f	10
h_1	360
h_2	250

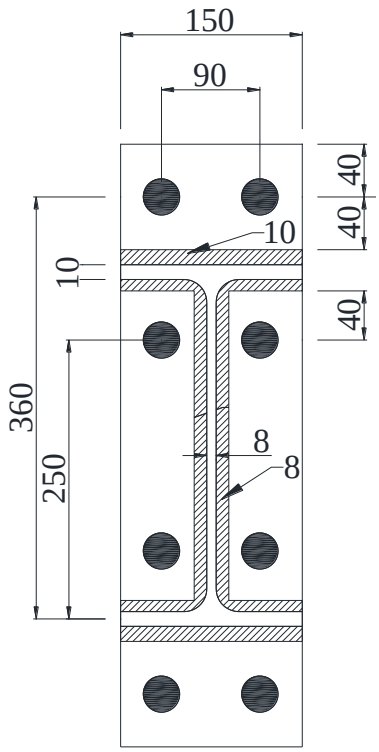

Fig. 9 The selected configuration

Table 2. The selected variables

Variables	Values				
Bolt Diameter (mm)	16	20	24	27	30
Thickness of End-plate (mm)	10	15	20	25	30

4. Results and Discussion

The results of the parametric study are given in Table 3 and moment-rotation curves are given in Figs. 10 and 11. Two different capacities of the end-plated connections are reported in Table 3. M_u represents the maximum moment observed in the models up to 0.04 rad rotation. On the other hand, $M_{j,Rd}$ is calculated from the intersection moment that passes from the initial and post stiffness. The moment design capacity ($M_{j,Rd}$) is also called plastic resistance [21, 24, 32]. It should also be noted that the plastic bending capacity of the beam is 283 kN.

Table 3. The results of parametric study

Models	$M_{EC,1}$	$M_{EC,2}$	$M_{j,Rd}$	M_u	$M_u/M_{j,Rd}$	$M_{EC,1}/M_{j,Rd}$	$M_{EC,2}/M_{j,Rd}$
M16-tp=10mm	54	65	87	142	1.6	0.62	0.75
M16-tp=15mm	98	105	147	182	1.3	0.67	0.71
M16-tp=20mm	143	143	153	200	1.3	0.93	0.93
M16-tp=25mm	156	156	176	222	1.3	0.89	0.89
M16-tp=30mm	169	169	195	237	1.2	0.86	0.86
M20-tp=10mm	54	73	114	180	1.6	0.47	0.64
M20-tp=15mm	119	129	186	237	1.3	0.64	0.70
M20-tp=20mm	167	186	223	270	1.2	0.75	0.83
M20-tp=25mm	224	224	239	284	1.2	0.94	0.94
M20-tp=30mm	241	241	256	297	1.2	0.94	0.94
M24-tp=10mm	54	73	128	210	1.6	0.42	0.57
M24-tp=15mm	122	155	195	271	1.4	0.62	0.79
M24-tp=20mm	192	211	283	301	1.1	0.68	0.75
M24-tp=25mm	253	283	283	314	1.1	0.90	1.00
M24-tp=30mm	322	322	283	314	1.1	1.14	1.14
M27-tp=10mm	54	77	153	231	1.5	0.35	0.50
M27-tp=15mm	122	173	221	295	1.3	0.55	0.78
M27-tp=20mm	213	237	283	310	1.1	0.75	0.84
M27-tp=25mm	275	311	283	314	1.1	0.97	1.10
M27-tp=30mm	351	373	283	314	1.1	1.24	1.32
M30-tp=10mm	54	82	164	250	1.5	0.33	0.50
M30-tp=15mm	122	183	283	314	1.1	0.43	0.65
M30-tp=20mm	216	265	283	314	1.1	0.76	0.94
M30-tp=25mm	300	342	283	314	1.1	1.06	1.21
M30-tp=30mm	375	431	283	314	1.1	1.32	1.52

It is seen in Table 3 that the ratio of $M_u/M_{j,Rd}$ varies between 1.1 and 1.6. As the thickness of the end-plate decreases, the ratio of $M_u/M_{j,Rd}$ increases. On the other hand, as the bolt diameter increase, the ratio of $M_u/M_{j,Rd}$ decreases.

Increasing thickness of the end-plate resulted in an increase in both plastic and ultimate moment capacity. However, when the bending moment capacity of the beam is lower than that of the connection, increasing the thickness of the end-plate has no influence on the capacity. The same results can be drawn for the diameter of the bolts.

The prediction of Eurocode using Method 2 ($M_{EC,2}$) is averagely 17% higher than that of Method 1 ($M_{EC,1}$). This ratio reached a maximum of 51% when a thin end-plate is utilized with large size of bolt. The ratio of $M_{EC,2}/M_{EC,1}$ is high when Mode 1 is governing failure mode. When governing failure mode is Mode 3, the prediction of Methods 1 and 2 is equal.

The ratio of moment prediction by Eurocode to the plastic moment capacity is averagely 0.77 and 0.87 for Methods 1 and 2, respectively. The accuracy of the Eurocode prediction is high when governing failure mode is Mode 2 and 3. However, the accuracy is relatively low when governing failure mode is Mode 1. The accuracy decreases as the bolt diameter increases. On the other hand, the accuracy increases as the end-plate increases.

It is observed in Fig. 10 that as the diameter of the bolt increases, the initial stiffness of the connection increases. The increase in the stiffness is more pronounced in the relatively thin plates. When the connection exceeds the bending capacity of the beam, the diameter of the bolts has a very slight influence on the initial stiffness of the connection.

It is observed in Fig. 11 that as the thickness of the end-plate increases, the initial stiffness of the connection increases. The increase in the stiffness is more pronounced in the relatively small bolts. When the connection exceeds the bending capacity of the beam, the thickness of the end-plate has a very slight influence on the initial stiffness of the connection.

Table 4 demonstrates the failure modes observed in the numerical models and the prediction of Eurocode. The failure modes defined in Eurocode are shown in Fig. 3. The corresponding failure modes captured by the numerical model are demonstrated in Fig. 12. The failure of the beam is also shown in Figure 13. It can be said that the failure modes predicted by Eurocode are quite accurate when it is compared with the results of numerical models.

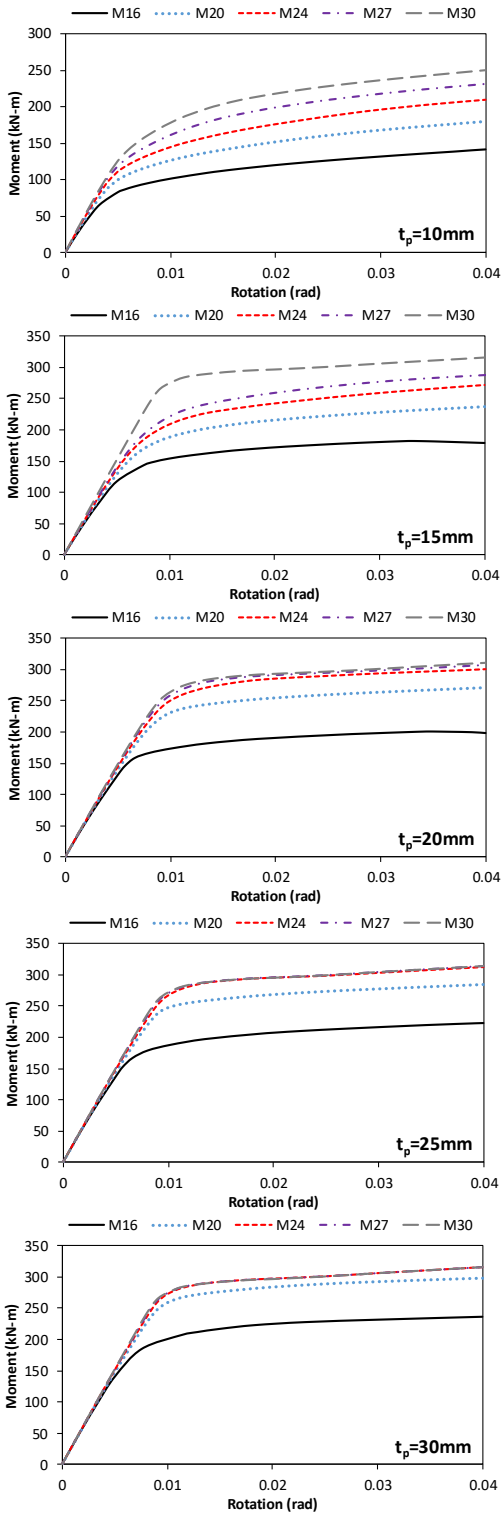

Fig. 10 The results of the parametric study of different bolt diameter

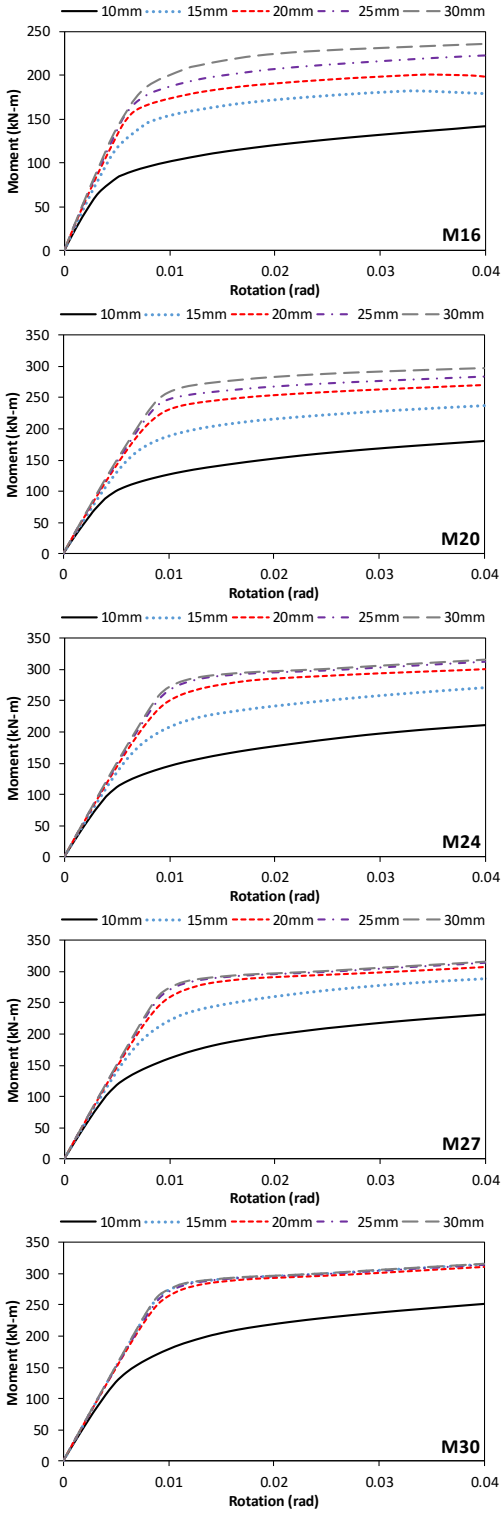

Fig. 11 The results of the parametric study of different end-plate thickness

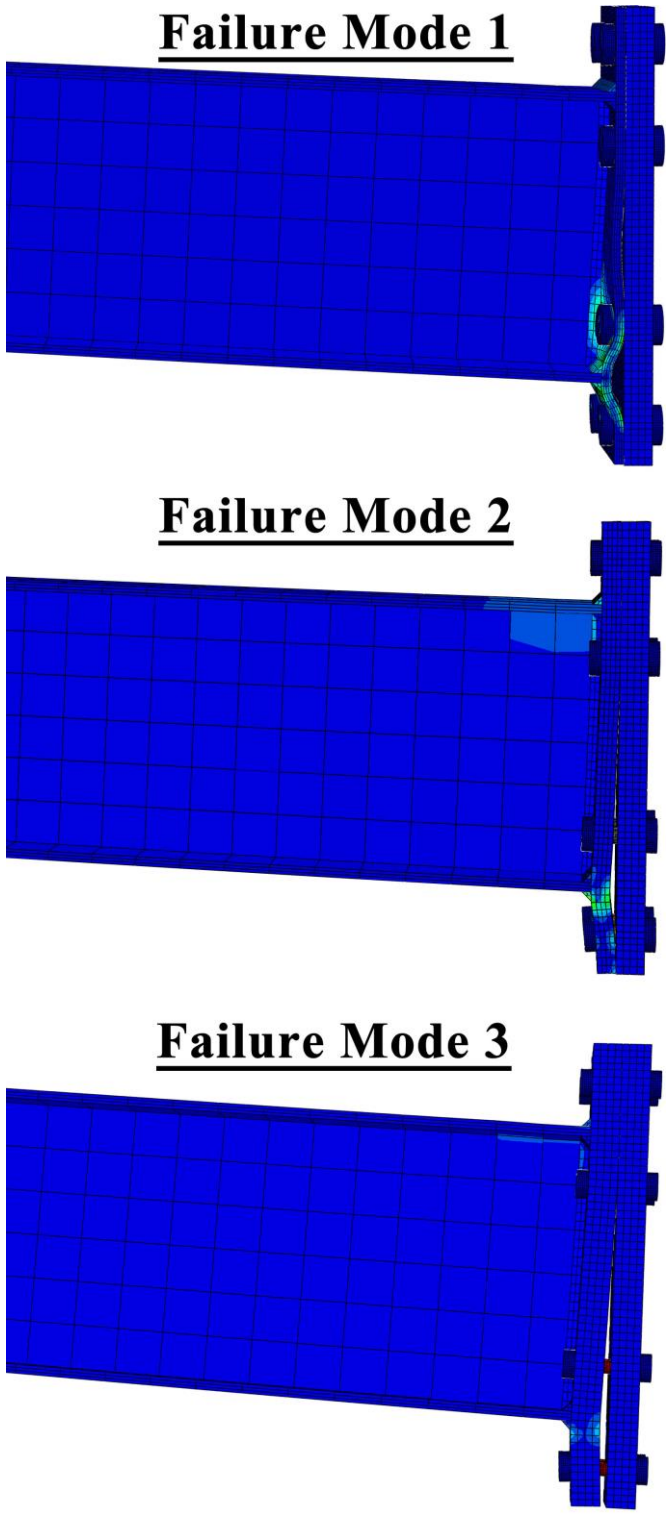

Fig. 12 Failure modes of end-plate

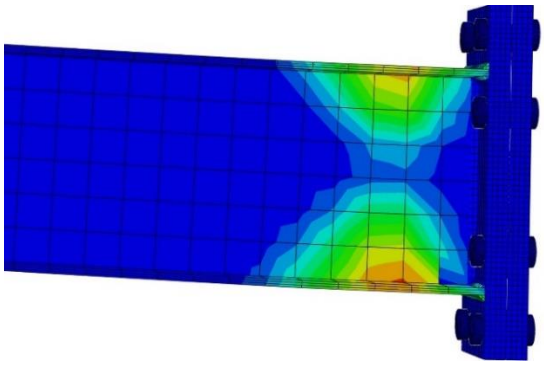

Fig. 13 Failure of the beam

Table 4. The results of parametric study

Models	Finite Element		Eurocode 3	
	Bolt Row 1	Bolt Row 2	Bolt Row 1	Bolt Row 2
M16-tp=10mm	Mode 1	Mode 1	Mode 1	Mode 1
M16-tp=15mm	Mode 1	Mode 1	Mode 1	Mode 2
M16-tp=20mm	Mode 2	Mode 2	Mode 2	Mode 3
M16-tp=25mm	Mode 3	Mode 3	Mode 2	Mode 3
M16-tp=30mm	Mode 3	Mode 3	Mode 2	Mode 3
M20-tp=10mm	Mode 1	Mode 1	Mode 1	Mode 1
M20-tp=15mm	Mode 1	Mode 1	Mode 1	Mode 2
M20-tp=20mm	Mode 2	Mode 2	Mode 1	Mode 2
M20-tp=25mm	Mode 2	Mode 2	Mode 2	Mode 3
M20-tp=30mm	Mode 2	Mode 2	Mode 2	Mode 3
M24-tp=10mm	Mode 1	Mode 1	Mode 1	Mode 1
M24-tp=15mm	Mode 1	Mode 1	Mode 1	Mode 1
M24-tp=20mm	Mode 1	Mode 1	Mode 1	Mode 2
M24-tp=25mm	Beam Failure	Beam Failure	Beam Failure	Beam Failure
M24-tp=30mm	Beam Failure	Beam Failure	Beam Failure	Beam Failure
M27-tp=10mm	Mode 1	Mode 1	Mode 1	Mode 1
M27-tp=15mm	Mode 1	Mode 1	Mode 1	Mode 1
M27-tp=20mm	Beam Failure	Beam Failure	Mode 1	Mode 2
M27-tp=25mm	Beam Failure	Beam Failure	Beam Failure	Beam Failure
M27-tp=30mm	Beam Failure	Beam Failure	Beam Failure	Beam Failure
M30-tp=10mm	Mode 1	Mode 1	Mode 1	Mode 1
M30-tp=15mm	Beam Failure	Beam Failure	Mode 1	Mode 1
M30-tp=20mm	Beam Failure	Beam Failure	Mode 1	Mode 1
M30-tp=25mm	Beam Failure	Beam Failure	Beam Failure	Beam Failure
M30-tp=30mm	Beam Failure	Beam Failure	Beam Failure	Beam Failure

5. Conclusion

A comprehensive numerical study was conducted to examine the effects of the bolt diameter and end-plate thickness on the behavior of the end-plated connections using the finite element tool, ABAQUS. Firstly, the developed numerical model is verified with an experimental study. Later, an extensive parametric study is carried out. The load-displacement curves, failure modes, plastic and ultimate moment capacities are presented. Moreover, the results were compared with the prediction of Eurocode in terms of the resistance and failure modes. The following conclusions can be drawn from this study:

- The ultimate capacity of the end-plated connection is significantly higher than the plastic capacity of the connection. The reason for this can be attributed to strain hardening [19]. The difference is more pronounced in thin plates with large bolts.
- Method 1 predicts moment capacity averagely 17% higher accuracy than Method 2 does.
- The accuracy of Eurocode prediction is higher when the governing failure mode is Mode 2 or Mode 3. The accuracy of Eurocode prediction is low when the governing failure mode is Mode 1.
- Eurocode significantly underestimates the capacity of the end-plated connection when a relatively thin end-plate is utilized. The accuracy decreases as end-plate thickness decreases or the bolt diameter increases.
- The initial stiffness of the end-plated connection increases as the bolt diameter or end-thickness increases.
- Eurocode is highly able to predict the failure modes of the end-plated connection.

In future studies, the reason for the conservative prediction of Eurocode for thin end-plated connections should be investigated. The capacity of the end-plated connection significantly depends on the yield line patterns [33]. The reason for this underestimation may be attributed to the distance between the yield lines, which is declared by Özkılıç and Topkaya [19]. Therefore, an extensive experimental program should be conducted to investigate the effects of the parameters including thickness of end-plate, width of end-plate, gage distance, bolt diameter, weld thickness, the distance between the bolt row and the flange and edge distance on the capacity of the end-plated connections.

References

[1] Inel M, Ozmen HB, Bilgin H. Re-evaluation of building damage during recent earthquakes in Turkey. Engineering Structures, 2008;30:412-27. https://doi.org/10.1016/j.engstruct.2007.04.012
[2] Işık E, Işık MF, Bülbül MA. Web based evaluation of earthquake damages for reinforced-concrete buildings. Earthquakes and Structures, 2017;13:423-32.
[3] Kalman Šipoš T, Hadzima-Nyarko M. Seismic risk of Croatian cities based on building's vulnerability. Tehnički vjesnik, 2018;25:1088-94. https://doi.org/10.17559/TV-20170708190145
[4] Hakan Arslan M. Application of ANN to evaluate effective parameters affecting failure load and displacement of RC buildings. Natural Hazards and Earth System Sciences, 2009;9:967-77. https://doi.org/10.5194/nhess-9-967-2009
[5] EN 1993-1-8: Design of steel structures, Part 1.8: Design of joints. 2005.
[6] Özkılıç YO. A new replaceable fuse for moment resisting frames: Replaceable bolted reduced beam section connections. Steel and Composite Structures, 2020;35(3):353-70. http://dx.doi.org/10.12989/scs.2020.35.3.353

[7] Nikoukalam MT, Dolatshahi KM. Development of structural shear fuse in moment resisting frames. Journal of Constructional Steel Research, 2015;114:349-61. https://doi.org/10.1016/j.jcsr.2015.08.008
[8] Moradi Garoosi A, TahamouliRoudsari M, Hosseini Hashemi B. Experimental evaluation of rigid connection with reduced section and replaceable fuse. Structures, 2018;16:390-404. https://doi.org/10.1016/j.istruc.2018.11.010
[9] Mahmoudi F, Dolatshahi KM, Mahsuli M, Nikoukalam MT, Shahmohammadi A. Experimental study of steel moment resisting frames with shear link. Journal of Constructional Steel Research, 2019;154:197-208. https://doi.org/10.1016/j.jcsr.2018.11.027
[10] Özkılıç YO. Experimental and numerical studies on replaceable links for eccentrically braced frames. Ph. D. Dissertation, Middle East Technical University, 2020. https://doi.org/10.1016/j.engstruct.2021.112225
[11] Özkılıç YO. Optimized stiffener detailing for shear links in eccentrically braced frames. Steel and Composite Structures, 2021;39(1):35-50. http://dx.doi.org/10.12989/scs.2021.39.1.035
[12] Özkılıç YO, Bozkurt MB, Topkaya C. Mid-spliced end-plated replaceable links for eccentrically braced frames. Engineering Structures, 2021;237:112225. https://doi.org/10.1016/j.engstruct.2021.112225
[13] Özkılıç YO, Topkaya C. Extended End-Plate Connections for Replaceable Shear Links. Engineering Structures, 2021;240:112385. https://doi.org/10.1016/j.engstruct.2021.112385
[14] Ng YH, Shanmugam NE, Yu CH, Liew JYR. Experimental Investigation of the Behaviour of End-Plate Connections. In Advances in Steel Structures: Proceedings of International Conference on Advances in Steel Structures, 11-14 December, 1996. https://doi.org/10.1016/B978-008042830-7/50055-3
[15] Yorgun C. Evaluation of innovative extended end-Plate moment connections under cyclic loading. Turkish Journal of Engineering and Environmental Sciences, 2002;26:483-92.
[16] Abidelah A, Bouchaïr A, Kerdal DE. Experimental and analytical behavior of bolted end-plate connections with or without stiffeners. Journal of Constructional Steel Research, 2012;76:13-27. https://doi.org/10.1016/j.jcsr.2012.04.004
[17] Girão Coelho AM, Bijlaard FSK, Simões da Silva L. Experimental assessment of the ductility of extended end plate connections. Engineering Structures, 2004;26:1185-206. https://doi.org/10.1016/j.engstruct.2000.09.001
[18] Zhu C, Rasmussen Kim JR, Yan S, Zhang H. Experimental Full-Range Behavior Assessment of Bolted Moment End-Plate Connections. Journal of Structural Engineering, 2019;145:04019079. https://doi.org/10.1061/(ASCE)ST.1943-541X.0002368
[19] Özkılıç YO, Topkaya C. The plastic and the ultimate resistance of four-bolt extended end-plate connections. Journal of Constructional Steel Research, 2021;181:106614. https://doi.org/10.1016/j.jcsr.2021.106614
[20] Bezerra LM, Bonilla J, Silva WA, Matias WT. Experimental and numerical studies of bolted T-stub steel connection with different flange thicknesses connected to a rigid base. Engineering Structures, 2020;218:110770. https://doi.org/10.1016/j.engstruct.2020.110770
[21] Chen C, Zhang X, Zhao M, Lee C-K, Fung T-C, Chiew S-P. Effects of Welding on the Tensile Performance of High Strength Steel T-stub Joints. Structures, 2017;9:70-8. https://doi.org/10.1016/j.istruc.2016.09.008
[22] Girão Coelho AM, Bijlaard FSK, Gresnigt N, Simões da Silva L. Experimental assessment of the behaviour of bolted T-stub connections made up of welded plates. Journal of Constructional Steel Research, 2004;60:269-311. https://doi.org/10.1016/j.jcsr.2003.08.008

[23] Guo H, Liang G, Li Y, Liu Y. Q690 high strength steel T-stub tensile behavior: Experimental research and theoretical analysis. Journal of Constructional Steel Research, 2017;139:473-83. https://doi.org/10.1016/j.jcsr.2017.10.007
[24] Liang G, Guo H, Liu Y, Li Y. Q690 high strength steel T-stub tensile behavior: Experimental and numerical analysis. Thin-Walled Structures, 2018;122:554-71. https://doi.org/10.1016/j.tws.2017.10.042
[25] Zhu X, Wang P, Liu M, Tuoya W, Hu S. Behaviors of one-side bolted T-stub through thread holes under tension strengthened with backing plate. Journal of Constructional Steel Research, 2017;134:53-65. https://doi.org/10.1016/j.jcsr.2017.03.010
[26] EN 1998-1: Design of structures for earthquake resistance-Part 1: General rules, seismic actions and rules for buildings. 2004.
[27] Bouchaïr A, Averseng J, Abidelah A. Analysis of the behaviour of stainless steel bolted connections. Journal of Constructional Steel Research, 2008;64:1264-74. https://doi.org/10.1016/j.jcsr.2008.07.009
[28] Massimo L, Gianvittorio R, Aldina S, da Silva Luis S. Experimental analysis and mechanical modeling of T-stubs with four bolts per row. Journal of Constructional Steel Research, 2014;101:158-74. https://doi.org/10.1016/j.jcsr.2014.05.004
[29] Brown D, Iles D, Brettle M, Malik A, Group BSC. Joints in Steel Construction: Moment-Resisting Joints to Eurocode 3. 2013.
[30] Yun X, Gardner L. Stress-strain curves for hot-rolled steels. Journal of Constructional Steel Research, 2017;133:36-46. https://doi.org/10.1016/j.jcsr.2017.01.024
[31] Qiang X, Wu N, Luo Y, Jiang X, Bijlaard F. Experimental and Theoretical Study on High Strength Steel Extended Endplate Connections After Fire. International Journal of Steel Structures,2018;18:609-34. https://doi.org/10.1007/s13296-018-0020-3
[32] Faralli AC. Large deformation of T-stub connection in bolted steel joints. Ph. D. Dissertation, University College London, 2019.
[33] Özkılıç YO. A Comparative Study on Yield Line Mechanisms for Four Bolted Extended End-Plated Connection. Challenge Journal of Structural Mechanics, 2021;7(2).

Research on Engineering Structures & Materials
journal homepage: http://jresm.org
Research Group

Technical Note

Fatigue behavior of flush reinforced welded hand-holes in aluminum light poles

Cameron R. Rusnak*[a], Craig C. Menzemer[b]

Auburn Science and Engineering Center (ASEC 210), Department of Civil Engineering, The University of Akron, Akron, Ohio, USA.

Article Info

Article history:
Received 22 Jan 2021
Revised 06 May 2021
Accepted 07 May 2021

Keywords:

Fatigue test;
Flush welded aluminum hand-hole details;
Fatigue comparison;
Design S-N curve;
High cycle fatigue

Abstract

Hand-holes are used in welded aluminum light poles which provide access to electrical wiring for both maintenance and installation. Light poles are usually slender and subjected to cyclic loading due to the response from wind. In the field, localized fatigue cracking around hand-holes has been observed but few studies have focused on the resistance of welded aluminum hand-holes. In this study, three-point bending fatigue tests were conducted on full-scale light poles samples. Specimens were constructed with a "flush" hand-hole utilizing reinforcement placed on the inside of the tube, with the handhole located 18 in from the base. Five of these poles, each containing two separate details were tested. Among the ten details that were tested, eight failed as a result of fatigue cracking and the resulting data is compared to current design S-N curves of the Aluminum Design Manual (ADM). A finite element model was created to help understand the local stresses around the hand-hole. this study, the estimation of shear force for blind shear ram type blowout preventer was investigated by using Finite Element Method (FEM). So, the effect of the blowout preventer working condition on shear force requirement for shear operation could be accurately approximated by simulating the entire process, and ram geometry could be optimized to reduce force and energy used to shear the tube by plastic deformation.

1. Introduction

Overhead luminaires are often supported by welded aluminum light poles and serve to illuminate sidewalks, roadways, parking lots and recreational areas among others. The material used in these types of applications is often aluminum. Aluminum has several advantages, including being light weight, possessing a high strength to weight ratio, good corrosion resistance, as well as ease of joining. Light Poles may be classified as slender structures that are subjected to wind loads. Both aluminum and steel structures that are exposed to repeated loads may fail due to localized fatigue cracking. Light poles often contain a hand-hole that gives access for maintenance and connection of electrical wiring. Electrical wiring runs through conduit and into the open hollow section of the pole where final electrical connections are made with the luminaires [1,2].

Stress concentrations occur when there is a change in the cross-section of a structural member. A change in cross section may be associated with connections, copes, keyways, and cutouts among others. Modern fatigue design utilizes a statistically determined lower bound of data for design S-N curves, established from full-scale testing [3, 4]. A series of S-N curves within specifications represent a ranking of the stress concentration condition and consist of common mechanical and structural details. A way to improve fatigue life is to eliminate low fatigue performance structural details and minimize changes in cross-

*Corresponding author: crr44@uakron.edu
[a] orcid.org/0000-0002-9048-594X; [b] orcid.org/0000-0002-6529-085X
DOI: http://dx.doi.org/10.17515/resm2021.248st0122tn

section. There are several structural details of interest in welded aluminum light poles. These include mono-tube arm joints, the pole to base connection, and electrical access hand-holes. Previous studies have primarily focused on steel light pole details and their behavior is well established. This is not the case of electrical access holes in welded aluminum structures [5].

Web report, NCHRP number 176, provided results of fatigue tests of unreinforced and reinforced hand-holes in welded steel structures. Lehigh University conducted fatigue tests on details associated with high mast steel light poles. Thirteen specimens with hand-holes possessing different geometries were evaluated. During testing, none of the hand-hole details cracked [6]. To compliment the experiments, a finite element study was conducted and was used to provide an estimate of the stress concentration around the different hand-holes. The numerical analysis in combination with test results found that the fatigue resistance of both the reinforced and unreinforced hand-holes were consistent with AASHTO Category E' [6].

Fatigue cracking associated with hand-holes has been observed in the field. NCHRP report number 469 describes fatigue cracks that have occurred in welded steel structures near hand-hole details in multiple states. These include New York, New Mexico, California and Minnesota [7]. After the failure of a high-mast welded pole in Iowa, multiple inspections found cracks associated with a hand-hole at another location. Some fatigue cracks were found in welded aluminum light poles mounted on the Mullica River Bridge after a violent storm in New Jersey in 2011 [8]. A fatigue failure associated with a more typical (not flush) hand-hole reinforcement on an aluminum light pole can be seen in Figure 1.

Fig. 1 Fatigue crack in welded aluminum light pole hand-hole in field

The University of Akron (UA) conducted a study on twenty light-pole samples with "typical" hand-holes containing the cast reinforcement shown in Figure 1. The cast reinforcement is joined to the outside of the poles with fillet welds. In addition to fatigue tests, several static tests were conducted in order to gain insight into the strain distribution around the hand-hole. This study found that typical reinforced welded hand-hole fatigue test data fell above both the category D and E design S-N curves of the Aluminum Design

Manual (ADM) [9]. Another study found that the change in diameter of the pole has some effect on the fatigue life [10].

Taghipoor and Damghani Nouri found that an increase in the cell angle of sandwich beams with an expanded metal core, up to θ = 90 degrees, increased axial and bending energy absorption by 624.4%. Numerical situations were also carried out using ABAQUS/EXPLCIT and the results were compared to the experimental data [11]. In a separate study, the same authors found that an increase in the size of the expanded metal cell core within a reasonable range improved the performance of a structure under bending collapse [12]. Tests of the sandwich beams were conducted in quasi-static three-point bending. Specific energy absorption of sandwich panels evaluated under axial impact was significantly improved by selection of an appropriate core [13].

During the current hand-hole fatigue study, five pole specimens, each containing two separate flush details were tested in high cycle fatigue. All poles were supplied to The University of Akron and were manufactured to standards typical for the industry. In addition to fatigue tests, a finite element model was created to aid in the understanding of the distribution of local stress around the handholes. The intention of this study was to examine the fatigue behavior of flush hand-hole details and to compare the results with previous work conducted at UA. In the field, "typical" reinforced hand holes are more common, but some prefer the flush insert design. The term "flush" denotes that the reinforcement is not visible from the outside. Rather the reinforcement is welded to the inside of the pole.

2. Experiments and Methods

2.1 Pole Geometry and Material Properties

Five aluminum specimens, with a total of ten details, were tested under cyclic loading to examine the fatigue behavior of the flush hand-holes. Each of the specimens were fabricated from 10 in (25.4 cm) diameter extruded 6063 aluminum alloy tubes with a ¼ in (0.635 cm) thick wall. Hand-holes measured 6 in (15 cm) in the longitudinal direction of the pole and 4 in (100 cm) in the transverse direction. Each hand-hole was reinforced on the inside of the pole with an extrusion that measured 9 ½ in (24 cm) in the longitudinal direction and 6.42 in (16.3 cm) in the transverse direction. Figure 2 depicts the design of this extrusion and Figure 3 shows the connection that uses longitudinal fillet welds to join the reinforcement extrusion to the inside of the pole around the hand-hole opening. The final samples measured 144 in (3.66 m) in length with the hand-holes placed 54 in (1.37 m) in from each end respectively. Each specimen consisted of three separate pieces as shown in Figure 4. The central tube containing the hand holes measured 72 in (183 cm) in length and had pole bases welded on either end. Hand holes in the center pole section were located 18 in (457 cm) from either end which represents the largest distance a welder can comfortably work inside of the 10 in (254 cm) diameter tube. Stub poles measuring 36 in (91 cm) were welded to a base and bolted to the base on either end of the center section. The stub pole sections were designed to increase the moment arm from the point of specimen bearing to the hand hole. Support rollers for the specimens were placed 6 in (15.2 cm) from each end. All specimens were Post-Weld Heat Treated (PWHT) [14]. Table 1 provides properties of 6063-T6 extrusions and the 4043-filler wire material.

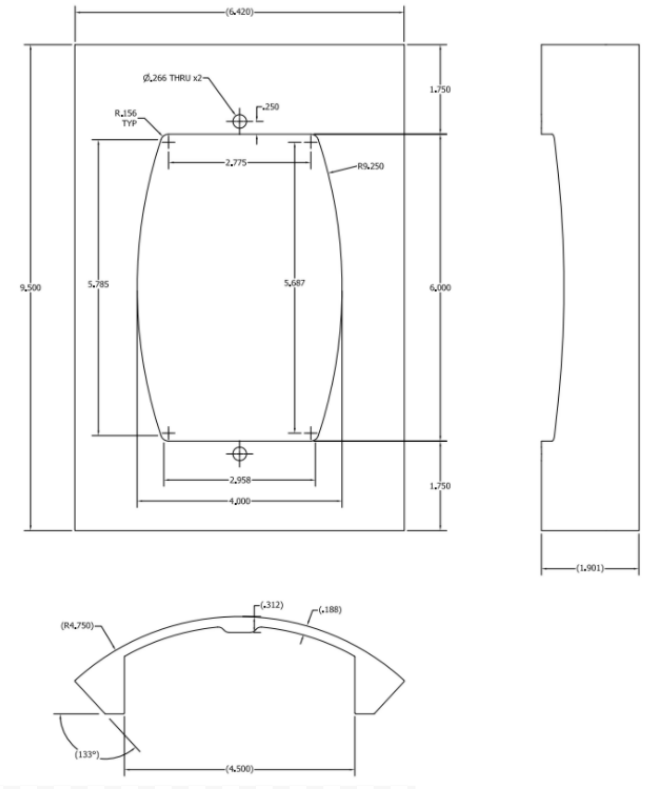

Fig. 2 Hand-hole reinforcement

Fig. 3 Welded insert plate

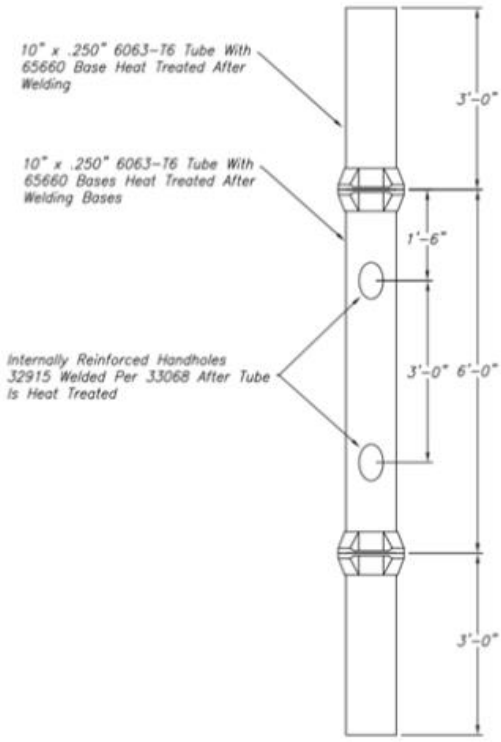

Fig. 4 Specimen design

Table 1 consists of the minimum mechanical properties of the aluminum and tube. Allowable bending strength of the tube used as a light pole is 13.6 ksi (94 Mpa).

Table 1. Mechanical properties of the aluminum hand-hole tubes along with the filler material.

Part Name	Alloy	Tensile Yield Strength	Ultimate Tensile Strength
Tube	6063-T6	213.7 MPa (31 ksi)	241.3 MPa (35 ksi)
Fillet Welding	4043	N/A	201.3 MPa (29.2 ksi)

2.2 Fatigue Tests

Figure 5 is a photograph of the three-point bending fatigue test setup in the Gas Turbine Testing Laboratory of The University of Akron. All of the earlier fatigue tests conducted at UA were in four-point bending. Three-point bending was used as the flush inserts were placed inside of the pole and limited the location of the hand hole to near the end of the specimens. Stub poles were added to increase the length and moment arm, but to ensure failure at the hand-hole required limiting the stress range at the base to tube connections.

Three-point bending provided the means to limit the stress range at the base connections and ensure failure at the hand-hole details.

A 55 kip (245 KN) MTS servo-hydraulic actuator and control system was used to apply the load to specimens. This actuator was mounted to a structural load frame that is capable of safely supporting 300 kips (1335 KN). Loads were applied to each of the specimens through a roller that was attached to the actuator. Supports consisted of rollers that were machined to fit the profile of the tubular specimens.

Fig. 5 Fatigue test set-up of flush welded aluminum hand-hole details

All the tests were conducted in load control, while strains were monitored using gages that were mounted around the hand-hole on the outside of the pole. Typical strain gage locations may be seen in Figure 6. On the first specimen tested, a strain gage was also placed at each 6 o'clock position and near each pole base respectively. Strain gages were ⅛ in (3.175 mm) in length with a resistance of 350 ohms. Strain readings were taken every two hours for 10 seconds using a Micro-Measurements System 8000 data acquisition device.

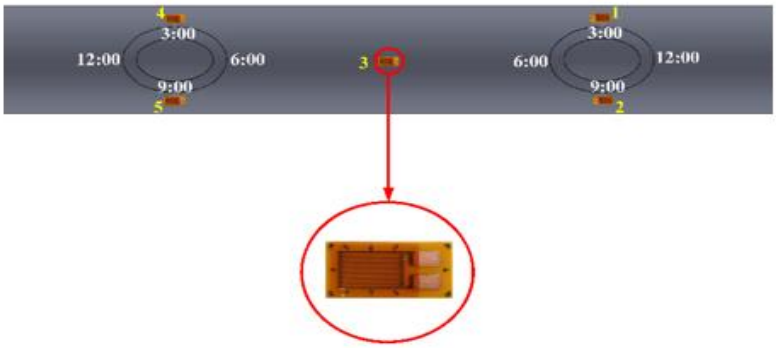

Fig. 6 Typical strain gage location and position around hand-hole

Each of the specimens was oriented so that the hand-hole openings were facing down and in tension during cyclical testing. An over-peak displacement limit was set in an attempt to ensure that cracking of one hand-hole would not lead to catastrophic failure of the specimen. This over-peak limit was set to a 10% larger displacement from the original test parameters. The 10% limit was determined from a previous study [15]. As larger displacements were indicative of cracking and the remaining cross section was close to failure. When one of the two hand hole details of a sample experienced fatigue cracking, the specimen's displacement would increase. When the displacement became larger than the original target plus 10%, the test would automatically shut down. After the first detail of the specimen failed, a moment clamp was placed on it for reinforcement. The test would then continue until the other hand-hole failed. The goal was to test the specimens and receive data from both details. Despite using the over-peak 10% detection limit, cracking around two hand-holes resulted in a catastrophic failure where the repair of the detail was not possible.

Five poles, each with two flush hand-hole details, were tested at a stress range between 14.2 MPa (2.06 ksi) and 49.6 MPa (7.2 ksi). The stress ranges were determined by taking the strain range at the point of loading and then converting to stress. Young's modulus of elasticity for aluminum is well known and a simplified conversion to stress was taken as the strain multiplied by the modulus [16]. Strain gages were installed adjacent to the hand-hole at the 3 and 9 o'clock position respectively with an additional strain gage in the middle of the specimen on the extreme tension fiber. On the first two specimens tested, strain gages were also placed at the 6 o'clock (Figure 6) position. In general, gages around the hand holes were placed within 2~3 times the tube thickness away from the edge of the hand-hole. Gages placed near the pole base were a thickness away from the weldment. All of the strain gages were connected to the data acquisition system to measure the strain during fatigue testing.

Specimens were cycled at either 1 or 2 Hz and tested around the clock. The difference between cycling at 1 and 2 Hz was negligible due to the size of the specimens and displacements in this study. It is generally accepted that corrosion fatigue is a rate limited process, and that the aluminum – water system is reactive. Differences in fatigue crack growth rates in aluminum under saturated water vapor conditions are not reaction rate dependent at low frequencies [17]. Specimens tested at a lower stress range were cycled at 2 Hz to decrease the time it took to conduct the test. Visual inspection of the hand-holes were conducted multiple times daily. Of the 10 hand-holes that were tested, 8 failed.

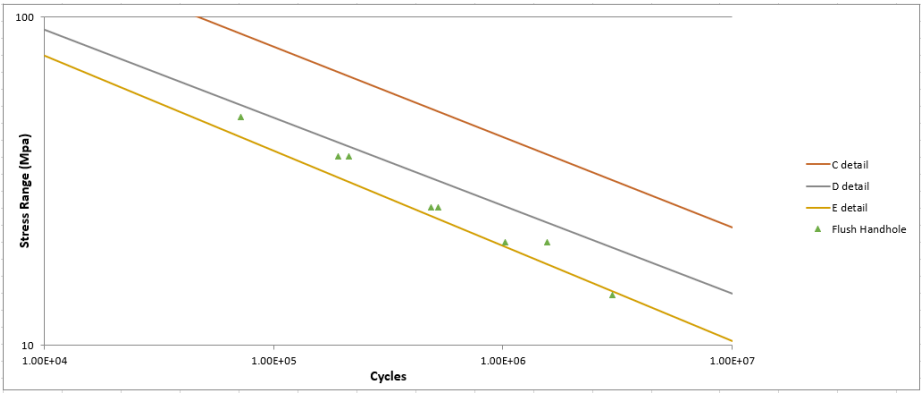

Fig. 7 Fatigue test results

Table 2. Tabulated fatigue results

Specimen	Handhole	N	Stress Range (MPa)	Hertz
1	A	485225	26.37	1
	B	522967	26.37	1
2	A	1558915	20.69	1
	B	1024092	20.69	1
3	A	2990006	14.22	2
	B	NA	14.22	2
4	A	191810	37.75	1
	B	213306	37.75	1
5	A	NA	49.64	1
	B	71648	49.64	1

The data collected from the fatigue tests can be seen in Figure 7 and tabulated results are available in Table 2. The stress range in Table 2 was calculated by subtracting the minimum stress in an average load cycle from the maximum stress in the same cycle. All of the data appears to follow the same trend, slightly above the "E detail" lower bound. Figure 8 shows a comparison between the flush details and a previous study conducted on 10in poles with a "typical" hand-hole detail. This figure shows that typical hand-hole details with reinforcement fillet welded to the outside of the tube (Figure 1) have a larger fatigue resistance as compared to flush hand-hole details.

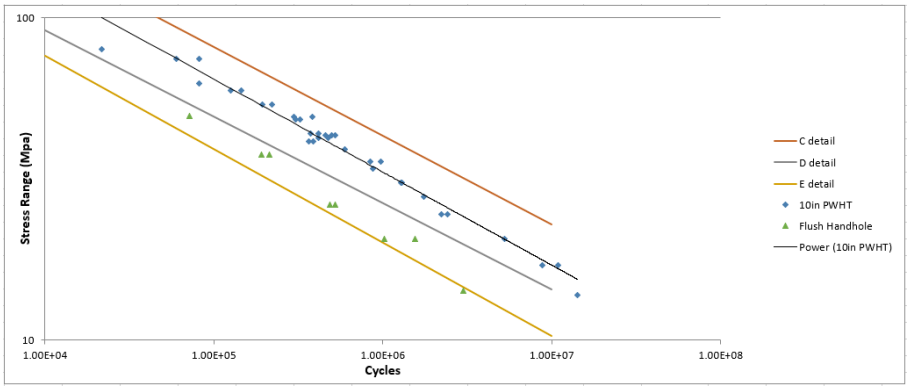

Fig. 8 Flush detail vs 10in poles with standard hand-hole reinforcement

During fatigue testing, the appearance of cracking was soon followed by failure. After cutting open several failed specimens, it became apparent that the hand-holes experienced failure that initiated in the weld that joins the reinforcement extrusion to the inside of the pole (closer to the load). Figure 9 shows the nature of the crack on the inside of the pole and Figures 10 and 11 show the weld removed from the pole. These images show how "jagged" the break is after failure and how initiation appears to coincide with the fillet weld termination. Often, fillet weld terminations in aluminum will contain shrinkage defects unless properly "buttoned up".

Fig. 9 Crack in weld

Fig. 10 Weld failure location

Fig. 11 Failure of pole sample

Final failure occurred as the crack broke though the surface of the tube, usually at the 6 o'clock position and propagated transversely in the pole until the displacement limit was reached and the test was stopped. In all of the specimens, initial cracking could not be observed due to the detail being inside of the pole. Figure 12 depicts a typical final failure. A few of the specimens contained a smaller crack, at about the 4 o'clock position. This still followed the same failure mode with the crack initiating within the weldment inside of the pole. Figure 13 shows an example of this type of cracking.

Fig. 12 Final failure

Fig. 13 Cracking in Pole Wall

3. Finite Element Modeling

A finite element (FE) model was constructed of the three-point bending specimen to help understand the stress distribution around the hand-holes. The model was created to represent the geometry of the specimens as manufactured and to examine the local stresses associated with the flush hand-hole design as compared to the more typical hand-hole detail with reinforcement welded to the outside of the pole. Local stresses are generally mesh dependent. Finer mesh sizes usually increase stresses local to important geometric details, whereas a course mesh often results in a reduction in local stresses. Elements used in this model consisted of both tetrahedral and hexahedral element types. The mix of element types provided a fairly accurate model of the specimen and provided for reasonable run times. If the model had been constructed with hexahedral elements only, the open handholes would not have been meshed in a realistic manner. A full model consisting of tetrahedral elements would make nodal loading more complex than necessary. A global mesh size of 0.25 was used and the model consisted of 1,347,205 nodes. One hundred twenty-six nodes were used to apply the load, each with a concentrated force of 0.0558 N and was identical to the load used in a previous study and made for easy comparison. One hundred twenty-six nodes were used to represent each support and were restricted in three degrees of freedom and acted as the rollers at each end. Figure 14 depicts the mesh.

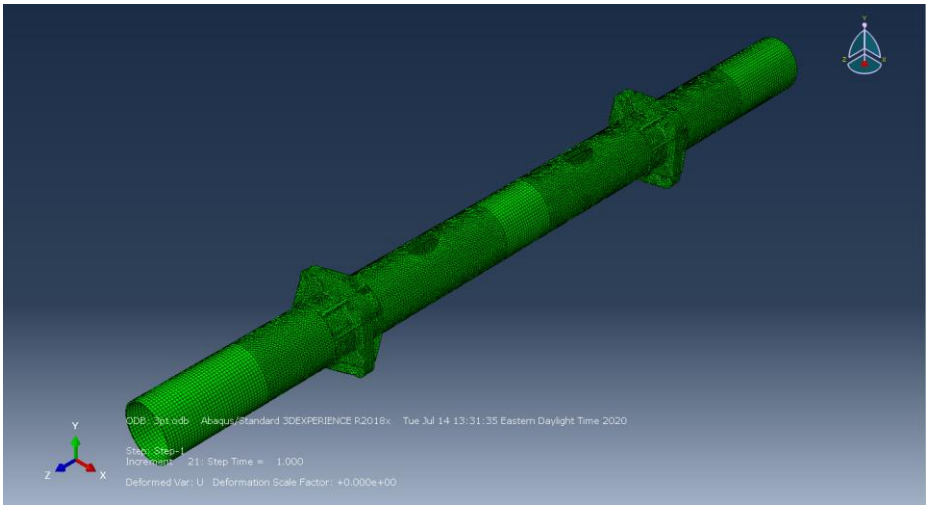

Fig. 14 Overall model

Stress “hot spots” indicate where fatigue cracking is likely to develop and where failure may occur. Figures 13-15 depict the stresses on the outside surface of the pole in X, Y, and Z directions respectively. The longitudinal stress corresponds to the Z axis and the transverse stress corresponds to the X axis. From Figure 13, there appears to be some concentration of stress around the reinforcement and at the corner of the reinforcement inside of the pole. Figure 14 shows how the stress formed around the reinforcement extrusion on the inside of the pole. Figure 15 depicts how the stress is transferred in the longitudinal direction.

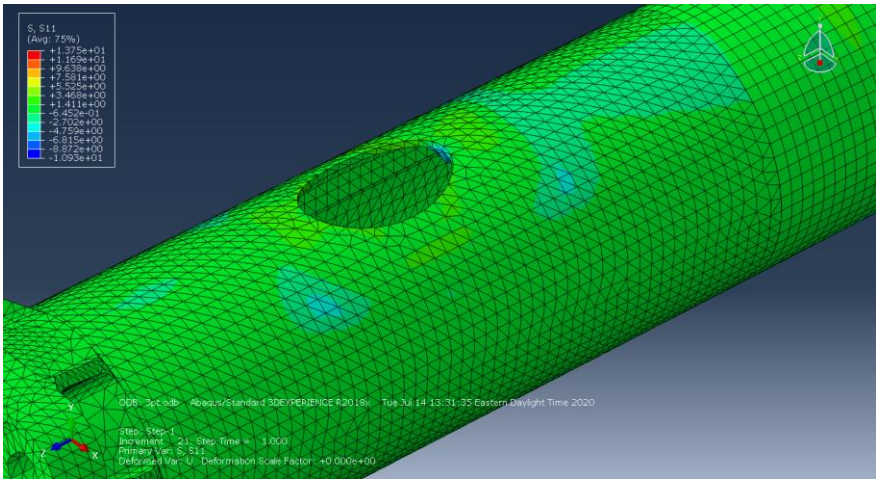

Fig. 13 Stress map in transverse direction

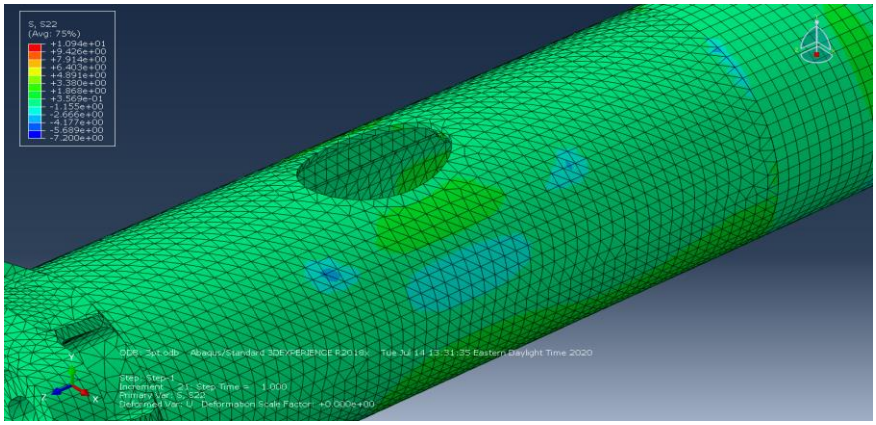

Fig.14 Stress map through the thickness of the pole

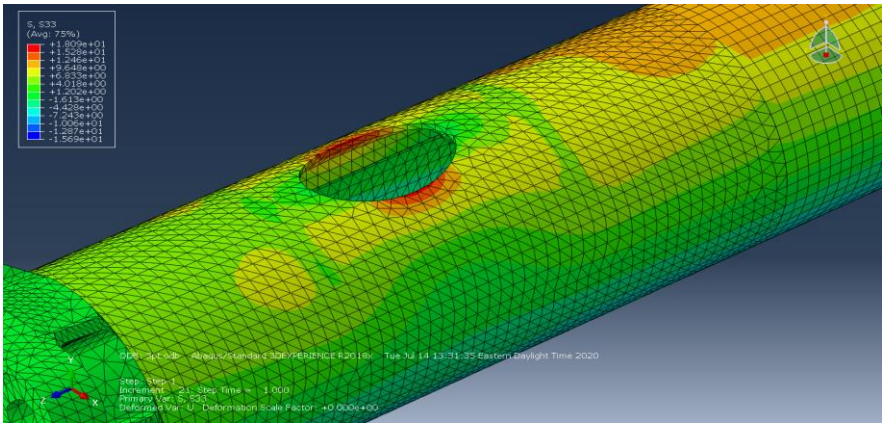

Fig. 15 Stress map in longitudinal direction

Figures 16-18 depict the same stress maps as Figures 13-15 but show the stresses on the inside of the pole. What was most interesting about these images is that one can see how the stress collected around the ends of the extruded reinforcement even without the weld being modeled. This was typically the initial point of cracking.

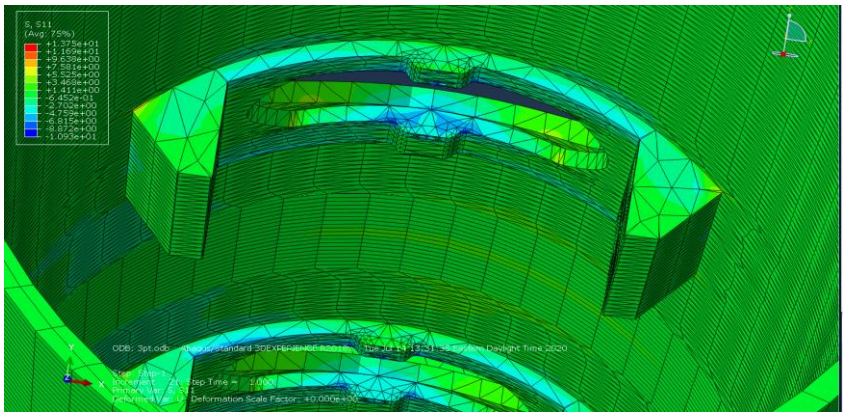

Fig. 16 Stress map in transverse direction inside pole

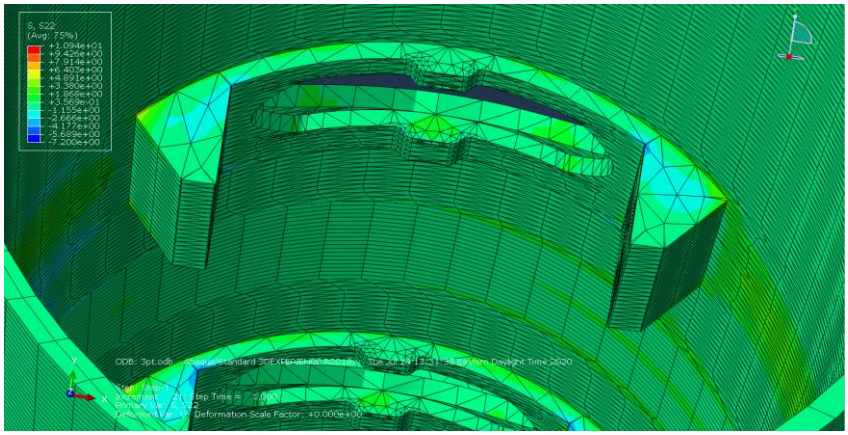

Fig. 17 Stress map through the thickness inside pole

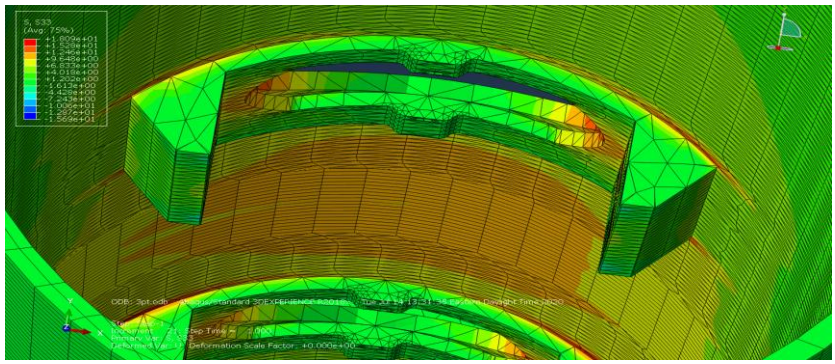

Fig. 18 Stress map in longitudinal direction inside pole

In comparing the finite element results to a previous study, the change in detail affects the stress concentration around the hand-holes. Figure 19 shows the stresses in the longitudinal direction of the specimen with a cast insert joined to the outside of the pole. In this figure, the stress is most prevalent around "ends" of the cast insert whereas the flush inserts had a larger and more prevalent stress concentration on the inside of the pole near the corners of the reinforcement extrusion.

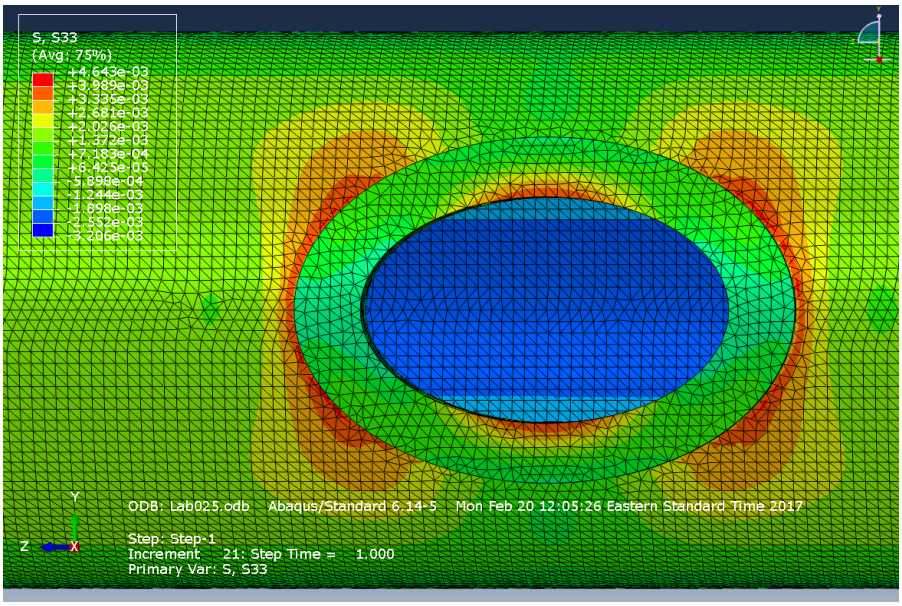

Fig. 19 Longitudinal stress map old study

4. Conclusions

Fatigue tests were conducted on aluminum light pole samples containing a welded flush hand-hole detail on the inside of the pole. The data collected shows the data being close to the "E detail" design S-N curve. It is important to note that lower bound is used to establish the design S-N curves. Additional test results would assist with evaluation of the data scatter and provide a better estimate of the lower bound, which would be expected to be lower than a category E detail. These test results were also compared to an older study that examined "typical" reinforced hand-hole details conducted at the University of Akron. In comparison, (Figure 8), the flush handhole details had significantly shorter fatigue lives than "typical" details that employed reinforcement joined to the outside of the pole.

Fatigue cracking of the flush details appeared abruptly, and the specimens failed shortly after a "crack" was visually observed. After further analysis it was determined that initial fatigue cracking occurred at the area on the inside of the pole where the fillet weld was terminated. In aluminum it is typical for weld terminations to contain shrink cracks if not properly "buttoned up" with additional weld metal. In this case, buttoning up of the termination is difficult with the detail on the inside of the pole. The fillet weld termination created an area that favored crack development.

A finite element model was created to show local stresses around the hand-hole in the flush design. The finite element model of the specimen with the flush detail was compared to the original model from the previous study of details with reinforcement joined to the outside of the pole. Examination of the images on both the outside and inside of the pole

reveals how the detail termination on the inside of the pole negatively affects the stress concentration. In the case of the longitudinal stresses, there was a concentration of stress near the "corners" of the internal reinforcement even without the weld explicitly modeled. Addition of the weld would complicate the model as difficulties including shrink cracks would require many additional elements. An amendment to the welding process could be recommended in order to reduce the possibility of shrink cracking.

In general, it was found that the older design had longer fatigue life as compared to that of the flush detail.

Acknowledgments

The authors would like to convey their gratitude to HAPCO Company for manufacturing the sample, providing valuable discussion, and funding for the study.

References

[1] Murthy MVV, Rao KP, Rao AK. On stresses around an arbitrarily oriented crack in a cylindrical shell. Int J Solids Struct 1974; 10: 1243-1269. https://doi.org/10.1016/0020-7683(74)90071-7

[2] Durelli AJ, Parks VJ, Feng HC. Stresses around an elliptical hole in a finite plate subjected to axial loading. J Appl Mech 1966; 33: 192-195. https://doi.org/10.1115/1.3624979

[3] Aluminum Design Manual: Specification for Aluminum Structures. The Aluminum Association, Arlington, VA, USA; 2010.

[4] Fisher JW, Kulak GL, Smith IFC. A fatigue primer for structural engineers. National Steel Bridge Alliance: AISC; 1998.

[5] AASHTO (American Association of State Highway and Transportation Officials). Standard specifications for structural supports for highway signs, luminaires and traffic signals (LRFDLTS-1), Washington, DC, USA; 2015.

[6] Roy S, Park YC, Sause R, Fisher JW, Kaufmann EJ. Cost-effective connection details for highway sign, luminaire, and traffic signal structures. NCHRP 10-70 web-only Doc. 176, Transportation Research Board, Washington, DC, USA; 2011.

[7] Dexter RJ, Ricker NJ. Fatigue-resistant design of cantilevered signal, sign, and light supports, NCHRP Rep 469. Univ of Minnesota, Minneapolis, MN, USA; 2002.

[8] Menzemer C. Examination of several Mullica river bridge light poles, corresponding to J. Bowman, Hapco, USA; 2012

[9] Daneshkhah AR, Schlatter CR, Rusnak CR, Menzemer CC. Fatigue behavior of reinforced welded hand-holes in aluminum light poles. Engineering Structures and Materials Vol 188. https://doi.org/10.1016/j.engstruct.2019.03.013

[10] Rusnak CR. Fatigue behavior in reinforced electrical access holes in aluminum light pole support structures. Master's thesis, the University of Akron, Akron, OH, USA; 2019.

[11] Taghipoor H, Damghani Nouri M. Axial crushing and transverse bending responses of sandwich structures with lattice core. J Sandw Struct Mater [Internet]. 2018 Feb 26. https://doi.org/10.1177/1099636218761321

[12] Taghipoor H, Noori MD. Experimental and numerical study on energy absorption of lattice-core sandwich beam. Steel Compos Struct [Internet]. 2018;27(2):135–47

[13] Taghipoor H, Eyvazian A, Ghiaskar A, Praveen Kumar A, Magid Hamouda A, Gobbi M. Experimental and numerical study of lattice-core sandwich panels under low-speed impact. Mater Today Proc [Internet]. 2020 Mar;27(xxxx):1487–92. https://doi.org/10.1016/j.matpr.2020.03.001

[14] Hilty E, Menzemer C, Manigandan K, Srivatsan T. Influence of welding and heat treatment on microstructure, properties and fracture behavior of a wrought aluminum alloy. Emerg Mater Res 2014; 3:230-242. https://doi.org/10.1680/emr.14.00006

[15] Schlatter CR. Fatigue behavior of the reinforced electrical access hole in aluminum light pole structures. Master's thesis, the University of Akron, Akron, OH, USA; 2017.
[16] The Aluminum Association. Aluminum Standards and Data 2017 Metric SI, USA; 2017
[17] Menzemer C, Srivatsan T.S. The effect of environment on fatigue crack growth behavior of aluminum alloy 5456. Materials, Science & Engineering 1999. https://doi.org/10.1016/S0921-5093(99)00222-1
[18] The Aluminum Association. Specification for Aluminum Structures: Aluminum Design Manual (ADM) Washington, DC, USA; 2015.

Research on
Engineering Structures & Materials

CONTENT

In This Issue

Research Article
331 **Atike Ince Yardimci, Ahmet Sabri Ogutlu, Deniz Ogutlu**
Oxidizer gases effects on the diameter-controlled synthesis of carbon nanotubes

Research Article
347 **Angelo Traina, Han J.G.E. Gardeniers, Burcu Gumuscu**
Self-powered microfluidic device for the colorimetric detection of lithium via sequential reagent mixing

Research Article
361 **Lütfiye Altay, Mehmet Sarikanat, Merve Sağlam, Tuğçe Uysalman, Yoldaş Seki**
The effect of various mineral fillers on thermal, mechanical, and rheological properties of polypropylene

Research Article
375 **P. N. Ojha, Brijesh Singh, Puneet Kaura, Abhishek Singh**
Lightweight geopolymer fly ash sand: an alternative to fine aggregate for concrete production

Research Article
393 **Hikmat Daou, Wassim Raphael**
A Bayesian regression framework for concrete creep prediction improvement: application to Eurocode 2 model

Research Article
413 **Ercan Işık, Ehsan Harirchian, Hüseyin Bilgin, Kirti Jadhav**
The effect of material strength and discontinuity in RC structures according to different site-specific design spectra

Research Article
431 **Ali Bozer**
Seismic performance of shallow depth tuned liquid damper

Research Article
445 **Yasin Onuralp Özkılıç**
Investigation of the effects of bolt diameter and end-plate thickness on the capacity and failure modes of end-plated beam-to-column connections

Technical Note
465 **Cameron R. Rusnak, Craig C. Menzemer**
Fatigue behavior of flush reinforced welded hand-holes in aluminum light poles

Research Group